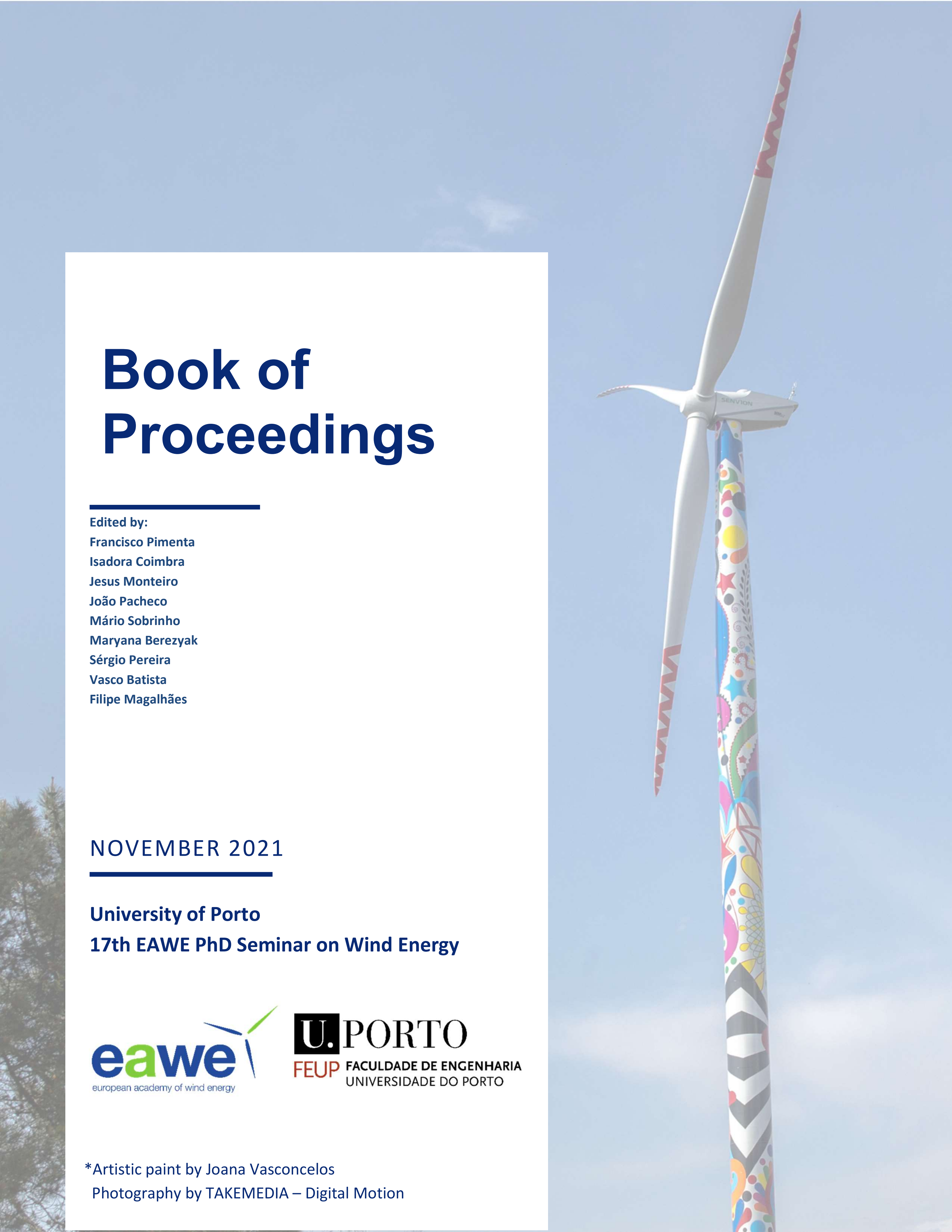

Book of Proceedings

Edited by:
Francisco Pimenta
Isadora Coimbra
Jesus Monteiro
João Pacheco
Mário Sobrinho
Maryana Berezyak
Sérgio Pereira
Vasco Batista
Filipe Magalhães

NOVEMBER 2021

University of Porto
17th EAWE PhD Seminar on Wind Energy

eawe
european academy of wind energy

U.PORTO
FEUP FACULDADE DE ENGENHARIA
UNIVERSIDADE DO PORTO

*Artistic paint by Joana Vasconcelos
Photography by TAKEMEDIA – Digital Motion

Index

AERODYNAMICS

A Data-Driven Analysis of Wake Mixing Dynamics

C. Muscari[a,b], P. Schito[a], A. Zasso[a], A. Viré[b], and JW van Wingerden[b]

[a]Politecnico di Milano
[b]TU Delft

E-mail: claudia.muscari@polimi.it

Keywords: IPC, Pulse, Wake, Horizontal Axis Wind Turbines, LES, Wake Mixing, DMD

In recent years, Dynamic Induction Control (DIC) started to gain popularity in the wind energy community. The goal of this family of wind farm control strategies is to promote wake mixing. This way, the velocity deficit within the wake recovers earlier and the inflow to the downstream turbine has a higher energy content.
An early important contribution to the field was given by Goit and Meyers in [1]. The work described a procedure for finding the optimal dynamic induction of turbines in a wind farm. However, this was done at a significant computational cost and resulted in an actuation with very large spikes. Munters and Meyers [2] observed that the optimal signal found in [1] closely resembled a sinusoid, which reduced the problem to determining the amplitude and frequency of the signal, while also reducing the detrimental effect on loads. The resulting control strategy is called the Pulse.
While the positive effects of DIC have been demonstrated in simulations and wind tunnel tests ([3]) we do not yet fully understand the dynamics of the wake.
This work aims to provide insight into it and in particular into the phenomena that promote the mixing. This is done by focusing on the evolution of the most relevant coherent structures and observing its dependency on the excitation frequency.
With Dynamic Mode Decomposition (DMD), we chose a data-driven approach to analyze high fidelity LES data. The Simulator fOr Wind Farm Applications (SOWFA, [4]), is used to generate this data.
The turbine considered in the study is the DTU 10 MW research turbine. Figures 1 and 2 result from a one turbine simulation. In this case,the blade pitches where collectively actuated with a sinusoidal signal with a 4° amplitude and $St = 0.2Hz$. The inflow was uniform with a wind speed of $9\,\mathrm{m/s}$.
The DMD is then applied on the flow field. Figure 1 represents the Power Spectral Density of the most energetic modes as a function of the Strouhal Number. We can observe that the natural frequency of the first one is very close to the excitation frequency.
In Figure 2 we isolate these same modes in the flow field representation. The same analysis is repeated for different excitation frequencies and amplitudes looking at the evolution in time and space of the dominant modes and commenting on the recognizable patterns. By focusing on the modes that contribute the most to the flow dynamics we gather insight on what causes the increased wake recovery rate in DIC techniques. This knowledge can then be used for the optimization of the signal parameters in complex layouts and conditions.

References

[1] Goit J P and Meyers J 2015 *Journal of Fluid Mechanics* **768** 5–50

[2] Munters W and Meyers J 2018 *Wind Energy Science* **3** 409–425

[3] Frederik J A, Weber R, Cacciola S, Campagnolo F, Croce A, Bottasso C and van Wingerden J W 2020 *Wind Energy Science* **5** 245–257

[4] Churchfield M, Lee S and Moriarty P 2012 *National Renewable Energy Laboratory*

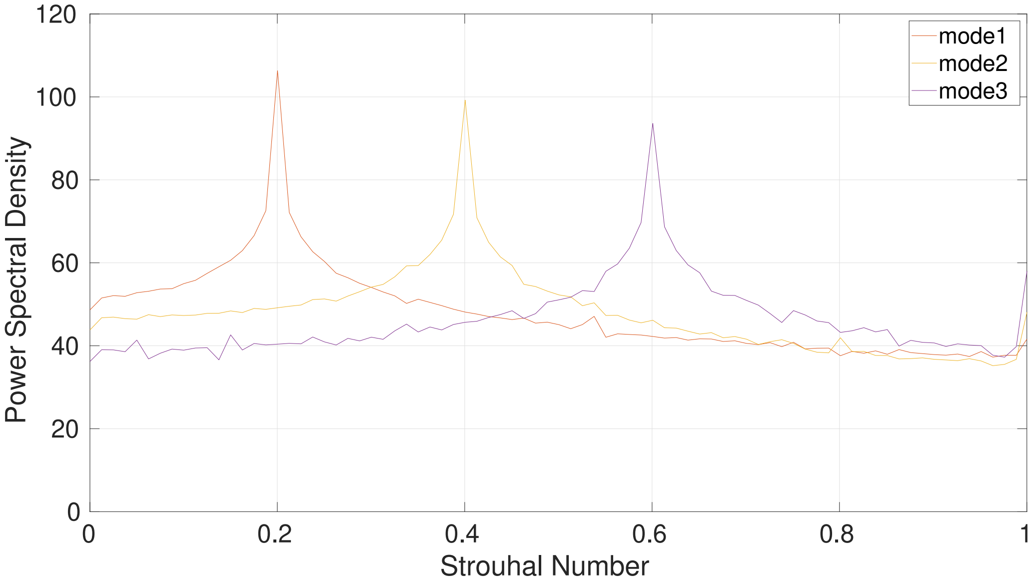

Figure 1: This spectrum is representative of the energy content of the first three modes, which are also shown in Figure 2. Their contribution accounts for abouy half of the energy content in the wake.

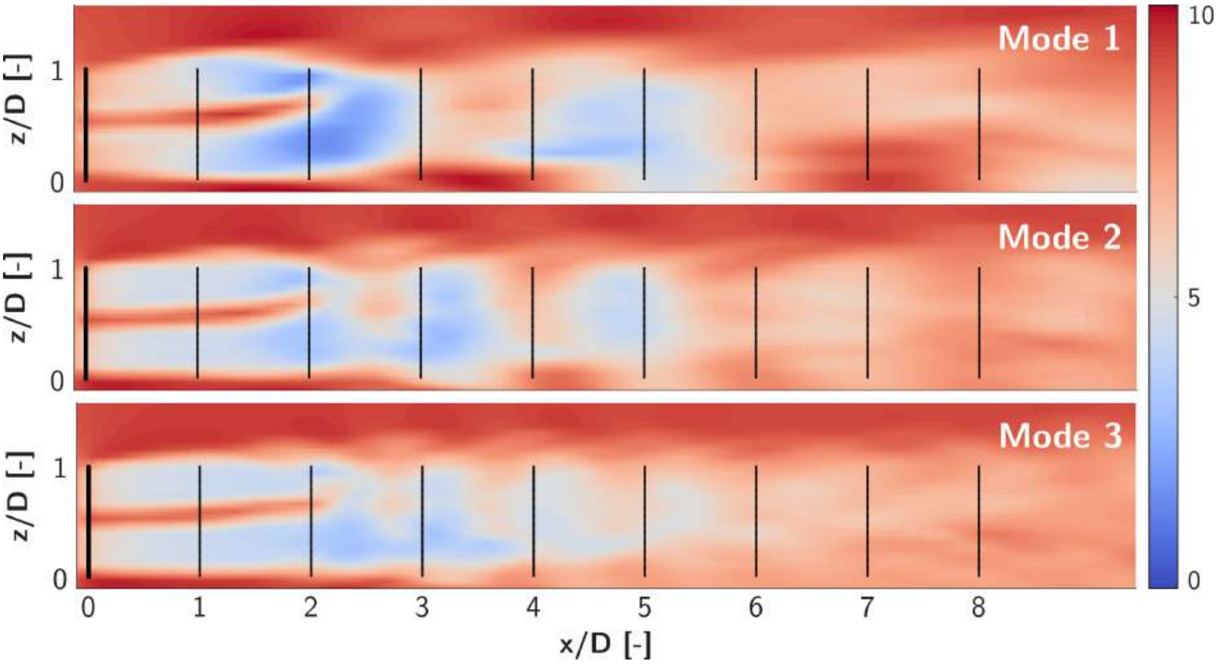

Figure 2: Vertical slices of the instantaneous stream-wise velocity at $y = 0$ and $t = 1600\,\mathrm{s}$. From top to bottom we can see the first, second and third DMD modes all superimposed to the zero mode which is representative of the mean.

Experimental investigation of the wake of a model floating wind turbine under idealized conditions

T Messmer[a], **M Hölling**[a], and **J Peinke**[a]

[a]Institute of Physics and ForWind, University of Oldenburg , 26129 Oldenburg, Germany

E-mail: `thomas.messmer@uni-oldenburg.de`

Keywords: FOWT's wake, aerodynamics, wind tunnel experiment, model turbine

1 Introduction

A floating offshore wind turbine (FOWT) interacts with the incoming wind field and ocean waves resulting in additional complex motions of the turbine compared to a bottom-fixed machine. These added movements affect the turbine itself as well as the generated wake and its development with increasing distance to the turbine (Fu, 2019) [1]. In a wind farm, the wake of a turbine might be the inflow for turbines located downstream inside the farm and result again in additional dynamics which might lead to higher extreme loads, fatigue loads and power losses. Due to the lack of full scale data, either wind tunnel experiments or numerical investigations might help to better understand the wake generated by floating turbines. In this study, the wake features of a model wind turbine submitted to mono-harmonic motions was investigated experimentally in the large wind tunnel of the University of Oldenburg (UOLD).

2 Experimental set-up

The tests were carried out in the closed-loop wind tunnel ($3 \times 3\ m^2$ inlet section) of the University of Oldenburg with the MoWiTO 0.6 turbine under idealized conditions, i.e laminar wind and imposed sinusoidal motion. The model turbine was mounted on top of a Stewart platform which allows to mimic the motions of a floating wind turbine in the six degrees of freedom (DoF). The picture of the figure 1 depicts the experimental set-up used for the measurement campaign. One-degree of freedom sinusoidal motion were imposed by the platform on the turbine, multiple amplitudes and frequencies of oscillation were tested. The six degrees of freedom of a FOWT were thus covered in this study. A total of 21 hot wire anemometers, arranged in cross-shape, were placed in the wake of the turbine at different downstream positions ranging from 2D to 10D (D being the rotor diameter, D = 0.58 m). This set-up enabled to measure the vertical and horizontal axial wind profiles in the wake with a sampling rate of 10 kHz.

Bayati et al. (2017) [2] measured wind speeds in the wake of a model turbine subjected to imposed sinusoidal motion in surge and outlined the relevance of the so-called wake reduced frequency, $f_{red} = f.D/U_0 = 1/V_w^*$, for the estimation of the level of aerodynamic unsteadiness. From the previous equation, the wake reduced velocity, V_w^*, can be interpreted for surge DoF as the number of rotor diameters that would travel an air particle flowing at a speed of U_0, during one motion cycle of the platform at the frequency, f. The larger the wake reduced velocity the lower the unsteadiness. Based on the capability of the platform, the experimental study covered a range of wake reduced frequencies from 0.02 to 0.4 with different amplitudes for each degree of freedom.

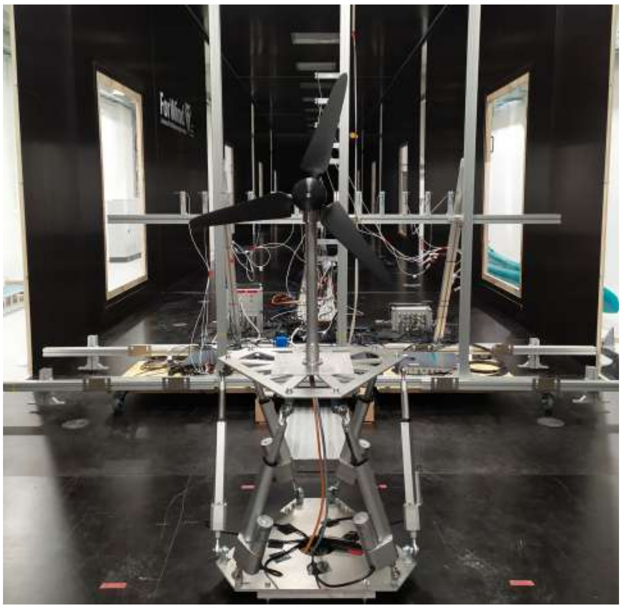

Figure 1: Picture of the MoWiTO 0.6 model turbine mounted on a Stewart platform and installed in the large wind tunnel of the UOLD

3 Preliminary results

The impact of the platform's motion (amplitude and frequency) as well as the degree of freedom on the wake was assessed regarding the following quantities:

- Profile of mean wind speed deficit
- Wake recovery
- Profile of turbulence intensity and turbulent energy content
- Spectral content
- 2^{nd} order turbulence features

The analysis of the wind speed signal measured will be presented at the conference.

Acknowledgements

This project has received funding from the European Union's Horizon 2020 research and innovation programme under the Marie Sklodowska-Curie grant agreement N°860879 as part of the FLOAting Wind Energy netwoRk (FLOAWER) consortium.

References

[1] Fu, S., Jin, Y., Zheng, Y., Chamorro, L. P. (2019). *Wake and power fluctuations of a model wind turbine subjected to pitch and roll oscillations.* Applied Energy, 253, 113605. doi:10.1016/j.apenergy.2019.113605

[2] Bayati, I., Belloli, M., Bernini, L., Zasso, A. (2017). *Wind Tunnel Wake Measurements of Floating Offshore Wind Turbines.* Energy Procedia, 137, 214–222. doi:10.1016/j.egypro.2017.10.375

A Vortex-Based Smearing Correction Applied to Coupled Aeroelastic - Actuator Method Computations in LES

E L Hodgson[a], **S. J. Andersen**[a], **N. Troldborg**[b], **A. Meyer Forsting**[b], **R. F. Mikkelsen**[a], and **J. N. Sørensen**[a]

[a]Technical University of Denmark, Department of Wind Energy, Anker Engelunds Vej 1, 2800 Kgs Lyngby, Denmark
[b]Technical University of Denmark, Department of Wind Energy, Frederiksborgvej 399, 4000 Roskilde, Denmark

E-mail: `emlh@dtu.dk`

Keywords: Actuator line, tip correction, large eddy simulations, wind farms

Abstract

Coupling actuator methods in LES with an aeroelastic solver can produce a higher fidelity modelling tool for representing wind turbines, as the body forces and actuator positions are influenced by the interaction between the modelled blades and flow. Hodgson *et al.* [1] verified the coupling between the EllipSys3D flow solver and the aeroelastic code Flex5, but peaks observed in blade loading at the root and tip for the actuator methods were attributed to the Gaussian smearing of the body forces in the domain. This work presents the implementation of the vortex smearing correction described in Meyer Forsting *et al.* [2] into the EllipSys3D - Flex5 coupling, which recovers the missing induction at the blade and therefore can remove the discrepancies seen. The correction methodology is also extended to account for flexible blade deformations. The beneficial impact on blade loading and steady state performance is demonstrated, with removal of the unphysical loading peaks, and improving of the power and thrust behaviour particularly when operating below rated velocity.

1 Introduction

Robust and accurate high-fidelity wind turbine and flow modelling is key to the effective planning and operation of wind farms. A coupling between the aeroelastic tool Flex5 and the EllipSys3D flow solver was verified by Hodgson *et al.* [1], using the Shen tip correction [3] for both actuator disc and actuator line computations. However, peaks in loading were observed at the blade root and tip, and were attributed to the Gaussian smearing used to apply the body forces to the domain. The vortex smearing correction [2, 4] is capable of rectifying this, as it recovers the missing induction at the blade by combining a near wake model for the trailed vorticity, and a Lamb-Oseen viscous core model. This method has also been extended to account for rotor coning by [5], by projecting the extracted velocities and blade positions by the cone angle. Therefore, the contributions of the present work are as follows: implementing the vortex smearing correction into the Flex5 - EllipSys3D coupling; and extending the method to account for prebend and flexible deformations of the blades.

2 Methodology

Simulations were conducted with the DTU10MW Reference Wind Turbine using coupled EllipSys3D - Flex5, and standalone Flex5 allowed comparison with BEM-based results. Validation of the vortex smearing correction implementation in the coupled setup was achieved through comparing blade loading with a standard AL in EllipSys3D. In the scenario with fixed rotational speed, pitch and cone angle, no flexibility or turbine control, and no flow forcing, identical results were observed.

After the validation, the implementation was extended to include flexibility. This is based on the same principle as the coning correction described in [5]; however instead of projecting by a fixed coning angle, individual angles are calculated at each blade section, therefore allowing for both prebend and instantaneous deformations to be accounted for.

3 Results

The impact of the vortex smearing correction on the coupled actuator simulations can be assessed through the steady state performance and blade loading; these results are shown below in Figure 1.

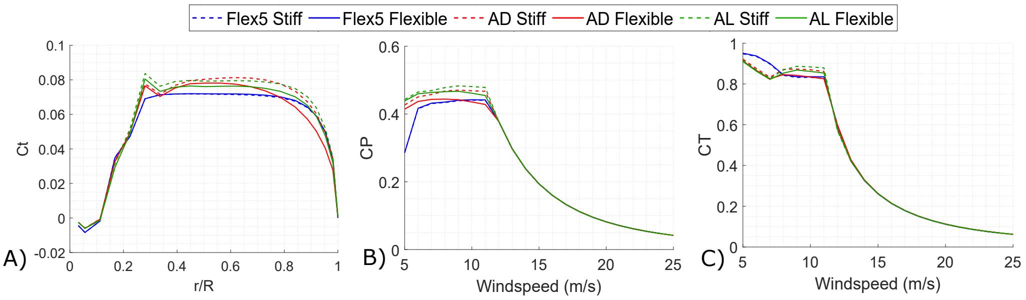

Figure 1: A) Tangential loading coefficient; B) CP; C) CT

The tangential loading graph shows that the vortex smearing correction substantially reduces the magnitude of the loading peaks at blade root and tip. Compared to the Shen correction results in [1] at the same inflow conditions, there is a 13% load reduction at both r/R = 0.3 and r/R = 0.9 for the flexible AL. This leads to a reduction in CP at below rated velocities, bringing the performance closer to that of standalone Flex5. The CT graph shows that with the new correction there is also a more consistent pitch regime between the four methods, as they all begin to reduce CT simultaneously. However, the trends between flexible and stiff turbine results are the same, with the flexible actuator disc having a lower loading towards the blade tip, as discussed in [1].

4 Conclusion

Coupling aeroelastic computations with actuator methods in LES allows the impact of flexibility to be studied, as the modelled blades can deflect and interact with the flow. The vortex smearing correction was created to address a fundamental issue in the actuator line formulation, and hence provides more physical loading predictions [2, 4]. This work combines these two advances in modelling and extends the smearing correction to include flexibility, and shows the impact in decreasing the non-physical load peaks and reducing CP at below rated conditions. Next, a full validation of the new coupled setup will be achieved against fully resolved simulations and experimental data in more complex flow cases.

References

[1] Hodgson E L, Andersen S J, Troldborg N, Forsting A M, Mikkelsen R F and Sørensen J N 2021 vol 1934 ISSN 17426596

[2] Forsting A R M, Pirrung G R and Ramos-García N 2019 *Wind Energy Science* **4**(2) 369–383 ISSN 2366-7451

[3] Shen W Z, Sørensen J N and Mikkelsen R 2005 *Journal of Solar Energy Engineering, Transactions of the ASME* **127**(2) 209–213 ISSN 01996231

[4] Dağ K O and Sørensen J N 2020 *Wind Energy* **23**(2) 148–160 ISSN 1095-4244

[5] Pirrung G R, Madsen H A, Kim T and Heinz J 2016 *Wind Energy* **19**(11) ISSN 10991824

Phase shift on surging wind turbines with a free-wake panel method

A F P Ribeiro[a], D Casalino[a]

[a] Delft University of Technology

E-mail: a.pintoribeiro@tudelft.nl

Keywords: offshore, wind energy, unsteady aerodynamics, hysteresis

1 Introduction

With the wind energy market leaning heavily towards the offshore market in recent years, floating wind turbines have become the focus of significant research. One of the many challenges of such configurations is that, due to oceanic waves, the rotor is subjected to large amplitude motions, making the aerodynamics of these turbines even more complex than that of traditional configurations. The UNAFLOW [1] project provided a simplified test case for a non-stationary rotor, by simulating a surging wind turbine in a wind tunnel, without any tilting of the tower.

We employ a source and doublet panel method [2] with free-wakes [3] and a vortex core model [4] in an attempt to capture phase shift effects on the aerodynamics of a surging wind turbine rotor. The code is initially validated with airfoil sections. We start with a thin airfoil and compare the results to Theodorsen theory [5].

Results are shown in figure 1 for a NACA0001 airfoil oscillating around the quarter chord at reduced frequency $k = 0.1$, where $k \equiv \omega c/2U$, where ω is the angular frequency $\omega = 2\pi f$, f is the frequency of the oscillations, c is the airfoil chord, and U is the freestream velocity. The oscillations follow $\alpha = \Delta\alpha \sin(\omega t)$, where α is the angle of attack, $\Delta\alpha$ is the amplitude of the oscillations (1°), and t is time. A large parametric study was conducted to investigate the source of the discrepancy, with most parameters not affecting the results at all (grid resolution, time step length, airfoil thickness, amplitude of oscillations, and airfoil span). We found that k was the only parameter that changed the accuracy of the simulations and that only very small values led to small errors.

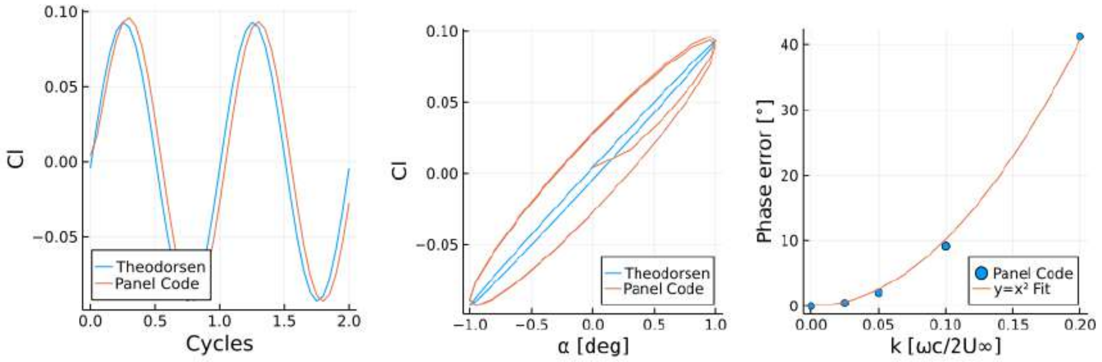

Figure 1 Theodorsen validation results.
(a) Time history for *k*=0.1. (b) Hysteresis loop for *k*=0.1. (c) Phase error versus *k*.

The UNAFLOW case has surging data up to f=2Hz, which (for U=4m/s, amplitude=15mm, at 241RPM) at the tip corresponds to k=0.002. Even though this is quite low, significant differences to experiments have been observed with BEM and lifting line methods coupled to dynamic stall models [1]. Figure 2 shows the time history of the thrust coefficient Ct for the aforementioned case and the amplitude and phase for several cases with the same flow conditions, but different values of surge frequency. The simulations match the experimental data well, showing phase of the thrust relative to the surging motion of about 90°.

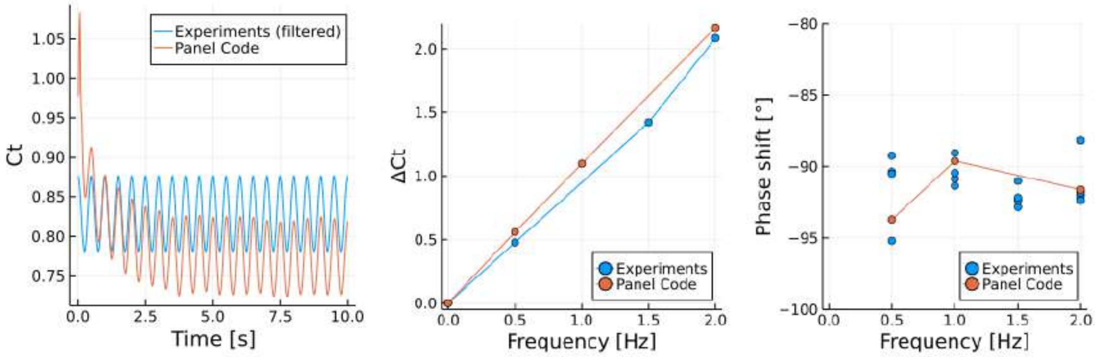

Figure 2 UNAFLOW validation results.
(a) Time history of *Ct* for *f*=2Hz. (b) *Ct* fluctuation amplitude. (c) Phase shift versus *f*.

Results from this study indicate that free wake panel methods achieve phase shift and amplitude levels which are similar to experimental data. The issues seen in the Theodorsen case are unlikely to appear in floating wind turbines due to tower motion, as those occur at very low frequencies [6], although high frequency velocity fluctuations could appear due to incoming turbulence.

Bibliography

[1] Bayati I, Belloli M, Bernini L, Boldrin D M, Boorsma K, Caboni M, Cormier M, Mikkelsen R, Lutz T, Zasso A, 2018, UNAFLOW project: UNsteady Aerodynamics of FLOating Wind turbines *Journal of Physics* **1037**

[2] Maskew B, 1987, Program VSAERO Theory Document: A Computer Program for Calculating Nonlinear Aerodynamic Characteristics of Arbitrary Configurations *NASA Contractor Report* **4023**

[3] Katz J, Plotkin A, 2001, *Low-Speed Aerodynamics* 2nd ed Cambridge University Press

[4] Ramasamy M, Leishman J G, 2007, A Reynolds number-based blade tip vortex model *Journal of the American Helicopter Society* **52** 214-223

[5] Theodorsen T, 1935, General Theory of Aerodynamic Instability and the Mechanics of Flutter *NACA Report* **496**

[6] Mahfouz, M Y, Molins, C, Trubat, P, Hernández, S, Vigara, F, Pegalajar-Jurado, A, Bredmose, H, Salari, M, 2021, Response of the International Energy Agency (IEA) Wind 15 MW WindCrete and Activefloat floating wind turbines to wind and second-order waves, *Wind Energy Science* **6** 867-883

17th EAWE PhD Seminar on Wind Energy
3-5 November 2021
Porto, Portugal

Preliminary data on Active Trailing Edge Flap aeroelastic models comparison

A Gamberini[a,b], **T Barlas**[b], and **A Gomez Gonzalez**[a]

[a]Siemens Gamesa Renewable Energy A/S, Brande, Denmark
[b]DTU, Dept. of Wind Energy, Roskilde, Denmark

`E-mail: andrea.gamberini@siemensgamesa.com`

Keywords: Trailing Edge Flap, Aeroelastic model, Validation

1 Introduction

Several studies have showed that actively controlled flaps located at the Wind Turbines (WT) blade trailing edge, so called Active Trailing Edge Flap Systems (ATEFS), are a promising technology on reducing fatigue and ultimate loads and increasing Annual Energy Production (AEP), see e.g. [1].
The validation of ATEFS aeroelastic engineering models and their load reduction applications at a full-scale is limited and not easy to perform. In [2], state-of-the-art BEM models of WT equipped with ATEFS have been compared with models of higher fidelity, including free-wake lifting line and fully resolved CFD models for an extensive code-to-code comparison. Subsystem validations have been performed with wind tunnel tests and on an outdoor rotating rig [3]. As for field tests on a full scale WT, only three are known: [4], [5]and [3]. These field tests confirmed the potential of ATEF in controlling the aerodynamic loads but also showed the need for further development and validation of the numerical ATEFS models. In this paper, the first results on the comparison of two ATEFS aeroelastic model are presents. The comparison aims to characterize the differences between the two models before they will be used in the ATEFS model validation based on field data obtained from a multi-megawatt WT prototype equipped with ATEFS.

2 Methodology

BHawC and HAWC2 aeroelastic codes have been selected for the ATEFS model comparison. Both are BEM-based aeroelastic tools: HAWC2 has been developed by DTU Wind Energy [6], including the Beddoes-Leishman type ATEFlap dynamic stall model [7]; BHawC is the SGRE internal aeroelastic tool [8]. For each tool, a model of the same reference WT equipped with ATEFS has been developed. The reference WT is the multi-megawatt SGRE WT prototype (SWT-DD-120) that has been equipped with an ATEFS on one of its blade in the VIAs project, a collaboration between SGRE and DTU Wind Energy Department [9]. The SGRE aeroelastic model of the WT prototype has been used as baseline for the development of the models in both BHAWC and HAWC2 codes.
The comparison of the two models has been focused on the blade root bending moments, Tower bottom bending moments and angle of attack along the blade. The comparison has the following structure:

1. Structural comparison, focused on mass, CoG and moment of inertia.
2. Modal analyses on WT modes.
3. Case 1A: Steady state comparison without ATEFS model with imposed WT operational parameters. To characterize the impact of the different structural and aerodynamic models of the two codes.
4. Case 1B: Steady state comparison with ATEFS and flap in neutral position. To evaluate the impact of the ATEFS models.

5. Case 1C: Steady state comparison with ATEFS and flap statically activated. To evaluate the impact of the ATEFS models.
6. Case 2A: Comparison with SGRE WT controller and without ATEFS model. Both steady state and turbulent wind (10% IEC turbulence intensity). To characterize the impact of the different implementation of the same SGRE controller on the two codes.

3 Results

The structural comparison of the two aeroelastic models of the WT PT has showed a difference below 1kg in the components mass, below 1 cm in the component CoG (except tower with 11 cm) and below 1% in the main WT moments of inertia. The modal analyses has showed a difference below 1.5% in the frequency of the first 20 WT modes. The comparison of the steady state simulations of the two aeroelastic WT models are summarized in table 1. The ATEF model with flap inactive (Case 1B) increases the difference of 1% in the blade root flapwise bending moment and reduces the difference of 2% in the tower bending moment. The full activation of the flap (Case 1C) further increase the blade root flapwise bending moment of another 1% but reduces the tower bending moment differences to 2%. The blade root edgewise bending moment is instead not affected by the ATEF model.

Case	Blade Root Flapwise Bending Moment		Blade Root Edgewise Bending Moment	Tower Bottom Bending Moment	
	Abs Max	Mean	Abs Max	Abs Max	Mean
1A	0% to 3%	0.5% to 2%	-2% to 1%	-2% to -8%	-2% to -3%
1B	-1% to 3%	0.5% to 3%	-2% to 1%	-2% to -6%	-1% to -3%
1C	-1% to 4%	0.5% to 4%	-2% to 1%	-2% to 2%	-2% to -1%

Table 1: Overview of the main load differences between HAWC2 and BHawC steady state simulations

4 Conclusions

The comparisons have showed a good agreement between the results of the aeroelastic model of the WT PT developed in BHawC and the one developed in HAWC2. The ATEFS models increase the load differences but still within an acceptable uncertainty value. The comparison where both the WT controller and turbulent wind are introduced will define the baseline difference between the two models that will be used in the next phase of the PhD project for the model validation with field data obtained from the VIAs project.

Acknowledgements

This industrial PhD is funded by Danmarks Innovationsfond, Case no. 9065-00243B, PhD Title: ”Advanced model development and validation of Wind Turbine Active Flap system”.

References

[1] Barlas T, Pettas V, Gertz D and Madsen H A 2016 *Journal of Physics: Conference Series* vol 753 (Institute of Physics Publishing) ISSN 17426596

[2] Prospathopoulos J M *et al.* 2021 *Wind Energy* **24** 357–378 ISSN 10991824 URL `https://doi.org/10.1002/we.2578`

[3] Gonzalez A G, Enevoldsen P, Barlas T K, Madsen H A and Olsen A S 2020 **1618** 52024 ISSN 17426596

[4] Berg J C, Barone M F and Resor B R 2013 *51st Aiaa Aerospace Sciences Meeting Including the New Horizons Forum and Aerospace Exposition 2013*

[5] Castaignet D, Barlas T K, Buhl T, Poulsen N K, Wedel-Heinen Jens J, Olesen N A, Bak C and Kim T 2014 *Wind Energy* **17** 549–564 ISSN 10991824, 10954244

[6] Larsen T and Hansen A 2007 *How 2 HAWC2, the user's manual* (*Denmark. Forskningscenter Risoe. Risoe-R* no 1597(ver. 3-1)(EN)) (Risø National Laboratory) ISBN 978-87-550-3583-6

[7] Bergami L, Gaunaa M and Technical Univ of Denmark R N L f S E W E D 2012 *ATEFlap aerodynamic model, a dynamic stall model including the effects of trailing edge flap deflection* ISBN 9788755039346

[8] Fisker Skjoldan P 2011 *Aeroelastic modal dynamics of wind turbines including anisotropic effects* (Risø National Laboratory) ISBN 9788755038486

[9] Gomez Gonzalez A, Enevoldsen P B, Madsen H A and Barlas A 2022 *TORQUE 2022*

17^{th} EAWE PhD Seminar on Wind Energy
3-5 November 2021
Porto, Portugal

The influence of meshing regarding the accuracy of CFD simulations

S C Breitkopf[a], **C Hartz**[a], and **S Turek**[b]

[a]TU Dortmund University, Chair of Structural Design, August-Schmidt-Str. 6, 44227 Dortmund, Germany
[b]TU Dortmund University, Institute of Applied Mathematics (LS 3)

E-mail: `sophie.breitkopf@tu-dortmund.de`

Abstract

The design of wind turbines, as almost purely functional structures, is mainly driven by efficiency. Part of the design approach is the accurate simulation of the overall wind behavior, including load cycles for fatigue analysis and aerodynamic optimization to increase the durability and efficiency of wind turbines. The current approach combining wind tunnel testing and computational structural analysis is an expensive and time-consuming process. CFD analysis has the potential for a combined assessment of fluid dynamics and structural mechanics applicable to each specific situation. A factor for the current lack of accuracy in CFD analysis is the quality of the mesh including the reproduction of turbulence in the model. The results can often be improved by a higher mesh density which requires more computational power. This study analyzes various meshing layouts and presents the range of results in quantified charts.

Comparable mesh convergence studies are undertaken for the flow around a cylinder benchmark (2D laminar flow at a low Reynolds-number, 1996) in *Ansys Fluent* and *OpenFoam*. The results are evaluated for the drag and lift coefficient as well as the pressure difference. Adjusted ratios between zones of different gradients are investigated within this research refining meshing guidelines resulting in an optimized mesh.

This research quantifies the accuracy regarding the mesh topology and required density. Seeking the same accuracy for the drag coefficient and pressure difference the mesh density varies by up to a factor of 10, the lift coefficient shows even higher variation with a factor of more than one hundred between different mesh topologies. A better understanding regarding the mesh topology and required density can lead to a more efficient performance-based design process for wind turbines using CFD analysis.

Keywords: aerodynamics, CFD, mesh topology, mesh density, mesh optimization

1 Introduction

Computational Fluid Dynamics (CFD) simulations are highly dependent on the mesh topology and density. In spite of their importance, meshes are often only a side issue in published CFD studies. This research focuses on the accuracy of CFD simulations for different mesh topologies and densities. As computational power imposes a constraint on complex CFD simulations the aim of this study is to ensure a high accuracy solution with a minimum number of cells.

The Navier-Stokes-Equation describing laminar and turbulent fluid flow is a complex non-linear problem. CFD uses discretization methods to retrieve approximate solutions for those differential equations. Spatial discretization requires a sufficient mesh and schemes to calculate algebraic solutions at different points throughout the mesh while temporal discretization uses time steps in transient solutions. In order to determine the influence of the mesh induced error regarding the accuracy of the simulation a benchmark example is needed. This study focuses on circular cross sections as used for wind turbine towers. For an incompressible laminar flow at a Reynolds number of 20 (compare figure 1) the analytical steady result of the drag c_D and lift c_L coefficient as well as the pressure difference Δ_p between luv- and leeward side are known with a minimum accuracy of 10^{-10} [1][2]. At this low Reynolds number only a narrow turbulence wake forms as the separations points lie close to the rear of the cylinder [3]. For laminar flow the near wall flow is also considered laminar and the wall shear stress is therefore less dependent on the distance between the first cell centroid and the wall than for turbulent flow [4]. The influence of the mesh in this laminar case can therefore be analyzed with the least amount of additional factors influencing the solution as faster turbulent flows require turbulence models, wall functions and are time dependent.

2 Meshing accuracy

In CFD simulations inaccuracies may occur due to model errors e.g. from the insufficiently simulated turbulence, discretization errors, (iterative) solution errors and integration errors [5]. This paper focusses on the discretization error from insufficient meshing.
Grid refinement studies are undertaken for each topology as normally a higher accuracy of the results and therefore a reduction of errors can be observed with mesh refinement. Being obligatory for CFD simulations the grid refinement studies or mesh dependency tests can prove that a solution is independent from the mesh and the accuracy doesn't change with further refinement [4][6].
The requirements for the accuracy of CFD simulations depend on their specific application. For example, when specifying wind loads on wind turbine towers with wind tunnel or CFD tests a safety factor of 1.5 has to be applied for the ultimate limit state of the structure according to the EuroCode [7].
For the wind velocities around buildings guideline [8] already states specified accuracies for the simulated velocity and turbulence intensity of ±5% or an absolute difference of < 0.01 compared to model results. This has to be fulfilled with a hit rate of 95% of the tested points in the domain. For the comparison with wind tunnel results the requirements even go down to ±25% or an absolute difference of < 0.06.
As meshing is not the only error source for CFD simulations it is important to know what influences the meshing alone can have on the accuracy of the results. This study quantifies the accuracy of the mesh by isolating all other influences.
In this research some general existing meshing guidelines are considered. The guideline for flows in the urban environment [9] suggest a small grid in regions of high gradient and an expansion ratio below 1.3 in adjacent cells in this region, while mentioning the smaller ratio of 1.2 in [10]. [5] advises to limit the factor between cell sizes to 2 and use quadrilaterals or hexahedra meshes as discretization errors on the parallel sides can partially cancel each other out. For the same accuracy a finer mesh of triangles and tetrahedra is required. To orientate mesh edges or surfaces along the streamlines can improve the accuracy of the solution. This study focuses on quadrilateral meshes with the ratio of 1.2 between cells. Figure 1 shows the benchmark itself and published reference coarse meshes for this simulation.

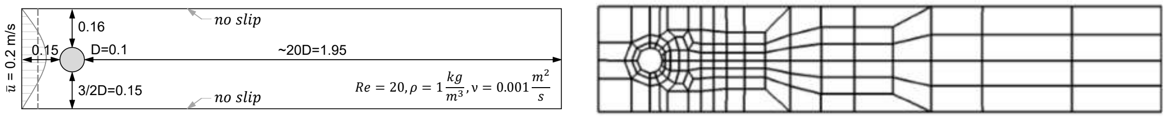

(A) Benchmarktest Re=20 [1][2]

(B) mesh from [2]

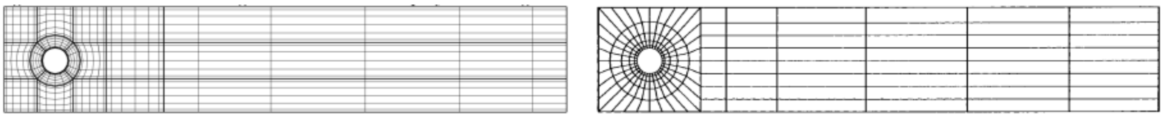

(C) mesh from [11]

(D) mesh from [12]

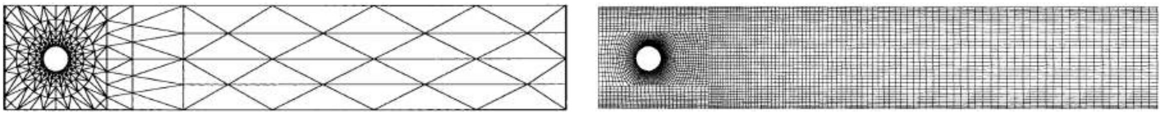

(E) mesh from [12]

(F) mesh from [6]

Figure 1: benchmark test Re 20 different mesh approaches displayed before refinement

3 Methodology

In order to reduce the number of cells in a mesh to a minimum while still retrieving values of high accuracy two structured meshes are designed with *Ansys ICEM* and *OpenFOAM blockMesh* adhering to the meshing guidelines. The geometrical constraints to obtain mainly square cells with a ratio of 1.2 are considered as displayed in figures 2 and 3 (compare 2). The chosen number of cells around the cylinder n_c determines the number of cells within the defined inflation or offset part n_o as given in equation (1). It depends on the diameter of the cylinder d_{cyl} and the depth of the offset x_0. Due to the almost central position of the cylinder the cells in the vertical n_v and horizontal n_h direction have to be equal. The element size at the border to the offset determines the number of used elements by ensuring a smooth transition in height and equal cell sizes.

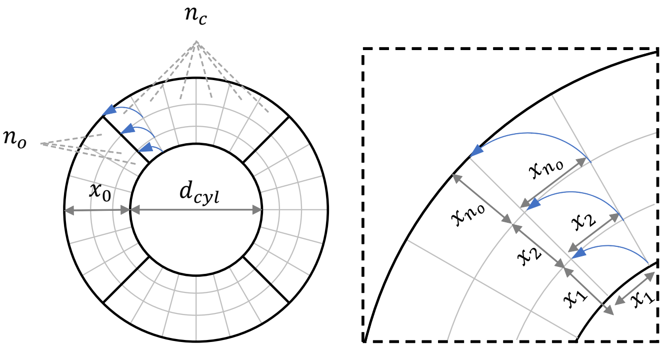

Figure 2: constraints for offset

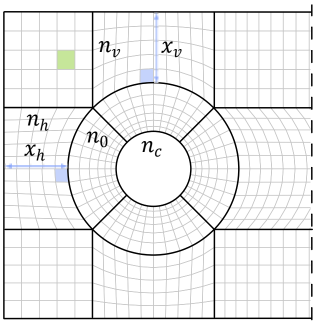

Figure 3: geometric constraints

$$n_o = \frac{n_c \cdot x_o}{\frac{\pi}{4}(d_{cyl} + d_{cyl} + 2 \cdot x_o) \cdot \frac{1}{2}} = \frac{n_c \cdot x_o}{\frac{\pi}{4}(d_{cyl} + x_o)} \tag{1}$$

The only other freely changeable parameter is the ratio in the downstream area R_{DS}. The amount of elements is derived from a chosen ratio according to equation (2) based on the formulae regarding the element sizes from [13]. The value is a function of the largest element size within the offset area x_{no} and the distance from the cylinder to the outlet x_{DS}.

$$n_{DS} = \frac{\log(R_{DS})}{\log\left(\frac{\frac{x_{no}}{x_{DS}} - 1}{R_{DS} \cdot \frac{x_{no}}{x_{DS}} - 1}\right)} + 1 \tag{2}$$

The resulting meshes are displayed in figure 4. The influence of both parameters, namely the thickness of the offset and the ratio of the downstream part, are varied throughout multiple simulations. For every mesh topology or parameter variation a mesh refinement study is run in order to compare its accuracy with the analytical values for the drag ($c_D = 5.57954$) and lift coefficient ($c_L = 0.01062$) as well as the pressure difference ($\Delta_p = 0.117520$) as characteristic values for the effects on the cylinder cross section.

The coefficients are determined based on equations (3) with the average inlet velocity of 0.2 m/s (u_{mean}) as required for the benchmark test [1]. They are derived from the total drag and lift force (F_D and F_L) as an integral over the cylinders surface.

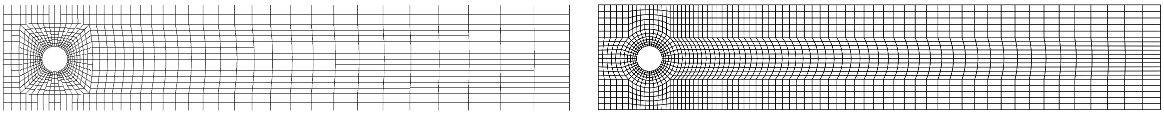

(A) *Ansys ICEM* (B) *OpenFOAM*

Figure 4: Structured meshes

$$c_D = \frac{2 \cdot F_D}{u_{mean}^2 \cdot d_{cyl}} \text{ and } c_L = \frac{2 \cdot F_L}{u_{mean}^2 \cdot d_{cyl}} \tag{3}$$

In principle, structured meshes with their structured algebraic systems can be solved faster than unstructured meshes. However, for most industrial simulations with their complex structures unstructured meshes have to be applied [6]. In order to quantify the decrease in accuracy multiple unstructured generated meshes are compared with the carefully derived structured meshes. Self-adaptive meshes or generated meshes with hanging nodes have not been included in this research. A selection of the tested meshes is displayed in figure 5. It can be seen that not all meshes appear to fulfil the criteria for high quality meshes. In order to analyze the accuracy the parts with ratios between adjacent cells exceeding 1.2 or skewed parts are still evaluated. As for the previous meshes, the ratio between the refined areas and the free stream is also used as a parameter for optimization.

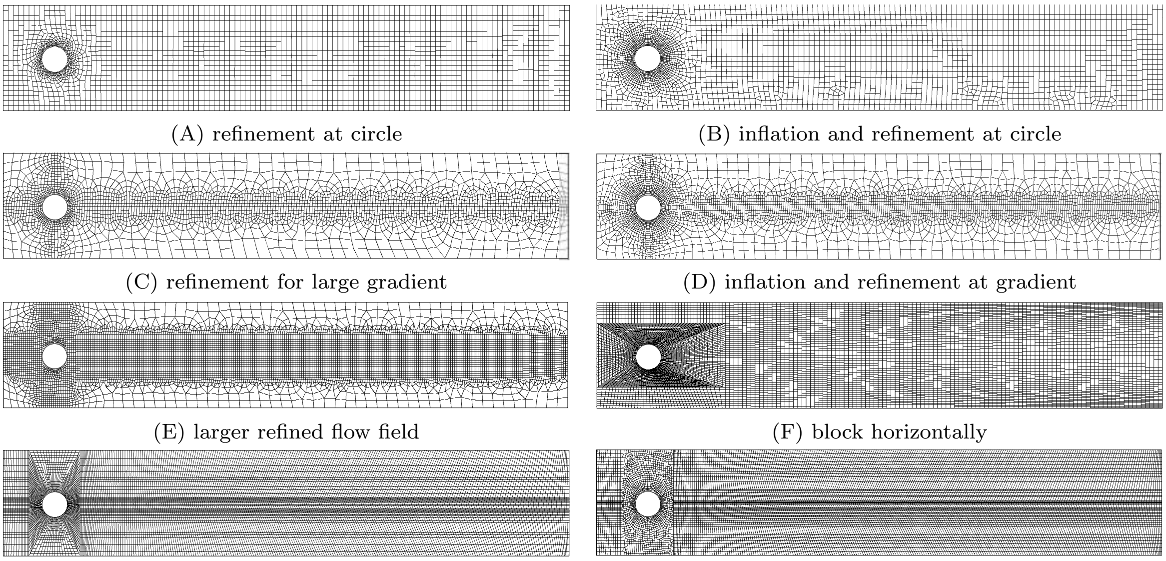
(A) refinement at circle
(B) inflation and refinement at circle
(C) refinement for large gradient
(D) inflation and refinement at gradient
(E) larger refined flow field
(F) block horizontally
(G) block vertically
(H) inflation and block vertically

Figure 5: Unstructured and less optimized meshes

For the grid refinement study the meshes are refined by a ratio of 1.2 of the cell length leading to around 45% more elements with each refinement step. Even though each mesh has to be generated again the refinement curve is more detailed than with the common technique of splitting each existing cell in 4 elements.
As the discretization schemes also have a major influence on the accuracy of the simulations the same schemes were chosen for the simulations for comparable results. For the gradient scheme the applied *least square cell based* approach ensures that no skewness error is induced for the unstructured meshes as would be the case for the *Green-Gauss cell based* approach. For the pressure the *second order* discretization also called central differencing method is used which ensures accurate converged results and doesn't cause oscillations in this case. The momentum equation is discretized with *second order upwind* scheme to also ensure a linear and accurate approach between two adjacent cells. Different solvers shouldn't influence the results and the *coupled* and *SIMPLE* solvers are applied with double precision to minimize round-off errors. The residuals are set to 10^{-6} and it was tested and confirmed that smaller residuals don't change the results of the simulations undertaken in this study. [14]

4 Results

In order to compare the meshes with regards to their accuracy the difference between the resulting coefficients and pressure differences of the various meshes and the analytical solution of the benchmark are displayed. Due to the significant difference in value the relative and absolute accuracy are given. When evaluating the relative accuracy, the lift coefficient with its small value is least accurate. The results of the high drag coefficient vary most regarding the absolute accuracy.

The results are displayed for the number of elements. As *OpenFoam* and *Ansys Fluent* have been used, which are Finite Volume methods that calculate the variables at the cell centroids, the degree of freedom of each simulation is linearly dependent on the number of cells. The only variables for the simulations are the velocity components (x and y for 2D) and the pressure scalar as temperature and turbulence are not included. Therefore, the degrees of freedom can be directly derived from the number of elements with a factor of 3.

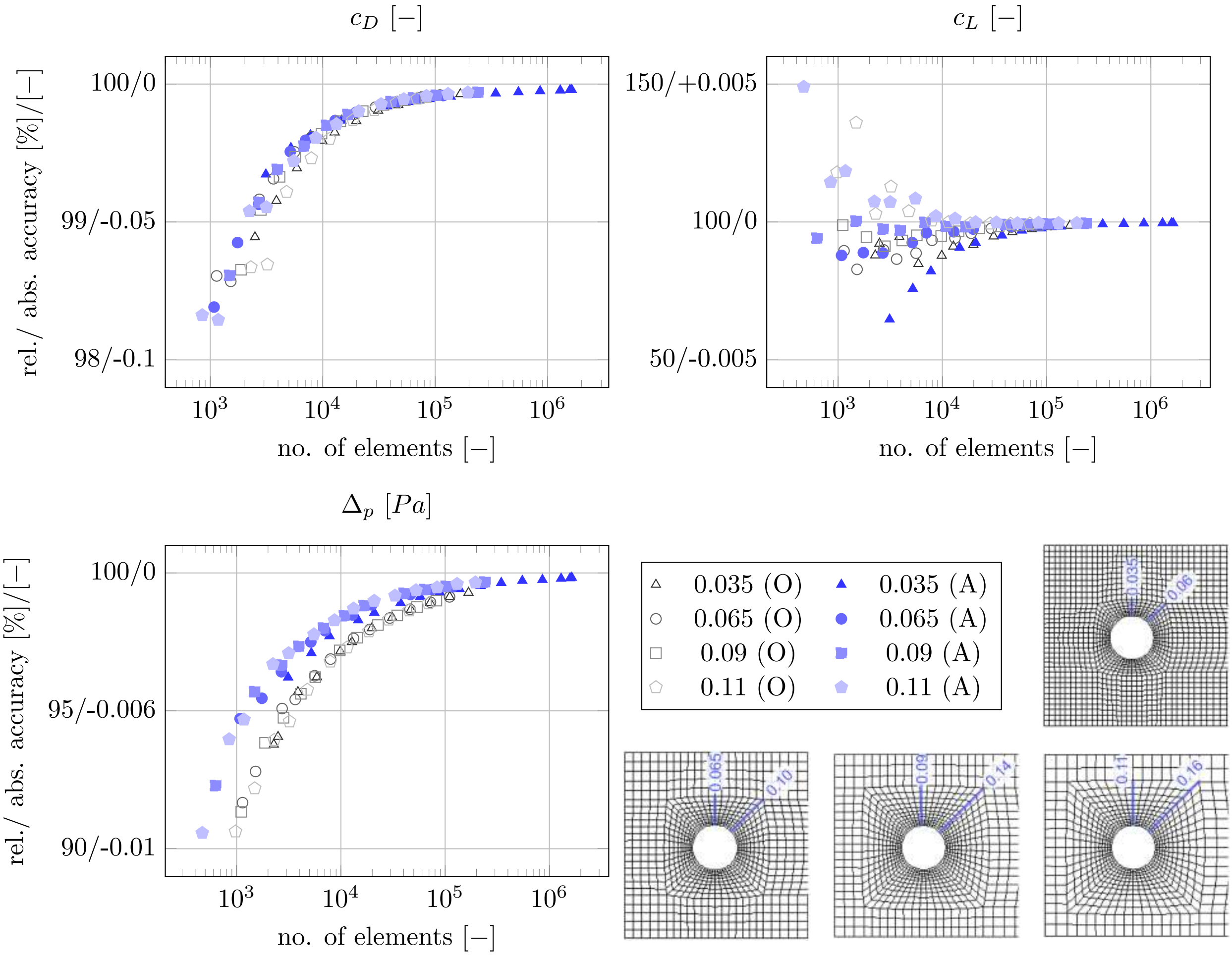

Figure 6: relative and absolute accuracy of different offsets (*Ansys* (A), *OpenFOAM* (O))

Figure 6 shows the results for the structured meshes of *Ansys* and *OpenFOAM* for different offsets. For all values from *Ansys* and *OpenFOAM* the results of the grid refinement lie mainly along one monotonously changing curve. At least from around 10^5 onwards the results appear to be mesh independent. For the drag coefficient the accuracy of the two mesh types is very similar and independent from the offset. For the lift coefficient the accuracy varies between ±20%. There is a boundary offset where results of the grid refinement converge towards the correct value of the lift coefficient from above instead of from below. For small or large offsets more cells are needed for the same accuracy while an optimum of high accuracy lies in between. This behavior can be confirmed when the walls are at a greater distance. The offset's influence on the mesh density downstream leads to a slightly different mesh density in the area of the narrow turbulent wake, which could be an explanation for the different convergence. However, this observation may still be of interest for error estimates from coarser meshes and ensures higher accuracy with less calculating effort. For the pressure difference the *Ansys ICEM* mesh is slightly more accurate and the same cell number leads to values 2.5 % closer to the exact value.

The results of the unstructured meshes are displayed in figure 7 alongside the best *Ansys* result (0.09 Offset) from the previous comparison as a reference. The area between the most and least accurate

results are marked to emphasize the range. For the drag coefficient and the pressure difference the same accuracy can be achieved with up to 10 times more cells in the low quality meshes. The lift coefficient is significantly different. To achieve the same accuracy as before, e.g. ±5%, the unstructured meshes need more than 100 times more elements and for the coarse meshes the results can even be off by more than ±50% .
The positive effect of the inflation layer around the cylinder wall leads to increased accuracies of around 0.2 % for the drag, around 10 % for the lift coefficient and around 1.5 % for the pressure difference. The convergence pattern throughout the grid convergence study is reflected in the convergence of each simulation. The results of the lift coefficient can oscillate until the residual target is reached while the other two coefficients approach the exact solution from below and only vary by 1% after 20% of the simulation time. The lift coefficient only stops changing by more than ±1% when around 50 % of the iteration steps are run.

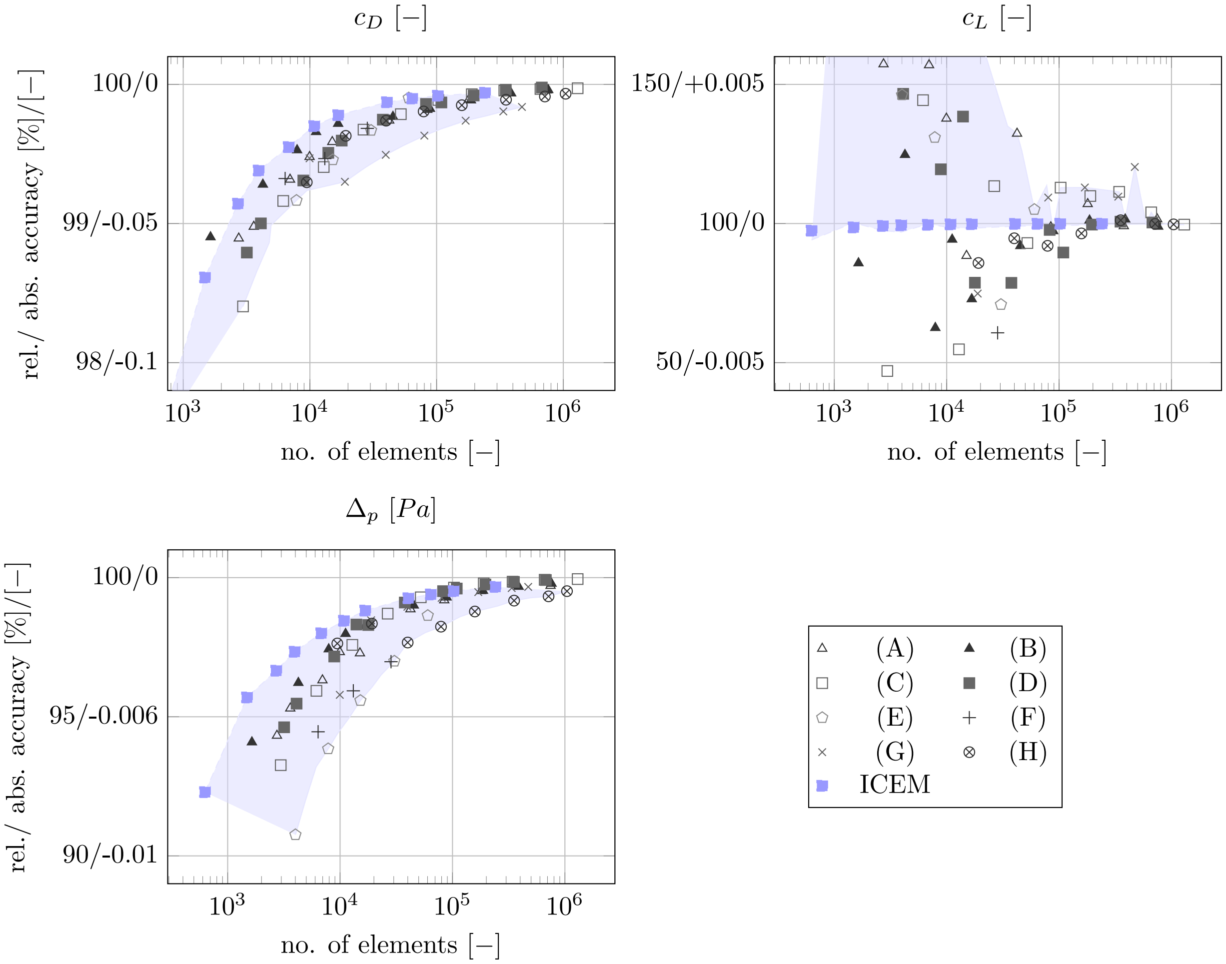

Figure 7: relative and absolute accuracy of different mesh topologies, ratios 1 : 5

Figure 8 shows the results of the different ratios that were analyzed in order to reduce the number of cells in regions of little interest and to judge if negative effects can be observed regarding accuracy. For the coefficients no clear monotonous pattern can be observed. It can be noted that for the coarse meshes the high ratios seem to have a slightly reduced accuracy for the drag coefficient and a slightly higher accuracy for the lift coefficient. For the pressure difference it can clearly be observed that the accuracy increases with higher and decreases with lower ratios. These observations are confirmed for the same evaluation of the structured meshes.

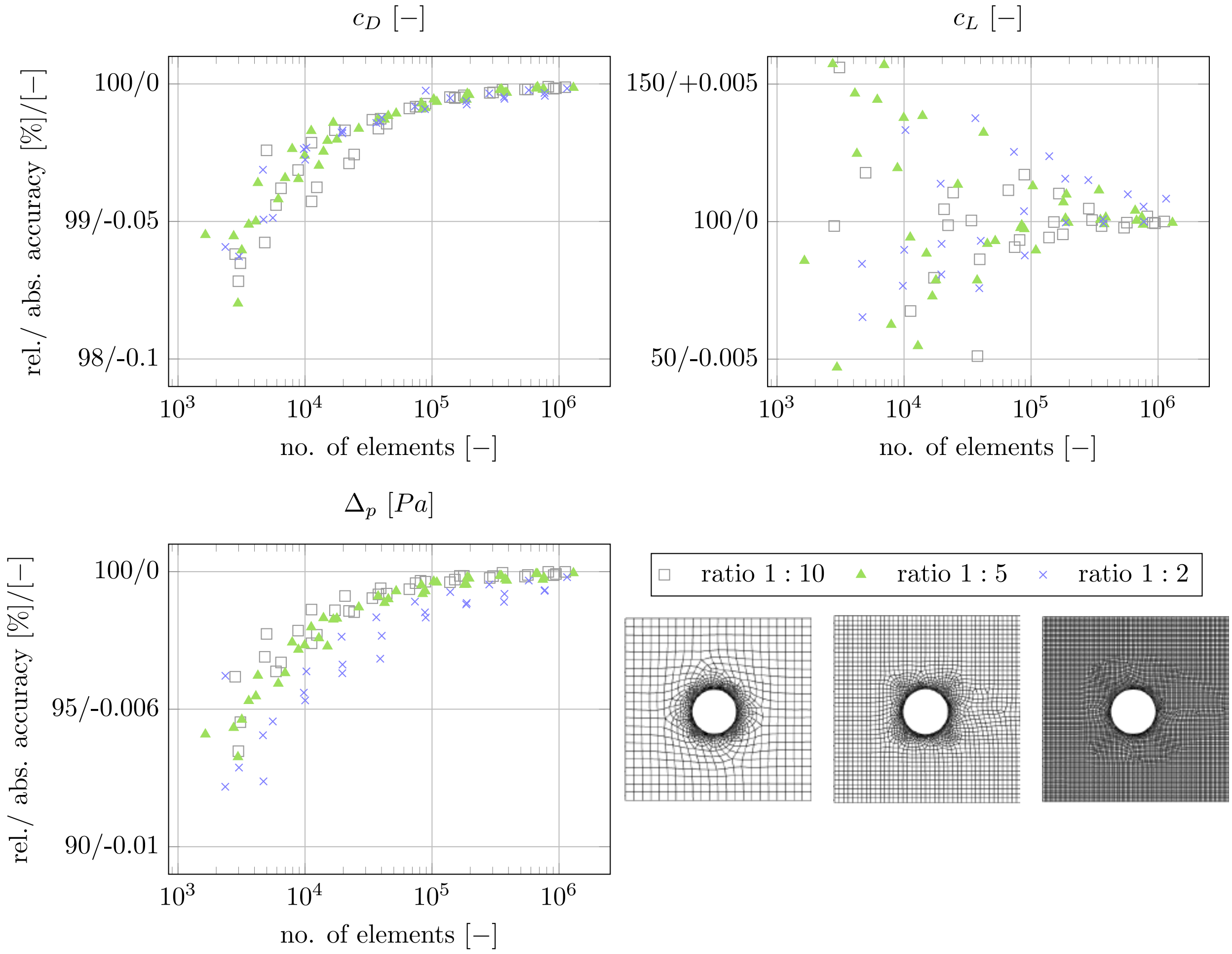

Figure 8: comparison of different ratios for meshes (A) to (D)

5 Outlook

For the flow around the wind turbine tower the Reynolds number is significantly higher and the flow is turbulent and separates from the tower. Depending on the wind speed alternating vortex shedding and therefore a Kármán vortex street can occur.
According to [15] the number of elements in a mesh has to be increased with an increasing Reynolds number. The CFD simulations have to be run in transient mode as the turbulence is time dependent. In order to correctly model the boundary layer along the cylinder the distance between cell centroid and wall (y^+ value) has to be considered. Within the inflation layers around the cylinder a high mesh density is required to correctly display the non-linear velocity profile. This leads to more cells along the diagonal in the offset area of the structured meshes and the ratio along it can be adjusted accordingly.
In order to display the vortex street a higher mesh density can be required in the downstream area.

6 Conclusion

This research quantifies the accuracy of CFD simulations for the incompressible flow around the cylinder benchmark at a low Reynolds number for structured and unstructured meshes. Aiming for the same accuracy the required number of cells between all analyzed meshes varies by a factor of 10 for the drag coefficient and pressure difference and by a factor of one hundred for the lift coefficient. Looking solely at structured meshes, significantly less dispersion occurs.
Adjusting the ratio between cells at high and low gradients does not result in a reduction of overall

required cells. Even though the meshes appear significantly different around the same number of elements are required for the same accuracy. Only for the pressure differences a small reduction of required elements with a higher ratio was observed.
The offset or depth of the inflation layer around the cylinder has a high influence on the convergence of the lift coefficient towards the analytical solution. While small offsets lead to underestimations with coarse meshes, larger offsets overestimate and converge to the correct solution from above throughout the refinement. With regards to error estimation this band width between two coarse solutions represents an interesting approach, if the effect can be transferred to more complex simulations.

References

[1] Schäfer M, Turek S, Durst F, Krause E and Rannacher R 1996 Benchmark computations of laminar flow around a cylinder *Flow simulation with high-performance computers II* (Springer) pp 547–566

[2] Turek S nd DFG flow around a cylinder benchmark 2D-1, laminar case Re=20 `http://www.featflow.de/en/benchmarks/cfdbenchmarking/flow/dfg_benchmark1_re20.html` [Online; accessed 06.01.2021, 13:15]

[3] Houghton E L and Carruthers N B 1976 *Wind forces on buildings and structures: an introduction* (John Wiley & Sons Incorporated)

[4] Versteeg H K and Malalasekera W 2007 *An introduction to computational fluid dynamics: the finite volume method* 2nd ed (Pearson education)

[5] Ferziger J H and Peric M 2008 *Numerische Strömungsmechanik* (Heidelberg, Berlin: Springer-Verlag)

[6] Ferziger J H, Perić M and Street R L 2002 *Computational methods for fluid dynamics* vol 3 (Springer)

[7] DIN 18088-1 2019 Structures for wind turbines and platforms - part 1: Basic principles and actions

[8] VDI Guideline 2017 *Prognostische mikroskalige Windfeldmodelle - Evaluierung für Gebäude- und Hindernisumströmung. VDI Handbuch Reinhaltung Luft*

[9] Franke J, Hellsten A, Schlünzen H and Carissimo B 2007 *Best practice guideline for the CFD simulation of flows in the urban environment: COST action 732 quality assurance and improvement of microscale meteorological models* (Hamburg: Meteorological Inst.)

[10] Scaperdas A 2004 *The QNET-CFD Network Newletter* **2** 28–33

[11] Nabh G 1998 *On high order methods for the stationary incompressible Navier-Stokes equations* (Interdisziplinäres Zentrum für Wiss. Rechnen der Univ. Heidelberg)

[12] John V and Matthies G 2001 Higher order finite element discretizations in a benchmark problem for incompressible flows *Internat. Journal Numer. Methods in Fluids* vol 37 pp 885–903

[13] Greenshields C J 2020 *OpenFOAM Foundation Ltd, version* **8** 243

[14] Jasak H 1996 *Error analysis and estimation for the finite volume method with applications to fluid flows.* dissertation Imperial College London (University of London)

[15] Hucho W H 2012 *Aerodynamik der stumpfen Körper: Physikalische Grundlagen und Anwendungen in der Praxis. 2., vollständig überarbeitete und erweiterte Auflage* (SpringerLink: Bücher. Wiesbaden: Vieweg+ Teubner Verlag)

Dynamic wake tracking based on wind turbine blade loads – methodology, simulation and experiments

David Onnen[a], Vlaho Petrović[a], Martin Kühn[a]

[a] ForWind - University of Oldenburg, Küpkersweg 70, 26127 Oldenburg, Germany

E-mail: david.onnen@uol.de

Keywords: Wake tracking, wake meandering, wind condition monitoring, rotor loads, wind tunnel

Facing the growing size of wind turbines and farms as well as the advances in their control strategies, *wind condition awareness* is of growing importance. In a wind park setting, the location of the wake, which a downwind turbine is exposed to, is of high interest. It can be used for closed-loop wake-steering control, ultimately leading to fatigue load reduction and higher power extraction, thus lower LCOE [1].

A method for dynamic tracking of the meandering wake center is proposed in this work. The term *dynamic* underlines that not only the time-averaged wake location but the meandering trajectory is aimed for. Existing wake tracking methods are either based on LiDAR measurements or rotor loads. The load based approaches use the rotor as a sensor, with the blades sampling through the non-uniform inflow patterns. They either aim at qualitative impingement detection [2,3] or time-averaged location tracking [4,5], where the meandering behaviour of the wake is not taken into account. The LiDAR based approaches include the wake deficit shape to the estimation [1,6] and partly also account for the dynamic meandering [6].

In this work, the measurement of the flapwise blade root bending moment and its decomposition into non-rotating yaw and tilt moments is used. The latter are directly linked to the lateral and vertical wake location via a parametric model, tuned with training data from aeroelastic simulations in HAWC2 to account for the aerodynamic and structural loading of the wake-exposed turbine. At this, the ambient wind conditions are assumed to be known (arguably estimated by a front row turbine). The implementation of an extended Kalman filter (EKF) adds robustness to the tracking and allows to include physical knowledge of the wake meandering to the estimation. At this, the governing equations of the dynamic wake meandering model (DWM) are used to describe the meandering motion as a random walk process driven by colored noise. The EKF formulation also provides the confidence in the tracked position, which can be effectively used for impingement detection or for a wake-steering controller to gauge whether a yaw maneuver is adequate. A test scenario at 10% turbulence intensity and 10 ms^{-1} ambient wind speed is shown in Figure 1.

So far, the method has been derived and tested in the consistent framework of aeroelastic simulations and the DWM model. Hence, it still has to prove its functionality outside this framework. Consequently, the possibility for field and wind tunnel verifications are next to be exploited. The wind tunnel of ForWind in Oldenburg features an active grid, which allows to tailor atmospheric turbulence [7]. Together with model turbines of suitable scaling and dimensioning, the generation of realistic test scenarios is currently investigated. Initial ideas will be shown and fruitful discussion and feedback within the PhD seminar is anticipated.

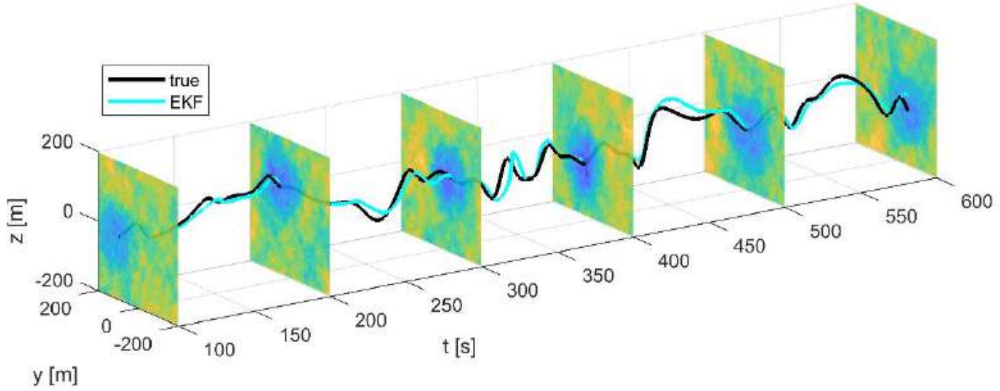

Figure 1: Timeseries of true and estimated wake position; scenario is a two-turbine-constellation of the DTU 10 MW RWT (178 m diameter) in a turbulent wind field created with the DWM model

Acknowledgements

This research was partly conducted in the scope of a master thesis hosted by DTU Wind Energy. Warm thanks to Gunner Chr. Larsen, Alan W. H. Lio and Jaime Y. Liew, who were supervising.

Bibliography

[1] Raach S, Schlipf D, Cheng P W 2017 *Wind Energy Science* **2.1** 257–267
[2] Bottasso C L, Cacciola S, Schreiber J 2018 *Renewable Energy* **116** 115-168
[3] Schreiber J, Bottasso C L, Bertelè M 2020 *Wind Energy Science* **5.3** 867-884
[4] Schreiber J et al. 2016 *Journal of Physics: Conference Series* **753.3** 0-7
[5] Cacciola S et al. 2016 *Journal of Physics: Conference Series* **753.3**
[6] Lio A W H, Larsen G C, Thorsen G R 2021 *Renewable Energy* **172** 1073–1086
[7] Neuhaus L et al. 2020 *Physical Review Letters* **125**.154503

Experimental study of mean and turbulent velocity fields in the wake of a two-rotor vertical axis wind turbine: Comparison with horizontal axis wind turbines

W van der Deijl[a, d], **C Matoug**[a, b, c], **M Obligado**[a], **C Sicot**[d], and **S Barre**[a]

[a]LEGI-CNRS, 1209 Rue de la Piscine, 38610 Gières, France
[b]HydroQuest, 16 Chemin de Malacher Bâtiment B, 38240 Meylan, France
[c]Ifremer, 1625 Route de Sainte-Anne, 29280 Plouzané, France
[d]ISAE-ENSMA, 1 Avenue Clément Ader, 86360 Chasseneuil-du-Poitou, France

June 30th 2021

`E-mail: wessel.van-der-deijl@univ-grenoble-alpes.fr`

Keywords: Vertical Axis Wind Turbines, Turbulence Modelling

Abstract

Previous computational and experimental research has shown that Vertical Axis Wind Turbines (VAWTs) have a faster wake recovery and may therefore have a higher wind farm output per unit of land area, as compared to Horizontal Axis Wind Turbines (HAWTs). It was also found that VAWTs only have a 5% reduction in output when spaced only 4 turbine diameters apart as shown by Dabiri. [2]). In order to utilise this benefit in a wind farm configuration wake models are needed, which require a better understanding of the wake of a VAWT.

Therefore, in this study the turbulent and mean velocity fields of a high solidty ($\sigma = 0.28$) scale model VAWT will be quantified through wind tunnel tests in the S602 wind tunnel of ISAE-ENSMA by using Particle-Image-Velocimetry (PIV). The turbine is an OWLWIND concept, consisting of two counter-rotating 0.5 diameter turbines, as shown in figure 1. The goal is to ultimately get a better understanding of the turbulent velocity field that drives the wake recovery of a VAWT, and compare this to HAWTs.

In addition to the turbulent velocity fields, the average fields will be measured to quantify general wake characteristics such as wake recovery, wake resorption and self-similarity. This will be done at different rotational speeds and different chord Reynolds numbers ranging from $2.0 \cdot 10^4 < Re < 5.7 \cdot 10^4$ and turbine diameter Reynolds numbers ranging from $1.0 \cdot 10^5 < Re < 2.0 \cdot 10^5$. Tip-speed-ratios of $2 < \lambda < 6$ will be investigated to study the effect of dynamic stall.

Preliminary experiments have been concluded with force sensors to characterise the performance of the wind turbine in the wind tunnel, see for example figure 2. The scale model performed well over the desired range of rotational speeds and wind speeds. Dynamic stall could be observed below tip-speed-ratio of $\lambda = 4$. The next step will be the wake measurements through PIV.

Acknowledgements

This project has received funding from the European Union's Horizon H2020 research and innovation programme under the Marie Słodowska-Curie grant agreement N°860579.

Figure 1: OWLWIND Vertical Axis Wind Turbine Scale Model in the S602 ISAE-ENSMA Wind Tunnel.

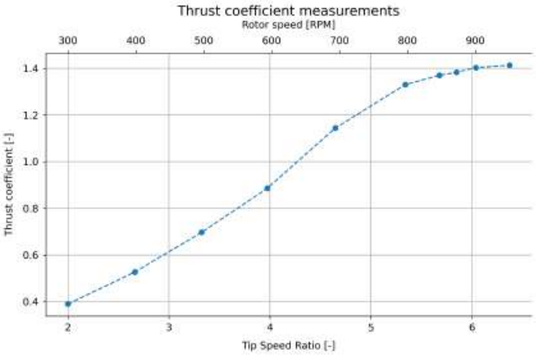

Figure 2: Thrust coefficient measurements of the OWLWIND VAWT.

References

[1] P. Bradshaw, D. H. Ferriss, and N. P. Atwell. “Calculation of boundary-layer development using the turbulent energy equation”. In: *Journal of Fluid Mechanics* 28.3 (May 1967), pp. 593–616.

[2] J.O. Dabiri. “Potential order-of-magnitude enhancement of wind farm power density via counter-rotating vertical-axis wind turbine arrays”. In: *Journal of Renewable and Sustainable Energy* 3.4 (July 2011), p. 043104.

Innovative aerodynamic rotor concepts for demand-oriented power feed in

D. Ribnitzky[a], M. Kühn

[a] Carl von Ossietzky Universität Oldenburg

E-mail: daniel.ribnitzky@uol.de

1 Abstract

We want to introduce an aerodynamic rotor concept for a 15 MW offshore turbine which allows an increased power feed at low wind speeds. As a reference the IEA 15 MW offshore reference wind turbine is used [2]. The main objective of the concept is to limit the loads (blade flapwise root bending moment (RBM) and thrust) to the maximum value of the reference turbine, while greatly increasing the swept rotor aera.

The outer part of the blade (e.g. outer 30% of the rotor) is designed for a higher design Tip-Speed-Ratio (TSR) and a lower axial induction than the inner part. In light wind conditions the rotor will be operated at the high TSR and the slender outer part contributes to the increased power capture. In stronger winds the TSR will be reduced, the torque generation will be shifted to the inner section of the rotor and the outer region can be greatly relieved. In this way the rotor disc gets more permeable, the lever arm of the resulting bending force is reduced and additional peakshaving ensures the limitation of the loads.

Within an iterative design process multiple design parameters are varied, namely the design axial induction distribution and design TSR in the inner and outer part of the rotor, the radial position of the change in these parameters, design lift coefficient and angle of attack distribution and a twist offset between the two blade sections. Further, the specific rating of the turbine and thus the radius is varied as a parameter. With static BEM simulations (as described in [1]) the characteristics of such turbine designs are investigated and an overall economic value of the turbine is calculated to consider the decreasing market prices with increasing wind speeds, as predicted by [3]. As a possible (but not mandatory) extension to the concept, the blade is equipped with trailing edge (TE) flaps in the tip region. A model for the change in aerodynamic polars is derived by XFoil-Simulations.

Our results show that the economic value can be increased by 22% compared to the reference turbine with an increase of rotor diameter by a factor of 1,277. Preliminary structural analyses showed promising results, considering tower bottom fore-aft bending moment and tip deflections.
With the use of the TE flaps with negative deflections in the strong wind regime, the tip region can be further relieved, less peakshaving is necessary and the power output near rated windspeed can be increased.

In future work aeroelastic simulations will be performed to better understand the advantages and shortcomings of the concept under realistic turbulent inflow conditions. To further limit the extreme loads advanced control strategies will be developed.

Bibliography

[1] Hansen Martin 2008 *Aerodynamics of wind turbines,* 2nd edition, earthscan London
[2] Gaertner, Rinker, Sethuraman, et al 2020 *Definition of the IEA 15-Megawatt Offshore Reference Wind turbine* National Renewable Energy Laboratory. NREL/TP-5000-75698. https://www.nrel.gov/docs/fy20osti/75698.pdf
[3] May Nils, Heuhoff Karsten, Borggrefe Frieder 2015 *Market incentives for system-friendly designs of wind turbines* DIW Economic Bulletin 24. 2015

CONTROL

17^{th} EAWE PhD Seminar on Wind Energy
3-5 November 2021
Porto, Portugal

Design of the power regulation strategy in wind turbine optimization

Jenna Iori

Wind Energy Department, Technical University of Denmark, Frederiksborgvej 399, 4000
Roskilde, Denmark

E-mail: jenio@dtu.dk

Keywords: Control, New Concepts, Optimization, Co-design

1 Introduction

In state-of-the-art multi-disciplinary optimization frameworks for wind turbine design, the power regulation strategy is often designed using two main operational regions: at low wind speeds, the maximum power coefficient is tracked and at high wind speeds the power production and rotational speed are both maintained constant [1] [2] [3]. However, studies on derating have shown that different choices of regulation strategy are possible and can be beneficial in terms of load alleviation [4] [5].

This works present a numerical method to include the power regulation strategy in aerodynamic design of wind turbine blade with full design freedom. The objective is to show how the regulation strategy can be used for load alleviation in the design process.

2 Methodology and Results

The design variables of the optimization problem are the chord and twist distribution (noted $\boldsymbol{x}$), the rotational speed for every wind speed in the operational range Ω as well as the pitch angle θ. The objective function of the optimization problem is shown in Eq. 1 and consist of two competing goals: increasing the power capture represented by the Annual Energy Production (AEP) and reducing the average thrust. The terms a and b are scaling factors. Constraints are enforced on the maximum power output, the maximum tip speed and the maximum thrust.

$$f(\boldsymbol{x}, \boldsymbol{\Omega}, \boldsymbol{\theta}) = \frac{1}{a} AEP(\boldsymbol{x}, \boldsymbol{\Omega}, \boldsymbol{\theta}) - \frac{b}{m} \sum_{i=1}^{m} T_i(\boldsymbol{x}, \Omega_i, \theta_i) \tag{1}$$

The aerodynamic properties of the wind turbine are calculated using the Blade Element Method (BEM) with a Prandlt tip loss correction [6]. The axial induction factor is assumed to be a third order polynomial function of the thrust coefficient, as described in [7]. The optimization problem is solved using IPOPT [8] version 3.12.

The intitial design used for the optimization problem is based on the IEA 10 MW reference wind turbine [9]. The maximum allowed power is 10MW, the maximum tip speed is 90 m/s and the maximum thrust is 1.3 kN.

Fig. 1 reports the power regulation strategy of the optimum design. It doesn't follow a classic two-region strategy but instead automatically finds the best operation point to reduce the thrust and respect the constraints. At high wind speeds, the rotational speed decreases in order to track the minimum thrust coefficient. When the thrust constraint is active, a region of peak-shaving automatically appears: the blade is pitched before having reached the rated power in order to reduce the thrust. Finally, the blade is pitched at low wind speeds in order to reduce the thrust. The thrust is reduced by 9.6% in average compared to the initial design while the AEP decreases by less than 1 %.

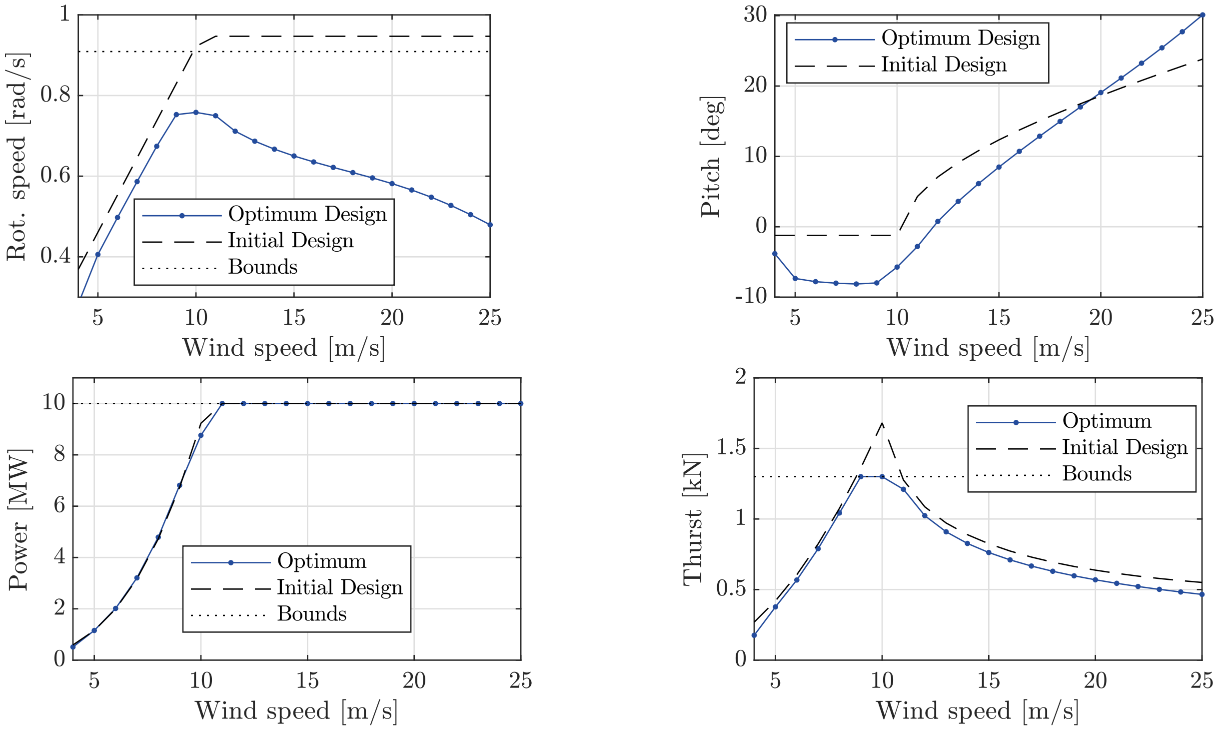

Figure 1: Power regulation strategy of the optimum and the initial design and resulting power and thrust curve in the operational range

Acknowledgements

This work was funded by the Technical University of Denmark. The authors thanks Mathias Stolpe and Michael McWilliams from DTU for their valuable feedback on this work.

References

[1] Ashuri T, Zaaijer M, Martins J, van Bussel G and van Kuik G 2014 *Renewable Energy* **68** 893–905

[2] Ashuri T, Martins J R R A, Zaaijer M B, van Kuik G A M and van Bussel G J W 2016 *Wind Energy* **19** 2071–2087

[3] Bortolotti P, Bottasso C L and Croce A 2016 *Wind Energy Science* **1** 71–88

[4] Lio W H, Mirzaei M and Larsen G C 2018 *Journal of Physics: Conference Series* **1037** 032040

[5] van der Hoek D, Kanev S and Engels W 2018 *Proceedings of the American Control Conference (ACC)* vol 2018-June (IEEE) pp 3116–3121 ISBN 978-1-5386-5428-6

[6] Glauert H 1935

[7] Madsen H A, Larsen T J, Pirrung G R, Li A and Zahle F 2020 *Wind Energy Science* **5** 1–27

[8] Wächter A and Biegler L 2006 *Mathematical Programming*

[9] Bortolotti P, Canet Tarrés H, Dykes K, Merz K, Sethuraman L, Verelst D and Zahle F 2019

17th EAWE PhD Seminar on Wind Energy
3-5 November 2021
Porto, Portugal

Implementation of Advanced Wind Turbine Controllers for Scaled Turbine Testing in a Wind Tunnel

M Sinner[a], V Petrović[b], and L Y Pao[a]

[a]University of Colorado Boulder
[b]ForWind, University of Oldenburg

E-mail: `michael.sinner@colorado.edu`

Abstract

Based on a series of two experimental campaigns testing advanced controllers on a scaled wind turbine operating in a wind tunnel, this contribution describes the overall experimental method, challenges faced, lessons learned, and opportunities for future work. The two campaigns, run in Fall 2018 and Fall 2019, tested unconstrained and constrained optimal blade pitch controllers, respectively, using preview disturbance measurements of the oncoming wind. Specifically, the first study considered an extension to the linear-quadratic regulator to include feedforward action, while the second deployed model predictive control to incorporate actuator constraints into the optimal control problem. The results of the campaigns have already been published in technical conference and journal papers on control systems; however, detail on how the controllers were implemented was not included in those works. We aim to fill that gap with this contribution, which is targeted at the wind energy community. We describe several aspects of the experimental setup, in particular providing details of the software and hardware used for the controller; share insight on several aspects of the procedure that were difficult and how we overcame those challenges; and summarize the key differences between simulation-based studies and physical testing. By doing so, we hope to share what we learned during our experimental campaigns and provide a point of reference for others looking to carry out experiments on scaled wind turbines operating in wind tunnel facilities.

Keywords: Scaled wind turbine model, hardware in the loop, active grid, feedforward control

1 Introduction

Over the past 20 years or so, as the deployment of wind energy across the globe has exploded [1] and the hunt for a lower and lower cost of renewable energy continues, a large body of literature exploring new methods for wind turbine control has developed. The majority of academic research focuses on two main actuators for turbine control: the electrical load provided by the turbine generator (referred to as "generator torque control") and the pitch angle of the turbine blades ("blade pitch control"). Generally speaking, generator torque control is used to maximize the power generated by the turbine when wind speeds are low, while at higher wind speeds, blade pitch control is used to regulate the turbine to its rated speed while the generator torque is fixed at its rated torque, thus producing the rated power of the turbine [2].

A full review of the literature on wind turbine control designs is out of the scope of this paper; we will briefly mention a few broad classes and direct the reader to Laks et al.'s survey on advanced control [3], Scholbrock et al.'s survey on lidar-enabled control [4], and Lio et al.'s survey on model predictive control [5] for further reading. The literature may be broadly divided into research into advanced control algorithms that use existing sensors and actuators, including optimal multi-input multi-output controllers, among others; development of new actuation techniques, of which individual pitch control has received particular interest for its ability to reduce structural loads on the turbine while maintaining a high power output [6]; and control approaches that make use of extra sensors, most notably lidar-enabled feedforward control [7, 4], which uses measurements of the wind upstream of the turbine to 'pre-actuate' and reduce the impact of disturbances; as well as combinations of the above. Over the years, many promising results have been reported from simulation-based studies indicating that advanced controls can increase power production and decrease turbine structural loading.

Despite numerous studies with positive results, it appears that industry has been sluggish to adopt new controllers. To the best of our understanding, most turbine manufacturers still implement a series of single-input, single-output control loops to achieve the desired behavior with the blade pitch and generator torque controllers designed largely independently; for an example of an industry-standard controller, see Jonkman et al.'s NREL 5MW reference turbine controller, which was designed to reflect industry practices [8, Section 7]. A likely explanation for this is the lack of physical implementations of advanced wind turbine controllers—the vast majority of results have been reported using computer simulations. Although several excellent high- and medium-fidelity turbine modelling packages exist for the express purposes of simulating the nonlinear wind turbine response (FAST [9], for example), they of course cannot capture all of the relevant physics and as such, may not be as convincing as a physical test to turbine manufacturers. On the other hand, testing novel controllers on utility-scale turbines can be a tall order for academics and researchers, due to the high cost and potential risk of utility-scale experimental campaigns. Some studies have been reported both on research turbines [6, 10] and from manufacturers [11]; however, due to the aforementioned barriers and also the time it can take to implement advanced controls for research purposes, many of the controllers reported in simulation-based work have yet to be tested on physical turbines.

While deployment on utility-scale wind turbines remains the gold standard for demonstrating controllers, testing on scaled wind turbine models presents an opportunity to validate control algorithms on physical turbines without the high costs and risks associated with experimenting on utility-scale turbines. Testing controllers on scaled wind turbine models bypass many of the barriers to utility-scale testing. The models are (relatively) low-cost (although the cost of the testing facility may be high) and present a lower safety risk, while generally being quicker to deploy and test controllers on. Moreover, they can be tested in controlled environments, meaning that various different control designs can be evaluated using the same set of inflow conditions, which is generally impossible to achieve using a utility-scale turbine operating in the atmospheric boundary layer. Scaled-model testing is not without its disadvantages: it is not generally possible to scale down all of the relevant structural and aerodynamic properties of a utility-scale wind turbine, meaning that the scaled model is still not a completely accurate reflection of all of the relevant physics. Obtaining representative Reynolds numbers is particularly difficult to achieve [12]. Time-scaling also presents both challenges and opportunities: while the time speed-up means that testing that would require hours on a utility-scale turbine can be completed in minutes on a scaled model, it also means that control algorithms should ideally be sped up, which is not always possible (in our tests [13, 14], we used a controller sample rate comparable to that of a utility-scale turbine, which made the controller relatively slow for the scaled model). As a result, scaled-model tests cannot completely replace utility-scale testing, but can be used as an important proving ground for physically-implemented controllers.

Such scaled wind turbine tests have been successfully carried out at various wind tunnel facilities around the world. Amongst others, the Delft University of Technology and the Politecnico di Milano operate tunnels with experimental setups for both individual turbine control [15] and wind farm control [16]; and the University of Texas have recently commissioned a wind tunnel that can be used for scaled wind turbine testing, among other applications. Further, recent interest in floating offshore wind turbines has driven the development of combined wind tunnel/wave tank testbeds such as that at the University of Maine. However, while there are a few papers that briefly describe the software used [17, 18], the literature on scaled-model testing focuses on the scientific results and does not tend to provide details on the controller implementation process.

The experiments upon which this paper is based were carried out at ForWind – Center for Wind Energy Research in the Institute of Physics at the University of Oldenburg in Oldenburg, Germany using the 1.8 m rotor diameter Model Wind Turbine Oldenburg (MoWiTO). The wind tunnel and experimental setup will be described in Section 2.3—for further details of the controller testbed, please refer to Petrović et al. [19]. We conducted two experimental campaigns, the first in the fall of 2018 [13] and the second in the fall of 2019 [14]. The first considered a preview-enabled version of the linear-quadratic regulator, and the second extended the corresponding optimal control problem to include blade pitch actuator constraints, resulting in a linear model predictive controller. The technical details and results from these studies can be found in our previous publications [13, 14]; the purpose of the present paper is to describe

Simulation-based studies	**Physical testing on the MoWiTO**
1. Generate a simplified (often linear) mathematical model of the wind turbine to use for controller design purposes using either a physics-based derivation or numerical identification approaches.	**1.** Identify a linear mathematical model of the scaled-model wind turbine using a system identification applied to input-output data from a higher-order FAST model of the turbine.
2. Construct a controller based on the simplified mathematical model according to control system design principles (see, for example, Franklin et al. [20] for a thorough text on the fundamentals of control system design and Laks et al. [3] and Pao and Johnson [2] for reviews of advanced controllers in wind turbine applications).	**2.** Construct a linear quadratic regulator-type controller (with a feedforward extension) based on the simplified mathematical model.
3. Test the controller in closed loop using a higher-fidelity (often nonlinear) simulation model of the turbine as the 'true' system to validate performance. Tune the controller based on the simulated response and repeat the simulations as needed.	**3.** Test the controller in a closed-loop simulation using the FAST model to represent the true behavior of the turbine. Retune the controller as needed.
	4. Implement the controller on the final control software and hardware, and verify behavior of controller implementation.
5. Test the controller in closed loop using the higher-fidelity simulation truth model and various randomly-generated inflow with various random seeds to validate the controller fully. Often, a reference controller representing industry standards is also simulated as a point of comparison.	**5.** Test the controller in closed loop with the scaled-model turbine using various repeated wind inflows. Test various controller configurations back-to-back to ensure consistency in the testing scenario.

Table 1: Summary comparison of the general approach used in simulation-based studies and the physical testing we conducted.

the steps taken to implement the controllers on the scaled-model turbine and our takeaways from the experiments. To that end, we describe the test setup, software development, and validation steps in Section 2 and present our conclusions and recommendations to others planning scaled-model testing of advanced turbine controllers in Section 3.

2 Experimental approach

As mentioned previously, the stated purpose of the experimental campaigns that we conducted was to demonstrate the effectiveness of advanced feedforward control techniques [13, 14] and, in particular, model predictive control [14] on a physical wind turbine in order to validate simulation-based results reported in a large body of literature. The experimental approach that we used differs from the approach used in many simulation-based studies; these differences are recorded in Table 1.

The approach we took for physical testing depended on the fact that we had a FAST model of the MoWiTO available for simulation. If no higher-order truth model is available for simulation, step 3 may need to be replaced with initial testing on the true physical system. Further, in that case, a data-driven system identification procedure could be used to generate a mathematical model for step 1. Often, for both simulation-based and physical studies, steps 2 and 3 may be repeated several times, with the controller being retuned in step 2 in order to improve its performance. In some cases, step 1 might also be repeated in the design loop if the mathematical model itself is deemed to be a source of poor performance.

We will now describe the key steps of the experimental approach used for physical testing in more detail. In reporting on our procedure, we hope to provide a reference to other researchers looking to implement wind turbine controllers on scaled-model testbeds.

2.1 Software development

We used Matlab [21] for controller development. The main reason for this is that there is a FAST interface for Simulink, making testing controllers in closed-loop simulations particularly easy using Matlab/Simulink. On top of that, qpOASES [22], which we used to solve the model predictive control problem online [14], has a convenient Matlab interface. If the controller can be represented by a relatively simple differential (or difference) equation (such as a linear state-feedback gain [13]), it may be easiest to implement this directly in Simulink using elementary blocks. On the other hand, if the controller is algorithmic (as is the case with model predictive control [14]), text-based code may be needed. In our Simulink implementation, we used a Level-2 Matlab S-Function to pass the controller inputs to a class object containing the controller code before returning the controller output (control input to the plant). This approach has the added benefit that several controllers can be simulated with no change to the Simulink model, simply by creating instances of different controller classes with similar method names. The process of simulating the controller on a higher-fidelity truth model (in our case, a FAST model) may be thought of as ‘software in the loop’ testing.

Once the controller had been designed and tuned (steps 2 and 3 of the testing procedure in Table 1), we then translated our Matlab/Simulink code into LabVIEW [23] for real-time use on the physical MoWiTO. We constructed our controller as a LabVIEW virtual instrument (VI) that took as inputs the feedback and feedforward signals at time index k and produced as an output the control action at time index k. This VI contained both the elementary control law but also a number of simple subVIs that handled controller output (plant control input) saturation, internal state integration, and fault handling in the case of the model predictive controller.

Relatively simple controllers [e.g. 13] can be implemented directly using LabVIEW blocks. However, algorithmic controllers such as model predictive controllers may need to be implemented using text-based code. To achieve this, we translated our model predictive controller code into C++; this essentially resulted in a MoWiTO-specific C++ wrapper for qpOASES, which is also written in C++. We compiled this code into a shared library that could be loaded and initialized prior to run-time, and interfaced with the LabVIEW controller using the LabVIEW-provided “Call Library Function” node. We used the node in the “Run in any thread” configuration—see Section 2.2.

2.2 Controller validation

Step 4 in Table 1 is perhaps the most important difference between simulation-based and physically implemented controller tests. In order to avoid damage to the physical system, it is important to validate the controller implementation. We did this in two steps: the first to validate the control software and the second to validate the control hardware.

To ensure that our translation of the Simulink/Matlab simulation controller to the LabVIEW/C++ real-time control software was accurate, we looked at the input/output behavior of the real-time control software in open-loop using controller input data from the Simulink model simulations. To do so, we developed a wrapper for our controller VI that read in controller input data generated during Simulink simulations, passed the data to the controller VI, and recorded the outputs. We could then compare the LabVIEW-based controller outputs to the Simulink-simulated controller outputs to verify that the controller software was behaving correctly and producing the expected input/output behavior.

The validation just mentioned looked only at the input/output behavior of the software in open loop, and importantly, did not include any real-time control hardware. A crucial step for validation is to check that the control software still runs as expected when implemented on the control hardware: in our case, a National Instruments CompactRIO (cRIO, see Section 2.3). Implementing the LabVIEW code onto the control hardware was straightforward, since both LabVIEW and the cRIO are National Instruments products; however, compiling the C++ code for the cRIO target (which runs on a version of Linux) was not entirely straightforward. After much trial and error, we were able to correctly compile the code using “C & C++ Development Tools for NI Linux Real-Time 2014, Eclipse Edition”, a version of the Eclipse integrated development environment tailored by National Instruments. We then checked the implementation using a hardware-in-the-loop (HIL) test environment developed by Syed Muzaher Hussain Shah at the University of Oldenburg. This setup allowed us to run the simulation FAST model in closed loop with the controller on the cRIO using a specially-developed shared library to handle communications between the FAST executable and cRIO-based controller.

Th HIL testing step proved extremely useful. We found that the solve time for qpOASES (the optimization package used to solve our model predictive control problem) was somewhat slower on the cRIO than it had been on a desktop computer, and we were able to adjust the prediction horizon length accordingly to make up for this difference [14]. Moreover, we identified during HIL testing that we should be using the "Run in any thread" (rather than the default "Run in UI thread") configuration for the Call Library Function node in our controller, which proved vital to achieving acceptable controller speed and behavior.

2.3 Physical testing

The MoWiTO (the scaled-model turbine used in our experiments) is designed as an aerodynamically scaled model of the NREL 5MW reference turbine [8] (although the blades and tower are stiffer than they would ideally be to represent the NREL 5MW), and was put together by Frederik Berger at the University of Oldenburg. As we mentioned in Section 1, it is not usually possible to match the Reynolds number on a scaled wind turbine model—in the case of the MoWiTO, the blade chord Reynolds number is approximately 100 times lower than the Reynolds numbers seen on the NREL 5MW turbine. To account for this, the blades were redesigned to achieve a lift distribution similar to the NREL 5MW under the lower Reynolds numbers. For full details about the MoWiTO, see Berger et al. [12].

The MoWiTO operates in the test section of a large, closed-circuit wind tunnel at the ForWind – Center for Wind Energy Research at the University of Oldenburg [19]. The tunnel test section, opened officially in 2017, is 3×3 m^2 in cross-section and 30 m long in the open configuration used for our testing. The ForWind tunnel has an active grid, described by Kröger et al. [24] and based on previous developments [25, 26], over the inlet to the test section that allows for generating complex atmospheric conditions during testing. For example, the active grid can be used to produce gust wind conditions (used for testing in our first experimental campaign [13]) and turbulent inflow (used during our second campaign [14]), as well as step changes in wind speed, sheared boundary layers, and other inflows. Importantly, the active grid can reproduce the same 'random' flows, which is easy to achieve in simulation but impossible to achieve in the field. This allows for direct side-by-side comparisons of different controllers [13, 14] in complex wind conditions. To reduce the effect of shear from the floor, the inlet to the test section is raised 1.5 m above the ground; the MoWiTO is therefore mounted on a support structure to raise it to the height of the main flow. See Figure 1 for a schematic and photo of the main components of the testbed.

The real-time control for the MoWiTO was handled by a National Instruments CompactRIO-9066 (cRIO) running the LabVIEW controller (see Section 2.1). This cRIO has a 667 MHz dual-core CPU and runs the National Instruments Linux Real-time operating system. Our controller VI was embedded in a larger, high-level operating code developed at the University of Oldenburg, which, among other things, handles the start-up and shut-down procedures for the MoWiTO; data logging; and controller selection. This piece of code is extremely useful for rapidly testing different control laws on the MoWiTO essentially by simply replacing the controller VI within the higher-level operating VI.

During testing, the cRIO was placed on the support table behind the MoWiTO (white box in Figure 1), with electrical cabling run from the turbine nacelle to the cRIO via the interior of the tower. To test feedforward control approaches, we used a hot-wire measurement of the wind speed upstream of the turbine. The analogue hot-wire signal was amplified and transmitted to the cRIO via coaxial cable. The hot-wire anemometer needed to be calibrated at the beginning of each session and recalibrated periodically during longer testing sessions to ensure consistency in the measurements. Finally, the communications between the real-time cRIO and monitoring desktop in the control room were managed via ethernet.

We ran tests with a variety of both deterministic and turbulent wind sequences. For shorter sequences (gusts and short turbulent inflows), the inflow was repeated ten times for each controller. A timing signal was used to ensure that the turbine signals were correctly aligned between the controllers during data post-processing. For more details about the inflows used in our testing, see Sinner et al. [14]; for details about how the active grid is used to generate inflows, please refer to Kröger et al. [24] and Knebel et al. [26].

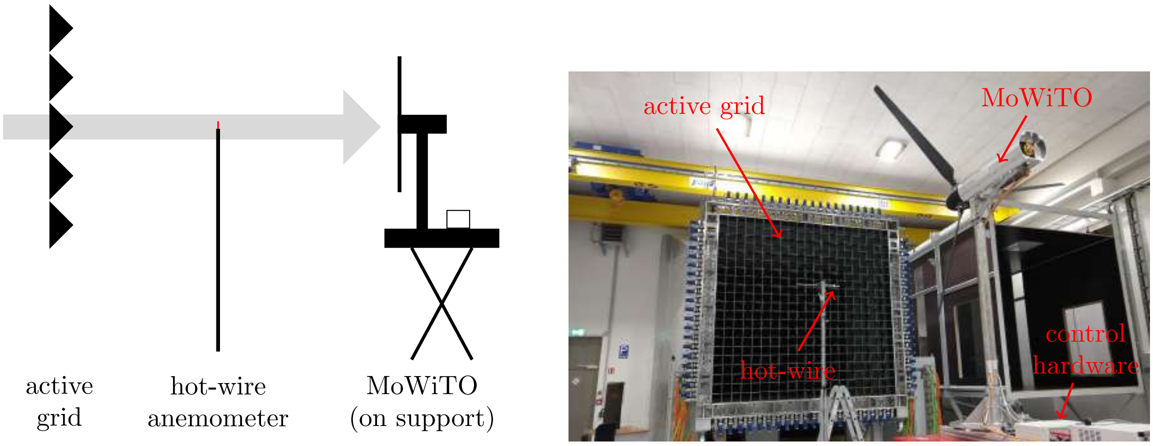

Figure 1: **Left:** Schematic of the MoWiTO wind turbine in the wind tunnel testbed. The gray arrow represents the wind flowing out of the inlet nozzle, through the active grid and across the MoWiTO. The white box on the support table represents the controller hardware that the controller was run on. **Right:** Labelled photograph of the experimental setup.

3 Conclusions and takeaways

Having documented our experimental approach, we will close by providing a handful of recommendations regarding different aspects of the approach. Some may seem obvious; others perhaps less so.

Control model accuracy. Determining how many of degrees of freedom to use in the mathematical model, and how carefully one needs to describe the modes included, is one of the major challenges faced by a control engineer and yet does not receive much attention in the literature. A higher order, more accurately identified model may lead to slight improvements in performance over a lower order, roughly identified model; however, one of the main benefits of feedback control is its robustness to plant uncertainty. Moreover, a simpler model is easier to work with and understand, and any improvement in performance from a more complex model may be negated due to a lack of understanding of the model behavior.

When testing advanced controllers on a physical testbed, we propose that the mathematical model be kept as simple as possible, at least initially. For our tests [13, 14], we modeled only the rotational mode of the turbine. This allowed us to 1) identify the model parameters very easily, 2) formulate the optimal control problem in a straightforward way, and 3) avoid the use of a state estimator. On the downside, we did notice that in some cases the main tower fore-aft mode was excited during testing, and for future work, a tower model could be worth including in the formulation.

We should also mention that ideally, software in the loop simulations and controller verification would take place with a plant model of higher fidelity than the mathematical control model. For our testing, we used a FAST model, which contains a nonlinear aeroelastic blade model on top of the main turbine rotational components.

Controller simplicity. Similarly, we suggest using a simple controller formulation. This is not to say that a simple control architecture should be used—the purpose of the testing we carried out is, after all, to test advanced controllers—but that choices should be made in the design of the chosen advanced controller that are easy to follow and understand and are reproducible. As with model selection, more complex tunings and choices may well lead to slight performance improvements; however the purpose of our testing, and we believe most of academic scaled-model testing, is to demonstrate that the controller works in a physical setting, rather than to maximize absolute performance.

Ideally, the complexity of the controller could be increased gradually. Our experiments took place over the course of two experimental campaigns, with the first investigating unconstrained linear-quadratic control [13] and the second investigating constrained linear-quadratic control [14]. Although this change meant that the controller implementation for the second experiments were considerably more complex than the first, mathematically the control problems were very similar; this meant that we could focus on the changes during the second experiment, rather than developing a model predictive controller from scratch. Even within the model predictive control framework, one could consider adding in constraints one at a time, perhaps beginning with simpler box input constraints and moving to affine input constraints and state constraints. We did not take that approach, but in hindsight, that may have helped us to understand where the main challenges lay in terms of computational speed.

Controller implementation. In this testing, we used a high-level language (Matlab/Simulink) for controller design and initial simulation testing before translating the design into a real-time code (LabVIEW/C++). While one could design the controllers directly in the real-time language, we find that the higher-level languages allow for quicker reworking of the code and therefore a quicker turnaround in design iterations. The downside to this is the extra step required to translate the code into the real-time language and then verify its behavior.

However the controller is implemented, we would like to underscore the value in hardware in the loop testing once the controller has been compiled on the real-time hardware. Having a suitable software testbed for HIL testing requires some effort; we were fortunate to have had the testbed set up beforehand, meaning that for us, HIL testing was very straightforward. If there are a series of physical tests planned, the upfront effort of developing a HIL testbed will likely be worthwhile.

Preparing early. As cliché as it is to say, being prepared early is perhaps the most important aspect of a test campaign. Often the window when the physical testbed is available is short, and it can be critical to keep that time open for addressing unforeseen issues in testing.

During our second campaign, the C++ code compilation for the real-time cRIO target was more complicated, and took considerably longer, than we had anticipated. For someone else, that step might have been straightforward, but more likely than not there will be challenges with the software that are best to overcome before the testing window opens. Once the testing window had begun, we had mechanical problems that needed to be addressed before the turbine was operational and responding correctly, limiting the amount of the testing window available for data collection. We were able to get everything done, but it would have been better if all of the software had been finalized and compiled before the testing window started, rather than having to work on both the software and hardware during that window. In the worst case, the testing simply finishes early!

Testing on scaled-model turbine testbeds is an important step in the process between theoretical control law design and industry acceptance, and we expect wind tunnel testing of turbine and farm controllers to continue to hold an important place in the literature. We hope that this documentation of our testing procedures and insights provides a useful reference for others that want to test controllers in physical, scaled-model testbeds, and we encourage readers to reach out to us with any questions that you have regarding our approach. We would be happy to provide further details where possible.

Acknowledgements

The experiments described in this paper would not have been possible without the travel funding from the German Academic Exchange Service (DAAD) and the Hanse-Wissenschaftskolleg in Delmenhorst, Germany. The state of Lower Saxony supported the wind tunnel campaign, active grid, and MoWiTO under the project “ventus efficiens.” We also thank the National Renewable Energy Laboratory and a Palmer Endowed Chair at the University of Colorado Boulder for ongoing financial support. Finally, we thank David Onnen for presenting this work in our absence.

References

[1] Wiser R and Bolinger M 2021 Land-based wind market report: 2021 edition Tech. rep. U.S. Department of Energy, Lawrence Berkely National Laboratory

[2] Pao L and Johnson K 2011 *IEEE Control Systems Mag.* **31** 44–62

[3] Laks J H, Pao L Y and Wright A D 2009 Control of wind turbines: Past, present, and future *Proc. American Control Conf.* (St. Louis, MO) pp 2096–2103

[4] Scholbrock A, Fleming P, Schlipf D, Wright A, Johnson K and Wang N 2016 Lidar-enhanced wind turbine control: Past, present, and future *Proc. American Control Conf.* (Boston, MA) pp 1399–1406

[5] Lio W H, Rossiter J A and Jones B L 2014 A review on applications of model predictive control to wind turbines *UKACC Int. Conf. Control* (Loughborough, UK) pp 673–678

[6] Bossanyi E A, Fleming P A and Wright A D 2013 *IEEE Trans. Control Systems Technology* **21** 1067–1078

[7] Harris M, Hand M and Wright A 2005 Lidar for turbine control Tech. Rep. NREL/TP-500-39154 NREL Golden, CO

[8] Jonkman J, Butterfield S, Musial W and Scott G 2009 Definition of a 5-MW reference wind turbine for offshore system development Tech. Rep. NREL/TP-500-38060 NREL Golden, CO

[9] Jonkman J and Buhl Jr M 2005 FAST user's guide Tech. Rep. NREL/EL-500-38230 NREL Golden, CO

[10] Dickler S, Wintermeyer-Kallen T, Zierath J, Konrad T and Abel D 2021 *Forsch Ingenieurwes* **85** 313–323

[11] embotech 2016 Optimal wind turbine control online; accessed April 2021 URL `https://www.embotech.com/wp-content/uploads/Vestas_story_embotech.pdf`

[12] Berger F, Kröger L, Onnen D, Petrović V and Kühn M 2018 Scaled wind turbine setup in a turbulent wind tunnel *Deep Sea Offshore Wind R&D Conf.* (*J. Physics: Conf. Series* vol 1104) p 012026

[13] Sinner M, Petrović V, Berger F, Neuhaus L, Kühn M and Pao L Y 2020 Wind tunnel testing of an optimal feedback/feedforward control law for wind turbines *Proc. IFAC World Congress* (Berlin, Germany)

[14] Sinner M, Petrović V, Langidis A, Neuhaus L, Hölling M, Kühn M and Pao L Y 2021 *IEEE Trans. Control Systems Technology*

[15] Verwaal N, van der Veen G and van Wingerden J W 2015 *Wind Energy* **18** 385–398

[16] Campagnolo F, Weber R, Schreiber J and Bottasso C L 2020 *Wind Energy Science* **5** 1273–1295

[17] Navalkar S T, van Solingen E and van Wingerden J W 2015 *IEEE Trans. Control Systems Technology* **23** 2101–2116

[18] Fontanella A, Bayati I and Belloli M 2018 Control of floating offshore wind turbines: Reduced-order modeling and real-time implementation for wind tunnel tests *Proc. ASME Int. Conf. Offshore Mechanics and Arctic Engineering* (*Ocean Renewable Energy* vol 10) (Madrid, Spain)

[19] Petrović V, Berger F, Neuhaus L, Hölling M and Kühn M 2019 Wind tunnel setup for experimental validation of wind turbine control concepts under tailor-made reproducible wind conditions *Proc. Science of Making Torque from Wind* (*J. Physics: Conf. Series* vol 1222) p 012013

[20] Franklin G, Powell D and Emami-Naeini A 2019 *Feedback Control of Dynamic Systems* 8th ed (Pearson) ISBN 0134685717

[21] The Mathworks Inc MATLAB URL `https://www.mathworks.com/products/matlab.html`

[22] Ferreau H, Kirches C, Potschka A, Bock H and Diehl M 2014 *Mathematical Programming Computation* **6** 327–363

[23] National Instruments LabVIEW URL `https://www.ni.com/en-us/shop/labview.html`

[24] Kröger L, Frederik J, van Wingerden J W, Peinke J and Hölling M 2018 Generation of user defined turbulent inflow conditions by an active grid for validation experiments *Proc. Science of Making Torque from Wind* (*J. Physics: Conf. Series* vol 1037) p 052002

[25] Makita H 1991 *Fluid Dynamics Research* **8** 53–64

[26] Knebel P, Kittel A and Peinke J 2011 *Experiments in Fluids* **51** 471–481

17^{th} EAWE PhD Seminar on Wind Energy
3-5 November 2021
Porto, Portugal

Linearized Free Wake Vortex Model for Adjoint Optimization

D.G. van den Berg, D. de Tavernier, and J.W. van Wingerden

Delft University of Technology, Delft Center for Systems and Control, Mekelweg 2, 2628 CD Delft, NL

E-mail: `d.g.vandenberg@tudelft.nl`

Keywords: Free Wake Vortex Model, Linearisation, Adjoint Optimization

1 Introduction

Wind power is often generated by wind turbines collected in a cluster as a wind farm. Turbines positioned downstream are subjected to the wakes of the upstream turbines reducing power capture. Recently dynamic (individual) pitching control schemes such as the Pulse [1] and Helix [2] have shown great potential in negating the adverse effects of the wake on downstream turbines. The optimal pitching frequency and overall shape of the signal for wake-mixing purposes is still undetermined. It is expected that the location of the downstream turbine will play a significant role in the type and frequency of the pitching. The optimization of these inputs is a difficult problem due to the complexity and computational cost of unsteady aerodynamic models. Therefore, we propose to derive and use a linearized free wake vortex model for optimization purposes.

2 Free Wake Vortex Model

For the purpose of this research, the wind turbine rotor is modeled as a thin 2D actuator disk. The thrust loading is assumed to act normal to the rotor plane and is distributed uniformly over the disk. This load distribution implies a vortex shedding at the locations where the pressure gradient is non-zero, i.e. only at the edges of the disk, see figure 1. A simple relation can be derived that relates the rotor loading to the shed vorticity. In a free wake vortex method, the vortices travel downstream under the influence of the free stream velocity and the induced velocity of all shed vortices in the field. The updated position for each of vortex element is defined by equation 1: The updated position for each of the particles can be calculated by solving equation 1:

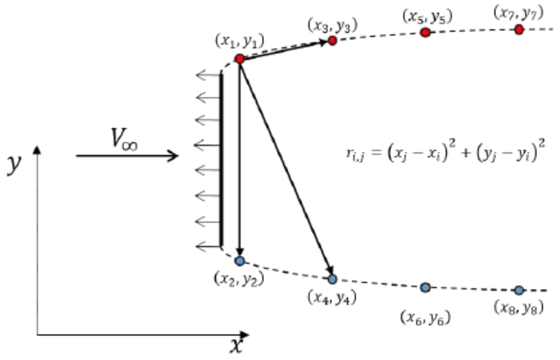

Figure 1: Schematic overview of the free vortex wake mode.

$$\begin{bmatrix} x_{n+1} \\ y_{n+1} \end{bmatrix} = \begin{bmatrix} x_n + (U(x_j, y_j, \Gamma_j) + V_\infty)\Delta t \\ y_n + V(x_j, y_j, \Gamma_j)\Delta t \end{bmatrix}, \tag{1}$$

with Δt the time step and where $U(x_j, y_j, \Gamma_j)$ and $V(x_j, y_j, \Gamma_j)$ are induced velocities modeled by the Biot-Savart law [3]:

$$U(x_j, y_j, \Gamma_j) = \sum_{j\neq i}^{n-1} \frac{\Gamma_j(y_j - y_i)}{2\pi(r_{i,j})}\left(1 - e^{\frac{-r_{i,j}}{c^2}}\right),\ V(x_j, y_j, \Gamma_j) = \sum_{j\neq i}^{n-1} \frac{\Gamma_j(x_j - x_i)}{2\pi(r_{i,j})}\left(1 - e^{\frac{-r_{i,j}}{c^2}}\right). \tag{2}$$

Here n is the number of shed vortices, i the current vortex point and c the core radius introduced to avoid numerical instabilities when $r_{i,j} << 1$.

3 Linearization and Outlook

The update equation (1) can be cast into a state space equation with a nonlinear term:

$$\bar{X}(k+1) = A\bar{X}(k) + f(\bar{X}(k)) + \bar{X}_0(k), \tag{3}$$

where the state vector is given by$\bar{X} = \begin{bmatrix} x_1 & \dots & x_n & y_1 & \dots & y_n & \Gamma_1 & \dots & \Gamma_n \end{bmatrix}^T$, $f(\bar{X}(k))$ is the non-linear velocity function and $\bar{X}_0$ represents the location and strength of the new shed vortices at time step k. This vector $\bar{X}_0$ can be considered as a linear input matrix (‘B matrix’) to the system. Matrix A can be seen as an update matrix that propagates the coordinates as well as the vortex strength, Γ_j, downstream. Through the choice of these states the velocity function $f(\bar{X}(k))$ is non-linear in all the states of the state space system. This fact can be exploited for the purpose of finding a linear model. Take for example the update step from x_1 to x_3, with u_1 the local induced velocity, it is given by

$$x_3 = x_1 + u_1\Delta t + V_\infty \Delta t = x_1 + \left(\sum_{j\neq 1}^{n-1} \frac{\Gamma_j(y_j - y_1)}{2\pi(r_{1,j})}\right)\left(1 - e^{\frac{-r_{i,j}}{c^2}}\right)\Delta t + V_\infty \Delta t. \tag{4}$$

Around the linearization point the induced velocity can be approximated by a Taylor series as

$$\sum_{j\neq 1}^{n-1} \frac{\Gamma_j(y_j - y_1)}{2\pi(r_{1,j})}\left(1 - e^{\frac{-r_{i,j}}{c^2}}\right) \approx \frac{\partial u_1}{\partial x_1}x_{1,e} + \dots + \frac{\partial u_1}{\partial x_n}x_{n,e} + \frac{\partial u_1}{\partial y_1}y_{1,e} + \dots + \frac{\partial u_1}{\partial y_n}y_{n,e} + \frac{\partial u_1}{\partial \Gamma_1}\Gamma_{1,e} + \dots + \frac{\partial u_1}{\partial \Gamma_n}\Gamma_{n,e}. \tag{5}$$

By doing the same Taylor approximation for each induced velocity the full linearized model is then of the form

$$\bar{X}(k+1) = \left(A + \frac{\partial f(\bar{X}(k))}{\partial \bar{X}(k)}\right)\bar{X}(k) + \bar{X}_0(k). \tag{6}$$

This model will be used within the adjoint optimization method [4] for optimizing the wake-mixing input. With the adjoint method an optimal control input for a generally non-linear system can be found based on its adjoint system dynamics. The first step of the optimization is to gain future state information given a certain control input. Once the state information is available the system adjoint equations are solved. To find a solution to these equations a linearized model as in (6) is required. Based on this information a gradient based optimization is formulated that minimizes the cost function as a function of control input. A technique like this opens up the possibility to explore different turbine control inputs for the goal of wake mixing.

References

[1] W. Munters and J. Meyers, “Effect of wind turbine response time on optimal dynamic induction control of wind farms,” *Journal of Physics: Conference Series*, vol. 753, Oct. 2016.

[2] J. A. Frederik, B. M. Doekemeijer, S. P. Mulders, and J.-W. v. Wingerden, “The helix approach: Using dynamic individual pitch control to enhance wake mixing in wind farms,” *Wind Energy*, vol. 23, no. 8, pp. 1739–1751, 2020.

[3] J. G. Leishman, *Principles of Helicopter Aerodynamics.* Cambridge University Press, 2nd ed., Dec. 2016.

[4] R. F. Stengel, *Optimal Control and Estimation.* Dover Publications, 1994.

17^{th} EAWE PhD Seminar on Wind Energy
3-5 November 2021
Porto, Portugal

Extending the Helix approach to a wind farm

H Korb[a], H Asmuth[a], and S Ivanell[a]

[a]Wind energy group, Uppsala University

E-mail: henry.korb@geo.uu.se

Keywords: Wind farm control

1 Abstract

Wind farm control to improve power production has been long aimed for by various methods. The first attempts date back to 1988 [1]. Many different approaches have been taken, which can mainly be divided into the categories of wake-steering and wake-mixing. However, static approaches could not show consistent increases and the increase proved to be highly dependent on the simulation method [2]. However, the examination of dynamic approaches has begun recently [3]. One promising approach utilizing individual pitch control is the helix approach [4]. By exerting a rotating moment onto the wake, this approach increases the wake mixing and leads to higher inflow velocities at downstream turbines. The approach showed increased total power production by 7.5 % in high fidelity simulations of a wind farm consisting of 2 turbines. A naive extension to a 3 turbine wind farm was done in [5]. It corroborated the results from the first study for the first two turbines, however, the effect could not be repeated after the second turbine. This phenomenon will be examined in this study. The work will include a thorough theoretical analysis of the Helix approach as well as an examination of multiple LBM-LES simulations to find a viable extension of the approach to larger wind farms. The theoretical analysis reveals, that there exists a phase shift between the helices caused by the individual turbines. It is shown, that this phase shift reduces the total force exerted onto the wake. By cancelling this phase shift, the force on the wake is maximized. Simulations are conducted to validate the assumptions made in the theoretical analysis. Simulations with single turbines show that there exists an area with an almost constant transport velocity of the helix, which is one of the major assumptions of the theoretical analysis. After this helix transport velocity has been determined, simulations with multiple turbines are conducted, with and without cancelling the phase shift. The results of the multi-turbine cases show that cancelling the phase shift leads to yet another increase in power production. These results points towards a successful extension of the helix approach to a full wind farm and justifying the theoretical analysis.

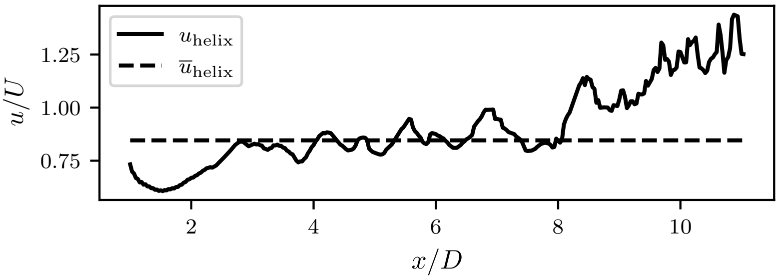

Figure 1: Helix transport velocity compared to mean helix transport velocity.

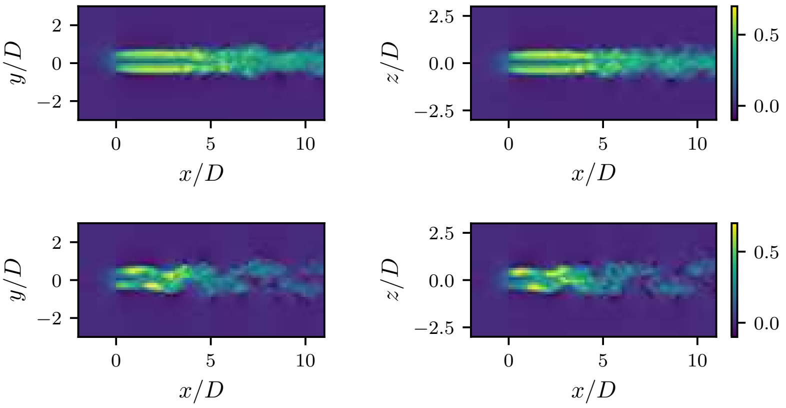

Figure 2: Comparison of instantaneous field of streamwise velocity of turbine controlled with Greedy Control (upper row) and Helix approach (lower row) at 9 m/s.

References

[1] Steinbuch M, de Boer W W, Bosgra O H, Peters S A W M and Ploeg J 1988 *Journal of Wind Engineering and Industrial Aerodynamics* **27** 237–246 ISSN 0167-6105

[2] Kheirabadi A C and Nagamune R 2019 *Journal of Wind Engineering and Industrial Aerodynamics* **192** 45–73 ISSN 0167-6105

[3] Munters W and Meyers J 2018 *Energies* **11** 177

[4] Frederik J A, Doekemeijer B M, Mulders S P and van Wingerden J W 2020 *Wind Energy* ISSN 1095-4244

[5] Korb H, Asmuth H, Stender M and Ivanell S 2021 *Journal of Physics: Conference Series* **1934** 012022 ISSN 1742-6588, 1742-6596

Identification of interacting turbines with time variant wind direction

F. Bernardoni[a], U. Ciri[b], M. A. Rotea[a], and S. Leonardi[a]

[a]Center for Wind Energy, University of Texas at Dallas, Richardson, Texas, USA
[b]Department of Mechanical Engineering, University of Puerto Rico at Mayagüez, Mayagüez, Puerto Rico, USA

E-mail: `stefano.leonardi@utdallas.edu`

Keywords: Wind farm, Wake interaction, Real-time

Extended abstract

An efficient strategy for maximizing the power production of a power plant is to control in a coordinated way only turbines that are aerodynamically coupled through wake effects[1]. The implementation of such control strategy thus requires, in first place, the knowledge of which clusters of turbines are coupled through wake interaction. However, these clusters vary as the wind changes direction. In order to apply any wake control optimization strategy in practical applications, it is then fundamental to track in real time turbine clusters with an algorithm able to promptly identify changes in wind direction and to discern when the application of coordinated control strategy would produce an actual power production gain. In a previous study[2], we identified turbine clusters with a method based on the correlation of the power production signal among all the turbines in the wind farm. When the method does not find any cluster in the farm, it means that the wake interaction is weak and that a coordinated optimization (yaw in this case) is not effective. While in the previous study we considered 4 different but constant wind directions, in this work we reproduce a realistic condition where the wind direction varies in time over a span of 60° (see black line of Fig.1b). In order to reproduce this scenario and simulate the necessary SCADA data, the flow field in a 4x4 array of turbines is simulated with Large Eddy Simulations. The layout of the wind farm is reported in Fig.1a. The average wind speed at the hub height is $0.8U_{rated}$. Turbulence obtained from a precursor simulation is superimposed to the mean flow so that the average turbulence intensity at the hub height is of 11%. Turbine rotors are reproduced with rotating actuator disk while the nacelles and towers are reproduced with immersed boundary technique. In order to identify the turbine clusters in real-time, we apply the same method described in the previous paper but with power correlation based on running average over time. An important factor to be considered when dealing with time varying wind direction is that an actual power gain from wake control strategy is obtained only when the wind direction remains consistent over a prolonged amount of time. A change in the wind conditions over a turbine or of a control set point affects the downstream turbines after a time delay which corresponds to the time the wake need to reach the downstream turbines. For large wind farms this can be of the order of several minutes. As an example, the blue line of Fig.1b shows the wind direction measured by the turbine T01, representative of the upstream turbines, while the red line reports the wind direction measured by the turbine T16, that is the most downstream turbine. The wind direction signals measured at the two turbines location present rapid fluctuations that are due to the turbulence and, for the case of T16, to the wake interaction as well. From the comparison between the blue and red lines we can observe a time delay of about 10 minutes from the time at which the wind direction changes at T01 to the time at which it changes at T16. During these transients the wind direction is not uniform across the wind farm and the imposition of yaw misalignment for wake steering control purposes may actually result in power losses.

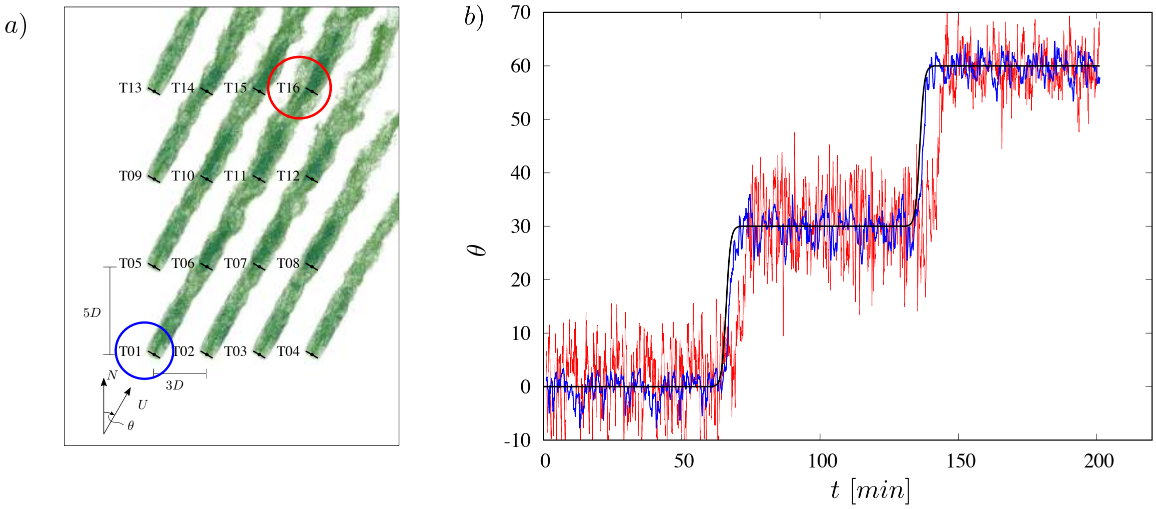

Figure 1: *a*) Layout of the wind farm and turbine wakes for 30° wind direction. *b*) Time variation of the wind direction: the black line corresponds to space-averaged wind direction at the inlet, the blue line corresponds to the wind direction measured at T01 and the red line corresponds to the wind direction measured at T16.

We address this issue by performing a parametric study of the length of the sliding time-window over which the power production correlation has to be computed at each time step in order to identify clusters of turbines coupled by the wake interaction. In particular sliding windows of 10, 20, 30 and 40 minutes of power production data are considered for the computation of the correlation coefficients and the identification of the turbine clusters. Results shows that 30 minutes is the best performing time frame over which the power correlation should be computed. With a too small time window, wakes cannot fully propagate across the wind farm. On the contrary, a too large amount of time does not allow a prompt identification of the clusters after the wind direction changes. Indeed, using a longer time interval of data implies that the transition of the wind direction affects the correlation of the power production over a longer period of time. Thus, clusters are identified with a larger time delay. When, for example, a sliding window of 40 minutes is used, the clusters are identified after about the same time (40 minutes) since the wind direction starts changing at the most upstream end of the wind farm. Using 30 minutes of data reduces this time delay in the cluster identification without reducing the accuracy. If the length of the sliding window is further decreased, the accuracy of the identification deteriorates until the limit case of 10 minutes time-window when no clusters are identified.

This study aims to test the turbine cluster identification method described in [2] under more challenging conditions and to develop the best practice guidelines for the applications of the proposed method to real operative wind farms.

References

[1] Fleming P, King J, Simley E, Roadman J, Scholbrock A, Murphy P, Lundquist J K, Moriarty P, Fleming K, van Dam J *et al.* 2020 *Wind Energy Science* **5** 945–958

[2] Bernardoni F, Ciri U, Rotea M A and Leonardi S 2021 *Journal of Renewable and Sustainable Energy* **13** 043301

LES verification of HAWC2Farm aeroelastic wind farm simulations with wake steering and fatigue load analysis

J Liew[a], SJ Andersen[b], N Troldborg[a], and T Göçmen[a]

[a]Department of Wind Energy, Technical University of Denmark (DTU), Frederiksborgvej 399, 4000 Roskilde, Denmark.
[b]Department of Wind Energy, Technical University of Denmark (DTU), Anker Engelunds Vej 1, 2800 Lyngby, Denmark.

E-mail: jyli@dtu.dk

Keywords: Wind farm control, yaw steering, fatigue loads, LES, multi-fidelity modelling

1 Introduction

Dynamic wind farm modeling tools have been the topic of a growing topic of interest in recent years. In particular, promising results have been investigated in the field of wind farm control, including wake steering [1], static induction control [2] and dynamic induction control [3]. Using these methods, power output in a wind farm can be increased by several percent as shown in various simulations, wind tunnel experiments and field tests [4]. Despite the promising results, there are very few studies which identify the dynamic loading experienced by the turbines when such control strategies are implemented. Past studies suggest that yaw steering can lead to varying fatigue loading in both the upstream [5] and downstream turbines [6].

Aeroelastic wind farm simulation platforms, such as FAST.Farm [7], can provide valuable information on the dynamic response of a wind farm. In this study, we introduce a new aeroelastic wind farm tool, HAWC2Farm. HAWC2Farm models each turbine using the aeroelastic code, HAWC2 [8, 9], while also dynamically modelling the wind field and wakes using the Mann turbulence model [10] and the dynamic wake meandering model [11] respectively (Fig. 1). Hence, we couple a mid-fidelity multi-body finite element solver and flow solver, providing a computationally efficient flow control oriented platform. We present a numerically verification of HAWC2Farm with wake steering and fatigue load analysis in a large wind farm using large eddy simulations (LES).

2 Conclusions

We present a numerical verification of a new dynamic aeroelastic wind farm simulation tool, HAWC2Farm. The verification compares HAWC2Farm to LES simulations, and includes wake steering and a fatigue load analysis. The presented study builds a foundation for future research using the numerical tool.

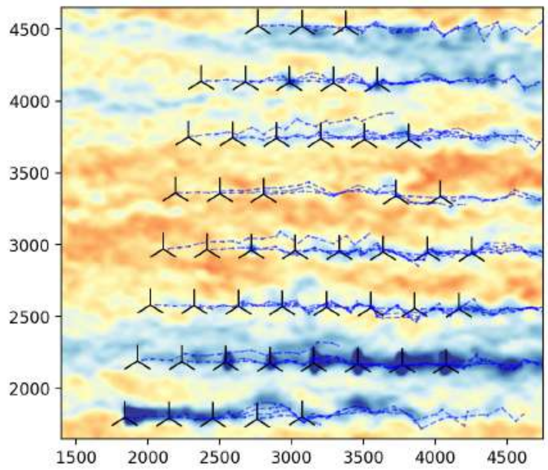

Figure 1: Overhead snapshot of HAWC2Farm simulations of the Lillgrund wind farm (wind direction: 198^o.)

References

[1] Gebraad P M, Teeuwisse F, Van Wingerden J, Fleming P A, Ruben S, Marden J and Pao L 2016 *Wind Energy* **19** 95–114

[2] Lio W H, Mirzaei M and Larsen G C 2018 *Journal of Physics: Conference Series* vol 1037 (IOP Publishing) p 032040

[3] Munters W and Meyers J 2018 *Wind Energy Science* **3** 409–425

[4] Kheirabadi A C and Nagamune R 2019 *Journal of Wind Engineering and Industrial Aerodynamics* **192** 45–73

[5] Kragh K A and Hansen M H 2014 *Wind Energy* **17** 971–982

[6] Kanev S, Bot E and Giles J 2020 *Energies* **13** ISSN 1996-1073 URL `https://www.mdpi.com/1996-1073/13/16/4088`

[7] Jonkman J, Doubrawa P, Hamilton N, Annoni J and Fleming P 2018 *Journal of Physics: Conference Series* **1037** 062005 URL `https://doi.org/10.1088/1742-6596/1037/6/062005`

[8] Larsen T J and Hansen A M 2007 *target* **2**

[9] Madsen H A, Larsen T J, Pirrung G R, Li A and Zahle F 2020 *Wind Energy Science* **5** 1–27

[10] Mann J 1998 *Probabilistic engineering mechanics* **13** 269–282

[11] Larsen G C, Madsen H A, Thomsen K and Larsen T J 2008 *Wind Energy* **11** 377–395

Control-oriented modelling of wind farms based on wind tunnel experiments

M A Zúñiga[a], V Petrović[a], M Kühn[a]

[a] ForWind – Center for Wind Energy Research, Institute of Physics, University of Oldenburg, Küpkersweg 70, 26129 Oldenburg, Germany

E-mail: manuel.zuniga@uni-oldenburg.de

Keywords: Wind Farm Flow Control, Wake Engineering Models

1 Background

Common practice in industry relies on the so-called greedy control at turbine level whose main objective is to maximize the individual performance of each turbine within a wind farm. This approach does not account for wake interactions among neighbouring turbines and with atmospheric boundary layer flows, resulting in a non-optimal plant performance [1]. Moreover, high wind energy penetration is leading to stricter grid codes that demand greater participation of wind farms in the provision of ancillary services. Cooperative wind farm control aims to cope with these issues by adopting suitable control strategies (e.g. power derating, wake steering) at farm level for alleviating wake-induced power losses and mechanical loads, while also improving grid integration [2]. Successful practical implementation goes through further investigation of the potential benefits and drawbacks of the adopted control strategies. Main challenges arise from the inherent complexity in predicting wakes accurately and fast enough to support model-based control optimisation, as well as the lack of validation of the control concepts.

2 PhD Project Description

The aim of this project is the development and validation of improved engineering wake models to support wind farm control applications. Wind tunnel experiments under tailored and repeatable turbulent inflow conditions are the chosen methodology to investigate and compare the potential benefits of two different induction control strategies: i) static pitch-based control, ii) dynamic collective sinusoidal-pitch control, both in terms of power maximisation and loads mitigation. Additionally, the employed strategies will be used to evaluate the capabilities for supporting short-term power boost. Although research in the field has focused primarily on wake steering control, recent studies suggest that strategies based on power derating remain promising. For instance, [3, 4] report positive power gains of about 1% for static-induction controllers tested in commercial wind farms. [5,6] find even higher gains ranging between 2-3% by applying periodic dynamic induction strategies in high-fidelity simulations and wind tunnel experiments.

The project will be carried out in three complementary stages: 1.) control-oriented model development, 2.) model-based controller design, 3.) evaluation and validation. For the first stage, the aim is to investigate the wake characteristics and generate data for calibrating and improving existing control-oriented wake models. The corresponding wind tunnel campaigns will be divided in two different phases, one for each controller strategy using: 1.1.) different derating levels and 1.2.) different imposed pitch sinusoids. For each case, the experiments will be conducted with up to three aligned model turbines spaced at five rotor diameters (5D) downstream. The model wind turbine Oldenburg (MoWiTO 0.6) with 0.58 m diameter, controllable collective pitch and generator torque will be used in all the experiments [7], see Figure 1a. It is of particular interest to study different scenarios with different turbulence intensities, shear levels and wind gusts, which can be generated using an in-house state-of-the-art active grid, see figure 1b. A WindScanner or an array of hot-wires will be used to obtain cross-sectional measurements of the wake at different downstream positions, while obtaining simultaneous measurements of thrust and power of each turbine. The collected data will be subsequently used to calibrate and compare existing control-oriented wake models. This will aid the selection of the model with better performance for controller synthesis. At a second stage, an open-loop model-based controller will be designed for each control objective. After the controller design, a first run of experiments will take place in the wind tunnel to evaluate the performance of the control algorithms. Thereafter, the controllers will be adjusted to better match the experimental data. Afterwards, some new experiments will be conducted to re-evaluate the performance of the tuned control schemes. At a final stage, an extensive validation for each controller will take place with the goal of evaluating the adaptability to different disturbances when deviating from the calibration setup, such as turbine repositioning, wind gusts, shutdown of certain turbines, etc.

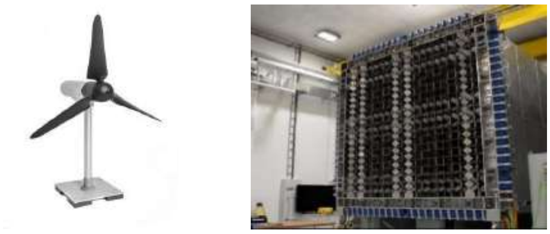

Figure 1. (a) MoWiTO 0.6; (b) Active-grid [8]

3 Results

Initial results from the first wind tunnel campaign will be presented during the PhD seminar. This will mainly consist of preliminary analysis to determine the optimal static pitch-based derating setpoints and optimal dynamic collective-sinusoidal pitch signal. As baseline case, the model turbines will be greedily operated at their individual optimal settings. Next, the first turbine will be derated by gradually increasing the pitch angle until reaching a desired power-reduction level. Thereafter, the first turbine will be actuated using sinusoidally varying pitch signals, with different amplitudes and excitation frequencies. In both cases, we want to find under which conditions the wind farm power is increased, decreased or stays the same as the baseline case. Similarly, we aim to determine what is the impact in loads due to the implemented strategies. The next step will be the measurement of wake profiles for the determined optimal control cases and comparison against engineering wake models.

Acknowledgements

This project is funded by the Deutscher Akademischer Austauschdienst (DAAD).

References

[1] Andersson L, Anaya-Lara O, Tande J, Merz K and Imsland L 2021 *IET Ren Power Generation* **15** 2085-2108
[2] Kheirabadi A and Nagamune R 2019 *J. Wind Eng. Ind. Aerodynamics* **192** 45–73
[3] Hoek D, Kanev S, Allin J, Bieniek D and Mittelmeier N 2019 *Renew. Energy* **140** 994–1003
[4] Bossanyi E and Ruisi R 2021 *Wind Energy Sci.* **6** 389–408
[5] Munters W and Meyers J 2018 *Wind Energy Sci.* **3** 409–425
[6] Frederik J, Weber R, Cacciola S, Campagnolo F, Croce A, Bottaso C, van Wingerden J. 2020 *Wind Energy Sci.* **5** 245–257
[7] Schottler J, Hölling A, Peinke J and Hölling M 2016 *J. of Physics: Conf Series* **753** 20-30
[8] Neuhaus L, Berger F, Peinke J and Hölling M 2021 *Experiments in Fluids* **62** 130-142

eawe
european academy of wind energy

U.PORTO
FEUP FACULDADE DE ENGENHARIA
UNIVERSIDADE DO PORTO

17th EAWE PhD Seminar on Wind Energy
3-5 November 2021
Porto, Portugal

Wind turbine power maximization using log-power PIESC

Devesh Kumar and Mario A. Rotea

Center for Wind Energy, The University of Texas at Dallas, Richardson, TX 75080 USA

`E-mail: Devesh.Kumar@utdallas.edu`

Abstract

This paper will describe a Log-of-power Proportional-Integral Extremum Seeking Control (LP-PIESC) algorithm for maximizing the power capture of a wind turbine operating in below-rated wind conditions. The conventional Extremum Seeking Control (ESC) algorithm suffers from slow and inconsistent convergence behaviour under changing wind speeds. One possible solution to this problem is to replace the feedback of the power signal with its logarithm. This results in an algorithm that is robust to variations in wind conditions. Also, recent studies have shown that replacing the conventional ESC with one of its variants; i.e., proportional plus integral ESC (PIESC) could result in faster convergence to the optimal conditions. In the current paper, a PIESC algorithm is used to maximize the log-of-power signal in below rated wind speeds. OpenFAST simulation results show the efficacy of the proposed algorithm to find the control settings that maximize power in real time.

Keywords: Wind turbine power maximization, Proportional-Integral Extremum Seeking Control (PIESC), Log-of-Power (LP) feedback.

1 Introduction

The operation of a wind turbine controller in below-rated conditions involves actively controlling the angular rotor speed to maximize the power extracted from the wind. The rotor power in below-rated wind speeds is proportional to the power available in the wind and the parameter of proportionality is the the power coefficient (C_p). In variable-speed variable-pitch turbines, the power coefficient (C_p) is a unimodal function of the tip-speed ratio (λ) and the blade-pitch angle (β)[1], which implies there are optimal tip-speed ratio and blade-pitch angle for achieving the optimal C_p and hence maximum output power. Manufacturer's specified optimal parameters can differ from the actual optimal tip-speed ratios and blade-pitch angles due to degradation of rotor components and site-specific complex aerodynamic effects.

Extremum Seeking Control (ESC) has emerged as an effective real-time optimization strategy to maximize power capture in region-2 despite lack of knowledge of optimal turbine parameters. Creaby *et al.* [2] studied ESC based region-2 control with power feedback for tuning the torque gain (i.e., a rotor speed control parameter), blade-pitch angle and yaw angle. Field test results of ESC region-2 controllers on the NREL CART3 turbine were presented by Xiao *et al.* in [3]. In spite of the demonstrated success of ESC studies, a drawback of these strategies is the inconsistent convergence behavior to the optimal control parameters under changes in wind speed within region-2. Rotea [4] analyzed the root cause of inconsistent convergence; he proposed a “log-power feedback strategy” for ESC-based wind turbine control. The improved and consistent convergence of the log-power ESC was demonstrated in [4] with a simple reduced order model. Later, Ciri *et al.* [5] demonstrated, through high-accuracy large eddy simulations, that the log-power feedback ESC calibrated at a given wind speed exhibits consistent and robust performance across all wind speeds within region-2 under realistic turbulent wind conditions.

The ESC is a gradient-based steepest ascent search algorithm to find (local) optima in real time. Guay *et al.* [6] has recently proposed an ESC algorithm that estimates the gradient using a variant of the recursive least-squares algorithm for parameter estimation. The technique in [6] introduces a proportional-integral approach to improve the transient performance of the extremum-seeking controller. The algorithm in [6] shall be referred to as PIESC.

This current paper contains results from [7], which introduced the log-of-power PIESC (LP-PIESC) scheme for region-2 power maximization and compared its performance with a conventional ESC algorithm also using a log-power performance index. The algorithms adjust the torque gain parameter k_g in the "classical $\tau_g = k_g\omega_g^2$" control law for region-2 power maximization, where τ_g is the reference generator torque and ω_g a filtered version of the measured generator speed. The simulation results in this paper demonstrate that the combination of the log-of-power transformation with the PIESC scheme yields a robust and fast algorithm for optimal tuning of the torque gain with less invasive dither signal than currently possible with the conventional log-of-power ESC (LP-ESC).

2 Background

2.1 Log-Power Maximization using Gradient-Based Algorithms

ESC and PIESC are gradient-based algorithms that tune parameters to maximize a system's performance index in real time. These algorithms operate without the need of a detailed physical models. The gradient of the performance index with respect to the parameters is estimated by perturbing the tunable parameters with a zero-mean periodic dither signal. The gradient estimate can be extracted by demodulating it from a measurement of the perturbed performance index (ESC) or by using variants of recursive least squares (PIESC) [6]. Then, the values of the tunable parameters are updated according to the estimated gradient. Starting from a sub-optimal guess of the parameter values, the optimum is reached asymptotically.

An ESC-based analysis was done in [4] for below-rated wind turbine control which justifies the advantages of using logarithm power (LP) feedback over power feedback under varying wind conditions. The power contained in incoming wind of velocity V is given by

$$P_{\text{wind}} = \frac{1}{2}\pi R^2 \rho V^3 \tag{1}$$

where, ρ is air density in kg/m^3, R is rotor radius in m, and V is the incoming wind speed perpendicular to the rotor plane in m/s. The rotor power produced can then be given by

$$P = P_{\text{wind}} C_p(u) \tag{2}$$

where, C_p denotes the power coefficient of wind turbine, and u is a manipulated input such as the generator torque (or equivalently torque gain), blade pitch angle or yaw measurement. With the rotor power used as the performance index for ESC, its gradient with respect to u is

$$\frac{\partial P}{\partial u} = P_{\text{wind}} \frac{\partial C_p(u)}{\partial u} \tag{3}$$

which depends on the wind speed. For a gradient search algorithm like ESC, a wind speed dependent gradient yields a wind speed dependent convergence rate. This explains why the appropriate gain has to be tuned under different wind speeds. In contrast, if the logarithmic power is used as the performance index, i.e. $J = \ln P$, the gradient becomes

$$\frac{\partial J}{\partial u} = \frac{\partial}{\partial u} \ln\left(P_{\text{wind}} C_p(u)\right) = \frac{1}{C_p(u)} \frac{\partial C_p(u)}{\partial u} \tag{4}$$

which is independent of the wind speed. Therefore, the ESC process thus designed will be less affected by wind speed fluctuation and, in theory, it maximizes the power coefficient C_p directly.

Note from (1) and (3) that the convergence properties of gradient-based algorithms using a direct power measurement is a strong function of V^3. Thus, without re-tuning, such algorithms will exhibit slow convergence at low wind speeds and may become unstable at high wind speeds [4, 5]. On the other hand, if a gradient-based algorithm is used to maximize the log-power performance index, then it follows from (4) that convergence and stability are independent of the wind speed V. This results in an easier to tune optimization algorithm with consistent performance across all wind speeds in region-2. This idea from [4] is patent pending [8]. The consistency and robustness of ESC with the log-power performance index is demonstrated in [5] using detailed large eddy simulations.

2.2 LP-ESC and LP-PIESC

In this paper we use conventional extremum seeking control (ESC) in continuous time with logarithm of the rotor power as the performance index to be maximized following the design methodology in [3]. We shall refer to this algorithm as the **LP-ESC**. A typical LP-ESC is shown in Figure 1,

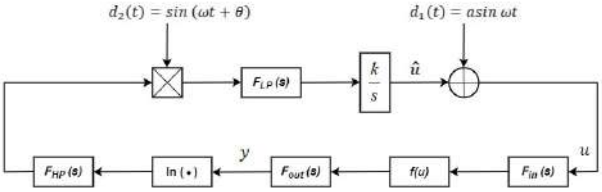

Figure 1: LP-ESC: Conventional ESC with log power feedback

where $F_{in}(s)$ and $F_{out}(s)$ are unity-gain linear time-invariant (LTI) approximation of the input and output dynamics, respectively, and $f(u)$ represents a static map of the performance index (rotor power). Periodic dither signal $d_1(t) = a\sin(\omega t)$ and demodulation signal $d_2(t) = \sin(\omega t + \theta)$ are applied to estimate the gradient $\partial f/\partial u$, where a is the dither amplitude, ω is the dither frequency and θ is the phase compensation. The high-pass filter $F_{HP}(s)$ is applied to the logarithm of the performance index $\ln(y)$ to eliminate the steady-state term of the objective function. Multiplication by $d_2(t)$, a low-pass filter $F_{LP}(s)$ to extract the gradient information, followed by an integrator with gain k complete the ESC loop.

The main goal of the present paper is to compare the LP-ESC with the so-called proportional plus integral extremum seeking control, developed by Guay *et al.* [6], applied to the log-power performance index. We shall refer to this gradient-based algorithm as the **LP-PIESC**. The PI-ESC holds the promise of faster convergence than the conventional ESC due to two main modifications: the use of a recursive least squares like method to estimate the gradient and the addition of a proportional term to accelerate convergence to the optimum. In the proposed proportional integral extremum seeking control, the gradient estimation is done using parameter estimation instead of conventional dither-demodulation technique. The development of the PI-ESC is based on a time-varying estimate of the gradient of the cost and a PI control law to drive the system to its optimal operating point.

The proportional-integral extremum seeking controller proposed in [6] is given by (5) and can be represented as in Figure 2:

$$\begin{cases} u = -k_p\hat{\theta}_1 + \hat{u} + d_1(t) \\ \dot{\hat{u}} = -\frac{1}{\tau_I}\hat{\theta}_1 \end{cases} \tag{5}$$

where, k_p is the proportional gain, τ_I is the time constant and $\hat{\theta_1}$ is proportional to the gradient $\partial f/\partial u$.

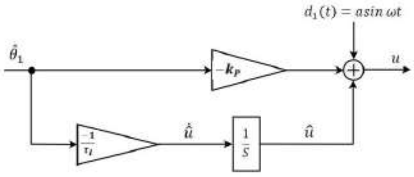

Figure 2: PI controller used for PI-ESC

The parameter to be estimated as presented in [6] is $\theta = [\theta_0, \theta_1]^T$, where the superscript T denotes transpose. In our application, θ is a real-valued vector of dimension two. Only the scalar component θ_1 contains the gradient information we need. The parameter θ_0 is a bias component needed for the parameter estimation to work properly. The parameter estimation update law is given by

$$\dot{\hat{\theta}} = \mathrm{Proj}(\Sigma^{-1}(c(e - \hat{\eta}) - \sigma\hat{\theta}), \hat{\theta}) \tag{6}$$

where, $\mathrm{Proj}(\cdot)$ is a Lipschitz projection operator designed to ensure that the estimates are bounded within the constraint set and guarantee stability. This projection algorithm was implemented as discussed in

Appendix E of [9] and the constraint set adaptation was adopted as per Adetola *et al.* [10]. The forcing term in the differential equation (6) is the prediction error e given by

$$e = y - \hat{y} \tag{7}$$

where y is the logarithm of the performance index to be optimized and $\hat{y}$ represents its prediction. The equation for the predicted output $\hat{y}$ is given by the following dynamics

$$\dot{\hat{y}} = \phi^T\hat{\theta} + Ke + c^T\dot{\hat{\theta}} \tag{8}$$

where $\phi = [1, (u - \hat{u})]^T$ and K is a positive constant to be assigned.

The time varying parameter c in (8) is the solution of the differential equation

$$\dot{c}^T = -Kc^T + \phi^T \tag{9}$$

An auxiliary variable η is introduced and its filtered estimate with dynamics is given by

$$\dot{\hat{\eta}} = -K\hat{\eta} \tag{10}$$

Σ is introduced to be the solution of the matrix differential equation

$$\dot{\Sigma} = cc^T - k_T\Sigma + \sigma I \tag{11}$$

with $\Sigma(0) = \alpha I$ and $\alpha > 0, \sigma > 0, k_T > 0$ i.e., they are positive constants. The inverse of Σ is given by the solution of the matrix differential equation

$$\dot{\Sigma}^{-1} = -\Sigma^{-1}cc^T\Sigma^{-1} + k_T\Sigma^{-1} - \sigma\Sigma^{-2} \tag{12}$$

with $\Sigma^{-1}(0) = \frac{1}{\alpha}I$. The estimation algorithm propagates Σ^{-1}, which is used in the parameter dynamics (6). Simulation results showed a robust and fast converging extremum seeking control.

3 Implementation of LP-ESC and LP-PIESC for Torque Control in Region-2

The LP-ESC and the LP-PIESC algorithms for region-2 wind turbine control are designed and simulated with the NREL 5MW turbine model in OpenFAST. The main parameters of the turbine model are listed in Table 1.

Table 1: Main parameters of NREL 5MW turbine

Description	**Value**
Rating	5MW
Rotor radius (R)	63 m
Gear Ratio (N)	97
Cut-in, Rated, Cut-out wind speed	3 m/s, 11.4 m/s, 25 m/s
Cut-in, Rated rotor speed	6.9 rpm, 12.1 rpm
Rotor Inertia (I_r)	35444067 kg·m^2

The generator torque (τ_g) is generally used as the control variable to maximize power in region-2 and is computed as a tabulated function of the filtered generator speed in NREL's baseline control strategy. The main control law to maximize power below-rated wind speeds is given by

$$\tau_g = k_g\omega_g^2 \tag{13}$$

where, ω_g denotes the generator speed and k_g is the generator torque gain which is used as the control parameter for the extremum seeking algorithms. The theoretical optimal value of k_g is obtained from [1]

$$k_\mathrm{opt} = \frac{1}{2}\frac{\rho AR^3}{N^3}\frac{C_{p,\max}}{\lambda_\mathrm{opt}^3} \tag{14}$$

where A is the cross-sectional area swept by the rotor and ρ is the air density given by 1.22 kg/m^3. For this turbine, the theoretical optimal tip-speed ratio is $\lambda_{\text{opt}} = 7.55$ and the corresponding maximum power coefficient is $C_{p,\max} = 0.48$ [11]. Then, the optimal generator torque gain takes the value $k_{\text{opt}} = 2.34$ Nm/(rad/s)^2.

The non-dimensional normalized torque gain introduced in [4] is used here as the control parameter u. The optimal value of normalized torque gain is

$$u_{\text{opt}} = \frac{k_{\text{opt}}}{I_{\text{r}}} \times N^3 \approx 0.061 \tag{15}$$

A high-level block diagram of the region-2 torque gain LP-ESC/LP-PIESC implementation is depicted in Figure 3. Input to the LP-ESC/LP-PIESC is the logarithm of the rotor power P normalized with respect to the rated power P_{r} =5 MW. A rate limit of 15 kNm/s is applied on the torque reference as per the definition of 5-MW turbine to avoid sudden change in the torque command [11].

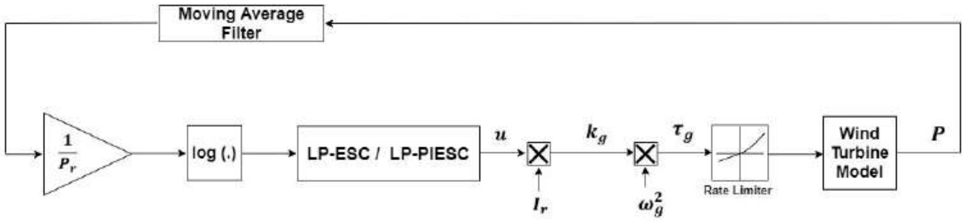

Figure 3: LP-ESC/LP-PIESC implementation.

4 LP-ESC/LP-PIESC Parameter Design

LP-ESC parameters are designed following the guidelines in [12]. The dither frequency is selected within the bandwidth of the plant dynamics. The rotor inertia and actuator dynamics yield the input dynamics, output dynamics is due to sensor dynamics and/or signal conditioning. To simplify the algorithm design, input and output dynamics are combined at the plant input and estimated using open-loop step test responses under constant wind input. The response of the rotor speed under staircase step changes in torque-gain indicates a first-order dynamics, as shown in Figure 4. The estimated time constant from the torque-gain to the rotor speed ranges from 7 to 8 secs. The largest time constant was adopted for ESC design, i.e., 8 sec. The corresponding bandwidth of the combined input-output dynamic for the torque-gain ESC is 0.125 rad/s. Since, dither frequency should be selected within the estimated bandwidth, it was selected as 0.02 rad/sec. The Bode plots for the estimated plant dynamic and the filters in ESC design are shown in Figure 5. The low-pass F_{LP} and high-pass F_{HP} filters (see Figure 1) are first order filters. The dither amplitude was selected using trial and error. The dither amplitude is about 33% of the optimal normalized torque gain in (15). The integrator gain k was designed to achieve a settling time T_s = 15 minutes, approximately for the 8m/s wind speed with 10% TI case and then same integrator gain was used for all other cases. The settling time T_s is defined as the elapsed time from the start of the dithering (control on) to the instant it takes to reach optimum torque gain value for the first time. The LP-ESC parameters used are listed in Table 2. The LP-PIESC scheme was designed to have the same dither frequency as the LP-ESC. After trial and error, the dither amplitude could be reduced significantly to 25% of the dither amplitude value of LP-ESC. This result is important because the external dither is a perturbation to the overall turbine. One plausible explanation for the smaller dither amplitude is that the method for gradient estimation in LP-PIESC, equations (6) to (12), is more sophisticated than the one used in the conventional LP-ESC. The parameters for LP-PIESC scheme are listed in Table 3.

5 Simulation Results

The LP-ESC and the LP-PIESC controllers with the algorithm parameters shown in Tables 2 and 3 are evaluated with OpenFAST simulations for different hub-height mean wind speeds of 4 m/s, 8 m/s and 12 m/s, no wind shear and under turbulence intensities (TI) of 10% and 15%, respectively. Figure 6

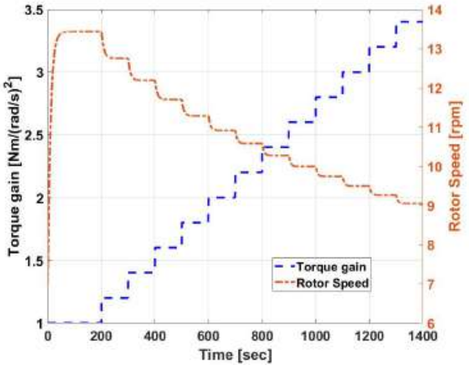

Figure 4: Rotor speed dynamics on step change in k_g

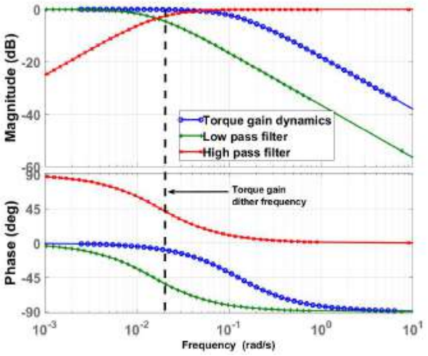

Figure 5: Bode Plot of input dynamics, LPF, HPF and the dither frequency

Table 2: LP-ESC Parameters of NREL 5MW Region 2 controller (see Figure 1)

Parameter	**Torque-gain ESC**
Dither Frequency (ω)	0.02 rad/s
Dither Amplitude (a)	0.02 (non-dimensional)
Cut-off Frequency of LPF	0.015 rad/s
Cut-off Frequency of HPF	0.018 rad/s
Phase Compensation (θ)	0.36 rad
Integrator Gain (k)	0.001 s^{-1}

Table 3: LP-PIESC Parameters of NREL 5MW Region 2 controller. See equations (6) to (12).

Parameter	**Torque-gain PIESC**
Dither Frequency (ω)	0.02 rad/s
Dither Amplitude (a)	0.005 (non-dimensional)
k_T	20 s^{-1}
K	20 s^{-1}
σ	$10^{-6}s^2$
k_p	0.000005 s
τ_I	2.8 (non-dimensional)

shows the hub-height wind time series for the three mean wind speeds (i.e., 4 m/s, 8 m/s and 12 m/s) used in the simulation study with 10% TI. These wind profiles are then used to evaluate the performance of LP-ESC and LP-PIESC in Figures 7 and 8, respectively. The top plot shows the normalized torque gain (u), middle plot shows the tip speed ratio (λ) and the estimated power coefficient (C_p) is shown in the bottom plot. Tip speed ratio (λ) and the estimated power coefficient (C_p) plots are obtained by applying a 100-second moving average filter on the OpenFAST outputs for these variables. The vertical dashed lines in Figure 7 show the time LP-ESC is turned on and the time for convergence to the optimum normalized torque gain u_{opt}. Both LP-ESC and LP-PIESC are turned on at 150s. It can be observed that the LP-ESC takes around 850s (i.e., $\approx$ 15min as designed) to converge to the optimum torque gain for 8 m/s and 12 m/s mean wind speeds. In stark contrast, the LP-PIESC converges to the optimum almost instantaneously for all cases.

Simulations with increased turbulence intensity (15% TI) are also used to evaluate the performance of LP-PIESC. The simulation results are shown in Figure 9. It can be observed that increasing the turbulent intensity does not affect the transient or steady-state performance of the LP-PIESC.

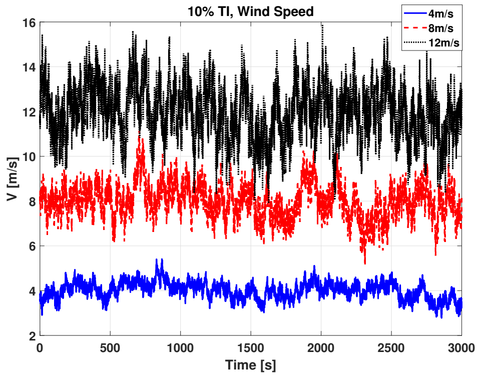

Figure 6: Wind speed time series at hub height: mean wind speeds 4 m/s, 8 m/s, 12 m/s and 10% turbulence intensity

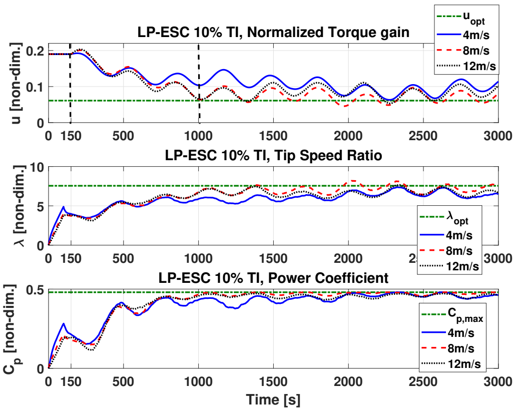

Figure 7: Performance of LP-ESC with the parameters shown in Table 2 and hub-height wind from Figure 6. Normalized torque gain u (top), tip speed ratio λ (middle), estimated power coefficient C_p (bottom). The dashed straight lines indicate optimal parameters u_{opt}, λ_{opt} and $C_{P,\max}$.

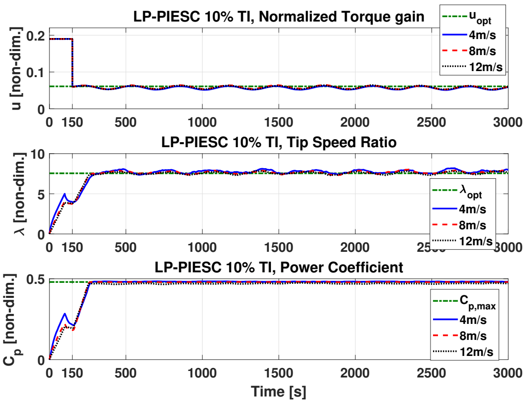

Figure 8: Performance of LP-PIESC with the parameters shown in Table 3 and hub-height wind from Figure 6. Normalized torque gain u (top), tip speed ratio λ (middle), estimated power coefficient C_p (bottom). The dashed straight lines indicate optimal parameters u_{opt}, λ_{opt} and $C_{P,\max}$.

We have also calculated the energy output using LP-ESC and LP-PIESC in the time interval [150s, 3000s] (47-minute duration), which is the time window with the control algorithms turned on. The results are shown in Figure 10. Using LP-PIESC in place of LP-ESC results in a 16% average energy improvement.

The results in this section provide evidence that LP-PIESC is faster to converge to the optimum value than LP-ESC and also robust to the variations in mean wind speed and turbulence intensities. The LP-PIESC requires a dither amplitude significantly lower than that for LP-ESC. These improvements translated to increased energy production.

6 Conclusion

This paper presented a log-power feedback PIESC (LP-PIESC) strategy for wind turbine power maximization in region-2. The proposed algorithm is compared with a conventional ESC with log-power feedback (LP-ESC) scheme. The 5MW NREL reference turbine model in OpenFAST is used to evaluate the performance of both the strategies. Simulations were performed under different below-rated wind conditions. The major improvements of the LP-PIESC, over the conventional LP-ESC, are: (i) faster convergence to optimal parameters, and (ii) smaller dither amplitude to estimate the gradient of power

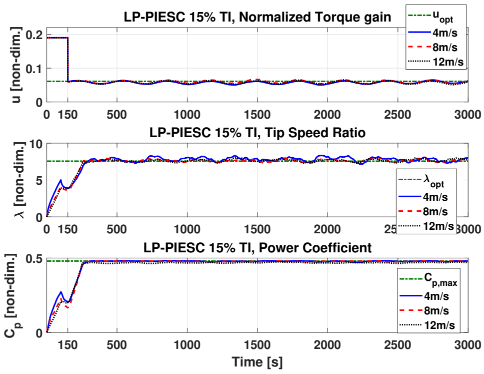

Figure 9: Performance of LP-PIESC with the parameters shown in Table 3 and wind input with 15% TI. Normalized torque gain u (top), tip speed ratio λ (middle), estimated power coefficient C_p (bottom). The dashed straight lines indicate optimal parameters u_{opt}, λ_{opt} and $C_{P,\max}$.

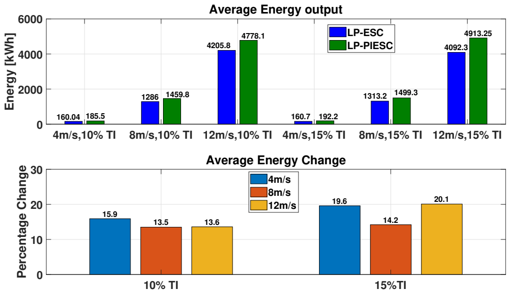

Figure 10: Energy output comparison: LP-ESC vs LP-PIESC. Average energy output with LP-ESC and LP-PIESC (top), percentage change in energy capture (bottom).

with respect to the control parameters. These initial results provide evidence supporting the hypothesis that the amalgamation of log-power feedback and PIESC technique would result in faster and consistent convergence across different below-rated wind speed conditions. However, design of the LP-PIESC algorithm requires tuning more parameters than the LP-ESC. Therefore, additional work is needed to establish practical guidelines for parameter design customized to control of wind turbines and wind farms.

References

[1] Pao L Y and Johnson K E 2011 *IEEE Control Systems* **31** 44–62

[2] Creaby J, Li Y and Seem J E 2009 *Wind Engineering* **33** 361–387

[3] Xiao Y, Li Y and Rotea M A 2018 *IEEE Transactions on Control Systems Technology* 1–9 ISSN 1063-6536

[4] Rotea M A 2017 *IFAC-PapersOnLine* **50** 4504 – 4509 ISSN 2405-8963 20th IFAC World Congress

[5] Ciri U, Leonardi S and Rotea M A 2019 *Wind Energy* **22** 992–1002

[6] Guay M and Dochain D 2017 *Automatica* **77** 61 – 67 ISSN 0005-1098

[7] Kumar D and Rotea M A January 2021 *AIAA Scitech 2021 Forum* pp 1–10

[8] Rotea M A US Patent App 16/617,911, 2020 Method and system for using logarithm of power feedback for extremum seeking control

[9] Krstic M, Kokotovic P V and Kanellakopoulos I 1995 *Nonlinear and Adaptive Control Design* 1st ed (John Wiley & Sons, INC.) ISBN 0471127329

[10] Adetola V and Guay M 2011 *International Journal of Adaptive Control and Signal Processing* **25** 155–167

[11] Jonkman J, Butterfield S, Musial W and Scott G 2009 Definition of a 5-mw reference wind turbine for offshore system development Tech. rep. NREL

[12] Rotea M A 2000 *Proceedings of the 2000 American Control Conference. ACC* 6 pp 433–437, vol. 1

FARM / WIND TURBINE MODELLING

Lattice Boltzmann Large-eddy Simulation of Neutral Atmospheric Boundary Layers

H. Asmuth[a], Ch. F. Janßen[b], H. Olivares-Espinosa[a], and S. Ivanell[a]

[a]Department of Earth Sciences, Wind Energy Group, Uppsala University, Cramérgatan 3, 62157 Visby, Sweden
[b]Institute for Fluid Dynamics and Ship Theory, Hamburg University of Technology, Am Schwarzenberg-Campus 4, 21073 Hamburg, Germany

E-mail: `henrik.asmuth@geo.uu.se`

Keywords: Geotechnics and Structural Integrity, New Concepts

Extended Abstract

Large-eddy simulations (LES) of wind farms can provide valuable insights into the aerodynamics of wind farms. Yet, the high computational demand of the method typically limits its use to selected academic case studies. The lattice-Boltzmann method has emerged to a promising alternative to classical computational fluid dynamics approaches.[1] In particular GPU (graphics processing units) implementations of the method have been shown to push the scope of LES due to significantly higher performance to cost ratios.[2] Recent studies have shown, that state-of-the-art lattice Boltzmann schemes can be readily applied to wind turbine simulations, e.g. using the actuator line model.[3] Yet, in contrast to simulations of wind turbines alone, experiences in simulating wall-modelled atmospheric boundary layers remains limited. This can largely be attributed to the fact that LBM-specific wall modelling approaches are still at an early stage of development. In this talk, we present recent progresses in the development of LBM-based wall models for the simulation of atmospheric boundary layers. We firstly outline the fundamentals of the so called inverse momentum exchange method (iMEM), a novel wall modelling approach that can be easily coupled to existing LBM boundary conditions.[4] Furthermore, we present results of neutral atmospheric boundary layer simulations and illustrate the benefits and challenges of the proposed method. This includes a comparison to results from a well-established staggered pseudo-spectral finite difference (PSFD) solver [5, 6], theoretical scaling laws as well as experimental results.

Exemplary results of the mean stream-wise velocity, velocity gradient and shear stress are shown in Fig. 1. The presented approach is found to capture the log-law in large parts of the surface layer. The largest deficiency remains an underprediction of the velocity at the first grid point that is associated with an over-shoot in the velocity gradient. Reasons and remedies for this overshoot problem have been widely discussed in the literature and will be further elaborated on in the talk. When it comes to second- and higher-order statistics (not shown here for the sake of brevity) the LBM framework also shows a satisfactory performance in comparison to the consulted references due to its low numerical dissipation.

In summary, the proposed wall-model and utilized numerical framework are shown to be a suitable method for boundary layer simulations. In conjunction with earlier studies [7, 3] this again highlights the potential of LBM-based models for efficient LES of wind farm flows.

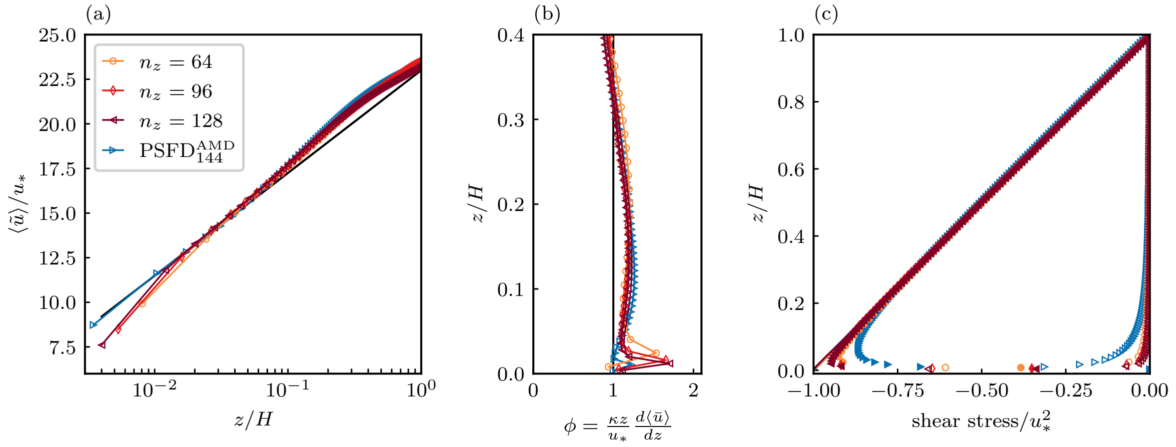

Figure 1: Vertical profiles of mean quantities with different grid resolutions in comparison to PSFD results by Gadde *et al.* [6]. (a) Mean stream-wise velocity. (b) Non-dimensional vertical velocity gradient. (c) Resolved shear stress $\langle u'w' \rangle$ (filled markers), modelled shear stress $\langle \tau_{xz} \rangle$ (empty markers) and total shear stress $\langle \tau_T \rangle$ (full lines).

References

[1] Krüger T, Kusumaatmaja H, Kuzmin A, Shardt O, Silva G and Viggen E M 2016 *The Lattice Boltzmann Method - Principles and Practice* (Heidelberg, Germany: Springer)

[2] Löhner R 2019 *Int. J. Comput. Fluid. D.* **33** 87–97

[3] Asmuth H, Olivares-Espinosa H and Ivanell S 2020 *Wind Energy Science* **5** 623–645

[4] Asmuth H, Janßen C F, Hugo O E and Ivanell S 2021 *Phyrics of Fluids* **In Review**

[5] Stevens R J A M, Wilczek M and Meneveau C 2014 *Journal of Fluid Mechanics* **757** 888–907

[6] Gadde S N, Stieren A and Stevens R J A M 2020 *Boundary-Layer Meteorol*

[7] Asmuth H, Olivares-Espinosa H, Nilsson K and Ivanell S 2019 *J. Phys.: Conf. Ser.* **1256** 012022

17^{th} EAWE PhD Seminar on Wind Energy
3-5 November 2021
Porto, Portugal

Validation of the generalized actuator disk wind turbine parameterization based on wake measurements of the full-scale Vestas V27 wind turbine at the SWiFT test site

B Kale[a,b], S Buckingham[a], J van Beeck[a], and A Cuerva Tejero[b]

[a]Environmental and Applied Fluid Dynamics Department, von Karman Institute for Fluid Dynamics, Rhode-Saint-Genèse, Belgium
[b]DAVE/UPM, E.T.S.I. Aeronáutica y del Espacio, Universidad Politécnica de Madrid, E-28040 Madrid, Spain

`E-mail: baris.kale@vki.ac.be`

Keywords: wind turbine wakes; numerical weather prediction model; large-eddy simulation; generalized actuator disk model; weather research and forecasting model; atmospheric boundary layer; scaled wind farm technology

1 Introduction

Numerical simulations of wind turbines to represent rotor aerodynamics with an appropriate wind turbine parameterization such as generalized actuator disk (GAD) or actuator line (GAL) models are often preferred over fully-resolved computational modeling due to being computationally less expensive. In addition, such a wind turbine model, for example, the actuator disk model, is capable enough to capture turbine-induced wakes when combined with large-eddy simulations (LESs). It parameterizes the wind turbine rotor as a permeable disk, taking into account flow rotation. Furthermore, the calculated aerodynamic forces at different radial sections along the blade are averaged over the rotor swept area. Because real-scale wind turbines operate within the lowest portion of the atmospheric boundary layer (ABL), non-uniformity and non-stationarity of the oncoming wind flow which are driven by dynamics of the atmosphere should be taken into account for accurate reproduction of temporal and spatial turbulence scales at the vicinity of the turbine. Since canonical Computational Fluid Dynamics (CFD) codes lack providing comprehensive information on unremittingly occurring chaotic turbulent structures during the diurnal cycle of the ABL, Numerical Weather Prediction (NWP) models (e.g., the Weather Research and Forecasting model (WRF) [1]), which solve prognostic flow equations considering interactions of many atmosphere physics, are therefore widely used in the wind community. It should be emphasized that validation of the results obtained from the WRF with the GAD model requires comparisons against field measurements. In order to estimate wind turbine aerodynamic loading and performance, a generalized actuator disk model is implemented into the WRF framework and the wake and power results are compared to the measurements collected from one of the full-scale Vestas V27 wind turbine at the Sandia Laboratories Scaled Wind Farm Technology (SWiFT) facility which was specifically designed for research in wind energy. One of the main importance of this work is that the WRF-LES with the GAD model has a high potential for multiscale modeling of wind turbine wake structures under real atmospheric forcing or laboratory conditions by taking into account advanced wind turbine features such as rotor yaw dynamics, turbine tilt, blade precone, rotor apex overhang, hub and tower effects, speed and pitch controller among others [2].

In this research, we evaluate the performance of a generalized actuator disk (GAD) wind turbine parameterization under neutral conditions characterized by the stability parameter, z/L (sensor measurement height divided by Obukhov length), which were observed at the SWiFT facility during the measurement campaign. Numerical results are validated against the wake measurements obtained with a rear-facing, nacelle-mounted spinner lidar. Additionally, generator power is compared with the available measurements [3].

To simulate neutrally-stratified atmospheric boundary layer (ABL), the surface kinematic heat flux is set to zero. Two telescopic WRF-LES domains are used in this study and the coarser domain is run for fifteen hours to obtain fully mixed turbulence field. The second domain is introduced at the beginning of hour 15 and the GAD model is run for additional one hour and ten minutes to model wind turbine effects during the measurement campaign at the SWiFT facility. Data used for the analysis are collected after ten minutes to allow for spin-up of the flows within the nested domain. 1.5-order TKE subfilter scale turbulence model is used to model small-scale structures.

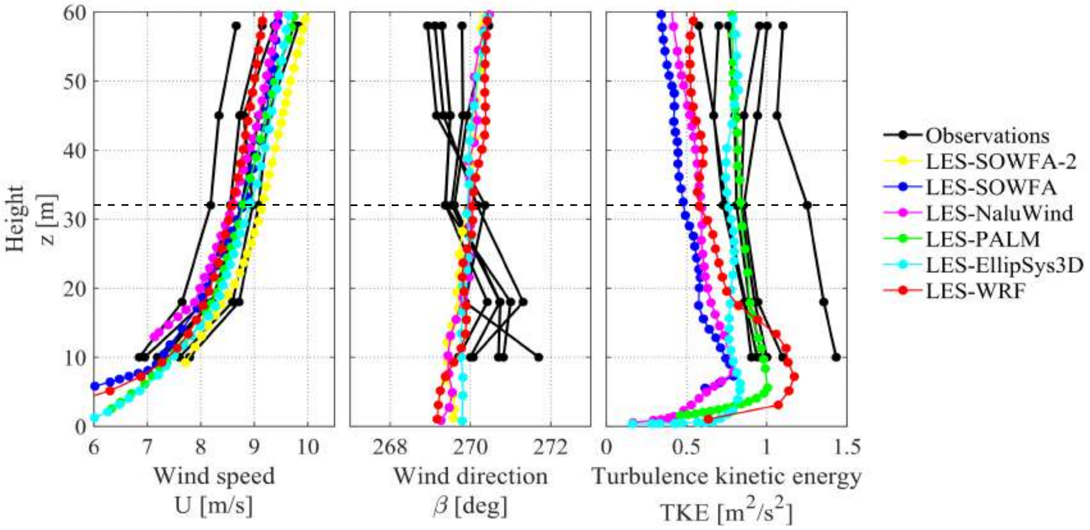

Figure 1: Time-averaged variables at the met mast location: Horizontal wind speed (left), wind direction (middle), and turbulent kinetic energy (right). Dashed horizontal line depicts wind turbine hub-height.

In Fig. (1), laterally and temporally averaged vertical profiles of horizontal wind speed, wind direction and turbulent kinetic energy at 2.5 D upwind of the turbine are given. Each black curve shows 10 m-average profiles for observations while colorful curves depict the results obtained from different numerical simulations. Our WRF-LES results for inflow calibration, shown in red, are in good agreement with *in situ* measurements and other simulations.

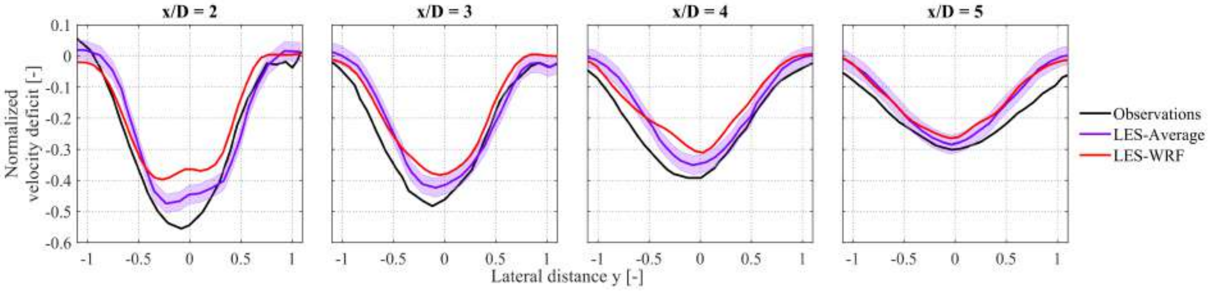

Figure 2: Time-averaged normalized velocity deficit profiles at different downstream locations in y-z plane.

In Fig. (2), normalized velocity deficit profiles at several downwind locations, $x/D = 2, 3, 4, 5$, are shown. It is clearly seen that all numerical models underestimate measurement data obtained from the nacelle-mounted spinner lidar. LES model results are collapsed into a single curve in magenta with corresponding shaded region in Fig. (2).

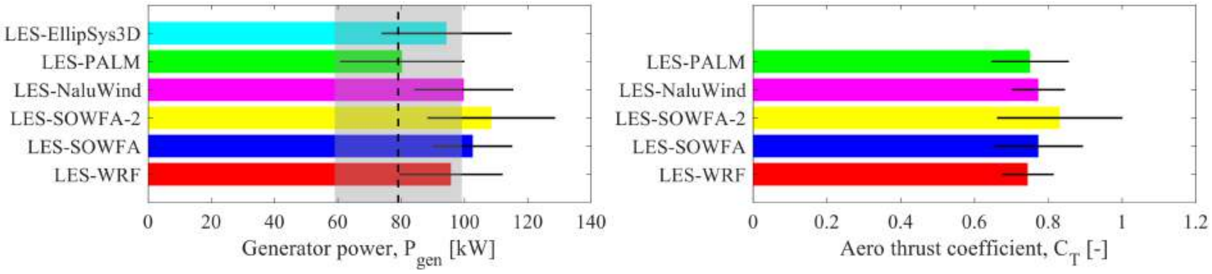

Figure 3: Ensemble averages of generator power and aerodynamic thrust coefficient. Black solid lines depict standard deviations around the mean. Measured values are shown with vertical dashed lines (mean) and gray shading (standard deviation).

Generator power and aerodynamic thrust coefficient computed by the GAD model are also compared with the available numerical and experimental data (Fig. (3)). Although the power output of the WRF-LES-GAD model resides in the gray-shaded region that marks the standard deviation of the power measurements, the WRF-LES-GAD model overpredicts the generator power output about 16 kW. Moreover, as given in the reference paper by Doubrawa *et al.* [3], mean generator power obtained from openFAST [4] simulations (not shown here) is around 80 kW while it is computed as 95.33 kW in WRF-LES simulations under neutral conditions. On the other hand, the GAD model shows reasonably good agreement in terms of the aerodynamic thrust coefficient when compared with other LES actuator line model results from different researchers. Due to the lack of field measurements of the thrust coefficient, only the numerical results were compared with each other.

To conclude, the generalized actuator disk model implemented into WRF-LES framework shows promising, reliable and physically consistent results compared with the measurement data that are obtained from the full-scale Vestas V27 turbine at the SWiFT test site under neutral conditions. Detailed investigations are required to evaluate the accuracy and reliability of simulated wake characteristics under different atmospheric stability conditions.

Acknowledgments

This research has been performed using computational resources of the von Karman Institute for Fluid Dynamics and has received funding from the European Union's Horizon 2020 research and innovation programme under the Marie Skłodowska-Curie grant agreement No 860101.

References

[1] Skamarock W C and Klemp J B 2008 *Journal of computational physics* **227(7)** 3465 – 3485

[2] Jonkman J, Butterfield S, Musial W and Scott G 2009 Definition of a 5-mw reference wind turbine for offshore system development Tech. rep. National Renewable Energy Lab.(NREL), Golden, CO (United States)

[3] Doubrawa P, Debnath M, Moriarty P J, Branlard E, Herges T, Maniaci D and Naughton B 2019 *Journal of Physics: Conference Series* vol 1256 (IOP Publishing) pp 012 – 024

[4] NREL 2019 Openfast repository `https://github.com/OpenFAST/openfast`

Modelling of loudspeaker sound propagation in complex atmospheric flows

Camilla Marie Nyborg[a], Ju Feng[a], Wen Zhong Shen[a], Tomas Rosenberg Hansen[c], and Andreas Fischer[a]

[a]Technical University of Denmark - Wind Energy, Frederiksborgvej 399, 4000 Roskilde, Denmark
[c]Siemens Gamesa Renewable Energy, Borupvej 16, 7330 Brande, Denmark

E-mail: cmny@dtu.dk

Keywords: Computational Aeroacoustics, Wind Turbine Noise, Model Validation.

1 Extended abstract

This study presents measurement results of the noise emitted from a loudspeaker attached to the hub of a wind turbine used for validation of different sound propagation models. This innovative measurement campaign uses seven microphones positioned in a line along the mean wind direction of $\theta = 225°$, spanning from microphone 1 at the IEC measurement position [1] ($d = 158$ m) to microphone 8 and 8b in the far field of the turbine. Figure 1 presents an illustration of the experimental setup. The setup also includes a meteorological mast, 2 profiling lidars and 2 sonic anemometers for inflow and wake measurements.

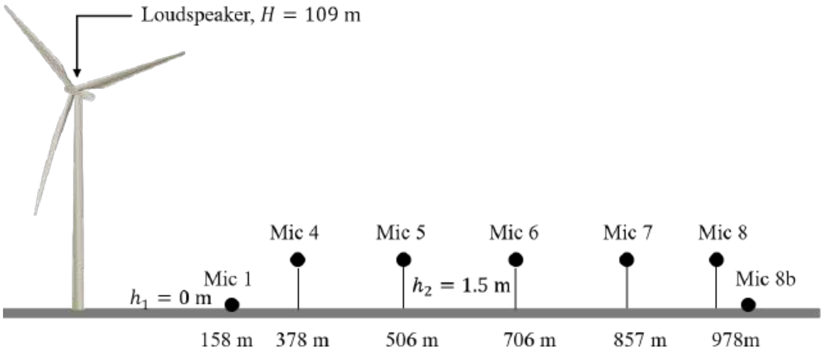

Figure 1: Sketch of the experimental setup with the loudspeaker attached to the hub of the wind turbine at height $H = 109$ m and the seven microphones positioned on the ground in a line spanning from the near field to the far field of the wind turbine. The sizes and the complexity of the terrain in the sketch are not to scale with reality.

The analysis of sound propagation from a sound source to the far field of the source presents a challenge for noise measurements in some conditions as the sound pressure level (SPL) reduces when propagating away from the source. This study uses a deconvolution method to obtain the loudspeaker noise signal when the signal to noise ratio is low in order to obtain a reliable background noise correction. The use of the deconvolution method also introduces the possibility of obtaining the variance of the loudspeaker noise signal.

The measurement results are applied in a model validation of a Parabolic Equation sound propagation model [2] and the ISO 9613-2 standard model [3],[4]. Besides the sound power level, the atmospheric attenuation and the geometrical spreading of the sound, the sound propagation depends on the propagation loss, ΔL. The propagation loss caused by e.g. atmospheric and ground effects is modelled by the DTU in-house sound propagation model WindSTAR-Pro and the standard propagation model ISO 9613-2. The sound power level is normally estimated as a point source from the measurements at the IEC position. However, in order to only compare the two propagation models, the difference of SPL between the different microphones can be evaluated without taking the source into account.

The evaluation of the models is performed in a statistical way, using the 2 minutes averaged measured meteorological conditions as inputs. Figure 2 presents the comparison of the experimentally obtained, and the WindSTAR-Pro and ISO 9613-2 modelled propagation spectra for 2 hours of loudspeaker noise. The results are presented in 1/3 octave bands. Figure 2 shows that the WindSTAR-Pro model captures the measured propagation and its variance caused by the varying meteorological conditions well, while the ISO 9316-2 model does not show significant variations in neither meteorological inputs nor frequency.

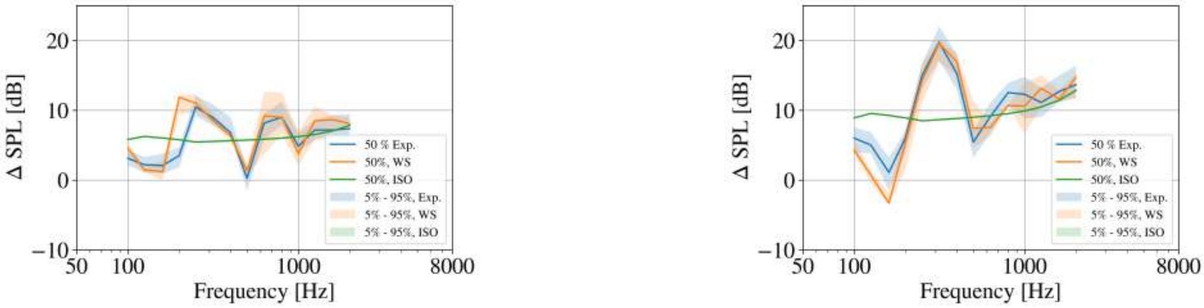

(a) Propagation between Microphone 4 and 6

(b) Propagation between Microphone 4 and 8

Figure 2: Comparison of the median and variance of the measured (Exp. in legend) and the WindSTAR-Pro (WS) and ISO 9613-2 (ISO) modelled sound propagation, Δ SPL, between microphones; (a) 4 and 6 (b) 4 and 8. The wind direction is $\theta = 235 - 250°$ and the wind speed is $U = 8 - 11$ m/s at hub height.

Acknowledgements

This work was funded by the Innovation Fund Denmark in the project entitled "DecoWind - Development of low-noise and cost-effective wind farm control technology" under project number (8055-00041B). Thanks Siemens Gamesa for the possibility of accessing their wind turbine. Thanks to Kurt Schaldemose Hansen and Franck Bertagnolio as well as the technicians Per Hansen, Andrea Vignaroli and Irene Ortega for helping with the field measurements. Moreover, thanks to Christian Weirum Claumarch and FORCE technology for assistance during the measurements and for contributing with the wind screens, and to Thomas Sørensen for the ISO 9613-2 computations.

References

[1] International Electrotechnical Commission (2012). *Wind turbine generator systems, Part 11: Acoustic noise measurement techniques* **IEC 61400-11:2012**

[2] Barlas E, Zhu W J, Shen W Z and Dag K O 2017 *The Journal of The Acoustical Society of America* **142 (5)** 3297–3310

[3] International Organization for Standarization (1993). *Acoustics- Attenuation of sound propagation outdoors - Part 1: Calculation of the absorption of sound by the atmosphere.* **ISO 9613-1:1993**

[4] International Organization for Standarization (1993). *Acoustics — Attenuation of sound during propagation outdoors — Part 2: General method of calculation.* **ISO 9613-2:1996**

AI-based offshore wind turbine design

E Panagiotou[a] and E Ntoutsi[a]

[a]Freie Universität Berlin, Berlin, Germany

E-mail: emmanouil.panagiotou@fu-berlin.de

Keywords: Artificial Intelligence, Machine Learning, Genetic Algorithms, Generative Design, Offshore Wind Turbines, Industrial Design.

Abstract

Although the performance of offshore wind turbines has been improved with time, the design space has not been adequately explored. Typical designs are based on monopile, three-bladed horizontal-axis structures and are evaluated only on the basis of their power generation efficiency. A holistic design approach that integrates information from the whole life cycle of a wind turbine, namely, from raw material extraction and manufacturing to installation, operation, maintenance, and recycling, would allow for designs that go beyond power performance and ensure other aspects like environmental sustainability and reduced greenhouse gas emissions.

Traditionally wind turbines are designed by human experts with the help of simulation tools. Recent advancements in Artificial Intelligence (AI) have the potential to revolutionize design generation. AI algorithms can formulate the design process as a multi-objective optimization problem, extrapolating rules in a data-driven manner and providing insight to previously unexplored aspects. Successful applications of AI range from the pharmaceutical industry to construction, architecture, and the automotive industry.

In this paper, we consider generative design algorithms that leverage AI methods to yield novel, cost-effective and efficient designs. We propose an approach for design generation based on Evolutionary Algorithms (EA). Given a design space, candidate designs are evolved and evaluated in a simulated environment. Our preliminary results show that this data-driven method creates unique and competent designs by exploring the design space.

1 Introduction

Traditional industrial design processes are commonly mandated by inevitable challenges, which ultimately lead to engineering trade-offs. Especially the domain of wind turbine design is dominated by the energy production factor, while other aspects like economic and environmental sustainability can be left in the background. This issue can be tackled with specific AI techniques that formulate the design processes as constrained optimization problems. Although these tasks are challenging, they can be addressed with Generative Machine Learning methods which compute, data, and performance-driven solutions.

Generative design algorithms are iterative processes that traverse a multidimensional parametric space, called the Design Space, in search of optimal solutions based on the input constraints and evaluation criteria [1]. A prevalent approach for solving such optimization problems lies in the use of Genetic Algorithms (GAs). Based on Darwin's Theory of evolution and natural selection, Genetic Algorithms are ideal for exploring the design space and approximating optimal solutions. Applications in the optimization of structural designs have been highly effective [2, 3, 4, 5].

Such approaches have also been employed in the field of wind energy. More specifically, horizontal axis wind turbines (HAWT) are parameterized and optimized using GAs, resulting in novel and beneficial designs [6, 7, 8, 9, 10]. The parameterizations considered in most studies are primarily centered around the blade structure, with the energy output of the rotor serving as the objective function to be maximized.

The aim of our research is to expand the design space with regard to the entire life cycle process of an offshore HAWT. By establishing a multi-objective cost function, based on real and synthetic data [11, 12], the design quality can be influenced significantly in order to facilitate the development of improved designs of future offshore wind turbines.

We propose a GA approach for producing optimal wind turbine designs while taking into account varying design parameters, including real-world data.

2 Necessary Background

Genetic Algorithms (GAs)

Genetic algorithms [13] are inspired by the process of natural selection in biology. A population of candidate solutions is evolved by an iterative process (the population in each iteration is called a generation), to produce better solutions for a target optimization problem.

The main components of a GA are the following:

- **Solution representation:** Each solution to the problem is specified by a set of genes called the genotype. The physical representation of the candidate is termed the phenotype.
- **Fitness function:** it evaluates the candidate solutions by computing a score that, when normalized, is considered as the probability of reproduction for the next generation.
- **Initial Population:** often, the initial population is randomly sampled in the Design Space.
- **Selection, Crossover & Mutation:** are important operations for the evolution of the solutions. During the selection phase, the most pertinent candidates are selected for reproduction. Each parent passes information stored in the genotype vector, to the next generation, via the Crossover method. A random crossover point from the vector is chosen, and information until that point is exchanged among the parents to create new offspring, which is added to the population. Random mutations can occur with a low probability, inducing variety to existing genetic information.

GA based solutions have been applied to wind energy problems, including wind farm layout optimization [14, 15], wind turbine controllers [16, 17], as well as airfoil and blade layout design [6, 7, 18, 8, 9, 10].

Generative Adversarial Networks

Generative Adversarial Networks (GAN) [19] are generative models, meaning that they aim to create synthetic data. These networks are consisted of two models. The Generator (G), tries to generate ”fake” data to fool the Discriminator (D), which classifies input data as real (belonging to a given dataset) or fake (created by the Generator).

The training process, that is reflected in the network’s loss function Eq. (1), is a min-max two player game.

$$\begin{aligned} \min_G \max_D V(D,G) =_{x\sim p_{data}(x)} [\log D(x)] \quad + \\ {}_{z\sim p_z(x)}[\log(1-D(G(z)))] \end{aligned} \tag{1}$$

where z is a noise vector and x is real data, from the data distribution p_{data}.

By training the two models against each other, the Generator learns to imitate the real data distribution, generating novel and diverse but plausible (with respect to the real data) instances.

The essential difference between the aforementioned techniques is that Genetic Algorithms rely on stochastic sampling to optimize input parameters according to the fitness function. Contrary, GANs compute the fitness of each individual using the Discriminator’s score, which also computes the derivatives of the fitness function with respect to each input parameter. Therefore, weights are updated according to those derivatives. Nonetheless, the concept of a Discriminator can be infused in the fitness function of a GA. This can help the algorithm to converge faster and aid it towards more plausible and meaningful results [20].

3 GA-based design generation framework

An efficient design can be capable of performing at an adequate level, although opportunities for enhancement are always a possibility. Therefore, an appropriate design methodology can be beneficial as it could deliver improved solutions, particularly if ML techniques are exploited. The discrete steps of the GA methodology for design generation are as follows.

Design Space

The first step is to determine the input parameters. Consequently, a Design Space has to be defined, consisting of values for respective variables as well as their type (continuous floats, integers, discrete values, etc.) and boundary conditions that may apply to them. Some constraints could reside in dependencies that exist between different parts of the design space. For example, the calculation of wind loads on the tower of a wind turbine could depend on the design of the substructure. Finally, a vector V is provided as input to the algorithm, comprised of continuous, as well as discrete, variables, noted as Y and X respectively. Unary conditions (expressed as bounded functions $g(Y)$) can apply to the continuous variables. Moreover, dependency constraints that induce correlations between variables can be formulated as multivariable functions.

Design Generation (G)

Using a well-defined design space, the GA can be initialized with random instantiations by assigning values that satisfy the constraints to all variables. Typically, this step is sufficient for the generation process, but in the case of a simulated environment being deployed for testing candidate designs, an important, and sometimes complex, task lies in translating the input parameter vector (genotype) into a format suitable for simulation that physically represents its features (phenotype). In the simplest case, for example, if the vector is comprised of values that define the number of blades of a WT, the input files of the simulation software are altered accordingly, resulting in functional simulation models. But for more intricate configurations, complications can occur e.g. customization and simulation of a complex substructure.

Design Evaluation (E)

For the algorithm to be able to reach optimal designs, a fitness function has to be specified. This function maps every candidate design to a score that can be used for evaluation. Wind turbine (WT) design is a multi-objective optimization problem, and therefore the fitness function's score should be derived from various sources. Mechanically driven evaluation can ensure that a WT model is performing as expected by testing it against simulated real-world conditions. Furthermore, the fitness of a design should ideally include aspects of the design process that are challenging to ascertain, e.g., manufacturing and maintenance costs, ease of production, and expert knowledge. If a dataset of existing designs with analogous and sufficient data is present, it can be used to train a predictive model. This can then serve as a fitness function, as it takes the features of a proposed design as input and predicts a corresponding score.

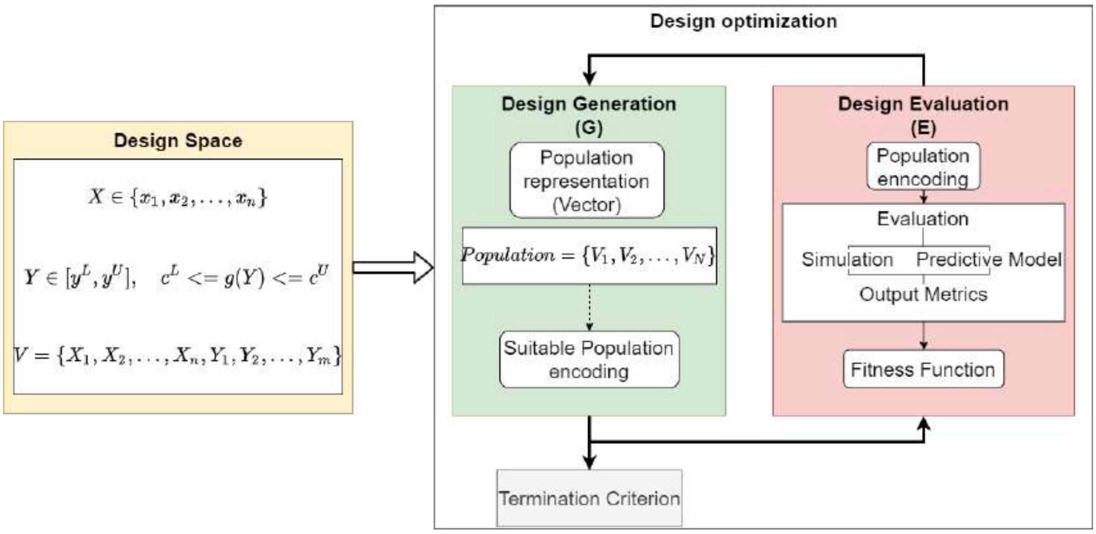

Figure 1: General overview of the approach

As described in Section 2 the actual optimization is attained during the iterative process of the algorithm. Population vectors, that are initially comprised of random values, are refined for each new generation until a maximum number of generations or a desired termination criterion is reached.

4 Preliminary Results

For the purpose of testing the general framework's efficacy a *proof of concept* experiment is deployed. The target of the optimization problem, is to improve the performance of a 10MW reference wind turbine [21], by modifying only the blade structure, and more specifically the Chord length [m] as well as the Thickness/Chord ratio [%] at 40 positions (points) across the blade span. Those parameters are presented in Figure 2. Consequently, the design space is consisted of 80 independent continuous variables with solely unary constraints applying to them in terms of min-max values. For this preliminary test case, a population of 20 candidates is randomly initialized and evolved, using a Genetic Algorithm, for 50 generations.

The assumption is that by adjusting the chord length and thickness of the blades at certain points, the rotor speed of the wind turbine is affected. The resulting structures are tested in a simulated environment using the aeroelastic code HAWC2 (Horizontal Axis Wind turbine simulation Code) [22]. HAWC2 tests structures in real time and against simulated wind conditions, providing time series output metrics. Depending on the nature of the problem that has to be solved, these can be used and combined to form a fitness score. In our test case, the rotor speed is chosen as a target for maximization as it can translate to increased energy production.

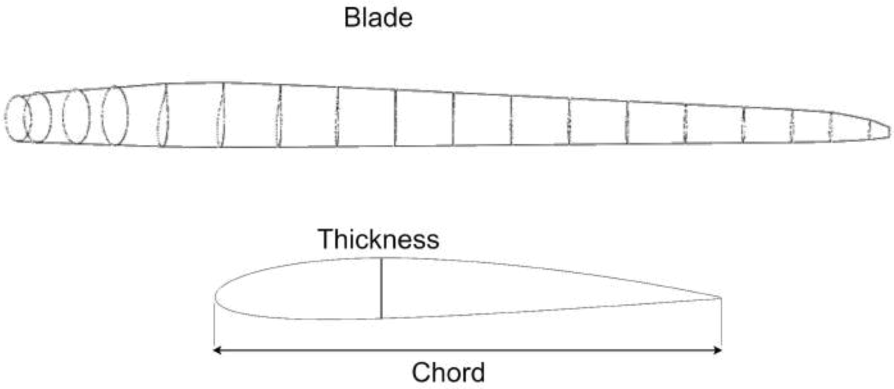

Figure 2: Blades are split into sections. At each section, chord length and thickness are defined.

Nevertheless, the fitness function has to map every design to a number (score) that regulates its probability of reproduction. Therefore, the mean rotor speed value, after convergence, is used for evaluation purposes. We presume that convergence is reached after half of the simulation has been executed, as seen in Figure 3.

In the ideal case, all designs produced by the GA should be scored by the simulation tool. Unfortunately, there is a possibility that a proposed design can lead the solver of the simulator into a state of non-convergence. In that case, we assign a negative score of -1 as a penalty to discourage the algorithm from picking erroneous designs.

The process of training the Genetic Algorithm is computationally expensive, especially in our case, where multiple simulations have to be executed in parallel, putting a heavy workload on the CPU. For this reason and due to resource constraints, the algorithm was tested on a restricted population size and for a limited number of generations [23]. Another hyperparameter that has to be set, and confined for computational reasons, is the simulation duration for which each design is tested. Regardless, the results (Figure 4) are informative and promising, as they seem to deviate from the norm.

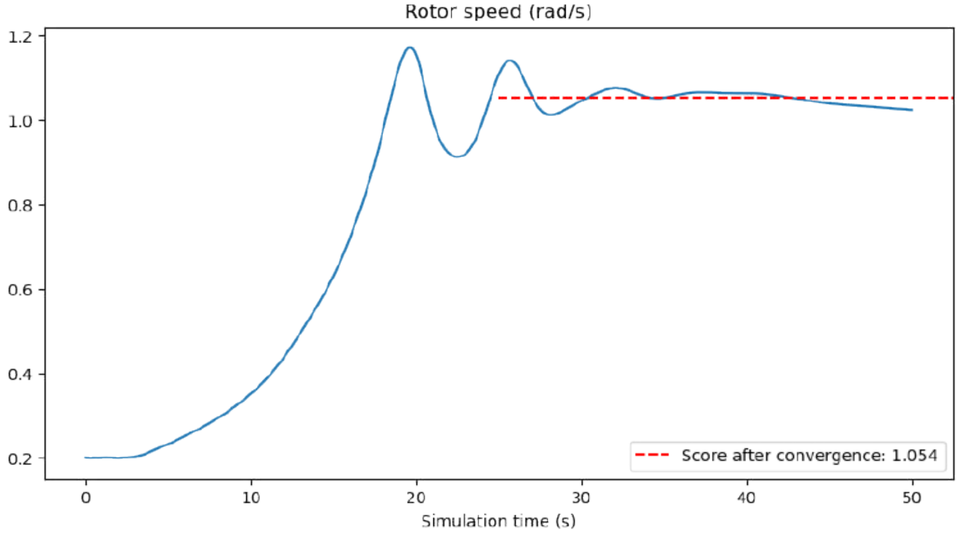

Figure 3: The fitness of the WT designs are determined by the convergence score, chosen as the mean rotor speed after half of the simulation time has passed.

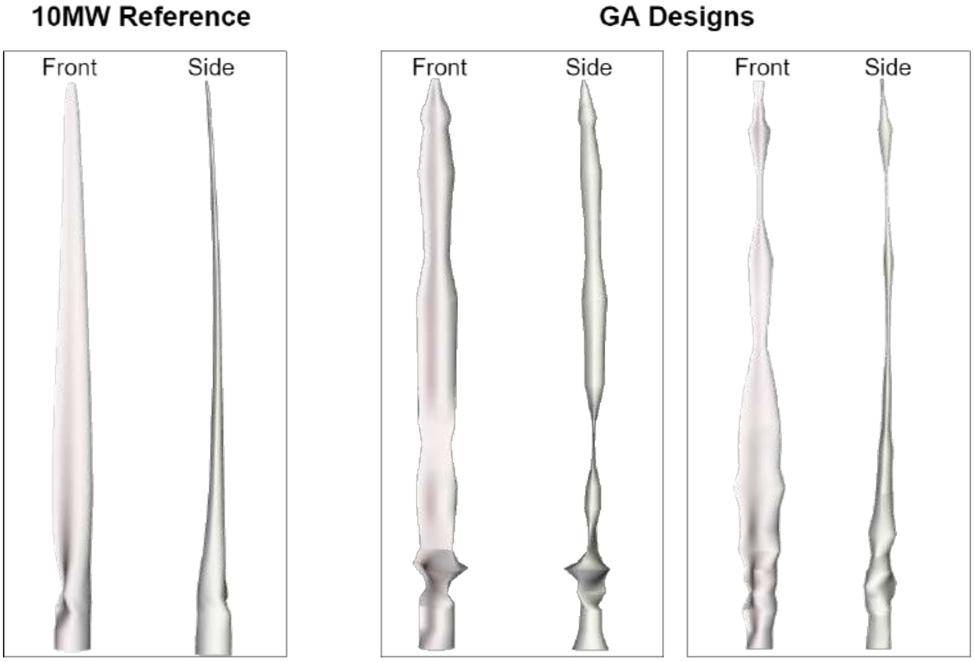

Figure 4: Front & side view of the 10MW reference WT blade, compared to designs generated by the GA.

Result Interpretation

A justification of a pattern that is detected in multiple resulting blade designs can be drawn from nature. More specifically, a series of smooth bumps are observed along the blades generated by the GA. This is also the case in Humpback whale's flippers, which have sinuous tubercles spanning across their edge [24].

Figure 5: Tubercles on Humpback whale's flippers compared to the generated design of a wind turbine blade.

This natural genetic modification has been evolved through time to aid the whales towards effortless hydrodynamic movement. The performance of tubercle wings has been tested in simulated and real (wind tunnel) environments, yielding efficient and stable results [25].

5 Discussion & Future Work

In this work, we consider the problem of optimizing wind turbine designs using Genetic Algorithms. Although our preliminary results are auspicious, a more comprehensive study in the future is imperative. Ultimately, the overall goal is to define and solve a multi-objective problem, incorporating information from the whole life-cycle design process. Nonetheless, even if synthetic data from realistic simulation environments are used, problems can occur.

Specifically, an issue when using the simulation framework for scoring generated designs arises when the initial population is compromised solely of designs that yield simulation errors. This can happen if many (unrestricted) parameters of a structure are modified simultaneously. As an example, abrupt changes of blade width at neighboring points across the blade span can lead to unfeasible models that result in erroneous simulation outputs. As mentioned in Section 4, a penalty score of -1 is assigned to these designs, but in the case of a completely flawed initial population, all designs will have the same (negative) score, and therefore the same probability of reproduction, leading the algorithm into a pitfall.

A method for addressing this problem is to implement biased initialization. If expert knowledge can be obtained, it can be used to form a "biased" dataset from which the algorithm can sample the initial population. This can be beneficial when known solutions need to be improved or (in our case) if a "head start" is required for the algorithm to be effective and reach convergence. A similar result can be achieved by using the concept of GANs (Section 2). More precisely, the output of a discriminative model that yields a similarity score in relation to real designs can be used in the fitness function to aid the GA towards more plausible and less erroneous results. Due to lack of real data, this method was not implemented.

An additional parameter that has to be set is the duration of simulations. Stopping simulations too early could lead to an inaccurate evaluation, but higher simulation times for each individual add up to a significant impact on computational cost. Alternatively, a measure of stability, or direction, of the time series output could be computed and used to augment the fitness function, with the assumption that more stable simulation outputs will not lead to erratic future behavior.

6 Acknowledgments

This project is Funded by the Deutsche Forschungsgemeinschaft (DFG, German Research Foundation) - SFB1463 - 434502799.

References

[1] Shea K, Aish R and Gourtovaia M 2005 *Automation in Construction* **14** 253–264

[2] Prendes Gero M B, García A B and del Coz Díaz J J 2006 *Journal of Constructional Steel Research* **62** 1303–1309 ISSN 0143-974X structural Steel Research in the Baltic Countries and Finland URL `https://www.sciencedirect.com/science/article/pii/S0143974X0600037X`

[3] Rajeev S and Krishnamoorthy C 1992 *Journal of structural engineering* **118** 1233–1250

[4] Srinivas V and Ramanjaneyulu K 2007 *Advances in Engineering Software* **38** 475–487

[5] Lemonge A C and Barbosa H J 2004 *International Journal for Numerical methods in engineering* **59** 703–736

[6] Pourrajabian A, Dehghan M and Rahgozar S 2021 *Sustainable Energy Technologies and Assessments* **44** 101022

[7] Bizzarrini N, Grasso F and Coiro D P 2011 *EWEA, EWEC2011, Bruxelles, Belgium* 14–17

[8] Xiong L, Yan C and Zhiquan Y 2006 *Acta energiae solaris sinica* **27** 180

[9] Selig M S and Coverstone-Carroll V L 1996

[10] Vesel Jr R 2009 *Optimization of a wind turbine rotor with variable airfoil shape via a genetic algorithm* Ph.D. thesis The Ohio State University

[11] Cooney C, Byrne R, Lyons W and O'Rourke F 2017 *Energy for Sustainable Development* **36** 44–54

[12] Boschert S and Rosen R 2016 *Mechatronic futures* (Springer) pp 59–74

[13] Holland J H 1992 *Scientific american* **267** 66–73

[14] Grady S, Hussaini M and Abdullah M M 2005 *Renewable energy* **30** 259–270

[15] Emami A and Noghreh P 2010 *Renewable Energy* **35** 1559–1564

[16] Hasanien H M and Muyeen S M 2012 *IEEE Transactions on Sustainable Energy* **3** 200–208

[17] Barrera-Cardenas R and Molinas M 2012 *Energy Procedia* **20** 207–216

[18] Neto J X V, Junior E J G, Moreno S R, Ayala H V H, Mariani V C and dos Santos Coelho L 2018 *Energy* **162** 645–658

[19] Goodfellow I, Pouget-Abadie J, Mirza M, Xu B, Warde-Farley D, Ozair S, Courville A and Bengio Y 2014 *Advances in neural information processing systems* pp 2672–2680

[20] Nigam A, Friederich P, Krenn M and Aspuru-Guzik A 2019 *arXiv preprint arXiv:1909.11655*

[21] Bak C, Zahle F, Bitsche R, Kim T, Yde A, Henriksen L C, Hansen M H, Blasques J P A A, Gaunaa M and Natarajan A 2013 *Danish Wind Power Research 2013*

[22] Larsen T J and Hansen A M 2007 *target* **2**

[23] Rylander S G B and Gotshall B 2002 *Population* **100** 900

[24] Fish F E, Weber P W, Murray M M and Howle L E 2011 The tubercles on humpback whales' flippers: application of bio-inspired technology

[25] Miklosovic D, Murray M, Howle L and Fish F 2004 *Physics of fluids* **16** L39–L42

Challenges in aeroelastic modelling of multi-MW Floating Offshore Wind Turbines

F. Papi[a], A. Bianchini[a]

[a] Dept. of Industrial Engineering, University of Florence, via di Santa Marta 3, 50139, Firenze, IT

E-mail: fr.papi@unifi.it

Keywords: Floating, Aerodynamics, Aeroelastic, HAWT

Floating Offshore Wind Turbines (FOWT) are one of the most promising technologies to increase wind energy power production. If wind energy will be able to supply 30 to 50% of global energy needs, proper understanding and modelling of the complex dynamics involved in FOWTs is crucial[1]. Another apparent trend is the increase in size of wind turbines. Particularly in an offshore setting, increase in turbine power is fundamental to lower overall project cost. Indeed, recent research [2] has shown how increasing wind turbine size has the potential to slash investments costs in half in some cases. The wind energy research community is actively involved on these topics. For instance, participants of IEA Task 30 are investigating the capabilities and attempting to identify and address the pitfalls of current wind turbine design codes in the simulation of FOWTs, IEA Task 47 will investigate wind turbine aerodynamics, focusing on large rotor motion as experienced in floating conditions, and many EU-funded projects, such as CoreWind [3] and FLOATECH [4] are attempting to address some of the discussed issues. Finally, a 15MW reference rotor has recently been developed in the framework of IEA Task 37, and is a testament of the industry trends of increase in wind turbine size. In summary, while upscaling and floating wind are logical from a cost and operations point of view, what are the challenges involved in the design and operation of a multi-MW FOWT?

We attempt to investigate this by simulating two reference wind turbines of very different size, the NREL 5MW [5] and the IEA 15MW [6,7]. The two turbines are simulated in OpenFAST [8] using Blade Element Momentum (BEM)-based aerodynamics in combination with second order potential flow derived hydrodynamics. Both the turbines compared in the present study are mounted on semi-submersible type floaters, with slack catenary mooring lines. The two machines are subject to identical inflow and sea conditions, as if they were installed in the same sea leg. We compare performance and loads, and attempt to understand and contextualize the effects of a rather marked increase in turbine power and size. As most likely is to be expected by analyst in the field, platform motion is found to increase loads significantly. Although motion is decreased for the larger turbine, the increases in component mass affects both gravitational and inertial component loading.

The research group is also active in the investigation of the aerodynamic capabilities of current wind turbine design codes. Since proper full blade-resolved CFD is still computationally prohibited, wind turbine simulation codes typically rely on a blade-element model for the wind turbine blade, while the wake can be modelled with several degrees of fidelity, ranging from a simple momentum balance to full CFD. In this context, potential effects of improved aerodynamic analysis in the context of floating wind are discussed.

Bibliography

[1] Veers P, Dykes K, Lantz E, Barth S, Bottasso C L, Carlson O, Clifton A, Green J, Green P, Holttinen H, Laird D, Lehtomäki V, Lundquist J K, Manwell J, Marquis M, Meneveau C, Moriarty P,

Munduate X, Muskulus M, Naughton J, Pao L, Paquette J, Peinke J, Robertson A, Sanz Rodrigo J, Sempreviva A M, Smith J C, Tuohy A and Wiser R 2019 Grand challenges in the science of wind energy *Science* **366** eaau2027

[2] Kikuchi Y and Ishihara T 2019 Upscaling and levelized cost of energy for offshore wind turbines supported by semi-submersible floating platforms *J. Phys. Conf. Ser.* **1356** 012033

[3] Anon COREWIND Project *COREWIND*

[4] Anon Floatech | The future of Floating wind turbines *Floatech*

[5] Jonkman J, Butterfield S, Musial W and Scott G 2009 *Definition of a 5-MW Reference Wind Turbine for Offshore System Development*

[6] Evan Gaertner, Jennifer Rinker, and Latha Sethutaman 2020 *Definition of the IEA 15-Megawatt Offshore Refence Wind* (IEA Wind)

[7] Allen C, Viscelli A, Dagher H, Goupee A, Gaertner E, Abbas N, Hall M and Barter G 2020 *Definition of the UMaine VolturnUS-S Reference Platform Developed for the IEA Wind 15-Megawatt Offshore Reference Wind Turbine*

[8] National Renewable Energy Laboratory OpenFAST *GitHub*

17th EAWE PhD Seminar on Wind Energy
3 – 5 November 2021
Porto, Portugal

Development of a dynamic wake model accounting for wake advection delays and mesoscale wind transients

B Foloppe[a], S Buckingham[a], W Munters[a], L Vandevelde[b], J van Beeck[a]

[a] Environmental and Applied fluid dynamics Department, von Karman Institute, Belgium
[b] Electromechanical, Systems and Metal Engineering Department, Ghent University, Belgium

E-mail: benoit.foloppe@vki.ac.be

Abstract. Over the last decade, the size and the number of offshore wind turbines and wind farms are constantly increasing and ongoing projects show that this will continue. With tip height often above 200 meters, currently installed wind turbines are interacting and impacting massively the atmospheric boundary layer. Therefore, the research intends to develop a new dynamic wake model that considers weather transient inputs. The Flow Redirection and Induction in Steady State (FLORIS) framework has been proven to be an easy to use, easy to tune, computationally inexpensive and powerful wake modelling tool even though lacking dynamical effects. Therefore, an extension of the FLORIS framework is presented in order to include wake advection delays between wind turbines, time-varying and spatially heterogeneous wind conditions. The new dynamical model is inspired by the FLORIDyn model presented in 2014. The so-called Observation Points (OPs) are generated at the rotor centre location. Following a Lagrangian approach, the OPs are convected downstream, along the wake of the wind turbine, defining the wake centreline. It is during this process that the dynamics of wind turbine wake and background flow field unsteadiness are included. Finally, using the same approach currently implemented for yaw-misalignment wake deflection, the wake is shifted to match the unsteady wake centreline. The developed model is validated against Large Eddy Simulation using the SOWFA tool. The validation is done for unsteady inflow, with both wind speed and direction changes, variable wind turbine control and wake interactions. The new model is applied to a simulation of the Horns Rev wind farm with a sinusoidally time-varying wind inflow direction to show an hysteresis in the wind farm power extraction curve.

Keywords: FLORIS, dynamic wake model, wake advection delays, unsteady flow field, SOWFA

1 Introduction

Over the last decade, the size and the number of offshore Wind Turbines (WTs) and wind farms are constantly increasing and this growth is expected to continue in the future. With tip height often above 200 meters, currently installed WTs are interacting and impacting massively the atmospheric boundary layer. In the future, wind farms will become even more important contributors to the electrical power system and will require additional flexibility in terms of farm control, ancillary services and response to weather transients as explained in [1]. It is crucial for fast control-oriented models to be informed of weather inputs but current models are almost always quasi-steady, hence internal wind farm dynamics are not accounted.

2 Objectives

The wind farm model should account for the unsteadiness of the background flow field. Two different main usages of this new model can be distinguished. The first one can be called “operational” usage where the flow field is obtained from a single measurement location. The model can inform wind-farm control algorithms and increase fidelity. Another usage can be done by coupling the model with a weather prediction model in order to estimate wind-power resources accounting for the influence of synoptic phenomena or to improve current wind farm parametrizations that are commonly used at mesoscale level by informing on sub-grid scale effects. Currently available wake models are only steady state models and thus not suitable for a coupling with time-varying mesoscale simulations. The objective is to develop a new dynamical wake model accounting for wake advection delays and mesoscale wind transients.

3 Methodology

The Flow Redirection and Induction in Steady State (FLORIS) framework has been proven to be an easy to use, easy to tune, computationally inexpensive and powerful wake modelling tool even though lacking dynamical effects. Therefore, an extension of the FLORIS framework is presented in order to include wake advection delays between wind turbines, time-varying and spatially heterogeneous wind conditions. The new dynamical model is inspired by the FLORIDyn model presented in [2]. The so-called Observation Points (OPs) are generated at the rotor centre location. Following a Lagrangian approach, the OPs are convected downstream, along the wake of the wind turbine, defining the wake centreline.

In the current paper, we consider cases where the vertical OP displacement is much smaller than the horizontal displacements (computed in following Large Eddy Simulation (LES) and also shown in [3]), justifying the use of a two-dimensional dynamical model at hub height z_t.The first point of the centreline ($p = 1$), of turbine t at time step k, is located at the WT rotor centre, $\boldsymbol{x_C}(t) = (x_C(t), y_C(t), z_C(t))$, which gives:

$$\boldsymbol{x_{t,p=1,k}} = \boldsymbol{x_C}(t)$$

The downstream convection of $\boldsymbol{x_{t,p,k}}$ to $\boldsymbol{x_{t,p+1,k+1}}$ is defined as follows:

$$\boldsymbol{x_{t,p+1,k+1}} = \boldsymbol{x_{t,p,k}} + \boldsymbol{U}_{t,p,k}\Delta\mathrm{K}$$

where ΔK is the time step. Thus, the previous expression can be simplified to:

$$\begin{pmatrix} x_{t,p+1,k+1} \\ y_{t,p+1,k+1} \end{pmatrix} = \begin{pmatrix} x_{t,p,k} \\ y_{t,p,k} \end{pmatrix} + \begin{pmatrix} u_{t,p,k} \\ v_{t,p,k} \end{pmatrix} \Delta\mathrm{K}$$

Using matrix notation, the time update laws of OPs are:

$$\begin{bmatrix} x_{t,1,k+1} & y_{t,1,k+1} \\ x_{t,2,k+1} & y_{t,2,k+1} \\ \vdots & \vdots \\ x_{t,N_p,k+1} & y_{t,N_p,k+1} \end{bmatrix} = [A] \begin{bmatrix} x_{t,1,k} & y_{t,1,k} \\ x_{t,2,k} & y_{t,2,k} \\ \vdots & \vdots \\ x_{t,N_p,k} & y_{t,N_p,k} \end{bmatrix} + [B][x_C(t) \quad y_C(t)] + [A] \begin{bmatrix} u_{t,1,k} & v_{t,1,k} \\ u_{t,2,k} & v_{t,2,k} \\ \vdots & \vdots \\ u_{t,N_p,k} & v_{t,N_p,k} \end{bmatrix} \Delta K$$

where $[A] = \begin{bmatrix} 0 & & & \emptyset \\ 1 & 0 & & \\ & \ddots & \ddots & \\ \emptyset & & 1 & 0 \end{bmatrix}$, $[B] = \begin{bmatrix} 1 \\ 0 \\ \cdots \\ 0 \end{bmatrix}$ and N_p is the number of OPs.

The local velocity vector $U_{t,p,k} = (u_{t,p,k}\ v_{t,p,k})$ is obtained with a steady FLORIS evaluation that reflects the background input velocities and turbine settings at time index k. It is important to note that N_p is increasing at the beginning of the simulation and thus the computational time is expected to increase during the first part of the simulation and then reach a plateau.

It is during this process that the dynamics of WT wake advection delays and background flow field unsteadiness are included. Finally, using the same approach currently implemented for yaw-misalignment wake deflection, the wake is shifted to match the unsteady wake centreline. This implementation differentiates from [2] in the fact that the original FLORIS modules (wake velocity, wake turbulence and wake combination modules) are kept and a new module accounting for the wake unsteady centreline deflection is added. The new tool is hereafter called Unsteady FLORIS (UFLORIS).

4 Results

4.1 Validation

The developed model is validated against LES using the SOWFA tool [4]. The validation was conducted for steady inflow and unsteady turbulent inflow conditions, with both wind speed and direction changes, variable WT control and wake interactions. The simulation shown in Figure 1 is done using a NREL 5MW WT represented by an actuator line model. The precursor domain has dimensions of 3 x 3 kms in the horizontal direction and 1 km in the vertical direction with a uniform resolution of 20 meters. The main simulation has a refinement region around the WT and the near wake so as to reach a resolution of 5 meters. The wind is coming from bottom left at a magnitude of 8 m/s at hub height and around 6% of turbulence intensity. In the main simulation, the time step is 0.125s. The same simulation is run with and without the wind turbine in order to obtain the background flow field to be inserted into UFLORIS. This can be considered as a one-way coupling between SOWFA and UFLORIS updated every 50s. In this simulation, the WT starts with a 30° yaw angle and at $T = 800s$ the turbine is rotating at a rate of 0.1°/s in order to retrieve a nominal position without yaw angle. For the UFLORIS simulation, the time step is 10s and the output flow field figure has a resolution of 15m. The wake deficit is computed using a gaussian wake model [5].

The centreline from SOWFA (in green in Figure 1 top left) is extracted by using the methodology from [6] and compared to the UFLORIS centreline presented in the previous section (in black). The figure on the top right corresponds to data extracted at the dashed black line position. It shows a value that is proportional to the amount of wind energy that is lost due to the upstream WT. A good agreement is found between the new model and LES. The small difference between the location of the two centrelines can also be observed on this figure. Finally, the bottom figure is showing the power generated by the wind turbine. The agreement is good considering the fact that there is a 50s updating lag which corresponds to these plateaus.

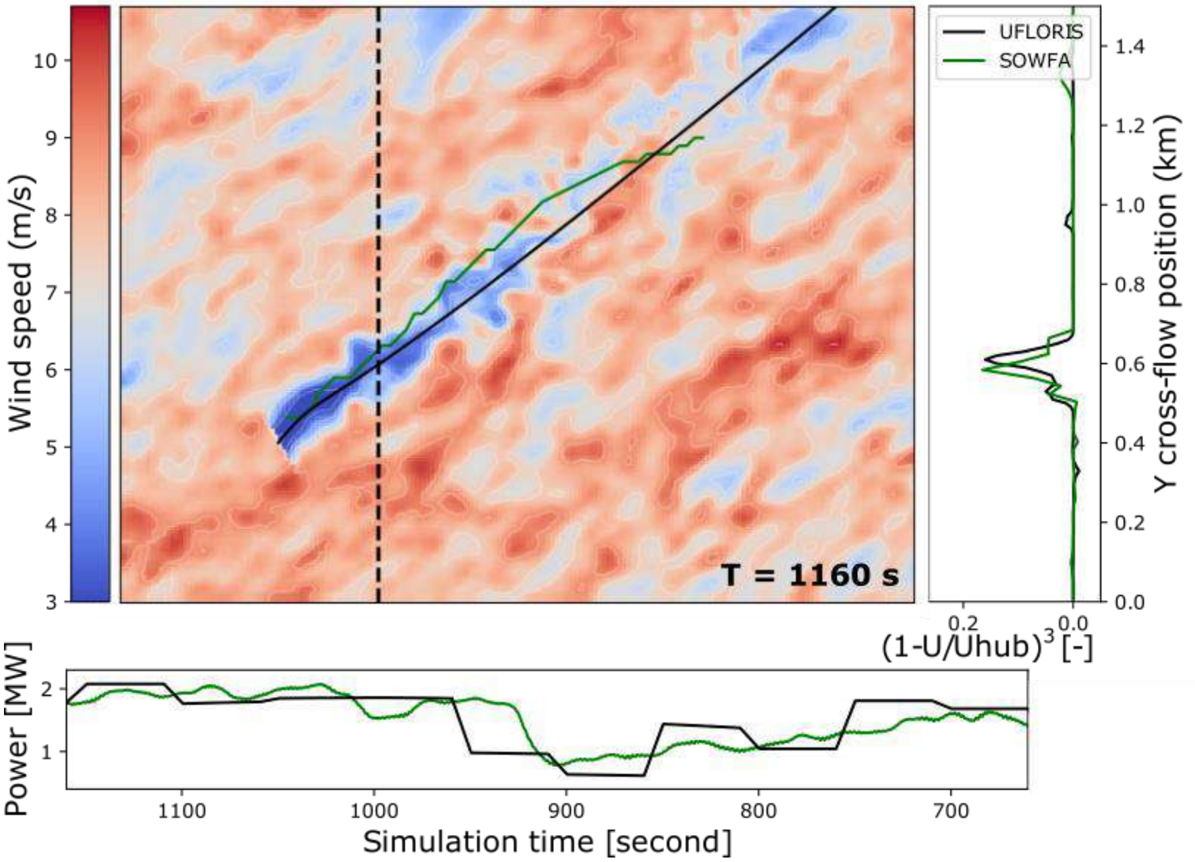

Figure 1 Instantaneous snapshot of wake centrelines from UFLORIS (black) and SOWFA (green) together with contours of background flow field from LES and model comparison of predicted power (bottom) and centreline cross-flow positions (right) at the dashed-black line position.

4.2 Application

The UFLORIS model is applied to a simulation of the Horns Rev wind farm with a sinusoidally time-varying wind inflow direction ($\theta(t) = 270° - 30° sin(2\pi t/T_\theta)$; $T_\theta = 1h$) as detailed in [7]. It is an ideal test-case to assess this new dynamical wake model because it involves dynamics of wake advection delays in wind farms and dynamical hysteresis effects in power production. Results are shown in Figure 2 where the normalized Horns Rev wind farm power is plotted as a function of the incoming wind direction. The UFLORIS simulation is capturing the dynamical effects despite not featuring lower power than the steady case as shown in [7].

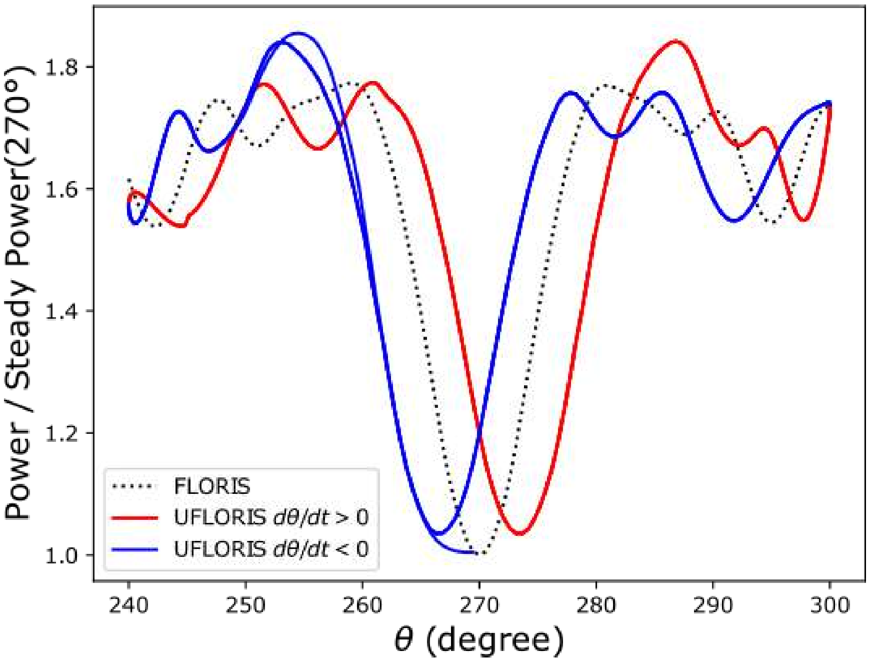

Figure 2 Normalized Horns Rev wind farm power as a function of the incoming wind direction.

5 Conclusions

In this abstract, the development of a dynamic wake model accounting for wake advection delays and mesoscale wind transients is presented. The new Unsteady version of the original FLORIS consists in the addition of a new module. It is computing the unsteady wake centreline position and shifting the wake. The implementation has been validated against LES and is applied to the Horns Rev wind farm subjected to sinusoidal wind direction changes in order to reproduce an hysteresis in the wind farm power extraction curve.

Bibliography

[1] Eguinoa I, Göçmen T , Garcia-Rosa P B and Das K 2021 Wind farm flow control oriented to electricity markets and grid integration: Initial perspective analysis *Advanced Control for Applications*.

[2] Gebraad P M O and van Wingerden J W 2014 A Control-Oriented Dynamic Model for Wakes in Wind Plants *Journal of Physics: Conference Series* **524** 012186

[3] Bossuyt J, Scott R, Ali N and Cal B 2021 Quantification of wake shape modulation and deflection for tilt and yaw misaligned wind turbines *Journal of Fluid Mechanics* **917**

[4] Sale D, Churchfield M and Bachant P 2020 dcsale/SOWFA: v1 (Version v1). Zenodo.

https://doi.org/10.5281/zenodo.3632051

[5] Bastankhah M and Porté-Agel F 2014 A new analytical model for wind-turbine wakes *Renewable Energy* **70** 116–123

[6] Coudou N, Moens M, Marichal Y, Van Beeck J, Bricteux L and Chatelain P 2018 Development of wake meandering detection algorithms and their application to large eddy simulations of an isolated wind turbine and a wind farm *Journal of Physics: Conference Series* **1037** 072024

[7] Munters W, Meneveau C and Meyers J 2016 Turbulent Inflow Precursor Method with Time-Varying Direction for Large-Eddy Simulations and Applications to Wind Farms *Boundary-Layer Meteorology* **159.2** 305–328

17th EAWE PhD Seminar on Wind Energy
3-5 November 2021
Porto, Portugal

Effect Of Vortex Shedding Modelling Choice On The Fatigue Loads Of A Wind Turbine Tower

Ricardo Fernandez-Aldama[a], Oscar Lopez-Garcia[a], Alvaro Cuerva-Tejero[a], Cristobal Gallego-Castillo[a], and Sergio Avila-Sanchez[a]

[a]Aircraft and Space Vehicles Department, Universidad Politécnica de Madrid, Plaza Cardenal Cisneros 3, 28040 Madrid, Spain

E-mail: `ricardo.fdealdama@upm.es`

Keywords: Vortex Shedding, VIV, Wind Turbine Tower, Fatigue, Turbulence

Abstract

Design rules for vortex-induced vibrations of structures are limited to oversimplified expressions of the maximum top section displacement, and thus may fail to provide an accurate estimate of the fatigue damage produced by these cross-wind vibrations. Time-marching simulations of aeroelastic models can be used to calculate fluid-structure interaction to a better degree of accuracy. For this, an appropriate vortex shedding model needs to be chosen from the wide variety present in the literature. As far as the authors are aware, a critical review of such models applied to wind turbine towers has not been carried out. As a starting step in this direction, three well-known levels of vortex shedding modeling are compared. These levels range from the simplest type A or forced system model, through type B or fluidelastic system model, to type C or coupled system model. Simulations are performed using classical modal analysis of an isolated wind turbine tapered tower, subjected to a sheared wind profile. Vortex shedding-induced loads and tower dynamics are limited to the cross-wind direction. Damage equivalent loads are included in the comparison, and a sensitivity analysis to type C parameters is performed. It is shown that the different models presented here produce results with important qualitative differences, notably that obtaining a similar result in the tower top displacement amplitude does not guarantee an equivalent behavior in the fatigue loading. The need to develop and adjust vortex shedding models based not only on displacement but also on fatigue damage is suggested.

1 Introduction

Vortex shedding is a well-known but little understood phenomenon which can drive the design of many engineering structures, and this fact has led to the development of a multitide of models to estimate the loads it produces ([1]). As far as the authors are aware, the only attempt at calculating the vortex shedding generated loads on a wind turbine tower has been done in [2] by means of spectral methods. In this work, an additional model, that of a wake oscillator, is used and compared to two spectral method variants, applied to time-marching aeroelastic simulations of a wind turbine tower, showing the differences obtained in the calculated fatigue loads as well as the structural dynamics. Firstly, the structural model is described in section 2. The aerodynamic models employed are presented next in section 3. Then, the fatigue calculation procedure is outlined in section 4. Simulation and fatigue calculation results for a range of wind speeds are presented in section 5. And, finally, some conclusions are drawn in section 6.

By showing the dynamics and fatigue obtained by applying different existing vortex shedding models to a wind turbine aeroelastic model, the present work intends to serve as a reference when choosing or developing models particular to this type of structures.

2 Tower Modelling

The wind turbine tower is modelled as a cantilevered Euler-Bernoulli beam, and classical modal superposition is used to reduce the system to a single degree of freedom, corresponding to the tower first lateral mode. The structural dynamic equation is thus:

$$m_1 \ddot{p}_1(t;\alpha) + 2m_1\zeta_{s,1}\omega_1\dot{p}_1(t;\alpha) + m_1\omega_1^2 p_1(t;\alpha) = \int_0^H f_{f\to s}\Psi_1(z)\,\mathrm{d}z, \tag{1}$$

where m_1 is the modal mass of the structure; $p(t;\alpha)$ is the modal coordinate of the tower lateral deflection $w(z,t;\alpha)$, such that $w(z,t;\alpha) = p(t;\alpha)\Psi_1(z)$, being $\Psi_1(z)$ the modal shape, and z the height from the ground at $z = 0$ to the tower top at $z = H$; $\zeta_{s,1}$ is the structural modal damping; ω_1 is the undamped natural frequency; α is the realization number of the stochastic process, being $\alpha = 1, \ldots N_\alpha$, where N_α is the total number of processes considered; and $f_{f\to s}$ is the external forcing of the fluid upon the structure.

3 Vortex Shedding Forces Modelling

Spectral models originally relied on experimental results of very rigid structures [3], and thus did not consider any effect of the structural motion in the vortex-induced loads; these type of models are here called type A, in accordance with the nomenclature used in [4]. A later development, presented in [5], included the effect of structural dynamics on the vortex-induced loads by means of non-linear damping terms; these type of models are called type B. On the other hand, wake oscillator models, as originally proposed in [6], couple the structural dynamics with a model for the wake dynamics which reproduces the main characteristics of vortex shedding, with the disadvantage that they have to be adjusted for each individual application; this type of models are called type C.

Thus, three levels of vortex shedding modelling are considered, which are, in increasing order of complexity, a type A model, or forced system model, a type B model, or fluidelastic system model, and a type C model, or coupled system model. Each model defines a different forcing on the structure $f_{f\to s}$ in equation (1). The details of this function $f_{f\to s}$ for each model are now presented.

3.1 Type A

For type A, a stochastic lift coefficient time series $c_L(z,t;\alpha)$ is defined, based on the spectral model first proposed by [3], and the coherence model proposed in [1]. The force produced by this lift coefficient follows the canonical form and is:

$$f_{f\to s}(z,t;\alpha) = \frac{1}{2}\rho\overline{U}^2(z)D(z)c_L(z,t;\alpha), \tag{2}$$

where ρ is the density of the fluid; $\overline{U}(z)$ is the average inflow speed; and $D(z)$ is the tower diameter. This model does not consider any effect of the structural motion on the vortex-induced loads.

3.2 Type B

For type B, the same lift force as in type A is used, and an additional force related to the structural motion is added, based on the formulation by [5]. The sum of the two forces is:

$$f_{f\to s}(z,t;\alpha) = \frac{1}{2}\rho\overline{U}^2(z)D(z)c_L(z,t;\alpha) + k_a(z)\left(\dot{w}(z,t;\alpha) - G\dot{w}^3(z,t;\alpha)\right), \tag{3}$$

where k_a is a nonlinear damping parameter which depends on the Reynolds number Re, the turbulence intensity I_u, and the reduced velocity $U_{\mathrm{red}}(z) = \dfrac{2\pi\overline{U}(z)}{\omega_1 D(z)}$; and G is a function of the limit amplitude value which is obtained from [7].

It can be seen that the new force is a nonlinear damping force, comprised of a linear damping term and a cubic damping term. The linear term models the self-excited nature of vortex-induced vibrations, and the cubic term models the self-limiting nature of vortex-induced vibrations; two important charactersitics observed experimentally (see [5])

3.3 Type C

For type C, vortex shedding is modeled via a wake-related variable q. For simplification, the wake variable is here assumed to have a characteristic shape which matches the modal shape of the structure, as done previously by [8] and [9], such that $q(z,t;\alpha) = \Psi_1(z)l(t;\alpha)$, where $\Psi_1(z)$ is the first mode shape of the tower. The wake equation with this prescribed shape reads (omitting the dependence on α for readability):

$$\int_0^H \Psi_1^2(z)\,\mathrm{d}z\,\ddot{l}_1(t) + \varepsilon\left(\int_0^H \Omega(z)\,\Psi_1^4(z)\,\mathrm{d}z\,l^2(t) - \int_0^H \Omega(z)\,\Psi_1^2(z)\,\mathrm{d}z\right)\dot{l}(t) + \int_0^H \Omega^2(z)\,\Psi_1^2(z)\,\mathrm{d}z\,l(t) = \int_0^H f_{s\to f}\Psi_1(z)\,\mathrm{d}z, \tag{4}$$

where $\Omega(z) = \dfrac{2\pi\mathrm{St}\overline{U}(z)}{D(z)}$, being St the Strouhal number; and ε is the strength of the van der Pol nonlinear damping term.

To define the forcing of the structure on the wake, $f_{s\to f}$, a single contribution is considered as proportional to the structural velocity, which is the preferred approximation for cases with high mass-damping, as argued in [10], being the proportionality constant defined as $\dfrac{B}{D(z)}$. On the other hand, to define the forcing of the fluid on the structure, $f_{f\to s}$, the following contributions are considered: (I) A lift force via a lift coefficient related to the wake variable as: $c_L = q\dfrac{c_{L,0}}{2}$, where $c_{L,0}$ is the stationary vortex-shedding lift coefficient. (II) A drag damping force, multiplied by the parameter $\dfrac{H}{c_D(z)}$ to account for the stalling behaviour of the flow, being c_D the sectional drag coefficient. And (III) the drag force induced by the turbulent wind, considered simply as the total drag force projected in the lateral direction by an angle of attack β. Therefore, the two external forcing terms are:

$$f_{s\to f}(z,t;\alpha) = \frac{B}{D(z)}\dot{w}(z,t;\alpha), \tag{5}$$

and

$$f_{f\to s}(z,t;\alpha) = \frac{1}{2}\rho\overline{U}^2(z)D(z)\left(c_L(z,t;\alpha) + H\frac{\dot{w}(z,t;\alpha)}{\overline{U}(z)}\right) + \frac{1}{2}\rho U^2(z,t;\alpha)D(z)c_D(z)\sin\beta(z,t;\alpha), \tag{6}$$

where $U = \sqrt{\left(\overline{U}+u_x\right)^2 + u_y^2}$, and $\beta = \arctan\left(\dfrac{u_y}{\overline{U}+u_x}\right)$, being u_x and u_y the turbulent components of the wind field in the longitudinal and lateral directions, respectively. Thus, ε, H and B are semiempirical parameters to be adjusted for each case.

4 Fatigue Calculation

The tower bottom bending moment time series is calculated from the simulated deflection time series, and then the fatigue damage it causes is computed using the rainflow-counting (RFC) algorithm as described in [11]. Using Miner's rule, in accordance with [12] the damage equivalent load (DEL) is obtained for 1000 cycles (DEL_{1000}) as:

$$\mathrm{DEL}_{1000} = \left(\frac{1}{1000}\sum n_i S_i^m\right)^{\frac{1}{m}}, \tag{7}$$

where n_i and S_i are the number of cycles and their amplitudes as obtained with the RFC algorithm, and m is the slope of the S-N fatigue curve.

5 Results and Discussion

In the present work, the results using the three different vortex shedding models described in section 3 are compared. The tower model used is that proposed for the NREL-5MW wind turbine in [13]. All

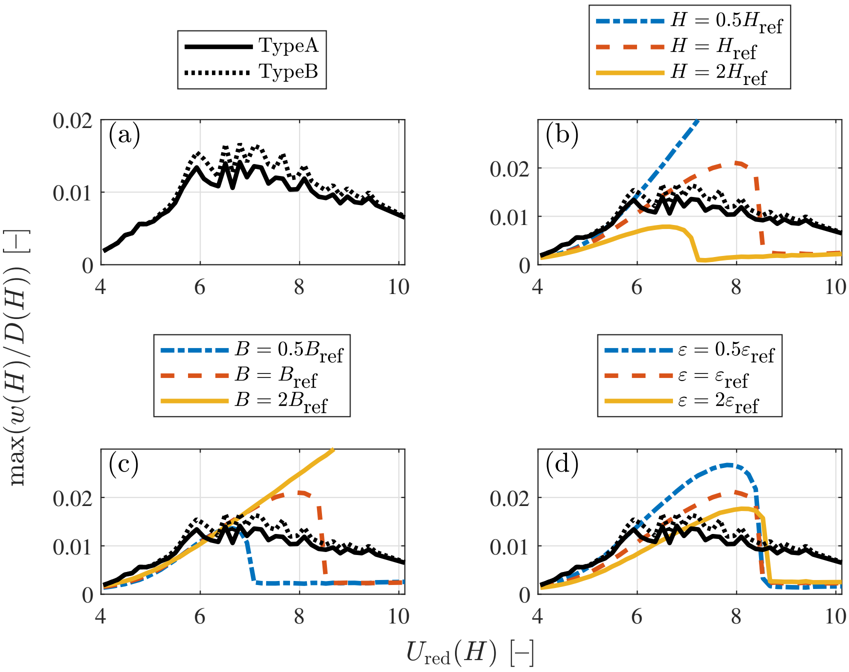

Figure 1: Non dimensional maximum deflection as a function of the reduced wind speed, at the tower top section, for vortex shedding models (a) A and B, (b) A, B, and C with three values of parameter H, (c) A, B, and C with three values of parameter B and (d) A, B, and C with three values of parameter ε.
.

simulations are carried out with the following general conditions: simulation time $t_{\text{sim}} = 600$s; simulation time step $\Delta t = 0.1$s; wind shear parameter $\alpha = 0.2$; turbulence intensity $I_{\text{ref}} = 0.12$; and Strouhal number $\text{St} = 0.2$. Regarding the parameters specific to each vortex shedding model, we have for type A and type B only the bandwidth parameter $B_0 = 0.1$, and for type C there is the stationary vortex-shedding lift coefficient $c_{L,0} = 0.3$ as usually taken, see [14]; the van der Pol nonlinearity parameter $\varepsilon_{\text{ref}} = 0.3$; the stall damping constant $H_{\text{ref}} = -33.3$; and the velocity coupling constant $B_{\text{ref}} = 297.5[\text{s}^{-1}]$. Statistics are calculated from $N_\alpha = 12$ realizations, based on the last 100s from each 600s simulation. The stochastic processes of lift coefficient (for types A and B) and of turbulent wind components (for type C) are synthesized as time series using the method presented in [15] and using Fast Fourier Transforms. The Kaimal spectra of turbulent wind as described in [12] are employed.

The results for the tower bottom fatigue damage equivalent load as a function of the reduced velocity U_{red} are shown in Figure 1. Peaks and troughs in Figure 1(a) are due to the stochastic nature of the lift coefficient calculation, so more realizations should smooth out the results.

Deflections are seen to be less than 2% of the tower top diameter, therefore the fluid-structure interaction is not dominating. This can be seen in Figure 1(a), where the inclusion of the negative damping introduced by the type B model does not alter the results significantly.

The deflection time series shown in Figure 2 show that type C fails to account for the effect of turbulence; namely, that low frequency turbulence contributions change the effective mean wind speed and thus the vortex shedding frequency, making it a broad-banded process, as can be seen in Figure 3 for types A and B. Additionally, it is questioned whether the stable change of branch that can be seen in the type C results in Figure 1(b-d) would still occur under turbulent conditions, or else the deflection might be underestimated for high velocities. On the other hand, the type B model is incapable of qualitatively reproducing said change of branch, nor the synchronization effect which makes the structure to vibrate mainly at a frequency different to its natural frequency, as can be observed in Figure 3.

The sensitivity analysis to the type C semiempiric parameters in Figure 2 shows the qualitative effect already described in [10], and the impossibility to match the results of the spectral (A and B) models. This is further confirmed when looking at the fatigue damage in Figure 4. It is worth noting that fatigue damage is not only affeceted by the amplitude of the vibrations, but also by their frequency, so the

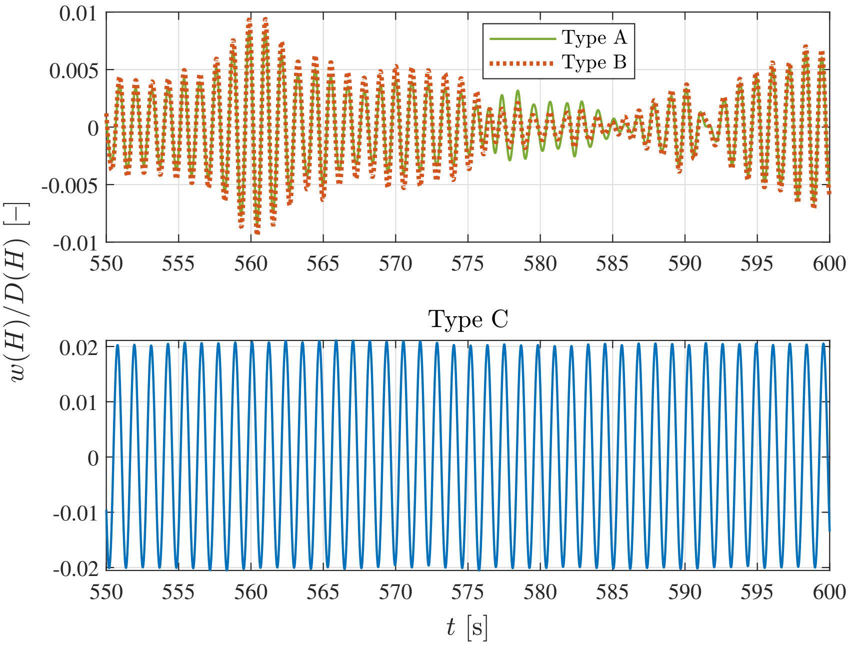

Figure 2: Last 50 seconds of the non dimensional tower top deflection time series, for vortex shedding models A and B (top), and model C (bottom), for a reduced velocity $U_{\text{red}}(H) = 5$.

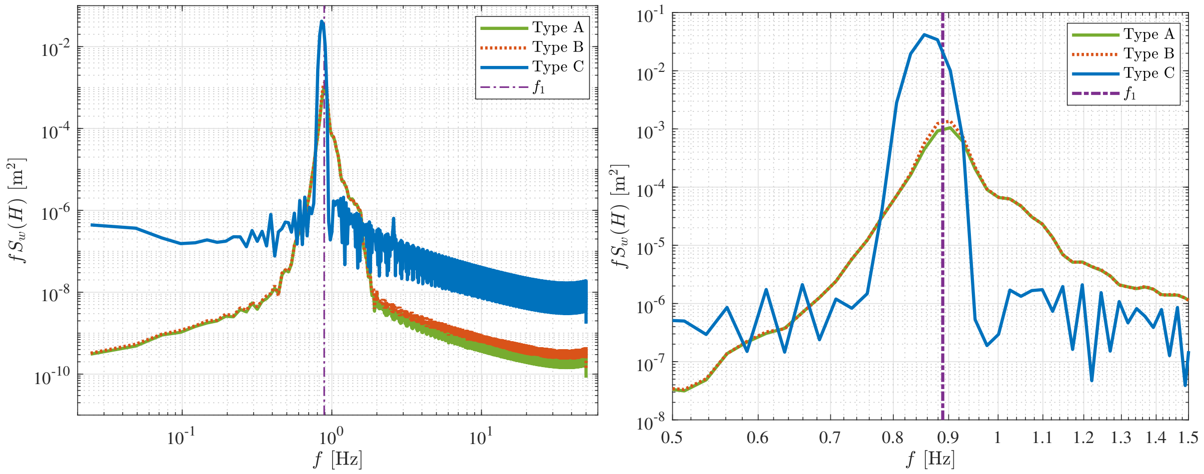

Figure 3: Left: Product of power spectral density of the tower top deflection and frequency, as a function of frequency, for vortex shedding models A, B and C, for a reduced velocity $U_{\text{red}}(H) = 5$.The tower natural frequency value is marked as f_1. Right: Same as Left, but zoomed around the natural frequency.

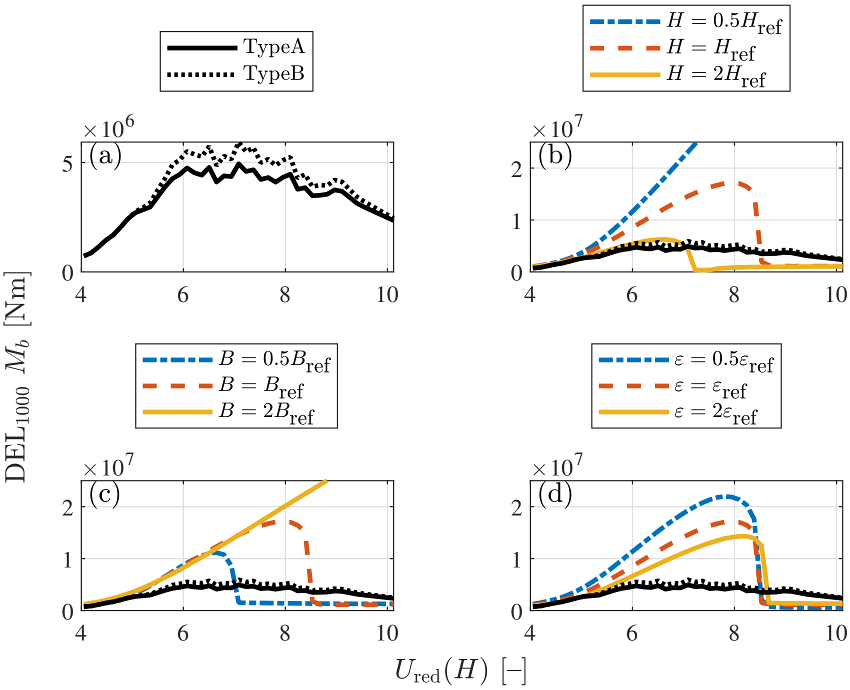

Figure 4: 1000 cycles damage equivalent load (DEL) of the tower bottom bending moment as a function of the reduced wind speed, for vortex shedding models (a) A and B, (b) A, B, and C with three values of parameter H, (c) A, B, and C with three values of parameter B and (d) A, B, and C with three values of parameter ε.

discrepancies shown in Figure 3 will have an effect on the fatigue calculation results.

6 Conclusions

Even though aeroelastic simulations using vortex-induced forces modelling are much richer in detail and dynamic description than design rule models, evident qualitative differences are shown between the presented types A, B, and C vortex shedding models that cannot be overcome by simple adjustment of the semiempiric parameters involved. None of the models seem to satisfactorily account for the vortex shedding loads in the tower dynamics. To allow for realistic time domain dynamic simulations, there seems to be a need to develop type C models where the turbulence effect is accounted for accurately, especially its low frequency components, keeping in mind that experimental adjustments should be made to properly reproduce the fatigue loading on the wind turbine tower.

Acknowledgements

The present work has been supported by the Spanish Agency of Science, Innovation and Universities under the project "Stochastic Models of the aeroelasticity of stopped wind turbines"(RTI2018-095592-B-I00). The first author's work has been supported under grant reference PRE2019-089821 of the Spanish Agency of Science, Innovation and Universities and the European Social Fund.

References

[1] Dyrbye C and Hansen S 1996 *English edition*

[2] Nunez-Casado C, Lopez-Garcia O, de las Heras E G, Cuerva-Tejero A and Gallego-Castillo C 2017 *Wind & structures* **25** 569–588

[3] Vickery B J and Clark A W 1972 *Journal of the Structural Division* **98** 1–20

[4] Païdoussis M P, Price S J and De Langre E 2010 *Fluid-structure interactions: cross-flow-induced instabilities* (Cambridge University Press)

[5] Vickery B and Basu R 1983 *Journal of Wind Engineering and Industrial Aerodynamics* **12** 49–73

[6] Hartlen R T and Currie I G 1970 *Journal of the Engineering Mechanics Division* **96** 577–591

[7] 1991-1-4 E 2005 *Brussels (Belgium): Comité Européen de Normalization (CEN)*

[8] Keber M 2012 *Vortex-Induced vibration of offshore risers: Theoretical modelling and analysis* Ph.D. thesis University of Aberdeen

[9] Wang D, Chen Y, Wiercigroch M and Cao Q 2016 *Applied Mathematics and Mechanics* **37** 1251–1274

[10] Xu K, Ge Y and Zhang D 2015 *Journal of Wind Engineering and Industrial Aerodynamics* **136** 192–200

[11] ASTM 1985 standard e 1049-85: Standard practices for cycle counting in fatigue analysis

[12] IEC 2005 *International Electrotechnical Commission*

[13] Jonkman J, Butterfield S, Musial W and Scott G 2009 *National Renewable Energy Laboratory, Golden, CO, Technical Report No. NREL/TP-500-38060*

[14] Facchinetti M L, De Langre E and Biolley F 2004 *Journal of Fluids and structures* **19** 123–140

[15] Veers P S 1988 Three-dimensional wind simulation Tech. rep. Sandia National Labs., Albuquerque, NM (USA)

Connecting the wind farm model FLORIDyn to heterogeneous flow and performing a sensitivity analysis

M. Becker, V.V. Dighe, D. Allaers, and J.W. van Wingerden

Delft University of Technology, Mekelweg 2, 2628 CD Delft, Netherlands

`E-mail: marcus.becker@tudelft.nl`

Keywords: Wind farm control, Sensitivity analysis and Wake steering

Abstract

Wind turbines are built to extract kinetic energy from the wind. By doing so, they locally slow down the wind and leave a wake in the wind field. When turbines are placed close to each other, wakes of upstream turbines can influence downstream ones and reduce the amount of energy they can extract from the wind. A wind farm control strategy can reduce the power loss due to wake effects. However, such a control strategy has to work under challenging circumstances: changing wind directions, heterogeneous flow conditions and a large number of turbines with complex wake dynamics. In recent years steady-state model based approaches have delivered control strategies which can cope with many of the mentioned challenges. However, these approaches neglect the dynamic behaviour of the wakes and the surrounding flow. This is where the FLOw Redirection and Induction Dynamics (FLORIDyn) model offers an alternative. At low computational cost it can simulate parametric wake models in a dynamic fashion. The reworked version of FLORIDyn from [1] allows for changing wind directions and heterogeneous flow conditions. In [2] it was further developed to incorporate flow estimators and further decrease the computational cost.

In this work, we utilize the new capabilities of FLORIDyn and couple the model with the high-fidelity simulation environment SOWFA. This coupling is done by including the Immersion and Invariance (I&I) estimator ([3]) in FLORIDyn that provides an effective wind speed estimation $u_{\text{eff,I\&I}}$ based on SOWFA data. We assume that for turbines in free stream $u_{\text{eff,I\&I}} = u_{\text{free}}$. For downstream turbines, affected by the wake of upstream turbines, this can not hold true. However, FLORIDyn does model the wake effects and provides and effective wind speed estimate $u_{\text{eff,F}} = u_{\text{free}}(1 - r_F)$, where r_F is the reduction factor

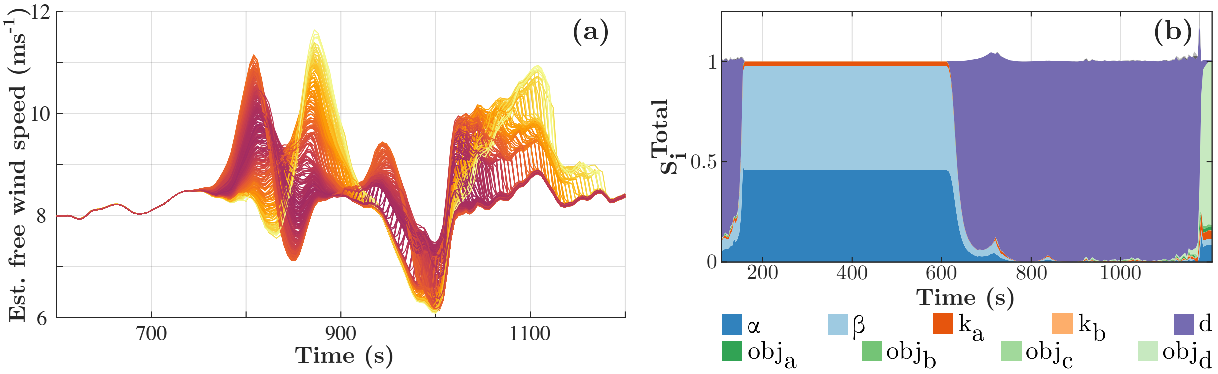

Figure 1: Results of Turbine 1 in a 9 turbine case: (a) the estimated free wind speed $u_{\text{free,I\&I,F}}$ for varying FLORIDyn parameters; (b) the total Sobol indices of the parameters, indicating how sensitive the variance of $u_{\text{free,I\&I,F}}$ is towards the change of a certain parameter.

based on the FLORIDyn wakes. If $u_{\text{eff,F}}$ is replaced by the more accurate $u_{\text{eff,I\&I}}$, we can estimate u_{free}:

$$u_{\text{free,I\&I,F}} = \frac{u_{\text{eff,I\&I}}}{1 - r_F} \tag{1}$$

This new estimate is sensitive to parameter changes of FLORIDyn and coefficient changes of the I&I estimator. The latter are fixed in this work. A sensitivity analysis (SA) for the FLORIDyn parameters is performed with $u_{\text{free,I\&I,F}}$ in a nine turbine case. During the simulation time, the turbulent flow changes its direction by 60 deg. As a result, the wakes of upstream turbines temporarily affect downstream turbines. The FLORIDyn wakes are based on nine parameters which can be roughly categorized: the parameters α and β regulate the length of the near wake area and thus how fast the wake recovers. The expansion of the wake is parametrized by k_a and k_b and the added turbulence in the wake is weighted by obj_a to obj_d. Lastly, the parameter d was added in this work, which influences the advection speed of the wake: how fast state changes propagate and how fast the wake reacts to new flow conditions.

For the SA, we follow [4] and consider one FLORIDyn model evaluation as an operator $\mathcal{M}(\theta, \mathcal{O})$ which returns the quantity of interest Y and is dependent on the uncertain model parameters $\theta = [\alpha, \beta, \ldots]$ and the set operating conditions $\mathcal{O}$. Since a high number of evaluations of $\mathcal{M}$ is needed in order to perform the SA, we approximate the model output behaviour using a polynomial chaos expansion (PC) surrogate model $\mathcal{M}^{\text{PC}}$:

$$Y = \mathcal{M}^{\text{PC}}(\theta, \mathcal{O}) \approx \mathcal{M}(\theta, \mathcal{O}) \tag{2}$$

where $\mathcal{M}^{\text{PC}}$ can be defined as sum of multivariate polynomials. The PC model is then used to calculate the variance D of the model output, which is then used to calculate the total order Sobol indices:

$$S_i^{\text{Total}} = \frac{1}{D} \sum_{\mathcal{K}_i} w^2, \quad i = 1, \ldots, N_\theta \tag{3}$$

where $\mathcal{K}_i$ is a subset of the $\mathcal{K}$ multivariate polynomials, w are the respective basis function coefficients and N_θ is the number of parameters. A total order Sobol index S_i^{Total} close to 1 indicates that the parameter i has a big influence on the variance of Y.

An initial result is that the coupling of FLORIDyn with the I&I estimator works and ensures a near perfect fit of the power generated with SOWFA. It is therefore admissible to neglect the power generated as a quantity of interest and focus on the wind speed. The SA shows that the preliminary dynamic parameter added plays a dominant role in the variance of the estimated free wind speed. The coefficients α and β play a significant role for second row turbines. For third row turbines, the added turbulence level parameters are more relevant, which is expected to become even more important for large scale wind farms.

For future work it is recommended to enhance the FLORIDyn simulation environment with additional estimators for other flow quantities like wind direction, turbulence intensity and wind shear. This can allow the model to become a more accurate digital clone of a wind farm at a low computational cost. Based on the SA findings, we recommend to further investigate the dynamic behaviour of the wake and substitute the added parameter d with a more differentiated function and parameter set. Furthermore, the importance of obj_a to obj_b for third row turbines indicates that parametric models without added turbulence intensity might not have the capabilities to accurately describe wake environments deeper into the wind farm. Lastly, the generated PC surrogate model can also be used to perform a computationally efficient parameter calibration using confidence intervals. This calibration can also indicate the uncertainty of the selected parameter values. This could show where the parametric model description is still insufficient and needs to be improved.

References

[1] Marcus Becker, Bastian Ritter, Bart M. Doekemeijer, Daan van der Hoek, Ulrich Konigorski, Dries Allaerts, and Jan-Willem Van Wingerden. FLORIDyn - A dynamic, control oriented wind farm model. *In preparation*, 2021.

[2] Marcus Becker, Dries Allaerts, and Jan-Willem Van Wingerden. FLORIDyn - A dynamic and flexible model for real-time wind farm control. In preparation for Torque 2022.

[3] Romeo Ortega, Fernando Mancilla-David, and Fernando Jaramillo. A globally convergent wind speed estimator for wind turbine systems. *International Journal of Adaptive Control and Signal Processing*, 27(5):413–425, 2013.

[4] Benjamin Sanderse, Vinit V. Dighe, Koen Boorsma, and Gerard Schepers. Efficient Bayesian calibration of aerodynamic wind turbine models using surrogate modeling. preprint, Design methods, reliability and uncertainty modelling, June 2021.

17^{th} EAWE PhD Seminar on Wind Energy
3-5 November 2021
Porto, Portugal

Multi-rate time stepping in wind farm LES with actuator line methods

K Ntrelia[a] and **J Meyers**[a]

[a]Department of Mechanical Engineering, KU Leuven, Celestijnenlaan 300A, 3001 Leuven

E-mail: `konstantina.ntrelia@kuleuven.be`

Keywords: large-eddy simulation, wind turbine modeling, numerical time integration

1 Introduction

Large eddy simulations (LES) have proven as crucial tools for the wind energy society in order to study and understand the complex physics phenomena that take place inside a wind farm. In these high fidelity models, wind turbines are usually represented through actuator models that represent the turbine forces acting on the flow. The actuator line model (ALM) by Sørensen & Shen [1] currently remains the most accurate model,taking into account the geometry of the turbine blades. However, its significant time-step limitations render the method computationally inefficient. The current study investigates the advantage of employing a multi-rate time-integration technique inside a LES framework, aiming to overcome the computational cost problem of ALMs. This multi-stepping technique enables the decoupling between the components of our system. To this end, by employing a fine temporal resolution for the rotor dynamics, the time step limitations of ALM methods are respected, while the rest of the wind farm flow field is resolved using coarser time scales. This time scale separation exhibits great benefits for LES using actuator line methods, by preserving the accuracy of the system but reducing the overall computational effort of such simulations.

2 Methodology

Multirate Generalized Additive Runge-Kutta Methods (MrGARK) [2] are specific instants of generic Runge-Kutta methods. The concept of MrGARK methods resides on the fact that the partitions of a system can evolve at different time scales, but are concisely coupled so as to properly advance in time.

Within this scope, a third order multi-rate scheme is employed as the time marching scheme inside the pseudo-spectral LES environment SP-Wind, where the wind turbines are modeled through the actuator line method. As a result, the governing equations of our system are accordingly divided into slow and fast evolving equations which correspond to the respective components. The forcing terms and the flow field that resides in a close vicinity to the turbines are discretized with fine time steps h, whereas the rest of the flow field is discretized using bigger time steps H.The two time scales are connected through the multi-rate separation ratio M, which is defined as the ratio of the two time steps, $M = H/h$. Information between the time scales is exchanged by properly coupling the terms of the system, so that they can homogeneously progress in time.

3 Results and discussion

The multi-rate time stepping techniques are implemented in the LES framework. In this case, the flow and the motion of the blades are decoupled. This means that the forcing terms, that are enacted on the flow by the wind turbines are discretized with a smaller time step h, influencing exclusively the flow field around it.Various high order schemes have been formulated by Sarshar, Roberts & Sandu [2] from which

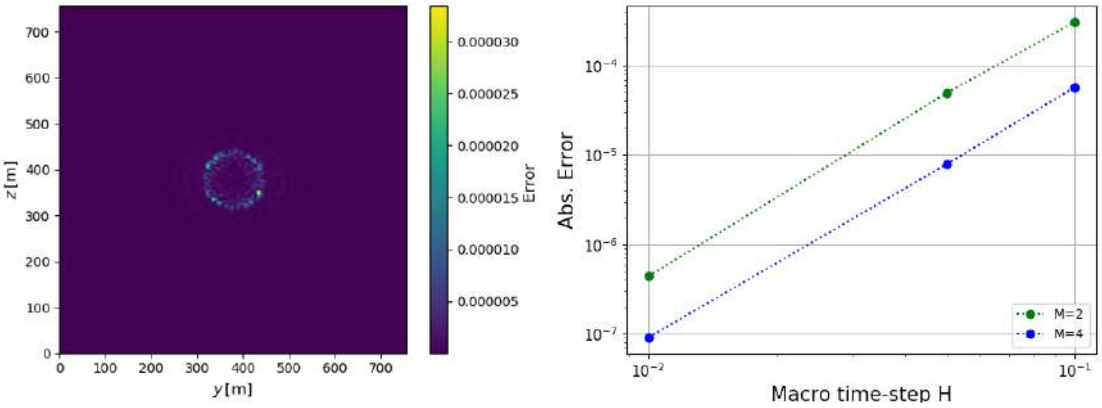

(a) (b)

Figure 1: Error plot of instantaneous axial velocity flow fields on wind turbine plane; comparison between single-rate fourth order Runge-Kutta ($H = 0.01sec$) versus flow field applying MrGARK Ex3-Ex3 3[S] ($M = 4, H = 0.01$) (a). Absolute error in reference to time step. A fixed macro-step time integration is carried out with varying multi-rate step ratios M using Ex3-Ex3 3[S] scheme (b).

an explicit third order scheme (Ex3-Ex3 3[S]) has been selected. The integration scheme is tested upon a study case with a uniform inflow of 8 m/sec using NREL 15MW wind turbine, different time steps $H = 0.01sec, 0.05sec, 0.1sec$ and separation factors $M = 2, 4$.

The performance of the scheme is tested through an error analysis. The error is computed using the L_1 norm and the reference case consists of a typical fourth order Runge-Kutta with a fine time-step of $H = 0.01sec$. The obtained results are presented in Fig.1, where the test case is compared against the reference case. From the figures above it is evident that the numerical solution is calculated with high accuracy, as the error around the turbine plane remains acceptable after one flow through(Fig.1(a)). Moreover, the numerical order matches the theoretical order for the tested mutli-rate step ratios.

4 Future Work

Having implemented and validated the performance of MrGARK methods through a preliminary case study, the next challenge involves a more thorough analysis of the system. This involves an investigation on the range of the separation ratios that can be used between the blade motion and flow time scales, as well as the computational gains that can be achieved are interesting subjects to be further studied. Finally, an extension and coupling with the structural model will reveal the true benefits that these methods hold for LES.

References

[1] Sørensen, J. N. and Shen, W. Z., 2002, *Journal of Fluids Engineering,* **Vol. 124** 393–399

[2] Sarshar A, Roberts S and Sandu A, 2019 *SIAM J. Sci. Comput.* **41(2)** 816-847

Numerical simulations for active power control of wind farms

S Tamaro[a] and Carlo L. Bottasso[a]

[a]Technical University of Munich, Wind Energy Institute, Boltzmannstrasse 15, 85748, Garching, Germany

E-mail: simone.tamaro@tum.de

Keywords: wind farm control, CFD, power tracking

1 Introduction

The uncertainty of the power output of wind farms is a relevant issue for manufacturers, transmission system operators (TSO) and wind farm operators, since it can introduce additional and relevant costs for the stakeholders in order to balance the electrical grid [1]. With the growing penetration of wind energy in the electricity market, active power control (APC) methods are gaining strong interest in the industry as valid tools to balance power production and power consumption. Although APC is nowadays a basic requirement in the industry, the current practice is to derate the individual turbines to build an active power reserve, necessary to respond to potential fluctuations in the grid [2]. The aim of this research project is to advance the current status of power tracking control for wind farms, by developing affordable and reliable APC methods to optimize the distribution of set points in a waked wind farm with the goals of extending its lifetime, reducing risks of failures and optimizing the energy extraction. A strong focus will be put on the application and development of innovative processing routines of real-time data to determine the status of each turbine in terms of stress, fatigue and power reserve, and to make these information available to the controller to improve its awareness.

2 Methodology

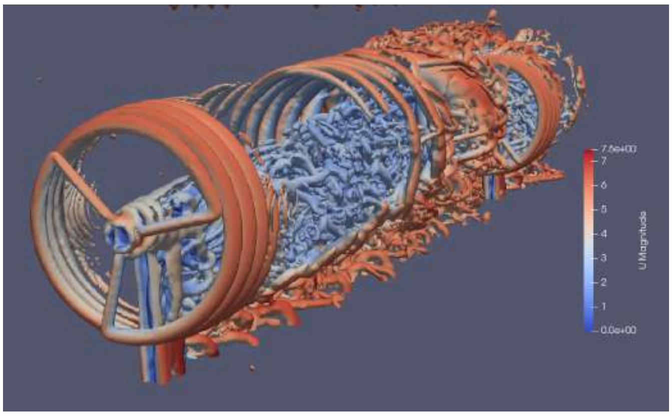

Figure 1: Iso-contours of Q criterion colored by velocity magnitude. Result obtained from a SOWFA simulation with two TUM G1 wind turbine models [3] and uniform inflow.

Computational fluid dynamics (CFD) will be used as main tool to research and to test new control strategies. A version of the open-source software SOWFA developed at TUM will be used due to its reliability and suitability to deal with the complex dynamics typical of wind turbine wakes and wake interactions [4, 5]. SOWFA couples an LES solver implemented in OpenFOAM with the blade element momentum (BEM) code FAST by NREL [6]. The actuator line method (ALM) [7] is used to model the blades, by projecting body forces computed with BEM onto the LES mesh grid.

The research methodology is based on the implementation of a feedback loop for APC in SOWFA. Feedback loop controllers for APC have been investigated extensively by [1, 8]. This controlling strategy takes as input a reference signal from the TSO and computes the optimal set points distribution to achieve a wind farm output that matches the reference power signal. The nonunique solution of the problem makes it possible to not only achieve power tracking, but also to introduce an additional goal, such as structural fatigue loads mitigation. A sketch of the feedback control system is showed in Figure 2. As a first step, the method proposed by [8] will be implemented and it will be used as benchmark for new methods that will be developed during the PhD. The data collected from CFD simulations will be used as benchmark for wind tunnel experiments, as well as lower-resolution solvers based on engineering wake models. The results carried out with this study will allow to improve the current control of wind plants, by providing the industry with methods at reduced costs and limited complexity.

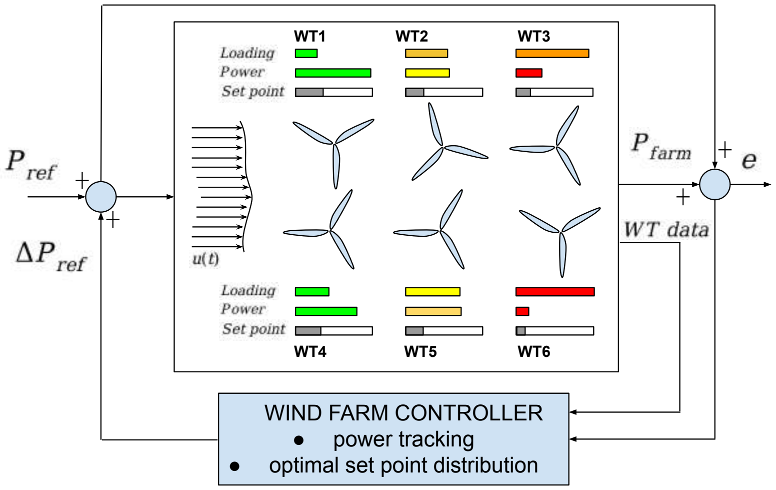

Figure 2: Schematic representation of an APC wind farm feedback control system with real time wind turbine data for power tracking and loads mitigation.

Acknowledgements

The authors acknowledge the support of the German Federal Ministry for Economic Affairs and Energy (BMWi) within the PowerTracker project to the present research project.

References

[1] van Wingerden J W, Pao L, Aho J and Fleming P 2017 *IFAC-PapersOnLine* **50** 4484–4491 ISSN 2405-8963 20th IFAC World Congress URL `https://www.sciencedirect.com/science/article/pii/S240589631730722X`

[2] Aho J, Buckspan A, Laks J, Fleming P, Jeong Y, Dunne F, Churchfield M, Pao L and Johnson K 2012 *2012 American Control Conference (ACC)* pp 3120–3131

[3] Campagnolo F, Petrović V, Schreiber J, Nanos E M, Croce A and Bottasso C L 2016 *Journal of Physics: Conference Series* **753** 032006 URL `https://doi.org/10.1088/1742-6596/753/3/032006`

[4] Wang J, Wang C, Campagnolo F and Bottasso C L 2019 *Wind Energy Science* **4** 71–88 URL `https://wes.copernicus.org/articles/4/71/2019/`

[5] Wang C, Wang J, Campagnolo F, Carraón D B and Bottasso C L 2018 *Journal of Physics: Conference Series* **1037** 062007 URL `https://doi.org/10.1088/1742-6596/1037/6/062007`

[6] Guntur S, Jonkman J M, Jonkman B, Wang Q, Sprague M A, Hind M, Sievers R and Schreck S J 2016 *FAST v8 Verification and Validation for a MW-scale Wind Turbine with Aeroelastically Tailored Blades* (AIAA) (*Preprint* `https://arc.aiaa.org/doi/pdf/10.2514/6.2016-1008`) URL `https://arc.aiaa.org/doi/abs/10.2514/6.2016-1008`

[7] Troldborg N, Sørensen J N and Mikkelsen R 2007 *Journal of Physics: Conference Series* **75** 012063 URL `https://doi.org/10.1088/1742-6596/75/1/012063`

[8] Vali M, Petrović V, Steinfeld G, Y Pao L and Kühn M 2019 *Wind Energy Science* **4** 139–161 URL `https://wes.copernicus.org/articles/4/139/2019/`

Learning and explaining intra-plant flow features from operational data - Application to the offshore wind farm Anholt

A Vad[a], R Braunbehrens[a], C L Bottasso[a]

[a] Technical University of Munich, Garching, Germany

E-mail: andi.vad@tum.de

Keywords: long-term wind farm effects, SVD, intra-plant flow effects, data-driven learning

1 Introduction

Several studies have shown that large wind farms can experience significant variations in the cross-wind inflow conditions [4, 5]. Furthermore, LES simulations of large finite-sized wind farms have shown that the flow conditions not only change in the entry region of the farm but also along the streamwise direction depending on the atmospheric condition [1, 6]. Terrain and layout effects add further complexity to correctly model the flow field within a wind farm without excessive computational cost.

2 Methods

In this study these intra-plant flow features are learned from SCADA measurements using the engineering simulation framework FLORIS. This is done by simultaneously tuning the existing wake parameters and learning the background flow field. The latter is modelled with additional parameters that are spatially distributed within the wind farm and depend on the wind direction and the atmospheric stability. To prevent that the estimation problem becomes ill-posed with such a large amount of parameters, a singular value decomposition of the Fisher information matrix is applied that only parameters with a high confidence level are tuned [2].

3 Results

The Anholt wind farm consists of 111 turbines and is situated in the Kattegat, about 20 km east of a peninsula of mainland Denmark in the west and about 25 km west of the island Anholt. Figure 1 shows the background flow field estimated from operational data. The flow is expressed in terms of speed-up factors with respect to a uniform flow field, and shows several effects:

- The identified wind speed fields for stable conditions deviate significantly from those in unstable conditions. As expected, in stable conditions intra-plant effects are generally more pronounced.
- For directions 0, 90, 120, 180, 330°, a speed up at the edges of the wind farm can be observed, which is described in literature as a “wall” or “edge” effect [3].
- For wind directions from the west a clear wind speed gradient can be observed, which is associated with the influence of the nearby coastline [4].
- In addition to the wind speed reduction caused by the turbine wakes, there seems to be a streamwise velocity decrease in the background flow field.

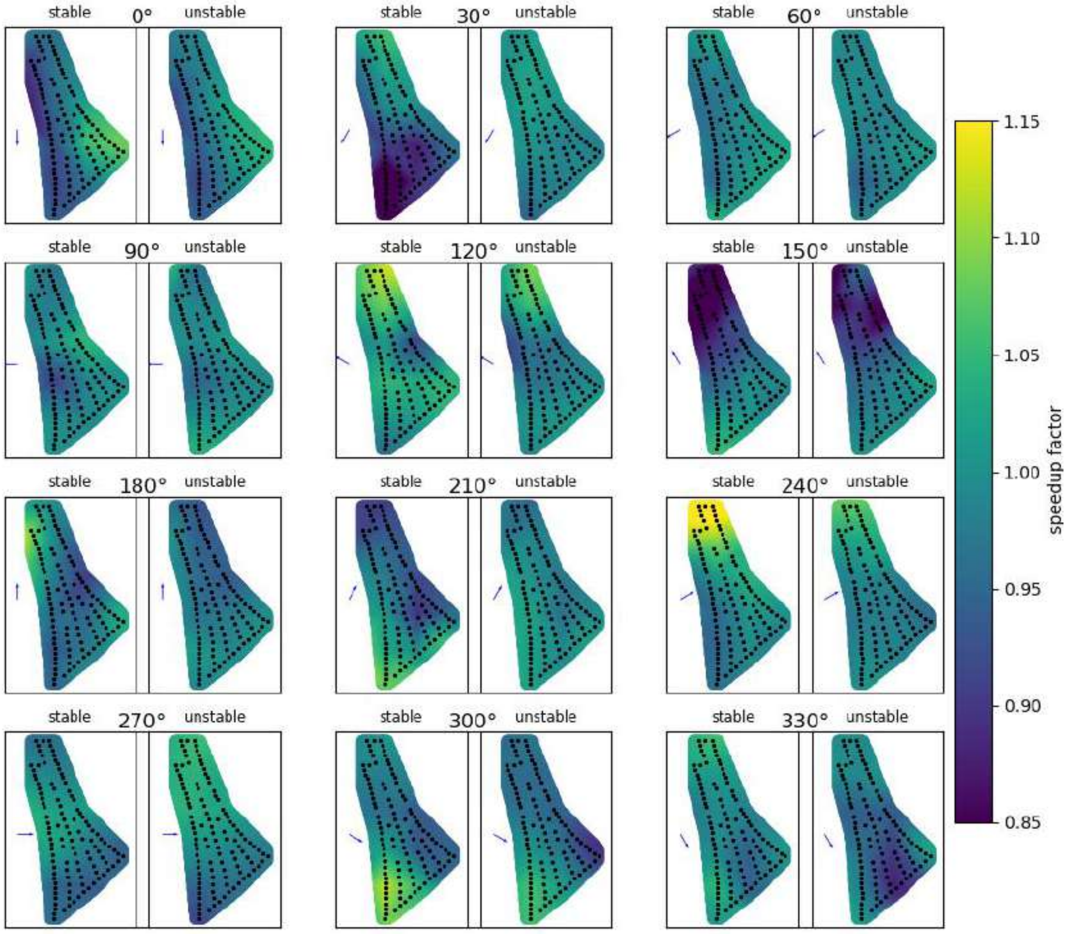

Figure 1 This plot provides an overview of the long-term wind speeds for all tuning directions with stable and unstable conditions. Different large-scale wind farm effects become apparent. For directions 0, 90, 120, 180, 330°: edge/wall effects. Directions 240° and 270°: Coastline effect. A deep array effect that can be observed especially for the high aspect ratio directions (North, South).

The identified flow corrections are very much in line with expectations, and lead to a very significant increase in the accuracy of the Floris-generated power predictions.
During the presentation, a more complete description of the methodology will be given, together with a deeper analysis of the results.

References

[1] Abkar, M. and Porté-Agel, F. 2015. Influence of atmospheric stability on wind-turbine wakes: A large-eddy simulation study. *Physics of Fluids* **27**, 3, 35104.

[2] Bottasso, C. L., Cacciola, S., and Iriarte, X. 2014. Calibration of wind turbine lifting line models from rotor loads. *Journal of Wind Engineering and Industrial Aerodynamics* **124**, 29–45.

[3] Mitraszewski, K., Hansen, K. S., Gayle Nygaard, N., and Réthoré, P.-E. 2013. Wall effects in offshore wind farms. *European Wind Energy Conference and Exhibition, EWEC 2013* 3, 1349–1358.

[4] Peña, A., Schaldemose Hansen, K., Ott, S., and van der Laan, M. P. 2018. On wake modeling, wind-farm gradients, and AEP predictions at the Anholt wind farm. *Wind Energ. Sci.* **3**, 1, 191–202.

[5] van der Laan, M. P., Peña, A., Volker, P., Hansen, K. S., Sørensen, N. N., Ott, S., and Hasager, C. B. 2017. Challenges in simulating coastal effects on an offshore wind farm. *J. Phys.: Conf. Ser.* **854**, 12046.

[6] Wu, K. and Porté-Agel, F. 2017. Flow Adjustment Inside and Around Large Finite-Size Wind Farms. *Energies* **10**, 12, 2164.

FOUNDATIONS
&
GEOTECHNICS

17th EAWE PhD Seminar on Wind Energy
3 – 5 November 2021
Porto, Portugal

Development of a real-time capable model to investigate coupled motions of work vessel and crane load during offshore wind turbine installation

Jannik Meyer[a], Arndt Hildebrandt[a]

[a] Ludwig-Franzius-Institute for Hydraulic, Estuarine and Coastal Engineering,
Leibniz University of Hannover
Nienburger Str. 4
D-30167 Hannover

E-mail: meyer@lufi.uni-hannover.de

Keywords: OWEC, Installation, Operation & Maintenance, Floating Structures

Extended Abstract

This contribution presents the development of a (semi-) analytical model to determine the coupled motion of installation ships and crane load. Two foci will be laid in the future: On the one hand, the real-time capable model will be developed based on the analytical equation of motion of floating structures. On the other hand, the input data for this analytical model will be generated by using results from potential theory while incorporating viscous effects by parametrized values from models tests and CFD investigations.
Both foci will be shortly explained in this extended abstract, starting with the (semi-) analytical model followed by the parametrization of the viscous effects.

To determine the motion of ships or other floating structures in real time, complex computational methods like potential theory models (e.g. Boundary Element Method, BEM) or even CFD models (e.g. Finite Volume Method, FVM) currently cannot be used due to their high computational demand. Thus, the most real-time models are based on the analytical equation of motion:

$$(m + a)\ddot{x} + b\dot{x} + cx = F(t) \tag{1}$$

with: Mass/Inertia m, added mass/inertia a, Damping b, Hydrostatic stiffness c and hydrodynamic force $F(t)$.
Solving this equation leads to amplitude and phase characteristics called the *Response Amplitude Operator* (RAO). The RAO is a frequency-domain presentation of a floating structure's motion characteristics in waves. To be able to use this information in a time domain model, which determines the structure's motion in irregular waves, this frequency-domain information is transformed into time-domain information called the *Impulse Response Function* (IRF) using an inverse FFT. The motion of the floating structure in waves will then be determined by a convolution integral of the IRF and the wave time series. This method has been developed by Cummins [1].
Currently, this model is developed for 1D motion, meaning that no coupling effects between single degrees of freedom (DOF) are considered. A comparison of the model with results from the commercial BEM solver *Ansys AQWA* is shown in Figure 1.

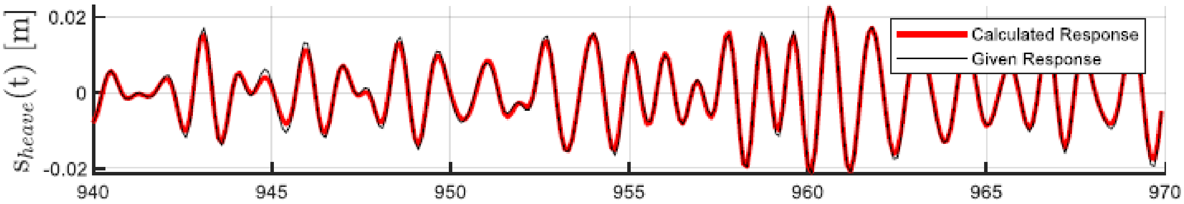

Figure 1: Comparison of the real-time model (red) with Ansys AQWA (black)

The next steps in the development of the model are an extension to a 6D-model that incorporates Eq. 1 not as a scalar equation but a matrix equation to include coupling between the DOFs. To include the influence of the crane, a further extension to a 8D-model is planned, with the crane motion as two further DOFs as shown in [2].
As Eq. 1 depicts a linear mass-spring-damper system, possible non-linearities will not be detected by the model. Thus, the inclusion of a non-linear extension based on the model of Ellermann & Kreutzer [3] will be investigated in the future.

The second focus of this work is the determination of the frequency-dependent hydrodynamic mass *a* and damping *b*, which will then be used in the real-time model. A first estimation of these coefficients will be derived by a BEM model. Additionally, the force vector *F(t)* and further quantities (e.g. body-to-body interactions by radiated wave field) are output from the BEM model and will be used in the real-time model. As BEM models are based on the potential theory, they do not consider viscous effects. This does lead to an underestimation of the damping, especially for DOFs with small wave radiation damping, like roll.
To incorporate viscous effects in the real-time model, existing approaches will be reviewed (e.g. the model of Ikeda for viscous roll damping [4] or the experimental values for added mass of simple structures by Newman [5]). Additionally, a new model data set will be generated using forced harmonic oscillation tests. Different model structures and attachments like heave plates or bilge keels will be investigated. Using this dataset, an OpenFOAM model will be validated using the experimental data. A snapshot of a model run is depicted in Figure 2.

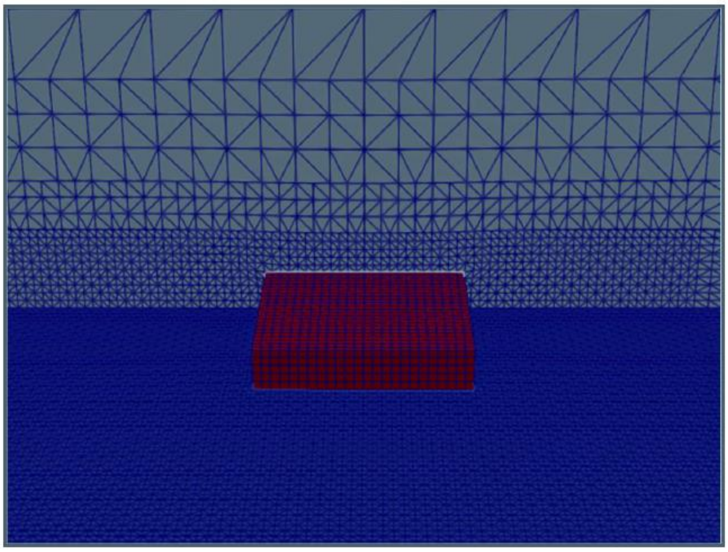

Figure 2: Snapshot of an OpenFOAM simulation of a heave decay test.

After validation, the model will be used to gain more detailed insights on the relationship between nearfield hydrodynamics (vortices, etc.) and the global coefficients of hydrodynamic mass and damping. Finally, these hydrodynamic coefficients will be parametrized using the findings from model tests and numerical simulations.

Bibliography

[1] Cummins WE 1962 The Impulse Response Function and Ship Motions. *Schiffstechnik* **47** 101-109
[2] Riekert T 1992 Die Dynamik von Schwimmkranen mit hängender Last. *Wilfer*
[3] Ellermann K, Kreuzer E 2003 Nonlinear dynamics in the motion of floating cranes *Multibody System Dynamics* **9(4)** 377–387
[4] Ikeda Y, Himeno Y and Tanaka N 1977 On eddy making component of roll damping force on naked hull *Journal of the society of Naval Architects of Japan* **142** 54-64
[5] Newman JN 1979 The Theory of Ship Motions *Advances in Applied Mechanics* **18** 221-283

Pore Pressure Response of Offshore Wind Turbine Structures

Rachel Keane

Department of Engineering Science, University of Oxford, Parks Road, Oxford, OX13PJ

E-mail: rachel.keane@bnc.ox.ac.uk

Abstract The offshore wind industry is playing a sizeable role in the fight to combat climate change. In efforts to minimise the cost of energy of offshore wind, optimisation of foundation design has come to the forefront of research. Previous design approaches used for offshore wind foundations were formed based on data from oil and gas platforms located offshore, which were low-height and static structures. Revision of monopile foundations to reflect the significant cyclic lateral loading of wind turbines due to incident wind and waves are required to maximise the efficiency of these structures for energy capture.

The soil surrounding the monopile provides resistance to environmental and operational loading imparted on the turbine structure at significant heights above the seabed. The pressure exerted on the soil matrix constantly fluctuates under cyclic loading. The soil matrix, made up of soil particles and seawater in the particle voids, reacts to these externally applied loads. The pressure of the fluid located in the voids is important to the maintenance of soil strength during loading activities. Rate effects of cyclic loading have the potential to generate pore pressures catastrophic to the wind turbine structure and require further investigation. Model testing is an economic way to emulate the full-scale pile-soil system and behaviours at a smaller scale. Through appropriate scaling of parameters and use of dimensional analysis, similitude can be achieved between model and prototype (field) scales. As larger diameter piles are required, effective modelling of monopiles in saturated sand will be carried out to investigate drainage conditions locally along the pile length and base, and effects of and influential factors on pore pressure accumulation will undergo further review.

Keywords: Offshore Wind Turbine Foundations; Geotechnics; Drainage Conditions; Pore Pressure Accumulation; Model Testing

1 Introduction

Climate change, and efforts to reduce carbon emissions, has resulted in a shift in the energy industry away from fossil fuels and towards renewable energy sources, like offshore wind. A more consistent wind resource in further offshore locations, makes offshore renewable technologies high yielding and favourable over onshore alternatives. Locating structures offshore requires increased design refinement as loading conditions are harsher than equivalent structures located onshore.

There are various foundation types for offshore wind turbines, including monopiles, tripod, caisson, jacket and floating. Currently, the most commonly used is the monopile [1]- a steel cylindrical tube driven into the seabed. The optimisation of monopile design for the offshore environment and wind turbine operational loads has the potential to reduce the cost of energy for the technology and spur further investment into the offshore wind sector.

2 Loading Conditions Typical of Offshore Wind Turbines

Offshore structures are subjected to cyclic loading imparted by strong winds and waves. For turbine structures that span great heights above the seabed, the incident wind and wave loadings test the lateral capacity of the foundation and surrounding soil. There is also cyclic loading of the structure due to the rotary movement of the blades involved in energy capture.

Previously, offshore foundation design codes were developed based on oil and gas platforms; these were low-height, static structures [2]. The design method, called the 'p-y' method, was developed based on data of flexible piles, or long and slender piles with a high L/D ratio. Offshore wind turbine piles are typically designed as rigid structures, with a low L/D ratio, due to a lower axial demand. Rigid piles differ in behaviour to flexible piles, as they develop a toe-kick under lateral loading and rotate rigidly about a point, whereas flexible piles deform by bending. The 'p-y' method typically accounts for cyclic loading effects by reduction of the ultimate lateral capacity, but no consideration is given to the accumulation of rotation or any changes in stiffness that may occur overtime. While ultimate capacity of any structure is a central consideration in design, so too is serviceability which may prove to be the more critical limit state for the design of offshore wind turbines. Installation methods, load characteristics and number of cycles are not included in standard pile design approaches, potentially resulting in an underestimation of pile displacements over the turbine's operational lifetime. Additionally, cyclic loading of the monopile causes constant fluctuation of the fluid pressure located in the pore space between adjacent soil particles which can affect the pile-soil response and warrants further attention.

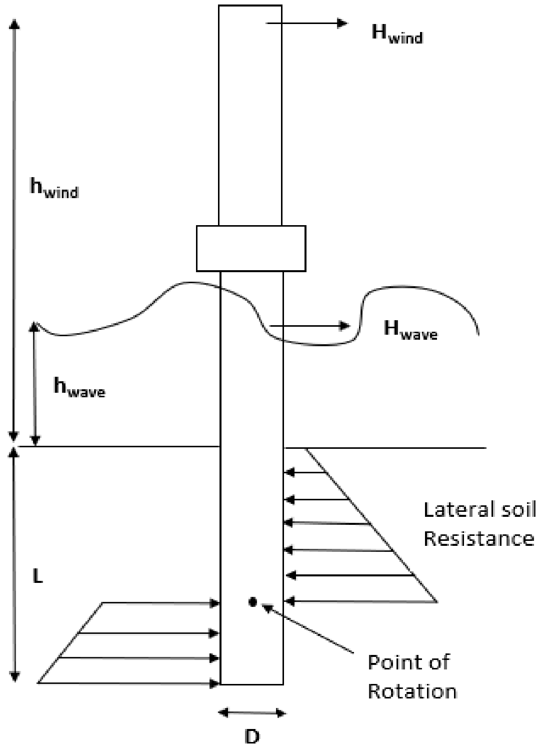

Figure 1 Loading conditions imposed on a monopile foundation supporting a typical offshore wind turbine.

3 Pore Pressure Response

3.1 Excess and Dissipation

When the soil matrix is in its initial stable state, the pore fluid pressure holds an equilibrium value called the hydrostatic pressure (u_s). Contact or effective stresses (σ') exist at the soil grain interfaces that together with pore fluid pressures make up the total stress in the soil matrix (σ). When external loading is applied to the ground, the pore fluid absorbs the total imparted stress on the matrix as water is incompressible, and the effective stresses remain unchanged initially. This increase or excess in pore fluid pressure (u_e) above the static value creates extra pressure in the voids and weakens contact stresses between adjacent particles. Thus, the effective stress, and soil strength are reduced while the pore pressures remain elevated.

Overtime, the excess pore pressure is transferred to the soil particles, and the pore pressure value reverts to its pre-loaded static value, as demonstrated in Figure 2(a). During excess pore pressure dissipation, consolidation occurs which results in a void volume reduction. Figure 2(b) displays this transfer of elevated pore pressure to effective stress in the time after loading, while a constant total stress is maintained. Undrained and drained behavioural bounds are also shown.

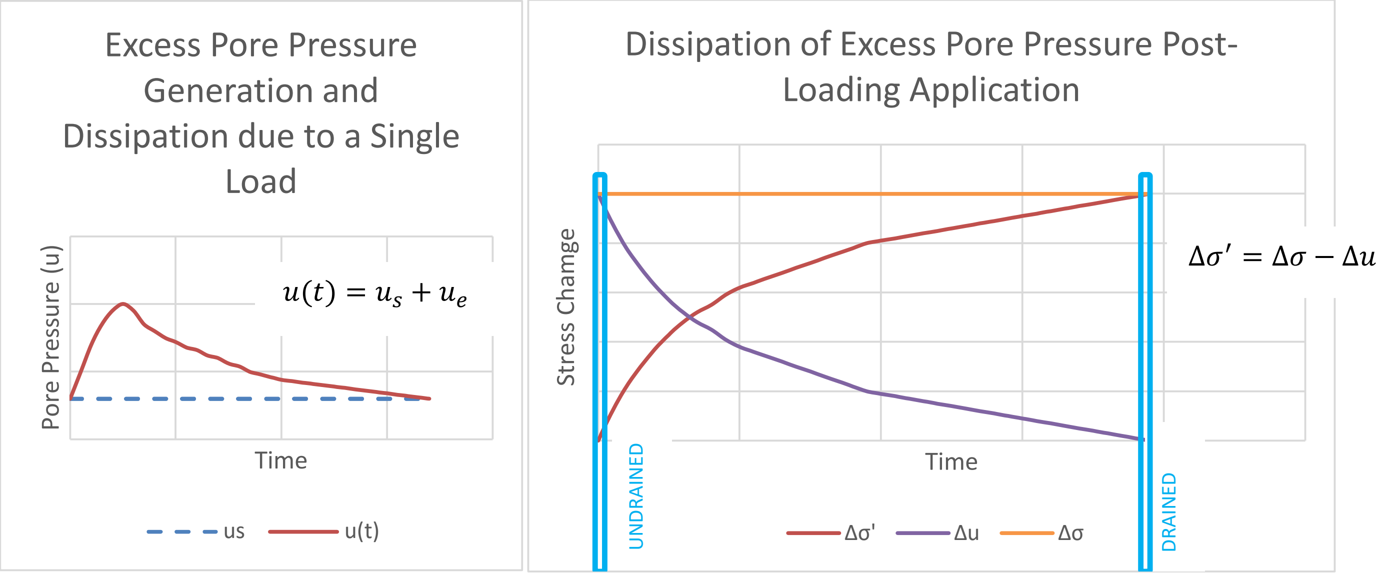

Figure 2 (a) Generation of excess pore pressure above static pressure due to the application of a single load. (b) Stress changes in time after load application in i) effective stress ii) pore pressure and iii) total stress.

Numerical investigations into the development of excess pore pressures in front of monopiles were undertaken by Cuellar [3] who modelled an increase in excess pore pressure at greater depths below the mudline, and closer to the monopile face. These observations were reaffirmed by similar numerical models and experimental validation carried out by Li, Zhang [4].

3.2 Drainage Conditions

A soil exhibits “drained” behaviour when the excess pore pressures dissipate instantaneously upon loading, and the soil skeleton absorbs the extra stress generated by the load. “Undrained” loading conditions exist when the transfer of excess pore pressures to effective stresses, generated upon loading, takes sufficient time after loading. “Partially-drained” soil behaviour exists in the period of time between undrained and drained conditions, when the transfer of extra stresses is ongoing between the pore fluid and the soil particles.

Sands typically demonstrate drained or partially drained conditions when loaded, due to its high permeability as a material. Monopiles installed in saturated sand induce an impermeable boundary and inhibits drainage of excess pore pressures generated during cyclic loading. As offshore monopile diameters increase further, the possibility of undrained behaviour in the surrounding soil is more likely. Zhu, Ren [5] carried out 1g model tests in saturated sand and found that fully and partially drained sands vary in response. This proves that drainage conditions affect pile performance in terms of bending, lateral resistance, and deflection, and possible undrained conditions should not be neglected. Investigation into the potential vertical and horizontal drainage paths in the surrounding soil of monopiles would also be of benefit.

3.3 Pore Pressure Accumulation

The dissipation of excess pore pressures may be incomplete between subsequent cycles of loading. Depending on the frequency of cycling, soil permeability and fluid properties, pore fluid pressures may not have sufficient time to fully revert to their static values and a build-up or accumulation of pore pressure could take place. Pore pressure accumulation weakens the soil's ability to resist shear and would greatly reduce the shaft frictional resistance of the pile-soil system. This could result in compromised serviceability of the turbine, or ultimate failure of the structure.

4 Model Testing

Model testing is a cost-effective method to emulate full-scale pile-soil behaviours in the lab. Appropriate scaling of parameters and dimensional analysis facilitates similitude between model and prototype (field) scales. In saturated sand model tests, pore fluid and sand material combination facilitate the modelling of drainage times realistic of the offshore environment. One way to model pragmatic drainage conditions is to use sand found in-situ with a pore fluid of increased viscosity, previously silicone oil has been used for this purpose. Alternatively, a sand of smaller particle size modelled with water as the pore fluid could also achieve desired drainage times. Model tests carried out at 1g on the laboratory floor are the simplest, most economic option, while more elaborate centrifuge model tests can be carried out at a chosen gravity level to reflect more realistic stress distributions of in-situ conditions. Reproduction of the prototype problem at model scale requires full similitude to ensure reliable results.

5 Outlook

Future work is required regarding pore fluid pressure response and drainage paths in the surrounding soil of cyclic laterally loaded monopiles. Sand material, pore fluid and pile properties must be carefully considered to ensure full similitude is achieved in the planned model tests. As offshore wind turbine sizes continue to grow, and their foundations increase in diameter, inhibited excess pore pressure drainage and potential accumulation may result in changes to the monopile response. Model testing of cyclic laterally loaded monopiles in saturated sand at lab scale will further current knowledge in this area of interest.

Bibliography

1. WindEurope (2019) Offshore Wind in Europe: Key trends and statistics. https://windeurope.org/wp-content/uploads/files/about-wind/statistics/WindEurope-Annual-Offshore-Statistics-2019.pdf.
2. API (American Petroleum Institute) (2010) RP2A-WSD- recommended practice for planning designing and constructing fixed offshore platforms, in Washington, DC, USA.
3. Cuellar P. (2011) Pile foundations for offshore wind turbines: Numerical and Experimental Investigations on the behaviour under short-term and long-term cyclic loading. PhD Thesis, Technischen Universitat Berlin.
4. Li S. et al (2019) Drainage conditions around monopiles in sand. *Applied Ocean Research*, 2019. **86**: p. 111-116.
5. Zhu B. et al (2021) Centrifuge modelling of monotonic and cyclic lateral behaviour of monopiles in sand. *Journal of Geotechnical and Geoenvironmental Engineering*. **147**(8).

NEW CONCEPTS

Robotic Lidar for Wind Measurements

Shahbaz Pathan[a], **Mikael Sjöholm**[a], **Jakob Mann**[a]

E-mail: shpa@dtu.dk

Keywords: Robotic Lidar, Signal Processing, Measurements

Abstract

Remote Sensing using Lidar provide a technique to measure wind speed, direction and other environmental parameters and hence is gaining interest day by day. For that purpose there is need of Lidar instrumentation that can steer on demand and can scan wind at higher degrees of freedom for further investigation of wind. So, in that connection, we have combined a 6 degrees of freedom Robotic arm with a Lidar. We are using a Robotic Arm by Universal Robots and Lidar (Lidic) developed by DTU. The automation of Robotic Arm is done by calculating its parameters and steering is done by creating the real time system level logic of transmission control algorithm and robot automation algorithm for motion of robotic arm in real time automation software. The Lidar (Lidic) is measuring the wind and signal conditioning of backscattered signals is performed in real time signal conditioning system.

The synchronization of robot position information with backscattered signals of lidar is done by transmitting the actual position information of robot to signal conditioning system by user datagram protocol (UDP) and the real time system level logic for transmitting and receiving UDP is created at both sides (Robot and Lidar). Before the deployment of robotic lidar for measurement the steering of the robot was tested through virtual machines (The steering signals were routed back to same system via internet protocol configuration and interference configuration protocol). The system developed is working properly and can be used for wind measurement applications on short ranges such as in wind tunnels.

Figure 1: Robotic Lidar

Bibliography

---

[a] DTU Wind Energy

[1] http://www.windscanner.eu

[2] https://www.msca-like.eu

[3] Mikael Sjöholm et al. (2017): Lidars for Wind Tunnels an IRP Wind Joint Experiment Project.14th Deep Sea Offshore Wind R&D Conference, EERA Deep Wind'2017, 1820 January 2017, Trondheim, Norway, Energy procedia (137), 2017, 339345.

---

[a] DTU Wind Energy

17th EAWE PhD Seminar on Wind Energy
3-5 November 2021
Porto, Portugal

Extended Definition of Efficiency for Vibration Energy Harvesters

Cristiano Martinelli[a], Andrea Cammarano[b], and Andrea Coraddu[a,c]

[a]Naval Architecture, Ocean & Marine Engineering, University of Strathclyde, U.K.
[b]James Watt School of Engineering, University of Glasgow, U.K.
[c]Department of Maritime & Transport Technology, Delft University of Technology, The Netherlands

Abstract

In the past decades, Vibration Energy Harvesters (VEHs) have received great attention from the scientific community. These devices are able to extract energy from environmental vibrations and from fluid-structure interactions. Several analytical models of VEHs have been proposed in the literature, but normally the energy analysis of such systems is neglected. The efficiency of the VEHs is based on energy contributions of the system and it is a crucial parameter for the optimisation of such devices. In literature, the proposed definitions of efficiency are often valid only for the specific analysed cases. In this paper, the authors are presenting a new methodology for the evaluation of the efficiency of VEHs. The methodology is based on the mechanical energy balance principle and aims to provide a mathematical definition of each energy contribution of the system at steady state condition. Firstly, the energy balance for a mechanical Single-Degree of Freedom (SDOF) system is presented and the mathematical representation of the efficiency is proposed. Then, the general definition is extended and applied to a Multi-Degrees of Freedom (MDOF) system. The energy balance approach can be applied to any VEH, thus, analytical and numerical applications for a Piezoelectric Energy Harvester (PEH) has been proposed. In the proposed case study, the simple cantilevered PEH is excited considering base excitement force. The variation of steady state energies and the associated efficiency have been analysed on the base of frequency highlighting the optimal conditions and the associated efficiency in the numerical applications. Finally, the general validity of the proposed energy analysis has been demonstrated by extending the efficiency definition to a Finite Element (FE) model developed with a commercial software.

Keywords: Energy Harvesting, Finite Element Analysis, Efficiency, Piezoelectric Transducers

1 Introduction

In the past decades, VEHs have been deeply investigated by the scientific community because of their ability to scavenge energy from environmental vibrations [1]. These devices can exploit different energy conversion systems to transform the mechanical energy into electrical energy; between them, piezoelectric, electromagnetic and electrostatic energy transducers are widely adopted [2, 3, 4]. Usually, VEHs find an application for powering devices located in remote locations where cables cannot be used and chemical batteries are not able to guarantee the required lifespan [5, 6]. In order to operate at the optimal condition, the harvester has to be optimised both from the electrical and mechanical point of view [7, 8]. The optimisation process tries to compare different possible configurations of the same device; in that context, the figures of merit can be adopted to perform such comparison [9, 10]. Many figures of merit have been proposed in literature: between them, the efficiency is one of the most crucial parameter for the performance evaluation of the energy harvesters [11, 12]. Richard et al. [13] investigated the efficiency for a micro-scale PEH. The authors provide a definition of the efficiency based on the Butterworth–van Dyke circuit model demonstrating that the efficiency depends on the electro-mechanical coupling and the quality factor. Shu et al. [14] studied the energy conversion efficiency for a rectified PEH and provided a definition of the efficiency for steady-state operation conditions. Their findings suggest that for weak electro-mechanical coupled systems, the optimal power transfer is achieved when the efficiency and electrical damping reach their maximum values, while for strongly coupled system, those parameters cannot be optimised at the same time. Kim et al. [15] proposed a closed form solution to compute the efficiency of a base excited bi-morph PEH with the additional base displacement degree of freedom [16]. The authors demonstrated that the optimal loading condition for power output is quite different from the optimal condition for efficiency, thus the system optimisation can be only achieved by considering a multi-objective optimisation approach. Recently, Yang et al. [12] proposed a definition of efficiency for a PEH. The system has been mathematically described by means of a lumped parameter model and the excitation has been provided from base excitement. The authors demonstrated that the efficiency depends on the phase shift between the input force and the structural response of the system and finally, they validated experimentally the proposed definition.

In all the previous examples [13, 14, 15, 12], the mathematical definition of the efficiency accounts for the specific electrical and mechanical conditions considered in the simplified model, generally described by means of a lumped mechanical SDOF model. Based on the knowledge of the authors, no general definition of the efficiency has been provided in literature, especially for complex mechanical MDOF systems or FE model.

In this paper, the authors propose a general approach to identify the steady-state energy contributions and the efficiency of VEHs, regardless the complexity and number of degree of freedom involved in the model definition. The procedure is developed and tested for PEH, but it can easily be expanded to other energy transformation mechanism, like the electromagnetic one. The energy contributions are obtained under the assumption of harmonic loading and steady state conditions and the efficiency is represented by the ratio between the input and output energy of the system over a cycle.

Moreover, the global efficiency is defined on the base of three energy conversions [12]. Firstly, the energy is transferred from the source to the VEH by means of mechanical vibrations (mechanical to mechanical energy conversion). Subsequently, mechanical to electrical energy conversion occurs in the transducer. During this transformation some energy is lost as heat due to phenomena like structural damping or air drag. The final transformation accounts for the losses which occur in the electrical circuit like Joule effect which, again, wastes energy under heat form (electrical to electrical energy conversion). Nonetheless, for the sake of simplicity, the authors have accounted only for the first two transformations, neglecting any kind of heat losses in the energy conversions. Nevertheless, the proposed efficiency definition does not lose generality since it is based on the energy balance principle and it can possibly be extended to complex system which account for more complex effects like the heat losses. The rest of the paper is organised as follows: Section 2 presents the theory behind the definition of the efficiency adopted and the application of the energy balance. Section 3 presents numerical examples of the methodology outlined in the previous section and discusses about the implications of the proposed energy balance and efficiency definition. Finally, Section 4 summarises the results and describes the conclusions of the paper.

2 Analysis and Methodology

2.1 Analytical Approach for the Efficiency Definition of VEHs

The general definition of the efficiency can be achieved by starting from a VEH model. In this case, a PEH system has been chosen and the associated representation is reported in Figure 1.

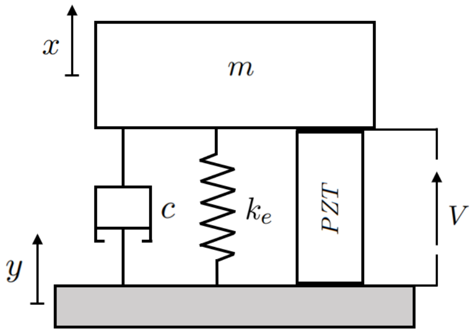

Figure 1: Piezoelectric energy harvester excited with base acceleration.

The PEH can be represented in its simplest form with a lumped parameter model which accounts only for the first mode-shape, thus considering only one mechanical Degree of Freedom (DOF). An additional electrical DOF is considered to account for the piezoelectric circuit. In this context, m represents the mass, c represents the mechanical damping and k_s represents the mechanical stiffness. Such model has been widely adopted in literature and it can be mathematically represented as described by Guyomar et al. [17] and by Leufeuvre [18]:

$$m\ddot{z} + c\dot{z} + k_e z + \alpha V = -m\ddot{y} \tag{1a}$$

$$I = \alpha\dot{z} - C_0\dot{V} \tag{1b}$$

where I represents the current in the equivalent piezoelectric circuit , V represents the voltage electrical degrees of freedom, z represents the mechanical degrees of freedom which is computed as relative displacement of the mass m from the base: $z = x - y$, k_e is the effective stiffness of the system which accounts for both the mechanical stiffness k_s and the piezoelectric stiffness at short-circuit condition k_{pe}, α is the force factor, and C_0 is the clamped capacitance.

In the simplest case, a single resistance is applied on the piezoelectric dipoles to create a very basic circuit. Under this condition, the current I can be mathematically substituted by V/R, according to the Ohm's law. Under the assumptions of steady-state condition and harmonic loading, it is possible to obtain the power balance of the system by multiplying, respectively, the mechanical part of Equation 1 by the relative speed $\dot{z}$ and the electrical part of the same equation by the voltage V. Then, to obtain the energy balance, the two equations have to be integrated over the half-period $T = \frac{2\pi}{2\Omega}$, where Ω is representing the forced frequency and t the time. Now, substituting the common terms and simplifying the equations, it is possible to obtain a single equation representing the energy balance. Moreover, the energy contributions associated to conservative forces like kinetic energy $\int m\ddot{z}\dot{z}\,dt$, elastic potential energy $\int k_e z\dot{z}\,dt$ and electric potential energy $\int C_0\dot{V}V\,dt$ have a net zero energy contribution over the half period, thus, the integral equation can be reduced as follows:

$$\int c\dot{z}^2\,dt + \int \frac{V^2}{R}\,dt = \int -m\ddot{y}\dot{z}\,dt \tag{2}$$

where the survived terms represent respectively, the dissipated energy per cycle due to the mechanical damping E_{diss}, the dissipated energy per cycle associated to the resistor E_{out}, thus the system energy output, and the input energy of the system E_{in}. Now, developing the integrals, it is possible to obtain the final steady-state energy balance:

$$\frac{\pi}{2}c\Omega|Z|^2 + \frac{\pi|V|^2}{2\Omega R} = \frac{\pi}{2}m\ddot{Y}|Z|sin(\varphi) \tag{3}$$

where $|\bullet|$ represents the amplitude of $\bullet$ and $\ddot{Y}$ is the constant base acceleration. The ratio between the amount of energy produced and the amount of energy introduced in the system per cycle represents the efficiency η:

$$\eta = \frac{E_{out}}{E_{in}} = \frac{|V|^2}{\Omega R m\ddot{Y}|Z|sin(\varphi)} \tag{4}$$

Even if it is possible to further develop the definition of the efficiency, the authors aim to present such definition as general as possible, thus no further simplifications have been applied to Equation 4.

The energy output E_{out} is strictly dependant on the structural response of system and on the equivalent electric circuit: in this simple case the main circuit parameter is the resistance, thus the power output is strictly dependant on its value. On the other hand, it is worth to notice that the energy input is dependant on the phase shift φ between the mechanical input and the system response as highlighted by Equation 3. These results agree with those obtained by Yang et al. [12]. From the physical point of view, the proposed model behaves as a simple linear mechanical oscillator which, for its nature, is able to perfectly balance the kinetic and potential energy at resonance. In this condition, the more energy is provided to the system the larger is the amount of energy stored by the oscillator. Mathematically speaking, this happens when $sin(\varphi) = 1$. Out of resonance, when $sin(\varphi) < 1$, the kinetic and potential energies are not perfectly balanced anymore and the system is not able to receive all the energy provided by the external environment, therefore it returns a portion of energy, reducing its performance.

2.2 Matrix Approach for the Efficiency Definition of VEH

In this Section, the energy balance and the efficiency definition for PEH are mathematically described adopting a matrix approach. This approach allows to extend the previously outlined methodology to MDOFs systems. The energy balance is obtained by starting from the PEH harvester described by Figure 1. First of all, the Equation of Motion (EoM) of the energy harvester is rewritten as follows:

$$\begin{bmatrix} m & 0 \\ 0 & 0 \end{bmatrix} \begin{Bmatrix} \ddot{z} \\ \ddot{V} \end{Bmatrix} + \begin{bmatrix} c & 0 \\ -\alpha & C_0 \end{bmatrix} \begin{Bmatrix} \dot{z} \\ \dot{V} \end{Bmatrix} + \begin{bmatrix} k_e & \alpha \\ 0 & \frac{1}{R} \end{bmatrix} \begin{Bmatrix} z \\ V \end{Bmatrix} = \begin{Bmatrix} -m\ddot{Y} \\ 0 \end{Bmatrix} \tag{5}$$

Or more generally:

$$[M]\{\ddot{u}\} + [C]\{\dot{u}\} + [K]\{u\} = \{F\} \tag{6}$$

where, $[M]$,$[C]$ and $[K]$ are respectively the generalised mass, damping and stiffness matrices, $\{F\}$ is the generalised force vector and $\{u\}$ is representing the system's DOFs. Again, in order to reach a power balance equation, the same approach adopted in Section 2.1 is applied in matrix form. The steady-state energy contributions can be computed by integrating over half-period time. In this case the energy contributions are just four, as reported by Equation 7:

$$\int \{\dot{u}\}^T[M]\{\ddot{u}\}\,dt = -\frac{i\Omega^2\pi}{4}[\{U\}^T[M]\{\bar{U}\} - \{\bar{U}\}^T[M]\{U\}], \tag{7a}$$

$$\int \{\dot{u}\}^T[K]\{u\}\,dt = \frac{i\pi}{4}[\{U\}^T[K]\{\bar{U}\} - \{\bar{U}\}^T[K]\{U\}], \tag{7b}$$

$$\int \{\dot{u}\}^T[C]\{\dot{u}\}\,dt = \frac{\Omega\pi}{4}[\{U\}^T[C]\{\bar{U}\} + \{\bar{U}\}^T[C]\{U\}], \tag{7c}$$

$$\int \{\dot{u}\}^T\{F\}\,dt = \frac{i\pi}{4}[\{U\}^T\{\bar{F}\} - \{\bar{U}\}^T\{F\}], \tag{7d}$$

where $\{U\}$ is the complex steady state solution and $\{\bar{U}\}$ is the complex conjugated steady state solution at the excitement frequency Ω. It is worth to notice that the contribution of the generalised mass and the stiffness matrix is zero only if the matrix is symmetric. This means that non-symmetric matrices could create a net energy contribution in the energy balance over one cycle. Nevertheless, if necessary, it is possible to separate the symmetric and non-symmetric contribution of those matrices. This can allow to distinguish each energy contribution and finally obtain the efficiency. By referring to the analysed PEH, the efficiency can be defined as:

$$\eta = \frac{E_{out}}{E_{in}} = \frac{[\{U\}^T[K]\{\bar{U}\} - \{\bar{U}\}^T[K]\{U\}}{[\{U\}^T\{\bar{F}\} - \{\bar{U}\}^T\{F\}]} \tag{8}$$

It is interesting to notice that this definition agrees with the results proposed by Kim et al. [15] since the efficiency is not only dependant on the mechanical properties of the system but also depends on the electrical ones. Indeed, the Equation 8 accounts for the complex steady state solutions and the electric properties of the system including the force factor α and the resistance R. Moreover, it can be mathematically proven that the definition of the efficiency obtained from the first classical analytical approach and the second matrix approach lead to the same expression if the steady state solutions of the same model are considered.

3 Applications and Numerical Example

3.1 Efficiency and Energy Balance for Analytical Models of Piezoelectric Energy Harvester

This section describes numerical examples and practical applications of the methodology outlined in Section 2. In particular, the piezoelectric energy harvester described in Section 2.1 is now numerically analysed. Additionally, the system is modified to implement a supplementary mechanical DOF which can be realised by adding a dynamic absorber on top of the PEH. It is worth to notice that the first definition of efficiency provided by Equation 4 does not hold anymore when the system is modified. Indeed, even small changes in the mathematical model could lead to the reformulation of the energy contributions and efficiency. In general, according to procedure outlined in Section 2.1, the argument of the integral changes every time that the EoM changes: sometimes the change is minor and allows to obtain easily the reformulation of the efficiency while, in other cases, the change could end to require the complete reformulation of one or more energy contributions. This problem can be overcome by adopting the matrix approach of Section 2.2: the integrals are solved in the matrix form, therefore any modification of the EoM does not affect the results of the integrals. This allows to keep the definition of Equation 8 still applicable even for the modified PEH.

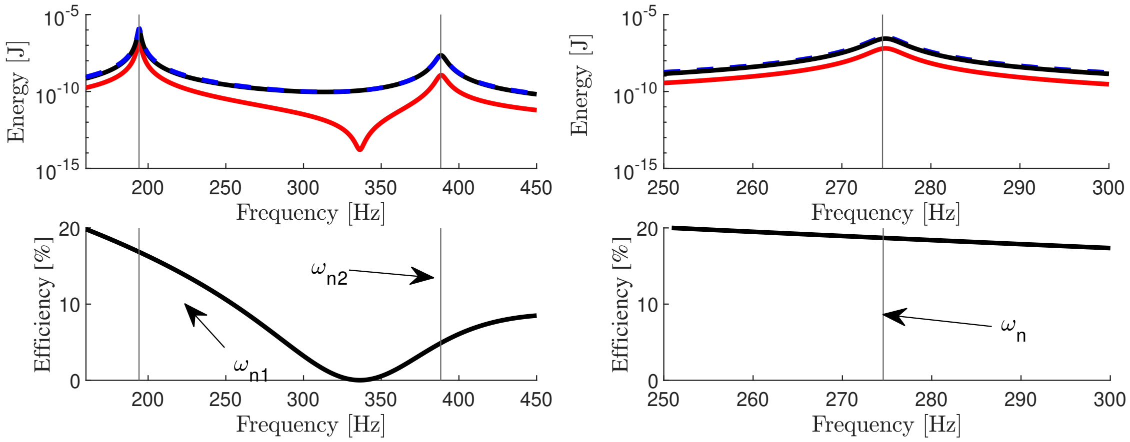

Figure 2: Efficiency and energy contributions trends - modified PEH (left) and original PEH (right).

Figure 2 shows the ability of the method to deal with MDOF systems and reports the trends of the efficiency and energy contributions against the frequency for the original and modified PEH. The blue dashed line is representing the input energy while the red and black lines are respectively the output energy and the energy dissipated by damper. The data adopted have obtained by [19] with a resistance value $R = 30,000\ \Omega$ and a constant acceleration $\ddot{Y} = 1\ m/s^2$. For the modified case, the following additional elements have been adopted: $m_2 = m/2$, $c_2 = c/2$ and $k_2 = k_e/2$. In the modified case, the system has two mechanical degrees of freedom, thus, the energy contributions show two peaks as reported in Figure 2. The second peak is evident also in the efficiency plot: this is due by the presence of an anti-resonance of the first mass m which reduces its oscillations and therefore the associate power output. When the anti-resonance is overcome, the system produces again some energy and the efficiency grows. As expected the efficiency is larger at the first resonance and lower at the second resonance. This is due by the higher amplitude oscillations induced by the first mode on the two masses. Conversely, second resonant peak is associated with a lower amplitude response, thus the piezoelectric crystal is less stressed and, therefore, less energy is produced. In both cases, the maximum energy production coincides with the first resonance: Figure 2 shows that high efficiency can occurs out of resonance where the output energy is very low. Therefore, as remarked in literature [12, 11], the value of efficiency should be considered only near to the resonance condition where the power and energy output are high enough to justify the implementation of the efficiency.

3.2 Efficiency and Energy Balance for Finite Element Models of Piezoelectric Energy Harvester

In literature, VEHs are generally represented with mechanical SDOF systems or analytical distributed parameters models [20, 21, 15, 18, 9, 14, 17]. Sometimes, FE models of VEHs are developed to analyse complex shapes which cannot be analysed with the simple approximated models [8, 22]. The matrix approach outlined in Section 2.2 can deal with FE models and it can be adopted to analyse the steady-state energy balance and compute the efficiency of the system.

In this case study, a PEH has been modelled in the commercial finite element software ANSYS [23]: SOLID45 elements have been adopted to describe the behaviour of the sub-structural material and tip mass, while SOLID5 elements have been embedded in the FE model to take into account the piezoelectric effect. In order to estimate the power production a simple resistor has been added to the piezoelectric by means of a CIRCU94 element. The piezoelectric, elastic anisotropic and dielectric matrices adopted in the FE computation are associated to PTZ-5H material [24]. The main dimensions adopted for the FE model are reported in the following table:

Finite Element PEH				
Parameter	Structure (Steel)	PTZ-5H	Tip Mass (Steel)	Unit
Length	60.0×10^{-3}	40.0×10^{-3}	8.0×10^{-3}	m
Width	20.0×10^{-3}	20.0×10^{-3}	20.0×10^{-3}	m
Thickness	1.8×10^{-3}	0.4×10^{-3}	4.0×10^{-3}	m
Resistance	$-$	10×10^3	$-$	Ω

Table 1: Data adopted in the FE model.

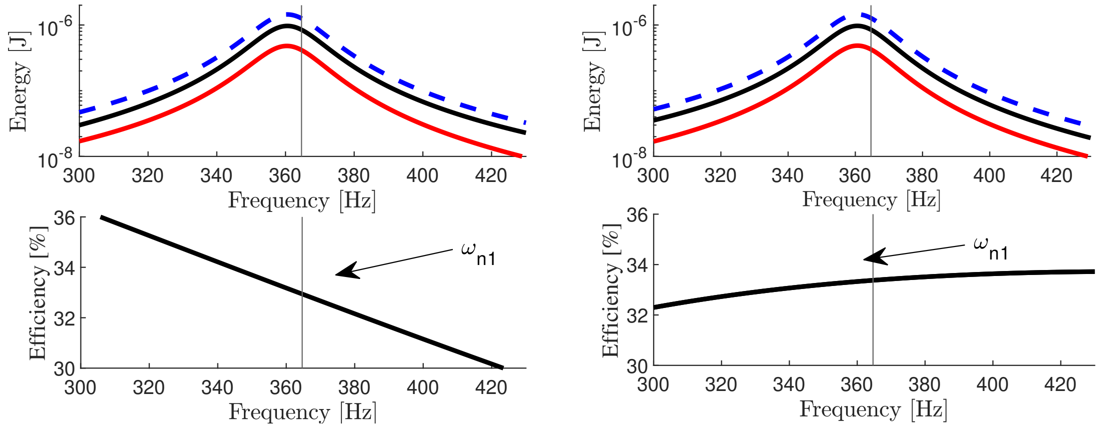

Figure 3: Energy contributions and efficiency for the PEH base excited with viscous Rayleight damping model (left) and structural damping (right). The vertical constant acceleration adopted is equal to 4.35 m/s^2, the coefficient β is equal to 1.78×10^{-5} and a constant structural damping equal to 0.02

The system is mechanically excited by imposing a sinusoidal acceleration with fixed amplitude along the Z direction. Finite element software, like ANSYS, allows to export the global stiffness, mass and damping matrices which can be easily implemented in the matrix energy balance formulation of Equation 7 and in the subsequent efficiency definition. In general, the energy contributions depends on the system definition: FE modelled with ANSYS builds the EoM by assembling all the contributions in three global matrices which are respectively the global mass, damping and stiffness matrices M_g, C_g and K_g, and the global load vector F_g. More than one model contribution can be assembled in the same global matrix, thus, it is necessary to separate the matrix contributions to properly obtain the associated energy over one cycle. In this case study, the complete EoM can be represented by Equation 9 [23]:

$$\begin{bmatrix}[M_s] & [0]\\ [0] & [0]\end{bmatrix}\begin{Bmatrix}\{\ddot{x}_s\}\\ \{\ddot{x}_e\}\end{Bmatrix}+\begin{bmatrix}[C_v] & [0]\\ [0] & [-C_{vh}]+\frac{1}{\Omega^2}[C_r]\end{bmatrix}\begin{Bmatrix}\{\dot{x}_s\}\\ \{\dot{x}_e\}\end{Bmatrix}+ \\ +\begin{bmatrix}i[C_s]+[K_s] & [K_z]\\ [K_z]^T & [-K_d]\end{bmatrix}\begin{Bmatrix}\{x_s\}\\ \{x_e\}\end{Bmatrix}=\begin{Bmatrix}\{F_a\}\\ \{L_a\}\end{Bmatrix} \qquad (9)$$

where $[M_s]$ represents the structural mass matrix, $[C_v]$ and $[C_s]$ represents the viscous and structural damping matrices, $[K_s]$ represents the structural stiffness matrix, $[C_{vh}]$ represents the dielectric damping matrix, $[K_z]$ represents the piezoelectric coupling matrix, $[K_d]$ represents the dielectric permittivity matrix, $[C_r]$ represents the electric damping matrix, $\{F_a\}$ represents the structural load vector, $\{L_a\}$ represents the electrical load vector. Finally, $\{x_s\}$ and $\{x_e\}$ represents the structural and electrical DOFs vectors. In this case, the efficiency can be computed by considering the energy contribution over a cycle associated to the electric damping matrix $[C_r]$ and the input energy created by the structural loads $\{F_a\}$. Even if the efficiency definition is slightly different from Equation 8 the approach does not lose generality since the energy contribution associated to matrix $[C_r]$ and to vector $\{F_a\}$ can be easily computed by adopting Equation 7. Moreover, in this case, it would be very difficult to obtain an explicit analytic representation of the input energy because of its dependence on all the active DOFs. Therefore, the matrix approach results in a much more convenient, simple and effective way to compute the energy contributions and the efficiency of such complex model. The final definition of the efficiency is:

$$\eta = \frac{\frac{\pi}{4\Omega}[\{U\}^T[C_r]\{\bar{U}\} + \{\bar{U}\}^T[C_r]\{U\}]}{\frac{i\pi}{4}[\{U\}^T\{\bar{F}_a\} - \{\bar{U}\}^T\{F_a\}]} \tag{10}$$

Lumped parameter models describe the energy harvesters with a certain degree of approximation; conversely, the FE models represent a more accurate way to describe the physical phenomena behind the VEH. In this context, the authors aim to highlight the ability of the matrix approach to determine the energy contributions per cycle and the efficiency of the system. To do that, two cases have been considered in this paper: in the first one the FE PEH adopts a pure viscous damping model while in the second one the system accounts for the structural damping model. Even if the best way to represent the damping is an hybrid model, the dichotomy of the two cases allows to highlight the effect of damping on the efficiency and on the energy dissipation. However, the considered cases represent only a small portion of the possible analyses that can be done on the energy exchanges in VEHs.

As described by Figure 3, when the viscous model is applied, the efficiency shows a very similar behaviour to the previous analytical case, with an almost monotonic decreasing around the first natural frequency. On the contrary, when the structural damping model is applied, the efficiency is growing around the first resonance. Thus, the difference in the trend is due to the damping model adopted: indeed, in the proposed model, the energy dissipation occurs only through the damping. The comparisons shown in Figures 3 have been carried out considering the excitation parameters and damping coefficients tuned so that the maximum power output and the maximum tip displacement are equal.

Finally, the majority of the mathematical models adopted in the literature are very similar to the ones analysed in this paper (e.g. similar PEH analytical models are described in [21, 18, 14, 17] and similar PEH FE models are adopted in [25, 8, 22], thus, this fact is giving great importance to the results reported in this work.

4 Conclusion

This paper investigated the definition of the efficiency based on the energy balance under the assumptions of steady-state conditions and harmonic loading. The efficiency is an important figure of merit which has to be accounted in the majority of the optimisation for VEHs. Moreover, it is an extremely important measure to compare different harvesters and it could help to standardise these systems for future industrial applications.

In this work, the authors have proposed a simple but effective definition for the efficiency which is able to deal with analytical MDOF systems and FE models. The analysis showed that the energy balance in matrix form is a very good tool to analyse the energy contributions of the system and allows to read the performance of the VEHs under the energy point of view. One interesting result of this analysis is the effect of damping model on the energy balance and efficiency. The analysis showed that the adoption of different damping models could change the efficiency, especially outside of resonance. Finally, a comparison between the harvested energy per cycle and the efficiency has been carried out: the energy per cycle and power output outside the resonance is too low in the most cases to justify even an high efficiency, in fact, as is commonly accepted in literature, the efficiency is a good metric for the VEHs only around the resonance where the power output is large enough to consider the effect of the efficiency.

References

[1] Wei C and Jing X 2017 *Renewable and Sustainable Energy Reviews* **74** 1–18

[2] Maamer B, Boughamoura A, Fath El-Bab A, Francis L and Tounsi F 2019 *Energy Conversion and Management* **199** 111973

[3] Beeby S P, Tudor M J and White N M 2006 *Measurement Science and Technology* **17** R175–R195

[4] Khan A, Abas Z, Soo Kim H and Oh I K 2016 *Smart Materials and Structures* **25** 053002

[5] Knight C, Davidson J and Behrens S 2008 *Sensors* **8** 8037–8066

[6] Adu-Manu K S, Adam N, Tapparello C, Ayatollahi H and Heinzelman W 2018 *ACM Transactions on Sensor Networks* **14** 10:2–10:50

[7] Wickenheiser A and Garcia E 2010 *Journal of Intelligent Material Systems and Structures* **21** 1343–1361

[8] Caetano V and Savi M 2021 *Journal of Intelligent Material Systems and Structures*

[9] Liu W, Badel A, Formosa F and Wu Y 2015 *Smart Material and Structures* **24** 125012

[10] Beeby S P, Torah R N, Tudor M J, Glynne-Jones P, O'Donnell T, Saha C R and Roy S 2007 *Journal of Micromechanics and Microengineering* **17** 1257–1265

[11] Aboulfotoh N and Twiefel J 2018 *Applied Sciences (Switzerland)* **8** 1075

[12] Yang Z, Erturk A and Zu J 2017 *Extreme Mechanics Letters* **15** 26–37

[13] Richards C, Anderson M, Bahr D and Richards R 2004 *Journal of Micromechanics and Microengineering* **14** 717–721

[14] Shu Y C and Lien I C 2006 *Journal of Micromechanics and Microengineering* **16** 2429–2438

[15] Kim M, Dugundji J and Wardle B L 2015 *Smart Materials and Structures* **24** 055006

[16] Kim M, Hoegen M, Dugundji J and Wardle B L 2010 *Smart Materials and Structures* **19** 045023

[17] Guyomar D, Badel A, Lefeuvre E and Richard C 2005 *IEEE Transactions on Ultrasonics, Ferroelectrics, and Frequency Control* **52** 584–594

[18] Lefeuvre E, Badel A, Richard C, Petit L and Guyomar D 2006 *Sensors and Actuators, A: Physical* **126** 405–416

[19] Guyomar D, Sebald G and Kuwano H 2011 *Journal of Intelligent Material Systems and Structures* **22** 415–420

[20] Aboulfotoh N and Twiefel J 2018 *Mechanical Systems and Signal Processing* **106** 1–12

[21] Erturk A and Inman D J 2008 *Smart Material and Structures* **17** 065016

[22] Townsend S, Grigg S, Picelli R, Featherston C and Kim H A 2019 *Journal of Intelligent Material Systems and Structures* **30** 2894–2907

[23] ANSYS Inc 2020 *Academic Research - Help System, Release 2020 R1*

[24] Jiashi Y 2006 *Analysis of Piezoelectric Devices* (Singapore: World Scientific)

[25] Upadrashta D and Yang Y 2015 *Smart Materials and Structures* **24** 45042

17^{th} EAWE PhD Seminar on Wind Energy
3-5 November 2021
Porto, Portugal

Influence of Clump Weights on Floating Wind Turbine Shared Mooring Line Tension

E M Schmitt[a] and M Muskulus[a]

[a]Norwegian University of Science and Technology NTNU, Department of Civil and Environmental Engineering

E-mail: `eva.m.schmitt@ntnu.no`

Keywords: Shared Mooring Lines, FOWT, Clump Weights, Mooring Line Tension

1 Introduction

For future floating wind farms, shared mooring lines offer the potential of cost reduction, as their implementation reduces the total mooring line length and number of anchors. However, being connected to multiple moving floaters simultaneously, high tension fluctuations can arise in shared mooring lines [1], leading to decreased fatigue life. Clump weights have been shown to reduce tension in FOWT mooring lines near the critical fairlead position [2].

The current study investigates, how the implementation of clump weights in a FOWT configuration with shared mooring lines impacts the mooring line tension.

Therefor, a case study is conducted: A semi-submersible FOWT, in a configuration of the Life50+ Nautilus-10 platform with the DTU 10MW reference wind turbine, is simulated with regular catenary chain mooring system, as well as in a typical shared mooring line configuration, and in a shared mooring configuration with clump weights. An optimization is carried out, to determine the optimal location of the clump weights, with respect to tension reduction.

The mooring line tensions are calculated using the software MoorDyn and the motion of the FOWT is solved as a simple mass-spring-damper system with one degree of freedom (surge). Wind and wave loads are applied in a simplified manner via the Actuator Disk Model and Morison's Equation respectively.

References

[1] Hall M and Connolly P 2018 *Volume 10: Ocean Renewable Energy* (Madrid, Spain: American Society of Mechanical Engineers) p V010T09A087 ISBN 978-0-7918-5131-9 URL

[2] Bruschi N, Ferri G, Marino E and Borri C 2020 *Energies* **13** 6407 ISSN 1996-1073 URL `https://www.mdpi.com/1996-1073/13/23/6407`

Structural analysis of a V-shape VAWT for different blade lengths

Adriana Correia Da Silva[a], Michael Muskulus [a]

[a] Department of Civil and Environmental Engineering, Norwegian University of Science and Technology (NTNU), Trondheim, Norway

E-mail: adriana.c.d.silva@ntnu.no

Keywords: VAWT, Multi-body solver, structural analysis

1 Introduction

The applicability of vertical axis wind turbines (VAWT) for offshore sites is emerging as an alternative that addresses the expensive challenge of installing and maintaining heavy equipment at great heights on the multi-megawatt horizontal axis wind turbines (HAWT). Benefiting from a lower centre of gravity, VAWTs have reduced gravitational fatigue loads and lower overturning moments - being more stable in floating platforms applications [1]. Also, the lower position of the generator, drive train and gearbox allow simpler installation and maintenance.

Different rotor configurations of VAWT have already been considered [2]. However, some disadvantages may be addressed to make VAWT commercial competitive. As the peak inefficiency occurs at lower tip speed ratios, a higher torque on the drive train is required to guarantee the maximum power production. This can affect the longevity of the main shaft and requires heavier drive train components [3]. Moreover, the lower aerodynamic efficiency influences the interest in developing VAWTs.

This work focusses on a V-shape configuration of a VAWT, that associate the benefits of lower-level drive train components with a reduced ratio between weight of structure and swept area. The impact on the stress distribution due to the increase of the blade length on a V-rotor VAWT will be evaluated.

The aerodynamic loads are calculated by an algorithm based on the Double Multiple Stream Tube model proposed by [4] and provided in terms of the blade element azimuthal and longitudinal position. Only normal operational conditions will be considered.

A flexible multi-body solver will used to perform the stress analysis. The blade cross-sections properties are represented by beams elements and the relative profile distribution is maintained constant with the increase in the blade length. The variation on the stresses is presented and discussed. The contribution from aerodynamic, centrifugal and gravity loads to the total overturning moment will also be presented.

Bibliography

[1] Tjiu, Willy et al., 2015. Darrieus vertical axis wind turbine for power generation II: Challenges in HAWT and the opportunity of multi-megawatt Darrieus VAWT development. Renewable energy, 75, pp.560–571.

[2] Tjiu, W. et al., 2015. Darrieus vertical axis wind turbine for power generation I: Assessment of Darrieus VAWT configurations. Renewable energy, 75, pp.50–67.

[3] Leithead, William et al., 2019. The X-Rotor Offshore Wind Turbine Concept. Journal of physics.

Conference series, 1356, p.12031. doi:10.1088/1742-6596/1356/1/012031
[4] Paraschivoiu, I., 2002. Wind turbine design: with emphasis on Darrieus concept, Montréal:

17th EAWE PhD Seminar on Wind Energy
3 – 5 November 2021
Porto, Portugal

Primary study of the integrated design process of offshore support structures

H Qian[a], S Marx[a]

[a] Technische Universität Dresden
Institute of Concrete Structures
August-Bebel-Straße 30/30A, D-01219 Dresden

E-mail: han.qian@tu-dresden.de

Keywords: offshore support structure, life process, integrated design, machine learning, systematic analysis

1 Introduction

According to the current state of research, the most technical design process of support structures including the tower and sub-structure for offshore wind turbine (OWT) concentrates only on the mechanical design of the structures, i.e. the removal of static and dynamic loads in particular arising from the wind and waves. With the specific loads and boundary conditions, the design of the structures is carried out through the assessments of extreme load cases and fatigue load cases. This means that only a small aspect of the life process of an OWT, i.e. the operating phase is considered directly in the technical design.

With the demands of higher rated power class of the future OWT with larger dimensions, the boundary conditions from the life phases of production, transport and installation of the structures or special requirements from maintenance also have an enormous influence on the feasibility and profitability of the OWT [1]. Therefore, the design of the future larger offshore support structures (OSS) must include all aspects of the life process. In this work, an integrated design methodology of OSS will be put forward, with which an improvement of the structure designs by the integration of all boundary conditions of the complete life process can be carried out in a very early design stage. On the other hand, in the integrated design process, the present design experiences and approaches are connected with suitable methods in the field of machine learning (ML) which can forecast the overall design quality with different design variants. Through expanding the design space in the whole life process of OWT and with the help of ML, an improved design approach of OSS can be carried out.

2 Process and methods of the research

2.1 Process of the research of the integrated design of OWT

The process of the research is divided into four stages to enable a systematic approach to achieving the research objective. Initially, in Stage 1, the life process of an OSS is investigated and the individual life phases will be described in parameterized form. Based on the parameterization of the individual life phases, real data sets will be collected in Stage 2 and a database with additional simulated data sets will be generated. The collected and artificially generated data sets are to be evaluated in Stage 3 by experts with regard to their design quality in relation to the life process. With the consolidation of the data sets and evaluations it is planned in Stage 4 to learn different ML algorithms for the prediction of the design quality. Various learned algorithms will be compared with respect to their prediction quality and interpretability. From this resulting comparison and evaluation of the methods, the best possible prediction model will be carried out. In the following, the work in Stage 1 is explained in detail.

2.2 Method of the systematic analysis of the life process of OSS

During the life process, an OWT passes through different life phases, which range, for example, from planning, transport to the final site and the subsequent complex installation to dismantling after the service life has been exceeded, as well as the subsequent disposal or recycling of the individual components. In order to apply ML methods for the holistic assessment of the design quality, these life phases must first be described and parametrized by their characteristics (features).

In Stage 1 of the research, the systematic analysis of the life process of OSS will be developed, in which all known life phases should be examined in more detail and multi-level refined into several aspects, in order to identify as many influences on the structure design as possible. For example, as shown in Figure 1, the operation phase depends on static/dynamic loads and the other factors. The load aspect is composed with permanent loads, variable functional loads, environmental loads etc. The wind turbine loads therein are in turn dependent on further factors, such as the tower shadow, wake effects, damping etc. [2]. After the systematic analysis, a first classification and parameterization of the influence factors will be set up regarding the importance of the life phases in the design process.

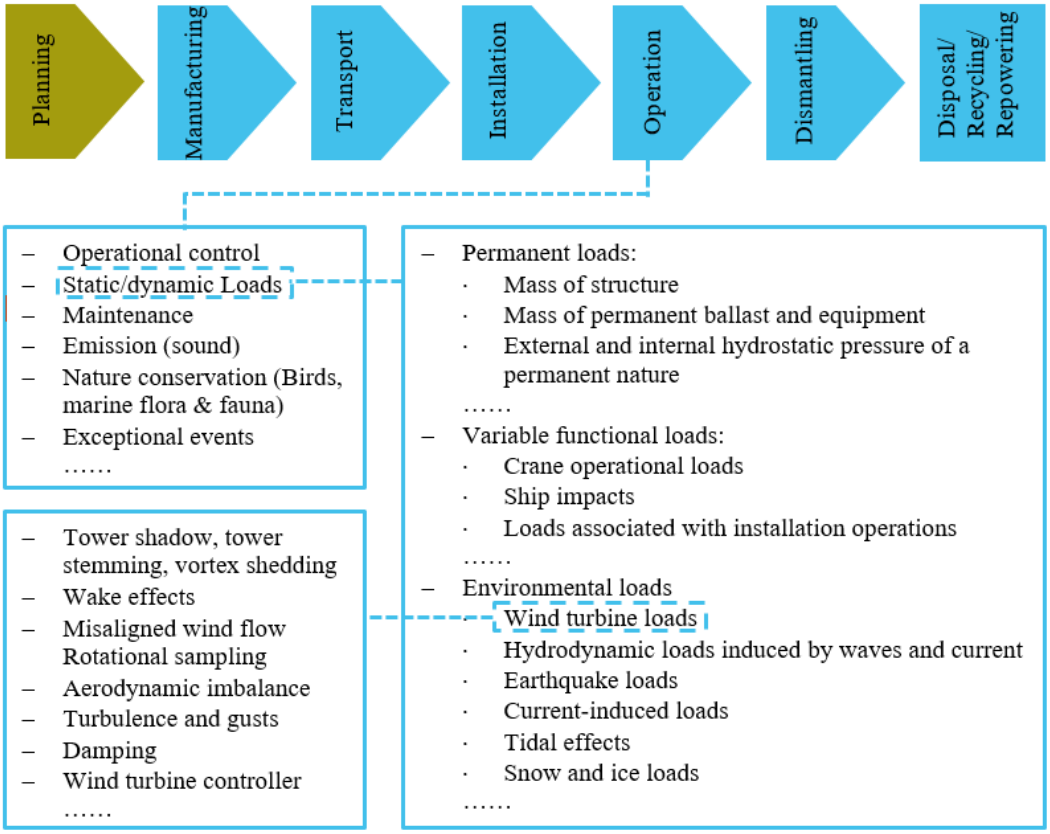

Figure 1 Exemplary representation of known life phases of a OWT with exemplary naming of influencing factors of the life phase operation

3 Outlook

Due to the great work of the literature research and the summary of influence factors in all life phases of OWT, the conclusions and results of research in Stage 1 are not yet available. The output of this stage is the classification of the most important factors with definition and holistic description that have an influence on the respective life phases. In addition, a visualization of all life phases will be created and placed in a temporal context.

Bibliography

[1] Seidel, M. 2010. Design of support structures for offshore wind turbines–Interfaces between project owner, turbine manufacturer, authorities and designer. *Stahlbau*, **79(9)**, 631-636

[2] Veritas, D. N. 2004. DNV-OS-J101-Design of offshore wind turbine structures

OFFSHORE MEGASTRUCTURES

17th EAWE PhD Seminar on Wind Energy
3 – 5 November 2021
Porto, Portugal

Experimental study on current- and wave-induced diffraction patterns in the near field of an offshore monopile

M Wynants[a], **A Schendel**[a], **N Kerpen**[a], **T Schlurmann**[a]

[a] Ludwig-Franzius-Institut
Nienburger Straße 4
30167 Hannover

E-mail: wynants@lufi.uni-hannover.de

Keywords: Water waves, Laboratory tests, Offshore Hydrodynamics, Offshore engineering, Diffraction, Monopile, Wave-Current Interaction, Dispersion, Doppler Shift

1 Extended Abstract

1.1 Objective

In order to meet the targets of reduced GHG emissions, the decarbonisation of the energy sector demands an integrated design process and safe operation of offshore wind turbines in the susceptible marine environment (IPCC 2021 [1]). The superposition of current- and wave-induced influences around the sub-structures of offshore wind turbines is a key factor to help improving design parameters and develop guidelines in the context of offshore mega-structures with hub heights > 200m and significantly increased footprint (Beyer 2019 [2]). The sheer structure's dimensions draw special attention to better understand the different load conditions with regard to pressure distribution around the pile in the design process and to advance knowledge on the structure-induced diffraction patterns on the marine environment.

1.2 Methodology

To analyse the influence of a current on wave-induced diffraction patterns, small scale hydraulic model tests were carried out with long-crested, regular waves in a 1:80 scale in the wave-current-basin of the Ludwig-Franzius-Institute, University Hannover. Within a three-phase test program, the diffracted wave field around an offshore monopile (prototype pile diameter $D_N = 11.2$ m) under the influences of waves, current and a 90° combination of both influences has been investigated. The generation and progression of diffracted waves has been observed while systematically varying the diffraction parameter D/L around the threshold of 0.2 (threshold to a hydrodynamic transparent structure, Isaacson 1979 [3]), with L representing the wave length, whereas $KC = 2\pi u/T$ has been kept constant at 1.00 with u defined as the horizontal orbital velocity. Wave heights remain constant around $H_N = 3.2$ m, while wave periods were varied between $T_N = 5.3$ and 8 s, with water depths ranging between $d_N = 8$ and 16 m.
Information and data of the diffracted wave filed at the structure and in its near-field have been acquired by measuring water surface elevations with ultrasonic wave gauges as well as through imaging techniques utilising consumer-grade cameras. The cameras have been oriented at the current-wise downstream wake, the wave-wise rear side of the pile and the interface between water-surface and

structure. To visualise the current-induced wake, a tracer was used to showcase the structure-induced effects in the marine environment. The set-up is schematically depicted in figure 1.

1.3 Boundary conditions

Due to limitations in the technical set-up and configuration of the model tests, a variability of boundary conditions needs to be considered carefully. A partial focus of the evaluation process has been set on the analysis of the water surface elevation of the individual components exerting the wave-current loadings while affecting the diffraction patterns. The aim to identify and isolate signal components influenced by the boundary conditions of the model set-up is pursued and discussed by different techniques and conceptual approaches. Undisturbed incident conditions have been derived to serve as a base case for further analysis. Influences from reflections along the basin length (figure 1a) as well as from shoaling along an offshore slope have been analysed comprehensively and were systematically removed from the obtained surface elevation measurements. Further attention has been given to pile induced reflections, which need to be interpreted in direct interconnection to the diffracted wave heights.

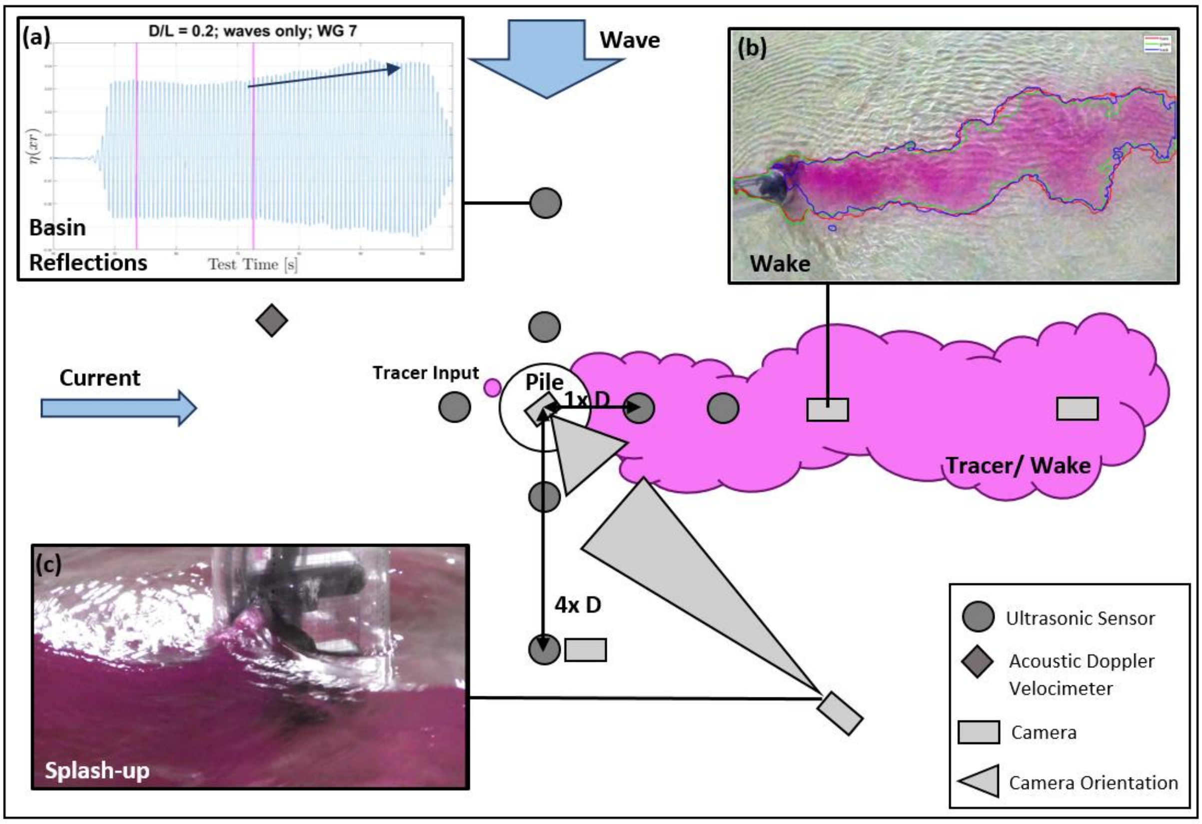

Figure 1: Schematic diagram of the model set-up with a representation of individual key aspects; (a) Exemplary time series of the water surface elevation at wave gauge 7 visualising the influence of reflection along the wave basin; (b) Tracing of the current induced wake behind the pile via imaging techniques; (c) Depiction of a splash-up wave at the rear side of the pile

1.4 Data analysis

The main focus of the analysis is set on the comparison of the waves-only-configuration versus the waves-plus-current-configuration in order to determine different load conditions and altered diffraction patterns. The influence of the current on wave heights, wave lengths and wave periods is primarily considered with regard to the water surface elevation. Building up on the underlying principle of dependency on the relative angle between wave and current direction, the hypothesis of prolonged wave lengths and attenuated wave heights for identical directions, shortened wave lengths and amplified wave heights for contrary directions and a deflection of wave heights in the direction of the current is tested

(Peregrine and Jonsson, 1983 [4] among others). The target variables are analysed to confirm, characterise and quantify these influences and effects on the marine environment.

Regarding the analysis of the video imaging, special interest is given to the influence of the current induced wake downstream of the pile on the wave directions and vice versa the change in dimension and orientation of the wake under varying wave conditions (figure 1b).

The interpretation of the results is predominantly guided by two analytical approaches. An analytic approach for diffracted waves is provided by MacCamy and Fuchs (1954) [5]. A classification of the influence of the current can be guided by the Doppler-shift approach (Jonsson 1990 [6]). Both approaches represent only isolated cases, respectively the influence of diffraction without the consideration of a current and the influence of a current on mono-directional waves.
A link between the approaches will be derived based on the conducted model tests. This linkage will be supplemented by the proposal of empirical formulations for the quantification of the current impact on the formation of diffracted wave heights and periods.

Lastly, as a major design condition for offshore megastructures, the wave-induced splash-up heights on the rear side of the pile are analysed by a double-step approach from surface elevation data and imaging techniques (figure 1c).

Bibliography

[1] IPCC, 2021. Climate Change 2021: The Physical Science Basis. Contribution of Working Group I to the Sixth Assessment Report of the Intergovernmental Panel on Climate Change *[Masson-Delmotte, V., P. Zhai, A. Pirani, S.L. Connors, C. Péan, S. Berger, N. Caud, Y. Chen, L. Goldfarb, M.I. Gomis, M. Huang, K. Leitzell, E. Lonnoy, J.B.R. Matthews, T.K. Maycock, T. Waterfield, O. Yelekçi, R. Yu, and B. Zhou (eds.)]. Cambridge University Press. In Press.*

[2] Beyer, M. 2019. Nonlinear interactions of waves with arbitrarily-sheared currents. Dissertation. *Imperial College (ICL), London, UK, 2019.*

[3] Isaacson, M. 1979. Wave-induced forces in the diffraction regime. *In: Mechanics of Wave-Induced Forces on Cylinders, (Ed. T.L.Shaw), Pitman Advanced Publishing Program* 68-89

[4] Peregrine, D. H. and Jonsson, I. G. 1983. Interactions of Waves and Currents. *Fort Belvoir, Virginia, United States of America. Report no.* **83-6**.

[5] MacCamy, R C, Fuchs, R A 1954. Wave forces on piles: a diffraction theory. *U.S. Army Corps of Engineering, Beach Erosions Board, Washington, D.C., Tech. Mem.* **69** 1 – 17

[6] Jonsson I 1990. Wave-current interactions. *The Sea: Ocean Engineering Science* **9 (A)** 65 – 120

17th EAWE PhD Seminar on Wind Energy
3 – 5 November 2021
Porto, Portugal

Sensitivity analysis of the natural frequencies of offshore wind turbines with respect to the manufacturing deviations and environmental conditions

Niklas Dierksen[a], **Clemens Hübler**[a], **Raimund Rolfes**[a]

[a] Leibniz University Hannover, Institute of Structural Analysis, ForWind,
Appelstr. 9a, D-30167 Hannover, Germany

E-mail: n.dierksen@isd.uni-hannover.de

Keywords: Sensitivity analysis, Sobol Sequence, Sobol Indices

1 Introduction

Nonlinear effects influence the dynamic behaviour of offshore wind turbines (OWT). To calculate this behaviour coupled nonlinear aero-elastic simulation models are needed, which is the main goal of the collaborative research centre 1463. It must be assumed that the dynamic behaviour of the simulation model will deviate from the dynamic behaviour of the real turbine. That is due to inaccuracies in the model or long-term changes of the structure or the constraints for example resulting from corrosion or scour development. To realise an accurate model, which represents the real turbine throughout the lifetime, an updating of the model is important. Model updating can improve the accuracy of the model, realise the adaptation to long-term changes of the structure or the constraints and be used for damage localisation as well. Saying this, model updating is suitable to realise the adaptation of the digital twin i.e. a digital copy of a real system. Later focus of this research project will be the development of model updating methods, which involve the non-reducible uncertainty that occurs at large offshore wind turbines.

A reduction of probabilistic parameters, which have to be considered for the robust model updating i.e. model updating taking into account uncertainty, is important in order to reduce the computational cost. To reduce the amount of parameters, sensitivity analysis have shown to be suitable. This work will present a sensitivity analysis of the natural frequencies of an OWT considering manufacturing deviations and varying environmental conditions.

2 Methodology

The used methodology is visualized in Figure 1, it is based on the variance-based sensitivity analysis described by Saltelli [1]. The model which is analysed is the “IEA 15MW Offshore Reference Wind Turbine” with a 240m rotor and a fixed-bottom monopile [4]. It is calculated with the finite element, multi-body system software DeSiO (Design and Simulation Framework for Offshore Support Structures) [3]. The model is a beam model with five individual beams for the tower, the pile and the three blades. The foundation is realised using horizontal springs attached to the pile.

The analyzed model is calculated multiple times for different parameter combinations. The input variables vary as a result of manufacturing deviations and environmental conditions [2]. The deviations of the single parameters are represented by probability distributions. In order to represent the parameter space well, Sobol' sequences are used for the sample generation. This is a pseudo random sampling method which converges much faster than random methods like Monte Carlo, because it has a better covering of the parameter space.

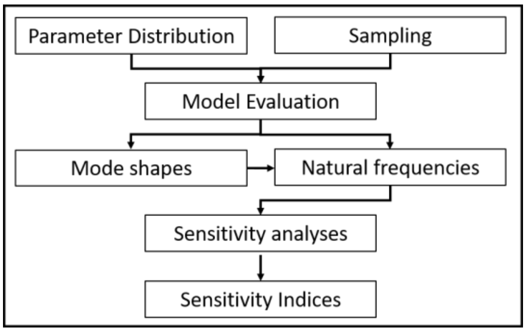

Figure 1: Methodology for Sensitiyity Analysis

In this process, the mode shapes and the natural frequencies of each calculation are evaluated. The natural frequencies and mode shapes are arranged in ascending order. However, with varying simulation settings, for example differences in the stiffness of the materials or the soil, new mode shapes can be found or the order can change. That means that the natural frequencies cannot be compared only on basis of their value and sequence. The comparison of the mode shapes on the other hand is clearer, that's why the mode shapes are compared using the Modal Assurance Criterion (MAC) in order to assign corresponding natural frequencies. The assigned natural frequencies are then used to calculate the sensitivity-indices. They are separated into two different values, first order coefficient (S_i) and the total effect index (S_{Ti}). S_i indicates the influence of parameter i on the variance of the output (value of the natural frequency). S_{Ti} describes how interactions of parameter i with other parameters influence the variance of the output. If a scattering parameter with sensitivity-indices below a threshold of 0.01 would be fixed as a constant value, this would result in an average approximation error of 2%.

3 Results

From the S_i-results it is clearly visible that not all parameters have a significant influence on the natural frequency. In most of the cases, only three to five parameters have an influence of over 0.01. The results of S_i and S_{Ti} are very similar, which indicates that there are only few interactions between the parameters. To refer to the introduction, this means for a model updating scheme, it would be reasonable to focus on only these few influential parameters in order to reduce the computational time

Acknowledgements

This work was Funded by the Deutsche Forschungsgemeinschaft (DFG, German Research Foundation) - SFB1463 – 434502799.

Bibliography

[1] Gebhardt C 2019 *Robust computational procedures for the nonlinear dynamic analysis of beam and shell structures*, habilitation dissertation.
[2] Hübler C, Gebhardst C, Rolfes R, 2017 *Wind Energ. Sci*., 2, 491–505.
[3] Saltelli A, Annoni P, Azzini I et al 2010 *Computer Physics Communications* 181 259–270
[4] Gaertner et al, 2020: *IEA Wind TCP Task 37 - Definition of the IEA Wind 15-Megawatt Offshore - Reference Wind Turbine - Technical Report*, National Renewable Energy Laboratory.

Comparison of environmental contour methods

A Rode[a], B Schmidt[a]

[a] Leibniz University Hannover
Institute of Concrete Construction (IfMa)
Appelstraße 9a, D-30167 Hannover

E-mail: rode@ifma.uni-hannover.de

Keywords: Environmental Contour, Highest Density (HD) Contour, Inverse First-Order Reliability Method (IFORM), Metocean Extremes

1 Extended Abstract

Offshore wind energy has become a more relevant topic in the energy production and the overall society during the last decades. As the importance of reducing carbon emissions is getting more and more important the demand for renewable energy resources is increasing continuously. Hence there is an upcoming need for an optimised wind energy turbine design. The research topic of new "Offshore Megastructures" with a rated power of $> 20\,MW$, is the main focus in the *Collaborative Research Centre 1463 Integrated Design and Operation Methodology for Offshore Megastructures* funded by the DFG [1]. For existing offshore wind energy turbines and for future offshore megastructures the estimation of the environmental parameters are an indispensable necessity, because they are constantly exposed to the loads derived from metocean parameters. The IEC 61400-3 therefore proposes the use of environmental contour methods [2]. Environmental contour (EC) methods are extremely necessary and helpful when estimating the temporal and directional correlation of metocean extremes [3], [4]. The further development of existing environmental contour methods specifically for "Offshore Megastructures" is part of the Collaborative Research Centre 1463.

In general for the calculation of an environmental contour a joint probability function and a chosen return period are obligatory regardless of which environmental contour method will be applied. Currently there are numerous different environmental contour methods with, in part, strongly divergent results [5]. Having methods that use a transformation of the environmental variables into a standard normal space, for example via a Rosenblatt transformation alongside methods using the existing environmental parameters in the physical space without any transformation, it is not easy to make a decision for one existing contour method [3].

Hence, this work will study the Highest Density (HD) contour method, proposed by Haselsteiner et al. [6] and compares it to existing results of temporal correlated metocean extremes. The original concept of deriving HD regions was already mathematically explained by Hyndmann [7] but it was firstly not intended to be used with metocean parameters as an environmental contour method. The HD contour method works without a transformation of the random variables into the standard normal space. Moreover it discretises the environmental variables directly in the physical space into equally sized grid cells. The probability density of the grid cells is calculated using numerical integration and the cumulative distribution function of the joint probability function of the random variables (environmental parameters), see equation (1) and (2).

$$\bar{f}_{X_1}(x_1) = \frac{F_{X1}(x_1 +\ 0.5\,\Delta x_1)\ - F_{X1}(x_1 - 0.5\,\Delta x_1)}{\Delta x_1} \tag{1}$$

$$\bar{f}_{X_2|X_1}(x_2|x_1) = \frac{F_{X_2|X_1}(x_2 +\ 0.5\,\Delta x_2)\ - F_{X2|X_1}(x_2 - 0.5\,\Delta x_2)}{\Delta x_2} \tag{2}$$

Under consideration of a return period, an exceedance probability α can be formulated and the according minimum probability density f_m can be found using $\bar{F}(f_m) = 1 - \alpha$. This minimum probability is needed to find the region with a higher density than f_m i.e. the highest density region [6].

One main aspect of this work is the sensitivity analysis of the stochastic parameters of the HD contour method. This implies the investigation of different stochastic probability distribution functions. The 2-parameter Weibull distribution, the 3-parameter Weibull distribution and the Gamma distribution will be used to derive HD contours. Differences between the probability distributions will be shown for HD contour and for IFORM contours. EC methods in general are highly sensitive on the change of the distribution functions [5]. Besides the sensitivity of the probability distributions on the HD contour method, also the parameter estimation methods used for deriving a 2-parameter Weibull distribution are compared. For this work the used estimation methods are the maximum likelihood estimation and the least squares estimation.

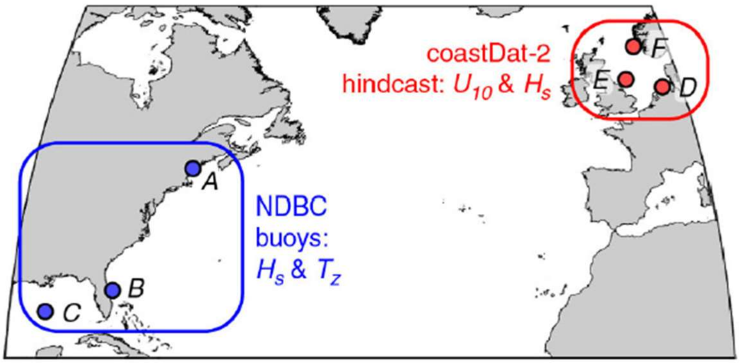

Figure 1 Map with the locations of the different dataset sites [5]

Further the influence of different sites and different metocean parameters will be examined (see Figure 1). Therefore, three sites off the US east coast (buoys-datasets) and additionally three in the North Sea (hindcast datasets) for each 1 and 20 year (US) or 1 and 50 year (North Sea) return periods are considered (see Table 1). In addition different time periods (10 year time period, 25 year time period) and return periods of one North Sea site (site D) are also examined. These sites and datasets, were already part of an international benchmarking exercise for EC [5]. Thus, many comparisons between different results can be done.

Table 1: Overview of datasets and sites

Location		**Time Period of data**	**Considered return periods for EC**
A	43.525N70.141W	10 years	1 year, 20 years
B	28.508N80.185W	10 years	1 year, 20 years
C	25.897N89.668W	10 years	1 year, 20 years
D	54.000N6.575 E	25 years / 10 year periods	1 year, 50 years
E	55.000N1.175 E	25 years	1 year, 50 years
F	59.500N4.325 E	25 years	1 year, 50 years

In Conclusion, the sensitivity analysis of the HD method will be compared to a former realised sensitivity analysis of the IFORM [8]. In general HD contours are more conservative than the IFORM contours [3]. The further result of this work shall then show the major differences and advantages between these two methods and might point out relevant aspects that should be considered for the further research of environmental contours.

Acknowledgements

Acknowledgement of DFG support for the Collaborative Research Center 1463 Integrated Design and Operation Methodology for Offshore Megastructures.

2 Bibliography

[1] Schuster D, Hente C, Hübler C and Rolfes R 2021 Integrierte Entwurfs- und Betriebsmethodik für Offshore-Megastrukturen *Bautechnik* **98** 563–70
[2] International Electrotechnical Commission 2019 Wind energy generation systems - Part 3-1: Design requirements for fixed offshore wind turbines *(*IEC 61400-3-1:2019*)* (VDE)
[3] Mackay E and Haselsteiner A F 2021 Marginal and total exceedance probabilities of environmental contours *Marine Structures* **75** 102863
[4] Hildebrandt A, Schmidt B and Marx S 2019 Wind-wave misalignment and a combination method for direction-dependent extreme incidents *Ocean Engineering* **180** 10–22
[5] Haselsteiner A F, Rode A, Schmidt B *et al.* 2021 A benchmarking exercise for environmental contours *Ocean Engineering* **236** 109504
[6] Haselsteiner A F, Ohlendorf J-H, Wosniok W and Thoben K-D 2017 Deriving environmental contours from highest density regions *Coastal Engineering* **123** 42–51
[7] Hyndman R J 1996 Computing and Graphing Highest Density Regions *The American Statistician* **50** 120
[8] Winterstein, S.R., Ude, T.C., Cornell, C.A., Bjerager, P. and Haver, S. 1993 *Environmental parameters for extreme response: Inverse FORM with omission factors*

17th EAWE PhD Seminar on Wind Energy
3-5 November 2021
Porto, Portugal

Modelling and Simulation of Scour Development at Offshore Megastructures: An Overview

R Satari[a], A Schendel[b], T Schlurmann[b], and I Neuweiler[a]

[a]Institute of Fluid Mechanics and Environmental Physics in Civil Engineering, Leibniz University Hannover, Appelstr. 9A, 30167 Hannover, Germany
[b]Ludwig-Franzius-Institute for Hydraulic, Estuarine and Coastal Engineering, Leibniz University Hannover, Nienburger Str. 4, 30167 Hannover, Germany

E-mail: satari@hydromech.uni-hannover.de

Abstract

The reliable prediction of scour development is an essential element of foundation structure design and will play an important role for the expansion of offshore wind energy. The formation of scour at offshore foundations is an active field of research with extensive literature on the subject. While numerous studies are available that deal with the development of scour at slender monopile structures in wave, current or combined conditions [39], studies considering more complex structures or more extreme boundary conditions in locations further from the coast are still scarce. This leaves open questions concerning the prediction of scour development at large offshore megastructures – structures with a diameter greater than 10 m – which will provide the foundation of future offshore wind turbines with capacities of more than 20 MW and thus significantly contribute to the expansion of offshore wind energy. As an example, the flow patterns around such structures could deviate strongly from that of slender monopile structures due to more extreme and different wave patterns in more exposed conditions and due to coupling of the flow-structure interaction to the upstream flow conditions. Strong changes in flow pattern could result in strong changes of scour development.

In this paper, a literature review is carried out in which the focus is mainly on scour development around large offshore structures such as large diameter piles and complex structures along with complex flow conditions. Finally, the research gaps are summarized and suggestions are made on how we contribute to close this gap.

Keywords: Offshore Wind Energy, Scour, Sediment transport, Laboratory tests, Numerical model, Megastructures

1 Introduction

In recent years, the offshore wind industry has developed rapidly due to the increasing demand for clean and renewable energy sources [50]. In offshore wind power projects, one fourth of the total cost is allocated to the foundation structure [19] which can even increase up to 40 % of the total cost in deeper water depths. As the cost for foundations significantly increases with water depths, several different types of foundation structures have been developed to minimize the costs with simultaneously providing improved serviceability, durability and stability [19].

When wind turbines are placed into the maritime environment, they have to withstand hydraulic loads induced by currents and waves, in contrast to their onshore counterparts. As the foundation structure of an offshore wind turbine acts as an obstacle to the flow, it causes a disturbance of the flow around it. A complex vortex system consisting of lee-wake vortices, horseshoe vortex and a downflow at the upstream side of the structure will emerge together with a general streamline contraction. For large diameter structures, additional wave diffraction and reflection effects occur. As a result of these effects, the flow velocity and thus the bed shear stress is locally increased, leading to general amplification of the sediment mobility in the vicinity of the structure. The emerging scour hole may lead to a significant reduction of the stability of the foundation structure [39, 32, 49].

As an essential element of foundation structure design, the reliable prediction of scour development plays a vital role for the expansion of offshore wind energy. Although extensive research has been carried out on this topic over the past decades, the occurrence, drivers and effects of scour have been investigated mostly for slender structures such as small-diameter monopiles. On the other hand, scour around larger and more complex foundation structures such as tripods, jackets or large-diameter monopiles was studied less thoroughly so far, although the necessary expansion of offshore wind into deeper waters relies on these very structures. As a result, the prediction of scour around these structures is still based on knowledge gained for slender monopiles, which means that the design of these structures tends to be rather conservative and uneconomical.

As part of the collaborative research centre "SFB 1463 Offshore-Megastrukturen", the scour development at large and complex foundation structures is thus systematically studied. We want to study the question of scalability of models and the predictive power of models validated for different conditions than that of the predictions they are used for. As basis for the upcoming experiments, this paper provides a state-of-the-art review on the scour development around large and/or complex offshore structures exposed to complex flow conditions. An illustration of different types of foundation structures are given in Figure 1.

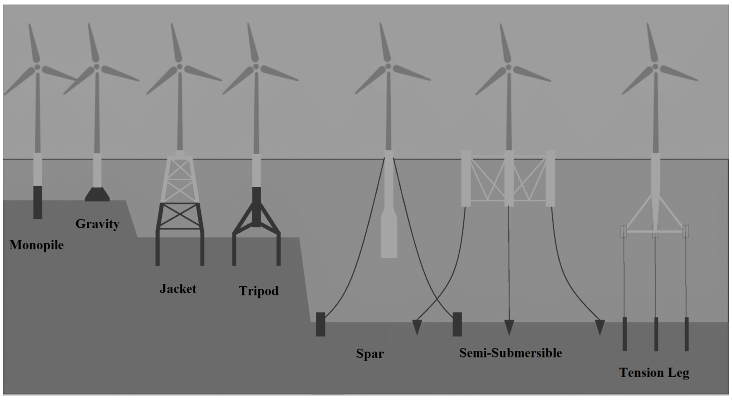

Figure 1: Types of support structure concepts. From left to right: monopile, gravity based, jacket, tripod, spar, semi-submersible platform and tension-leg platform. Figure is adapted from [8].

2 State-of-the-art

Numerous studies have been carried out on the scour development at piles under current [17, 27], wave [40, 28] or combined wave-current load [45, 34]. Under current flow conditions, the scour process is mainly driven by the formation of the horseshoe vortex (see Figure 2), which itself depends on the boundary layer thickness, the pile Reynolds number and the bed roughness [22]. An important distinction can also be made between clear-water scour and live-bed scour. In live-bed conditions, flow velocities are larger than the threshold of sediment motion, leading to a mobile sediment bed and potential refilling of the scour hole by the upstream sediment transport. In clear water conditions, sediment is only set in motion by the flow disturbance of the structure as described above.

In the case of waves, the formation of the flow pattern is also determined by the Keulegan-Carpenter number (KC), a dimensionless number defined as,

$$KC = UT/D, \tag{1}$$

in which $U[m/s]$ is the amplitude of the orbital velocity, $T[s]$ is the wave period and $D[m]$ is the pile diameter. Only for values of $KC > 6$ both horseshoe and lee-wake vortices form with a strength that allows a significant influence on the scouring process. For smaller values of KC the scour is mainly caused by steady streaming [39].

As a recent example, [20] investigated in a physical experiment the local scour and pore-pressure response around a pile in small KC wave and current conditions ($0.44 \leq KC \geq 3.65$). The experimental procedure indicated that the superimposition of waves on currents results to larger scour depths than under isolated current conditions. The authors also reported a larger maximum flow velocity for the following-current case than for the opposite-current case. This difference in velocities has effects on the time development of scour depths and equilibrium scour depths.

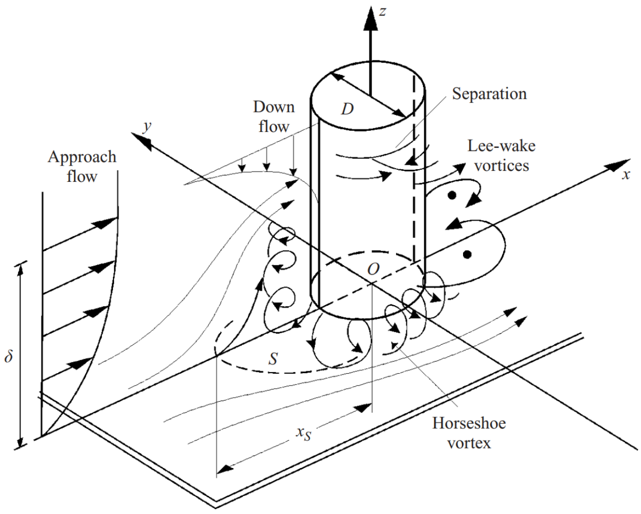

Figure 2: Flow around a pile/pier. S is the separation line, δ is the bed boundary layer thickness. Figure is taken from [22].

As we will now focus on the scour development at large and more complex offshore structures, for further fundamental studies about scouring process and an overview of recent studies, the interested reader is referred to [39, 49, 36, 31, 9, 14, 7].

2.1 Large Structures

In coastal and offshore engineering practices vertical circular structures, i.e. piles and piers, are widely used and as such will be the main focus of this section. In case of wave load, the formation and structure of the flow field around a pile depends on the ratio of pile diameter to wave properties. Important parameters determining the scour development are the diffraction parameter (D/L) and Keulegan-Carpenter (KC) number, where $D[m]$ is the diameter of the circular cylinder and $L[m]$ is the wave length. With reference to the KC number, [39] classified piles into slender, medium large and large piles. A value of $KC > 6$ corresponds to slender piles and $KC < 1$ to large piles, whereas KC in between ($1 \leq KC \leq 6$) refer to medium large piles.

For large piles (small KC number) no flow separation and vortex formation occurs and the scour process is thus mainly driven by steady streaming at the pile [35, 38, 37]. There are two kinds of wave-induced flow around the pile, the phase-resolved flow and the steady streaming. The steady streaming is caused by nonuniform oscillatory motion, which is caused by the presence of the pile itself and is indicated to be a major factor responsible for scour around a large pile [38, 33, 41, 12]. In addition, waves might be diffracted around large piles which, in interaction with wave reflection on the upstream side of the pile, can lead to locally increased wave heights near the pile. According to [11], diffraction effects become important when the diffraction parameter is larger than 0.2.

Due to complexity of the flow system around a large pile, especially in waves, the mechanism of sediment transport and scour formation around larges piles was mainly studied by laboratory experiments [38, 37, 24, 12]. However, over the past years attempts have also been made to numerically simulate the scour process around a large circular cylinder [24, 25, 13, 1].

As one of the first studies, [12] experimentally investigated the mechanism of sand movement around large circular cylinders to provide information regarding the design of scour protection around large offshore structures. The authors described two flow phenomena responsible for the incipient movement of sand particles: the wave-induced uniform flow near the cylinder and a more complex boundary layer formation.

[24] presented a numerical model which was validated using laboratory experiments carried out in a wave basin to reproduce the local scour around large pile placed in the wave fields. In the experiment the wave basin was filled with well-sorted sand of $d_{50} = 0.2mm$ in median diameter and a pile of diameter $D = 52.2cm$ was installed. The wave model was based on linear diffraction theory, assuming that the change in the topography around the pile was small compared to the water depth $h = 16.5cm$. In the experiment it took the bottom topography four hours to reach equilibrium. The numerical model was able to predict the scour, however, some discrepancies in the scour pattern between numerical and experimental results were noticed in front of the cylinder. The author emphasizes that these were due to the inadequacy in estimating the shield parameter and also due to use of linear diffraction theory.

[13] simulated the scour process around different numbers of large piles under wave actions by applying the linear diffraction theory assuming small wave length. It was concluded that the bottom configuration, the area and depth of the local scouring around cylindrical structure are changed according to the number of cylinders, their diameter, the incident wave angle and size of the sediments. With increasing diffraction parameter, the authors found the scour depth to become larger. Moreover, their proposed numerical approach well evaluated the bottom topographical change around structures. However, incorporating linear theories such as diffraction theory [16], which assumes a constant water depth, is not straightforward when the topography of the sea bed is not flat as it would be in case of a sloped beach or sea bed deformations [52].

In studies discussed above [24, 13], the wave model was based on the linear diffraction theory, in which the water depth is assumed to be constant. To overcome the limitation of a flat bed topography in the linear diffraction theory, [52] presented a numerical model in which the wave model was based on the elliptic mild slope equation proposed in [4]. which can simulate wave fields with variable bed levels. The authors investigated an identical case of the experiments carried out in [24], with $D = 52.2cm$, $D/L = 0.5$ and $KC = 0.41$. It was observed that their results were identical in the case of constant water depth. Moreover, the scour pattern in front of the cylinder is better predicted when compared to the model presented in [24]. Effects of the grain size diameter on the scour process were also investigated. It was observed that the depth of bed change reduces when the the grain size increases, however, the effect of grain size on the position of maximum scour is relatively small.

In an experimental study, [38] investigated the scour process under progressive waves around large vertical cylinders of diameter ($D = 0.54$, 1 and 1.53 m) installed on a basin filled with sand of mean diameter $d_{50} = 0.2mm$. In this experiment the effects of KC number and diffraction parameter D/L on scour were studied within the ranges of $0.2 \leq KC \leq 1.2$ and $0.08 \leq D/L \leq 0.3$. It was concluded that the scour characteristic mainly depends on the KC and D/L (in the case of live-bed) and the maximum scour depth S/D increases with increase in these parameters, see Figure 3.

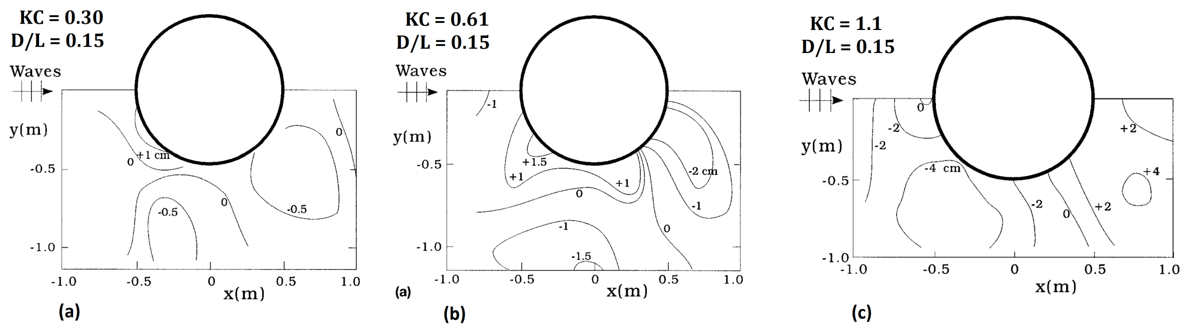

Figure 3: Contour plot of bed topography in equilibrium stage; Numerical figures indicate scour (-) and deposition (+) in centimeters [cm]: (a) $KC = 0.30$ & $D/L = 0.15$, (b) $KC = 0.61$ & $D/L = 0.15$ and (c) after $8h$ test time for $KC = 1.1$ & $D/L = 0.15$. Figure is adapted from [38].

In a separate study [35] experimentally investigated the time scale for scour development around large piles. The time scale is mainly a function of the KC number, the diffraction parameter D/L and the Shields parameter θ. The authors found out that time scale increases with KC and decreases with the Shields parameter.

Recently, in an attempt to numerically model scour, [1] used REEF3D - a 3D open-source software, in order to simulate the flow field and sediment transport around large piles under varying wave condition. The numerical simulation was carried out using three different values of KC, $KC = 1.0$, 1.1 and 1.2. To validate the model for $KC = 1.1$ and diffraction parameter $D/L = 0.15$, the experiment carried out in [38] is used, in which the diameter of the pile is $D = 1m$ and the experiment was conducted for 8 hours. After eight hours simulation a maximum scour depth of $5.2cm$ was obtained, which is in close agreement with the $4.7cm$ observed in the experiment [38]. Additionally, the numerical model has also predicted well the location of the maximum scour depth. The validated model is then used to simulate scour development with the other values of KC. It was observed that reduction of KC results in a decrease in scour area and maximum scour depth of $4.6cm$ and and increase in KC from 1.1 to $KC = 1.2$ results in an increased maximum scour depth of $5.5cm$. The authors also concluded that for low values of KC, the horseshoe vortices and wake shedding do not contribute to the local scour.

2.2 Complex Structures

Scour formation around complex offshore foundations such as tripods and jacket type foundation are comparatively more complex than the simple cylindrical structures. Despite being widely used in offshore engineering, little is known and limited studies (experimental and/or numerical) are carried out regarding the scour around such complex foundations. Often classical scour depth formulations developed for pile foundations are used for complex foundations as well. However, instead of the pile diameter, an equivalent diameter describing the overall foundation is used. These approaches are largely affected by uncertainties, leading to an over- or under-estimation of scour depths especially around the main pile [23] and, consequently, often to an uneconomic design of scour protection measures. Additionally, incorporating existing pile scour approaches often leads to nonphysically large, theoretical scour depths [28].

Besides the in-situ measurements and laboratory experiments on scour around complex structures (e.g. jacket and tripods), attempts have also been made to develop numerical models, which will be briefly summarized here.

2.2.1 Physical Modeling

Knowledge on scour formation around complex foundation types such as jacket and tripods are mainly carried out through laboratory experiments and as such physical models are developed and presented. Recently, experimental studies using complex foundation types such as jacket foundation [43, 26, 45, 51, 6, 5, 3] and tripods [51, 28, 29] were conducted, to physically model the scour formation and its underlying processes.

[6] conducted laboratory experiments under tidal currents and perpendicular approaching waves with jacket type foundation structures for conditions in the Strait of Taiwan. The jacket structure was modelled in a 1:36 scale, referring to prototype dimensions of $D = 2.08m$ for the pile diameter and a spacing distance between the piles of $14m$. Besides local scour depths at the individual piles also the global scour extension was evaluated. The pile located in upstream wave and current direction saw the largest scour depths. Overall, the combined loads of tidal currents and wave lead to a scour depths between $S/D = 0.2 - 1.3$.

[45] conducted physical model tests and studied scour development and time scale of scouring process around a complex jacket structure for different wave-current conditions and as a result proposed a practical formulation for the reliable prediction of local scour depths around a jacket foundation in combined wave-current conditions. Based on this, [44] also investigated the influence of individual structural elements of the jacket structure on the scour formation. The authors found that decreasing the distance of the structure's lowest node to the sea bed leads to an increase erosion beneath the structure, especially in current-dominated flow conditions.Finally, [46] presented a new method to analyse the spatial erosion pattern underneath and in the near field of a jacket structure, see Figure 4. The method allows to assess the structure-induced morphological footprint by evaluating the volume of eroded and deposition sediment for different reference areas around the jacket structure.

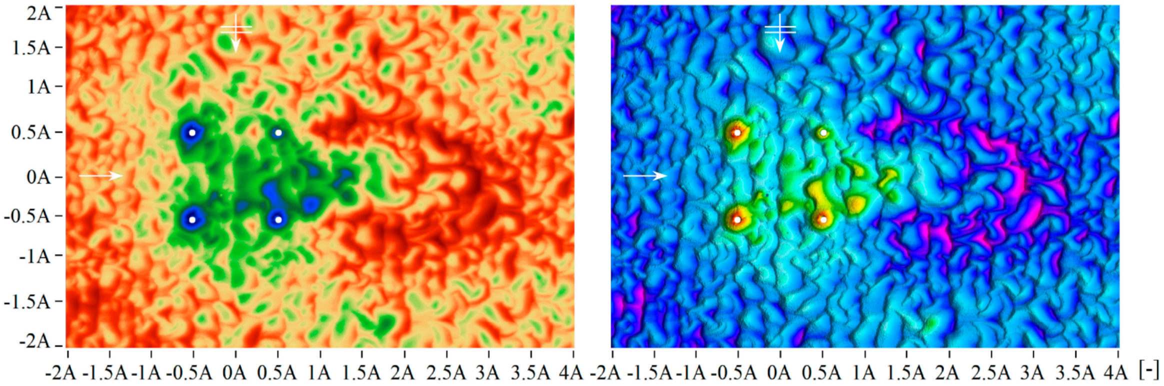

Figure 4: Bed topography measured, top view on erosion and deposition around the jacket structure, current is coming from left to right, waves are propagating in 90° to the current; (**left**) optimized illustration to differentiate between local (blue) and global (green) erosion depths as well as deposition (red); (**right**) HSV colourmap to differentiate between different elevations. Figure is taken from [46].

Experiments were carried out using tripods as well. [30, 29] investigated experimentally the scour around a tripod foundation under both regular (see Figure 5) and irregular wave conditions and for different model scales. The authors conducted the laboratory experiments in intermediate scale 1:40 in small wave flume and 1:12 large-scale physical model tests in a large wave flume and compared them with the field data measurements acquired from the alpha-ventus offshore wind farm in the North sea. The large-scale experiments and the field measurements were in good agreement, as scour holes were similar both locally and globally. Additionally, deposition areas are also similar between the field and experiments. However, scour depths in the field are in general bigger than the physical model. The author points to the simplified hydrodynamics conditions in the laboratory test as the main reason for the smaller scour depths, since the experiments were conducted without the influence of a current.

[51] conducted a laboratory experiment using tripods under steady flow conditions in a scale of 1:60 considering piles of diameter $D = 5.4cm$. The experiment were conducted in a flume of ($16.5m$ long, $2.4m$ wide and $0.3m$ deep) under clear-water conditions for two current velocities and four flow depths. The authors found out that maximum scour depth increased with a rising flow depth and an increasing current velocity. For the highest water depth of $0.25m$ and the highest current velocities, a maximum equilibrium depth of $S/D = 3.2$ was reached. It should be noted that the maximum scour depths in all tripod tests in [51] have been measured at one of the tripod legs and not below the large main pile, as it was done in [29, 30].

[18] has proposed an approach to calculate the effective diameter for the tripod and exapod models under steady current condition. This effective diameter will be then used to predict the equilibrium scour depth using methods developed for monopiles.

2.2.2 Numerical Modeling

In order to analyze the scour around jacket type foundation structures, [2] used REEF3D - a 3d open-source software and a morphological model. Moreover, the modeling of the local scouring process considers bed load and suspended sediment transport. The numerical validations were carried out using different KC number in a range of ($6 \leq KC \leq 12$) for the local scour around a pile under wave based on [40] and scour under a steady current for the large vertical pile $D = 0.20m$ based on [15]. The results of the numerical model were in good agreement and thus the validated model was used to analyze the scour around a jacket structure. The jacket structure is comprised of four vertical piles of diameter $D = 2.0m$, and the highest water depth is $h = 30m$. The median grain size is $d_{50} = 0.30mm$ and the critical Shields number $\theta_c = 0.05$. Due to high computational cost of such large numerical model, a coarse grid is used and the numerical model is applied on steady current and wave induced simulations of the scour around the jacket structure.

[28] presented a 3D model, and implemented a sediment transport model approach simulating both bed

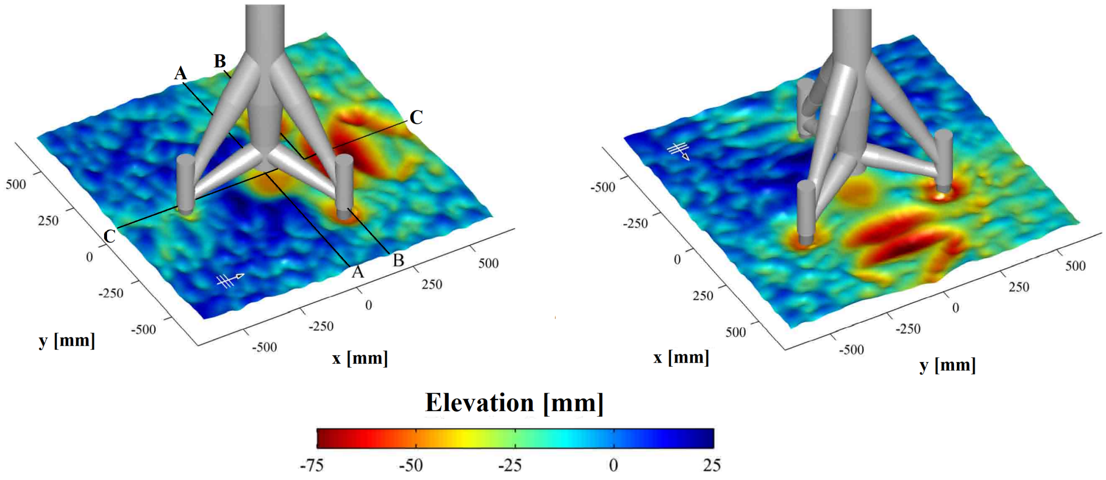

(a) **(b)**

Figure 5: Results of scour development after 3000 wave cycles: (a) front view, (b) rear view. Figure is adapted from [28].

and suspended load transport in the framework of and open-source software OpenFOAM. The obtained results from the presented numerical model were satisfying for scour development around pile under steady current condition and a complex tripod foundation under regular waves.

2.2.3 Field Data

Field data on scour development at complex offshore foundations have rarely been reported in the past. However with the current development of the wind energy sector, more information on in-situ measurements on actual scour development cases is available, see e.g. the reports in [3, 5, 48, 42, 47, 10, 23]. Here, some results regarding complex foundations are briefly summarized.

[23] investigated the scour around jacket structures installed in a moderate water depths of 25m in the southern North Sea under wave and current load over the period of several years. The field measurements were carried out on two different jacket type structures: a production platform (standing on six legs with a diameter of $D_1 = 1.5m$ each and a spacing of 16 and $20m$ between the legs) and jacket wallhead structures (four legs with a diameter of $D_1 = 1.1m$ each and spacing of 20 and 17m between the legs). Measurements of the seabed topography revealed local scouring of up to $5m$ deep, exceeding the predictions carried out using empirical approaches for a single pile by a factor of about 3 to 4.

[5] investigated the scour around a jacket structure at the C-Power wind farm at Flemish coast in Belgium, in order to design protection measures. The seabed pile of the structure had a diameter of $D = 2m$ and a spacing between the piles of $18m$. Before the jacket installation - around 2.5 month after pre-piling, local scour holes with an average depth of $1.3m$ were already observed. After the jacket installation the average local scour depth increased to about 1.4 to $1.9m$ within six month. The maximum scour depth increased simultaneously to a depth of $2.7m$. In contrast to the findings of [23], the theoretically predicted scour depths were reasonable close to the observed values. [3] also presented the field data of the same structure studied in [5]. Unlike [5] the authors studied the long term evolution as well as the continuous scour development and the associated hydrodynamic conditions over a period of 3 years.

[29, 30] have also used the measurements from a prototype foundation installed in the alpha-ventus test site [21], in order to physically and numerically model the scour around tripod structures.

2.3 Summary

In this paper a literature survey is carried out on existing physical and numerical studies on the scour development around large and complex foundation structure in the marine environment. Although there are some studies addressing this issue, further research is required to better understand and clarify the scouring processes. This paper is presented as an initial work for a new series of studies which will be carried out as part of the collaborative research center ”CRC 1463 Offshore Megastructures”.

References

[1] N. Ahmad, H. Bihs, M. S. Afzal, and Ø. Arntsen. Three-dimensional numerical modeling of local scour around a non-slender cylinder under varying wave conditions. 06 2015.

[2] N. Ahmad, A. Kamath, and H. Bihs. 3d numerical modelling of scour around a jacket structure with dynamic free surface capturing. *Ocean Engineering*, 200, 03 2020.

[3] L. Baelus, A. Bolle, and V. Szengel. Long term scour monitoring around offshore jacket foundations on a sandy seabed. pages 383–392, 10 2018.

[4] J. Berkhoff. Computation of combined refraction - diffraction. *Coastal Engineering Proceedings*, 1:23, 01 1972.

[5] A. Bolle, J. D. Winter, W. Goossens, and G. Dewaele. Scour monitoring around offshore jackets and gravity based foundations. *Proc. of Sixth International Conference on Scour and Erosion (ICSE), 27.-31. August 2012 in Paris*, 08 2012.

[6] H.-H. Chen, R.-Y. Yang, and H.-H. Hwung. Study of hard and soft countermeasures for scour protection of the jacket-type offshore wind turbine foundation. *Journal of Marine Science and Engineering*, 2:551–567, 07 2014.

[7] P. Diaz-Carrasco, S. Croquer, V. Tamimi, R. Lacey, and S. Poncet. Advances in numerical reynolds-averaged navier–stokes modelling of wave-structure-seabed interactions and scour. *Journal of Marine Science and Engineering*, 9, 06 2021.

[8] E. Dornhelm, H. Seyr, and M. Muskulus. Vindby—a serious offshore wind farm design game. *Energies*, 12, 2019.

[9] A. Gazi, M. S. Afzal, and S. Dey. Scour around piers under waves: Current status of research and its future prospect. 10 2019.

[10] M. Høgedal and T. Hald. Scour assessment and design for scour for monopile foundations for offshore wind turbines. 01 2005.

[11] M. Isaacson. Mechanics of coastal sediment transport (world scientific. pages 68–69, 1979.

[12] H. Katsui and T. Toue. Inception of sand motion around a large obstacle. *Coastal Engineering Proceedings*, 1:95, 01 1988.

[13] C.-J. Kim, K. Iwata, Y. Miyaike, and H.-S. Yu. Topographical change around multiple large cylindrical structures under wave actions. 1995.

[14] B. Liang, S. Du, X. Pan, and L. Zhang. Local scour for vertical piles in steady currents: Review of mechanisms, influencing factors and empirical equations. *Journal of Marine Science and Engineering*, 8, 2020.

[15] O. Link. Untersuchung der kolkung an einem schlanken zylindrischen pfeiler in sandigem boden. *Wasser Abwasser GWF*, 147:421–422, 2006.

[16] R. C. MacCamy and R. A. Fuchs. Wave forces on piles: a diffraction theory. 1954.

[17] B. W. Melville and Y.-M. Chiew. Time scale for local scour at bridge piers. *Journal of Hydraulic Engineering*, 125:59–65, 1999.

[18] X. Ni and L. Xue. Experimental investigation of scour prediction methods for offshore tripod and hexapod foundations. *Journal of Marine Science and Engineering*, 8:856, 10 2020.

[19] K.-Y. Oh, W. Nam, M. S. Ryu, J.-Y. Kim, and B. I. Epureanu. A review of foundations of offshore wind energy convertors: Current status and future perspectives. *Renewable and Sustainable Energy Reviews*, 88:16–36, 2018.

[20] W.-G. Qi and F.-P. Gao. Physical modelling of local scour development around a large-diameter monopile in combined waves and current. *Coastal Engineering*, 83:72–81, 2014.

[21] RAVE. Rave - research at alpha ventus. eine forschungsinitiative des bundesministeriums. *Fraunhofer-Institut für Windenergie und Energiesystemtechnik IWES, Kassel, Germany*, 2010.

[22] A. Roulund, B. M. Sumer, J. Fredsøe, and J. Michelsen. Numerical and experimental investigation of flow and scour around a circular pile. *Journal of Fluid Mechanics*, 534:351–401, 2005.

[23] D. Rudolph, K. J. Bos, and A. Luijendijk. Scour around offshore structures-analysis of field measurements. 2004.

[24] E. Saito, S. Sato, and T. Shibayama. Local scour around a large circular cylinder due to wave action. *Coastal Engineering 1990*, pages 1795–1804.

[25] E. Saito and T. Shibayama. Local scour around a large circular cylinder on the uniform bottom slope due to waves and currents. pages 2799–2810, 06 1993.

[26] J. Sarmiento, R. Guanche, A. Iturrioz, T. Ojanguren, A. Ávila, and C. Yanes. Experimental evaluation of dynamic rock scour protection in morphodynamic environments for offshore wind jackets. *Energies*, 14:3379, 06 2021.

[27] D. M. Sheppard, M. Odeh, and T. Glasser. Large scale clear-water local pier scour experiments. *Journal of Hydraulic Engineering*, 130:957–963, 2004.

[28] A. Stahlmann. Numerical and experimental modelling of scour at foundation structures for offshore wind turbines. *Journal of Ocean and Wind Energy.*, 1(2):82–89, 2013.

[29] A. Stahlmann and T. Schlurmann. Physical modeling of scour around tripod foundation structures for offshore wind energy converters. *Proceedings of 32nd Conference on Coastal Engineering, Shanghai, China, 2010.; sediment.67*, 1, 01 2010.

[30] A. Stahlmann and T. Schlurmann. Investigations on scour development at tripod foundations for offshore wind turbines: Modeling and application. *Coastal Engineering Proceedings*, 1, 12 2012.

[31] B. Sumer. Mathematical modelling of scour: A review. *Journal of Hydraulic Research - J HYDRAUL RES*, 45:723–735, 11 2007.

[32] B. Sumer, N. Christiansen, and J. Fredsoe. Influence of cross section on wave scour around piles. *Journal of Waterway Port Coastal and Ocean Engineering-asce - J WATERW PORT COAST OC-ASCE*, 119, 09 1993.

[33] B. Sumer and J. Fredsoe. Wave scour around structures. 4:191–249, 06 1999.

[34] B. Sumer and J. Fredsoe. Scour around pile in combined waves and current. *Journal of Hydraulic Engineering-asce - J HYDRAUL ENG-ASCE*, 127, 05 2001.

[35] B. Sumer and J. Fredsoe. Time scale of scour around a large vertical cylinder in waves. *Proceedings of the International Offshore and Polar Engineering Conference*, 12, 01 2002.

[36] B. Sumer, R. Whitehouse, and A. Tørum. Scour around coastal structures: A summary of recent research. *Coastal Engineering*, 44:153–190, 12 2001.

[37] B. M. Sumer, N. Christiansen, and J. Fredsøe. The horseshoe vortex and vortex shedding around a vertical wall-mounted cylinder exposed to waves. *Journal of Fluid Mechanics*, 332:41–70, 1997.

[38] B. M. Sumer and J. Fredsøe. Wave scour around a large vertical circular cylinder. *Journal of Waterway Port, Coastal, and Ocean Engineering*, 127(3):125–134, 2001.

[39] B. M. Sumer and J. Fredsøe. *The mechanics of scour in the marine environment.*, volume 17. World Scientific - New Jersey - Singapore - London - Hong Kong., 2002.

[40] B. M. Sumer, J. Fredsøe, and N. Christiansen. Scour around vertical pile in waves. *Journal of Waterway Port, Coastal, and Ocean Engineering*, 118(1):15–31, 1992.

[41] T. Toue, H. Katsui, and K. Nadaoka. Mechanism of sediment transport around a large circular cylinder. pages 2867–2878, 06 1993.

[42] D. Van den Eynde, R. Brabant, M. Fettweis, F. Francken, V. Van Lancker, M. Sas, and J. Melotte. Monitoring of hydrodynamic and morphological changes at the c-power and belwind offshore windmill sites-a synthesis. *Offshore wind farms in the Belgian part of the North Sea: Early environmental impact assessment and spatio-temporal variability*, pages 19–36, 01 2010.

[43] M. Welzel. Wave-current-induced scouring processes around complex offshore structures. *Coastal Engineering Proceedings*, 09 2021.

[44] M. Welzel, A. Schendel, N. Goseberg, A. Hildebrandt, and T. Schlurmann. Influence of structural elements on the spatial sediment displacement around a jacket-type offshore foundation. *Water*, 12:1651, 06 2020.

[45] M. Welzel, A. Schendel, A. Hildebrandt, and T. Schlurmann. Scour development around a jacket structure in combined waves and current conditions compared to monopile foundations. *Coastal Engineering*, 152, 06 2019.

[46] M. Welzel, A. Schendel, T. Schlurmann, and A. Hildebrandt. Volume-based assessment of erosion patterns around a hydrodynamic transparent offshore structure. *Energies*, 12, 08 2019.

[47] R. Whitehouse, J. Harris, J. Sutherland, and J. Rees. An assessment of field data for scour at offshore wind turbine foundations. 01 2008.

[48] R. Whitehouse, J. Harris, J. Sutherland, and J. Rees. The nature of scour development and scour protection at offshore windfarm foundations. *Marine pollution bulletin*, 62:73–88, 10 2010.

[49] R. J. S. W. Whitehouse. *Scour at marine structures: A manual for practical applications.* Thomas Telford Publications, London, 1998.

[50] WindEurope. Offshore wind in europe: Key trends and statistics 2018. Technical report, WindEurope, 2019.

[51] C. Yuan, B. Melville, and K. Adams. Scour at wind turbine tripod foundation under steady flow. *Ocean Engineering*, 141:277–282, 09 2017.

[52] M. ZHAO, B. TENG, and L. CHENG. Numerical simulation of wave-induced local scour around a large cylinder. *Coastal Engineering Journal*, 46:291–314, 2004.

OFFSHORE WIND

Development of a genetic algorithm code for the design of cylindrical buoyancy bodies for floating offshore substructures

V. Benifla[a] and F. Adam[a]

[a]Lehrstuhl für Windenergietechnik, University of Rostock, 18051 Rostock, Germany.

E-mail: `victor.benifla@uni-rostock.de`

Keywords: Floating offshore wind, buoyancy body, structural analysis, design optimization, genetic algorithm, LCoE reduction.

1 Introduction

Offshore wind farms' role in supplying clean energy for the increasing demand is becoming more important. Ecological and economical boundary conditions have major influences on further developments of these offshore technologies. Especially floating foundations, which have a great potential for offshore wind farms in water depths greater than 40 m, will be a driver for the industry. The Levelized Cost of Energy (LCoE) for floating offshore wind must decrease significantly to be competitive with fixed offshore wind projects or even with onshore wind projects. A floating offshore wind system includes many different components and one of the most relevant in terms of cost is the floating substructure. Therefore it is important to consider in the early phase of its development an optimized substructure's design in terms of production, transport and maintenance costs. Recently, different substructure concepts and modular components, such as buoyancy bodies, have been developed with the aim of reducing the production cost by serializing the fabrication procedure [1]. Current substructures' designs involve buoyancy bodies in their configuration, which are similar particularly for Tension Leg Platform (TLP) and semi-submersible substructures. An universal buoyancy body could be integrated as a standardized component in the primary structure of floating wind turbine foundations [3].

2 Universal Buoyancy Body Design Optimization

In this study, the focus is set on cylindrical buoyancy body design optimization by working with a genetic algorithm code. Currently, different foundation concepts with different structural designs exist and can be roughly separated into three types; Spar, Semi-submersible and TLP [2]. The structural design of these floating foundations is usually strongly orientated towards ship structure design with lateral and vertical stiffeners that requires a significant manufacturing period. To reduce the cost and the manufacturing time of floating substructures significantly, the concept and design of a Universal Buoyancy Body, strongly orientated on the design and manufacturing process of monopiles and which could be integrated to different substructures, is presented here. To verify the design and to estimate potential cost reduction, the presented universal buoyancy body design, is compared to a current typical ship oriented structure buoyancy body of the GICON-TLP. In addition, a design optimization tool based on genetic algorithm, that parameterizes the universal buoyancy body depending on loads acting on the structure as well as manufacturing and floater specific dimension restrictions, is also detailed here.

3 Preliminary Results

A first Universal Buoyancy Body design is modeled with the Finite Element Method tool ANSYS using APDL scripts. This first design have the same height as the old buoyancy body used for comparison, and is scaled to provide the same buoyancy force. Relevant design loads such as tendon rope loads and hydrostatic water pressure loads are derived from from multi body load simulation. The strength in the Ultimate Limit State (ULS) and the fatigue resistance in the Fatigue Limit State (FLS) are analyzed and verified according to standards. Most critical structural parts of the buoyancy body, such as the weld seams of the welded steel layers are also locally modeled and verified.

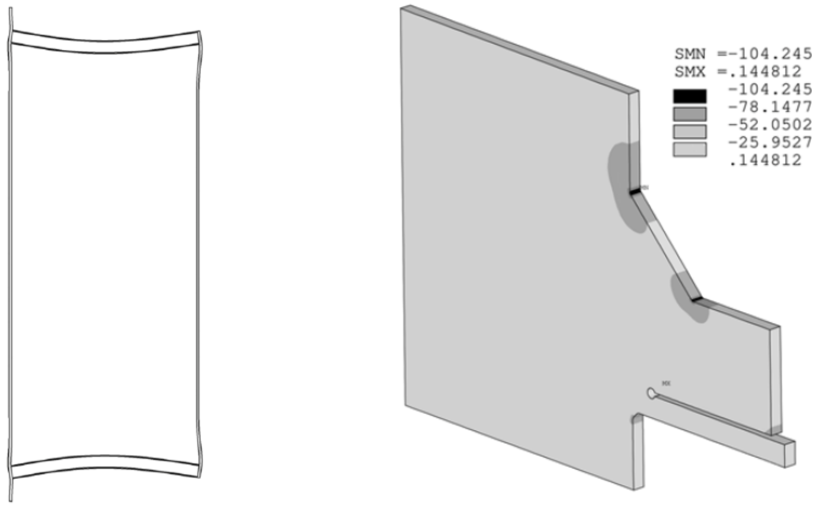

Figure 1: Exemplary results for global model and most critical weld seam in the FLS.

The optimization tool developed is then capable of generating multiple geometries of the Universal Buoyancy Body and propose the best options based on the chosen objective of the optimization process (minimize mass/cost, stress etc...). Different Genetic Algorithms are also implemented to speed up the process and to be able to perform multi-objective optimization.

Acknowledgments

This research is made in the context of the FLOAWER project which has received funding from the European Union's Horizon 2020 research and innovation program under the Marie Sklodowska-Curie grant agreement N° 860879. A special thanks also to GICON – Großmann Ingenieur Consult GmbH to take over the responsibility as hosting institution for secondment and for providing the figures and basic buoyancy body models as example to be optimized.

FLOAWER
FLOAting Wind Energy networK

This project has received funding from the European Union's Horizon 2020 research and innovation programme under the Marie Skłodowska-Curie grant agreement N° 860879.

References

[1] F. Adam, C. Behr, D. Walia, U. Ritschel, and J. Grossmann. A modular tlp floating substructure to maximize the flexibility within the supply chain. In *27th International Ocean and Polar Engineering Conference*, San Francisco, California, USA, 06 2017.

[2] S. Butterfield, W. Musial, J. Jonkman, and P. Sclavounos. Engineering challenges for floating offshore wind turbines. In *2005 Copenhagen Offshore Wind Conference Copenhagen, Denmark*, United States, 09 2005. National Renewable Energy Laboratory (NREL).

[3] M. Lutz, D. Walia, and F. Adam. *Development of a universal useable and in series production manufacturable buoyancy body design for TLP and semi-submersible*. Elsevier, Lisbon, Portugal, 1 edition, 10 2020. papers presented at the 4th International Conference on Renewable Energies Offshore (RENEW 2020).

Sensitivity analysis of Storm Ciara to WRF physics parameterizations

A Vemuri[a], S Buckingham[a], W Munters[a], J Helsen[b], and J van Beeck[a]

[a]von Karman Institute for fluid dynamics
[b]Vrije Universiteit Brussel

`E-mail: adithya.vemuri@vki.ac.be`

Keywords: Mesoscale modelling, extreme weather phenomena, Belgian North Sea, wind energy and Storm Ciara

Abstract

This extended abstract presents work that is part of the cSBO SeaFD project that aims at providing a deeper insight into extreme weather phenomena found responsible for early drive-train failures of commercial wind farms located in the Belgian offshore concession zone. The case of Storm Ciara on the 10th February 2020, pertaining to fast changes in wind direction over a short period of time as observed by a commercial offshore wind farm, is considered for this study. This work utilizes the numerical weather prediction model, Weather, Research and Forecasting (WRF) to perform a single-event sensitivity analysis for the extreme weather case of Storm Ciara. The study considers hourly and 3-hourly reanalysis dataset for initial boundary conditions combined with scale-aware and non-scale aware physics parameterizations defined within WRF physics library. The results indicate an advantage in better representation of dynamics of local weather systems, evaluated against RADAR and SCADA data, when simulated with hourly reanalysis dataset and scale-aware physics parameterizations.

1 Introduction

Extreme Weather Events (EWE) play a significant role in determining the operational lifetime and power production levels of a commercial wind farm, making them critical for determining representative ultimate and fatigue loading conditions. This work aims at analyzing EWE that are found responsible for early drive-train failures observed in the Belgian North Sea. Extreme weather events such as low level jets, high wind shear, high wind veer and wind gusts are observed to be part of the local weather systems over the North Sea [1]. The case of Storm Ciara that occurred on the 10th February 2020 over the European continent is selected for this sensitivity analysis.

2 Methodology

The WRF mesoscale modelling framework [2], is utilized to predict fast changes in wind direction as experienced by offshore wind farms located in the Belgian offshore concession zone during the early hours of 10th February 2020 during Storm Ciara. A sensitivity analysis is conducted to evaluate the optimal WRF set-up to accurately predict the dynamics of the local weather systems during this time period. The respective numerical experiments are evaluated against RADAR data from the Royal Meteorological Institute - Belgium (KMI-B) and SCADA data from a commercial offshore wind farm located in the Belgian North Sea. The sensitivity analysis considers hourly and 3-hourly reanalysis dataset for the initial boundary conditions combined with scale-aware and non-scale aware physics parameterizations for: Planetary Boundary Layer (PBL), cumulus and microphysical representations. A total of 12 simulations considering aforementioned combinations of WRF options are considered for this sensitivity analysis.

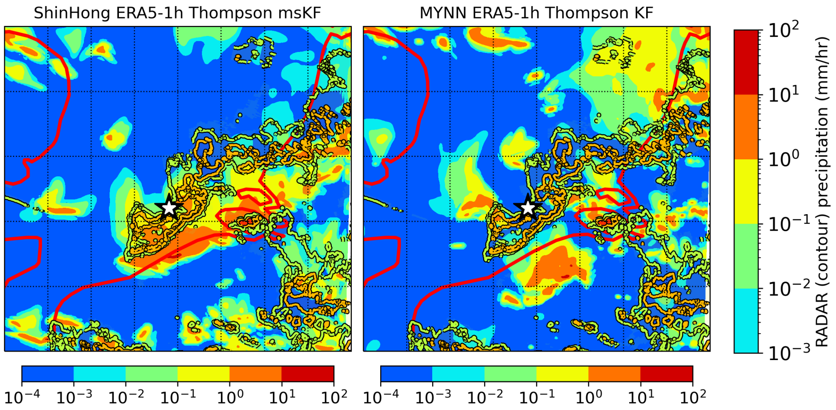

Figure 1: Presented plots compare 2 WRF physics setups considering scale-aware physics parameterizations and non-scale aware physics parameterization for PBL and cumulus schemes respectively. The simulations are compared to observed RADAR reflectivity (in mm/hr) from KMI-B. WRF simulated reflectivity is represented by filled contours and observed RADAR reflectivity by contour lines. Color profile for either plots are normalized, therefore similar color will represent similar magnitude of reflectivity/precipitation.

3 Results and conclusions

For brevity purposes this abstracts presents the results for 2 simulations considered for the sensitivity analysis. The simulations presented here consider hourly reanalysis dataset along with: 1) scale-aware Shin-Hong PBL, multi-scale Kain Fritsch cumulus and Thompson microphysics schemes, and 2) non-scale aware MYNN PBL, Kain Fritsch cumulus and Thompson microphysics schemes. Figure 1 presents the comparison of simulated RADAR reflectivity versus observed RADAR reflectivity for the aforementioned WRF setups. The simulated and observed RADAR reflectivity are converted to precipitation metric in mm/hr using the Marshall-Palmer relation. The results indicate, the WRF setup with scale-aware physics parameterizations to better overall represent of observed precipitation cell (represented in contour lines in fig. 1) versus the non-scale aware WRF setup. The Belgian offshore wind farms are represented by *star* in said plots.

Overall, the simulated Radar reflectivity evaluated against RADAR observations from KMI-B are found most sensitive to cumulus and microphysical parameterizations for the event considered. A clear advantage in utilizing scale-aware cumulus over non-scale aware cumulus parameterizations for the better representation of local weather systems is observed. Similarly, scale-aware PBL scheme performed better (against SCADA data) in comparison to non-scale aware PBL scheme for the event considered.

Acknowledgements

Work by the author(s) was supported by Agentschap Innoveren and Ondernemen (VLAIO) through the Strategisch Basisonderzoek voor Clusters (cSBO) project SeaFD. Observed RADAR reflectivity was provided by the dual-polarization C-band radar from the Royal Meteorological Institute of Belgium (KMI-B), located in Jabbeke at the Belgian North Sea coast.

References

[1] Kalverla, C P, Steeneveld G J, Ronda R J and Holtslag A A 2017 *Journal of Wind Engineering and Industrial Aerodynamics* **165** 86–99

[2] Skamarock W C, Klemp J, Dudhia J, Gill D, Barker D, Duda M, Huang X, Wang W and Powers J 2008 *Natl. Ctr. Atmos. Res., Boulder, CO* **7**

17th EAWE PhD Seminar on Wind Energy
3-5 November 2021
Porto, Portugal

Uncertainties of long-range lidar measurements in the far wake offshore

P M S Orozco[a], J J Trujillo[a], M Kühn[b], and T Neumann[a]

[a]Renewables, UL International GmbH, Ebertstrasse 96, 26382 Oldenburg, Germany
[b]Institute of Physics, ForWind – Carl von Ossietzky University of Oldenburg,
Küpkersweg 70, 26129 Oldenburg, Germany

E-mail: `priscila.orozco@ul.com`

Keywords: lidar; wind speed uncertainties; far wake; sea surface leveling; large-eddy simulations

1 Introduction

The mounting flexibility of lidars combined with their ability to provide detailed wind field measurements at large distances makes them best suitable for studying far wakes. They can be mounted in rough site conditions such as in offshore wind farms and on top of the nacelle of wind turbines, thus following the turbine movements and consequently simplifying data analysis. Previous efforts to measure wakes with nacelle-mounted lidars [e.g., 1–3] have proven that they are capable of capturing wake dynamics with good spatial and temporal resolution. On the other hand, similarly as any other measurement unit, nacelle lidars have measurement uncertainties.

Few research works [4, 5] have considered uncertainties in nacelle lidar measurements in the wake of a wind turbine. In case the uncertainty in the lidar's measurement points were considered, the common practice is to calibrate lidars on the ground before they are mounted on the nacelle [such as in 6], but never on site. For this purpose, the Sea Surface Leveling (SSL) technique offers the possibility of assessing the lidar mounting orientation on an offshore site against the sea surface level. Tilt and roll time series are derived from the the application of SSL on nacelle lidar scans, configured to measure over 360° pointing at the sea surface (thus forming an inverted conical shape). Finally, the mounting error of a nacelle lidar is retrieved. It is particularly important to quantify this error when measuring wind speed in far wakes since its effect increases with range.

Here we aim to quantify the uncertainties in lidar measurements in the far wake of a wind turbine arising from the lidar unleveled mounting and nacelle vibrations. We use SSL to quantify the mounting error in the wind speeds measured by a nacelle lidar from the RAVE PARKCAST project at the alpha ventus offshore wind farm (German Bight). We apply SSL on nearly one month of StreamLine-XR lidar 360° scans. Within this process, we use optimized least-squares to fit an ellipse to the estimated sea surface positions, which results into tilt and roll offsets (Fig. 1 shows an example). We have been conducting simulations by means of a lidar solver embedded on a Large-Eddy-Simulations (LES) wind field, coupled with an actuator disk model. Our aim is to assess the effect of nacelle vibrations on the lidar measurement positions. Simulations to test the assumption of a Gaussian pulse shape have also been carried out to quantify the associated uncertainties in wind speed.

2 Results

After computing tilt and roll offsets from the lidar scans, we analyze time series of 10-min tilt and roll averages derived from the lidar inclinometer and SSL. We find mean mounting errors of -0.06° and -0.21° in tilt and roll, respectively. When comparing our findings to a similar lidar deployed on a turbine transition piece, we identify that the roll error is one order of magnitude larger for the nacelle condition while the tilt error is similar. This is unforeseen in the sense that nacelle lidars are known to be more sensitive to tilt instead of roll.

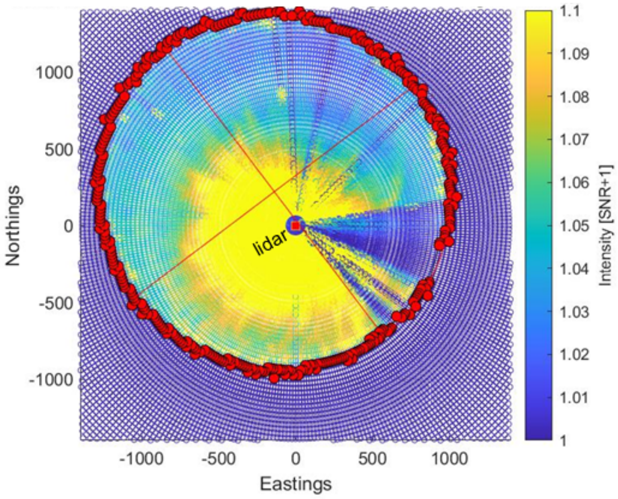

Figure 1: Example of a SSL lidar scan, showing the estimated positions where the lidar beams touched the water (red dots). An ellipse is fitted to this circular shape (main and minor axes indicated by the red lines) to retrieve tilt and roll offsets.

3 Conclusions

We find that the mounting error in roll for a nacelle lidar is unexpectedly one order of magnitude larger than that of a similar lidar mounted on a transition piece. Therefore, we hypothesize that the nacelle vibrations are likely embedded in the lidar's mounting errors in this study. If confirmed through lidar-LES simulations, the nacelle vibrations are then more pronounced in the cross-stream direction, supported by the high roll error. Besides any particularities of the measurement conditions in this study, we conclude that mounting errors cannot be neglected in the far wake when using nacelle lidars. Furthermore, the extrapolation of measurements from lidars mounted on a wind turbine transition piece to the nacelle and vice-versa should be carefully considered.

Acknowledgements

This research is carried out within the scope of the LIdar Knowledge Europe (LIKE) project, H2020-MSCA-ITN-2019. The authors would like to thank the funding provided by the European Union, grant no. 858358, and the data made available by the RAVE (research at alpha ventus) initiative, the latter funded by the German Federal Ministry of Economic Affairs and Energy (BMWi; see www.rave-offshore.de).

References

[1] Trujillo J J, Bingöl F, Larsen G C, Mann J and Kühn M 2011 *Wind Energy* **14** 61–75

[2] Aitken M L and Lundquist J K 2014 *Journal of Atmospheric and Oceanic Technology* **31** 1529–1539

[3] Trujillo J J, Seifert J K, Würth I, Schlipf D and Kühn M 2016 *Wind Energy Science* **1** 41–53

[4] Trabucchi D, Trujillo J J and Kühn M 2017 *Energy Procedia* **137** 77–88

[5] Trujillo J J 2017 *Large scale dynamics of wind turbine wakes: Measurement and modelling in the full field* Ph.D. thesis Carl von Ossietzky University of Oldenburg

[6] Wagner R, Courtney M S, Pedersen T F and Davoust S 2016 *Wind Energy* **19** 1269–1287

17th EAWE PhD Seminar on Wind Energy
3-5 November 2021
Porto, Portugal

Kinematics of Partially Installed Turbines

Aljoscha Sander[a,b], Albert Baars[c], and Eize Stamhuis[a]

[a]Energy and Sustainability Research Institute Groningen, Unversity of Groningen, Groningen, the Netherlands
[b]Institute for Integrated Product Development (ForWind – Center for Wind Energy Research), University of Bremen, Bremen, Germany
[c]City University of Applied Sciences Bremen, Bremen, Germany

E-mail: `aljoscha.sander@rug.nl`

Keywords: single blade installation, structural response, wind loads, wave loads

Abstract

Offshore wind will become one of the main sources of renewable energy. Available offshore wind capacity in Europe, the Americas and Oceania exceeds even conservative estimates of future electricity demand [1]. Unfortunately today, offshore wind must still compete with fossil fuels. To further improve competitiveness of offshore wind, turbine size and capacity have been steadily increasing. However, it stands to reason, that the already difficult and expensive installations of offshore wind turbines will become even more difficult in the future, specifically single blade installation: already today relative motions between blade root and rotor hub induced by wind and waves put heavy constrains on the allowable weather during installation and thus induce long waiting times. If the weather limits are exceeded collision between the blade root and the rotor hub may lead to damages, which in turn further delay the installation and may require repairs and premature maintenance. Now, with increasing component size, motion amplitudes will naturally increase as well, thus exacerbating the challenges associated with single blade installation. In a recent measurement campaign, Sander et al. [2, 3, 4] found, that partially installed turbines vibrating transversely under wind and wave loads show intricate kinematic patterns - orbits - where direction, and amplitude of vibrations change rapidly during installation. Figure 1 illustrates the formation of orbits during single blade installation.

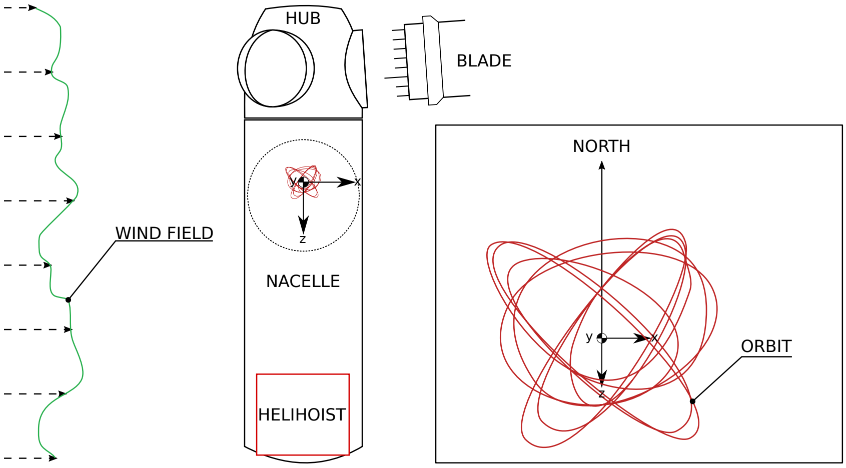

Figure 1: Orbits observed during single blade installation of the wind farm *Trianel Windpark Borkum II.*

In the PhD project presented here, the kinematics (orbits) of partially installed offshore wind turbines, where tower and nacelle are present, but no blades have been installed, are to be investigated. Possible mechanisms have been identified that could contribute to the formation of orbits: anisotropic damping and stiffness, caused by soil inhomogeneity or structural imperfections may induce the transfer of energy into a mode different from the predominant direction, leading to the formation of orbits. The eccentricity of the nacelle's mass may lead to orbits by inducing torsion. Different phenomena pertaining to the sea state, such as wave spreading, current loads or crossing sea states may further contribute to rapid changes in direction. Finally vortex shedding and turbulent buffeting present the least understood phenomena that may contribute strongly to orbit formation. Whether a specific phenomenon can be singled out to explain the kinematics observed or whether the combination of several effects, resulting in general perturbations of the oscillating turbine remains to be seen. To investigate the different possible mechanisms, three approaches have been chosen:

- A cantilevered beam undergoing transverse vibrations will be investigated experimentally. Two dimensional excitation will allow to investigate different types of loading. Mounting different eccentric masses on the free end of the beam will reveal the interaction between the eccentric inertial forces acting on the beam and different types of loading.
- Numerically modelling the transversely vibrating beam as a two dimensional, driven, damped oscillator will allow the examination of the vast parameter space of forcing functions that may lead to the formation of orbits.
- High-fidelity computational fluid dynamics simulations with a coupled structural model to account for fluid structure interaction will be used to explore the effects of vortex shedding and turbulent buffeting on the formation of orbits. The open source software OpenFOAM will be used to implement the simulations.

In situ data from both offshore and onshore installation measurement campaigns will be used to validate simulations and experiments. The results obtained through this dissertation will contribute to better understand the kinematics of offshore wind turbines under installation and subsequently help to improve future installations.

Acknowledgements

The author acknowledges the support from University of Bremen.

References

[1] Deng Y Y, Haigh M, Pouwels W, Ramaekers L, Brandsma R, Schimschar S, Grözinger J and de Jager D **31** 239–252 ISSN 0959-3780 URL `http://www.sciencedirect.com/science/article/pii/S0959378015000072`

[2] Sander A, Haselsteiner A F, Barat K, Janssen M, Oelker S, Ohlendorf J H and Thoben K D (American Society of Mechanical Engineers Digital Collection) URL `https://asmedigitalcollection.asme.org/OMAE/proceedings/OMAE2020/84416/V009T09A069/1093136`

[3] Sander A, Meinhardt C and Thoben K D pp 2189–2205 URL `https://www.easdprocedia.org/conferences/easd-conferences/eurodyn-2020/9178`

[4] Sander A Oscillations of Offshore Wind Turbines undergoing Installation I: Raw Measurements URL `https://zenodo.org/record/4498779`

A Deep Learning Model for the Structural Health Monitoring of Floating Offshore Wind Turbine Mooring Lines based on Modal Parameters

N Gorostidi[a,b] and V Nava[b,c]

[a]University of the Basque Country, Leioa, Spain
[b]Basque Center for Applied Mathematics, Alamaeda Mazarredo 14, 48009 Bilbao, Spain
[c]TECNALIA, Basque Research and Technology Alliance (BRTA), Parque Tecnológico de Bizkaia, Edificio 700, 48160 Derio, Spain

`E-mail: ngorostidi@bcamath.org`

Keywords: Offshore wind, Deep Neural Network, Structural Health Monitoring, Mooring line, Frequency-based, Biofouling, Anchoring, Inverse problem

Abstract

Although the installation of floating offshore wind turbines presents numerous technical and environmental benefits, excessive maintenance costs keep these systems economically unfeasible. This study, developed within the VIVIR Project sponsored by Iberdrola Foundation, aims at designing an assisting tool for the remote planning of mooring line maintenance operations. A multi-class classification Deep Neural Network (DNN) structure is implemented to detect and predict different kinds of mooring line failure modes in real time based only on the horizontal displacements of the platform caused by wave, drift and wind forces. A simplified 1-DOF model is solved combining calibrated structural and metoceanic parameters to generate an extensive database, which contains the necessary time and frequency-based features of the system's response to be fed into the DNN. Promising results show 97% accuracy when predicting severe biofouling and anchoring failures, that is, ±10% changes on mass, damping coefficient and linear stiffness of the system. Global accuracy seems proportional to sea state duration, peaking when three-hour-long responses are used. The algorithm's performance drops when modelling less severe forms of damage. Sensibility studies were carried out on each failure mode individually considering different degrees of severity, allowing for the prediction of multiple failure modes occurring at once and the estimation of remaining component life. Sea state duration can be significantly reduced when more severe damage is expected without compromising network accuracy. The inverse modelling approach seems generalisable for more comprehensive numerical models and other subsystems within floating offshore wind turbines.

Keywords: Offshore wind, Deep Neural Network, Structural Health Monitoring, Mooring line, Frequency-based, Biofouling, Anchoring, Inverse problem

1 Introduction

Environmental conservation constitutes one of the greatest challenges humanity is facing in this modern era. Sustainable recovery is crucial after the most recent economic downturn caused by the coronavirus pandemic. Nonetheless, high installation and maintenance costs usually keep green forms of energy less profitable than fossil fuels. Because of this, governments and international institutions have implemented policies and regulations to encourage the deployment of sustainable energy systems. Wind power has seen a rapid development over the last few decades, currently generating more than 35% of the EU's total renewable energy [1]. Controversy, however, has arisen around the issue of noise pollution following the recent massive installation of onshore wind farms, which might potentially lead to long-term human health effects such as headaches, stress or cardiovascular disease. That is just one of the many reasons for which governments and companies are currently investing in research and development of offshore wind systems. Not only are they beneficial from an environmental perspective but, from a technical standpoint, offshore wind is much faster and steadier than on-land wind, thus yielding higher and more reliable energy production. Floating Offshore Wind Turbines (FOWTs) are one of the latest trends in wind energy research, as the installation of wind power systems further away from coastlines could maximise wind availability while keeping noise and visual pollution to a minimum. In fact, multinational companies such as Iberdrola have already started floating wind projects worth billions of euros [2]. The main issue about these systems is that their excessively high installation, maintenance and commissioning costs keep them away from economic feasibility. A 2019 study by Nava et al. [3] shows how all these expenses, usually labeled O&M costs for Operation and Maintenance, represent over half the total cost of an offshore wind project. The structural health monitoring of offshore wind systems has over the recent past been the object of numerous studies evaluating the reliability of multiple subsystems within both fixed and floating turbines [4, 5]. These papers apply the notion of FMEA, short for Failure Modes and Effects Analysis, to relate failure frequency and economic impact of different kinds of damages so that maintenance operations can be planned and coordinated in advance. The first derivation of the theoretical fundamentals behind this inverse problem was introduced in the late 1960s by Lifshitz and Rotem [6], who observed the variations of the dynamic modulus, that is, the stress-to-strain ratio under vibrating loads, to identify damages in composite materials. This approach has since then been applied to a wide range of engineering fields, such as the mechanical, aerospace and civil industries. Chang et al. [7], for instance, applied these concepts for the condition monitoring of floating oil platforms. A review of vibration-based methods was presented by Doebling et al. [8]. AI-based approaches are nowadays the most employed methods for the structural health monitoring of offshore wind turbines. Recent studies have designed neural networks to monitor offshore wind turbine gearbox failures based on their dynamic response in both time and frequency domains [9, 10, 11]. The implementation of deep learning algorithms coupled with vibration-based methods for the structural health monitoring of mooring lines nonetheless constitutes a complete innovation in the field of floating offshore wind. Further approaches applied to O&M cost reduction, such as thermal imaging and acoustic emission monitoring, have been extensively reviewed by Martinez-Luengo et al. [12] and Joshuva et al. [13]. This research aims at reducing these costs by applying deep learning algorithms to predict failure in FOWT mooring lines in real time. A simple yet generalisable numerical approach is presented to model the fluctuating displacements of the turbine platform caused by wave and wind conditions, from which several key statistics are computed. The implemented neural network is trained with these frequency-domain parameters only, ultimately being able to predict whether the studied turbine is failing or not, thus eliminating the need for complex sensorization and unnecessary commissions. This inverse approach is intended to assist companies in the optimisation process of their planning for maintenance operations.

2 Mathematical Description

The implemented 1-DOF model predicts the health status of mooring subsystems within a floating offshore turbine based only on the surge of its platform, that is, the x-displacements as shown in Figure 1(a). Due to the unavailability of real data, an extensive set of synthetic data representing the platform's response is obtained by solving the non-linear second-order ODE

$$M \cdot \ddot{x} + C \cdot \dot{x} + K_3 \cdot x^3 + K_1 \cdot x + K_0 = F_{wave}\left(H_S, T_P, t\right) + F_{drift}\left(H_S^2\right) + F_{wind}\left(V\right), \tag{1}$$

from which M is the system's mass, C is its damping coefficient, K_3, K_1, K_0 are its stiffness coefficients, H_S is the wave's significant height, T_P is its peak period and V stands for wind velocity. Wave forces are calculated by applying an inverse Fourier Transform on the Pierson-Moskowitz spectrum [14], which relates the distribution of energy of the ocean waves to their frequency using the equation

$$S_{wave} = \frac{5}{16} \cdot H_S^2 \cdot \omega_P^4 \cdot \omega^{-5} \cdot e^{-\frac{5\cdot\omega}{4\cdot\omega_P}}, \tag{2}$$

leading to a time-variant force. The drift force is simply assumed as a proportionally quadratic interpolation with respect to H_S between standard values, while wind forces are calculated by digitizing the experimental correlation derived by Wan et al. [15]. While metoceanic parameters are combined using arrays of values to add comprehensiveness and accuracy to the implemented model under different

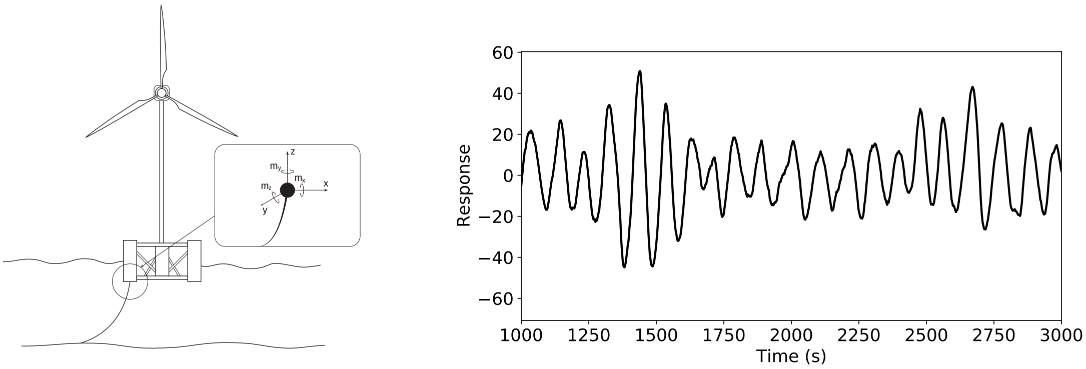

(a) (b)

Figure 1: (a) Schematic representation of degrees of freedom of a floating offshore wind turbine's mooring lines and (b) evolution of the platform's surge over any given time frame.

conditions, variations are induced to the structural parameters to recreate a series of damaged configurations, which ultimately provide health status labels. The obtained displacements and their evolution in time help the program calculate some key statistical parameters, including for instance signal and period means and standard deviations, peak frequencies and several momenta, which eventually are the inputs from which the DNN predicts failures in the system. The DNN then interprets these inputs and matches them to one of the health status conditions. In this study, biofouling damages occur when mussels, algae and other marine microorganisms attach to the mooring chains, thus making the lines heavier, which evidently causes changes in their behaviour. Mooring failure refers to alterations on the chain's stiffness caused by wear and/or fatigue stress, and anchoring damages are produced upon undesired displacements of the mooring line foundation. The numerical modelling of these configurations is presented in Table 1.

Condition	**Minor Damage**	**Severe Damage**
Undamaged	–	–
Biofouling	$+5\% M, C$	$+15\% M, C$
Mooring	–	$+10\% K_3$
Anchoring	–	$+10\% K_1$

Table 1: Implemented damaged configurations, which ultimately represent the five categories to which the neural network assigns cases: one for each failure mode, plus an extra one considering minor biofouling damage.

A sample extracted from one of the many obtained responses is presented in Figure 1(b), where it can be appreciated that its period corresponds to a frequency of approximately 0.01 Hz. Once the differential equation has been solved, a Fourier Transform is performed on the obtained response to obtain its frequency spectrum, from which most of the simulation outputs are computed. These parameters are stored alongside the time-domain statistics and the metoceanic variables defining each sea state as seen on Table 2, ultimately assembling an extensive set of synthetic data, used for the training and validation stages of the DNN. Each statistic represents an input to the network. By combining all inputs, an 11D representation is built to estimate the output probabilities for each category, with which the cost of the algorithm is established. All of these parameters have been included, albeit some of them seemingly redundant, in the dataset as obtained from time signals and Power Spectral Densities, or PSDs, thus leaving room for further dataset optimisation. From this, the network corrects all weigths and biases used by the algorithm thanks to the mathematical procedures known as gradient descent and backpropagation. In order to accomplish that, and after a series of data analysis and visualization tasks, the program splits the obtained data in a training set and a validation set, the latter being employed to estimate the accuracy of the model as it is trained in a simultaneous manner, thus storing its transient behaviour. A graphical representation of the complete simulation, training and validation processes is shown in Figure 2, while the characteristics of the implemented DNN can be seen in Figure 3.

Variable	Definition	Variable	Definition
H_S	Significant Height	$T_{peak,1}$	Highest Peak Period
T_P	Peak Period	$f_{peak,1}$	Highest Peak Frequency
V	Wind Velocity	$T_{peak,2}$	Second Peak Period
$\bar{X}_{signal}$	Signal Mean	$f_{peak,2}$	Second Peak Frequency
σ_{signal}	Signal Standard Deviation	m_0	Momentum-0
$\bar{X}_{period}$	Period Mean	m_1	Momentum-1
σ_{period}	Period Standard Deviation	m_2	Momentum-2

Table 2: Stored outputs at the end of the simulation. H_S, T_P and V, unlike the rest, are not inputs of the deep neural network, but are used for filtering and other data analysis purposes.

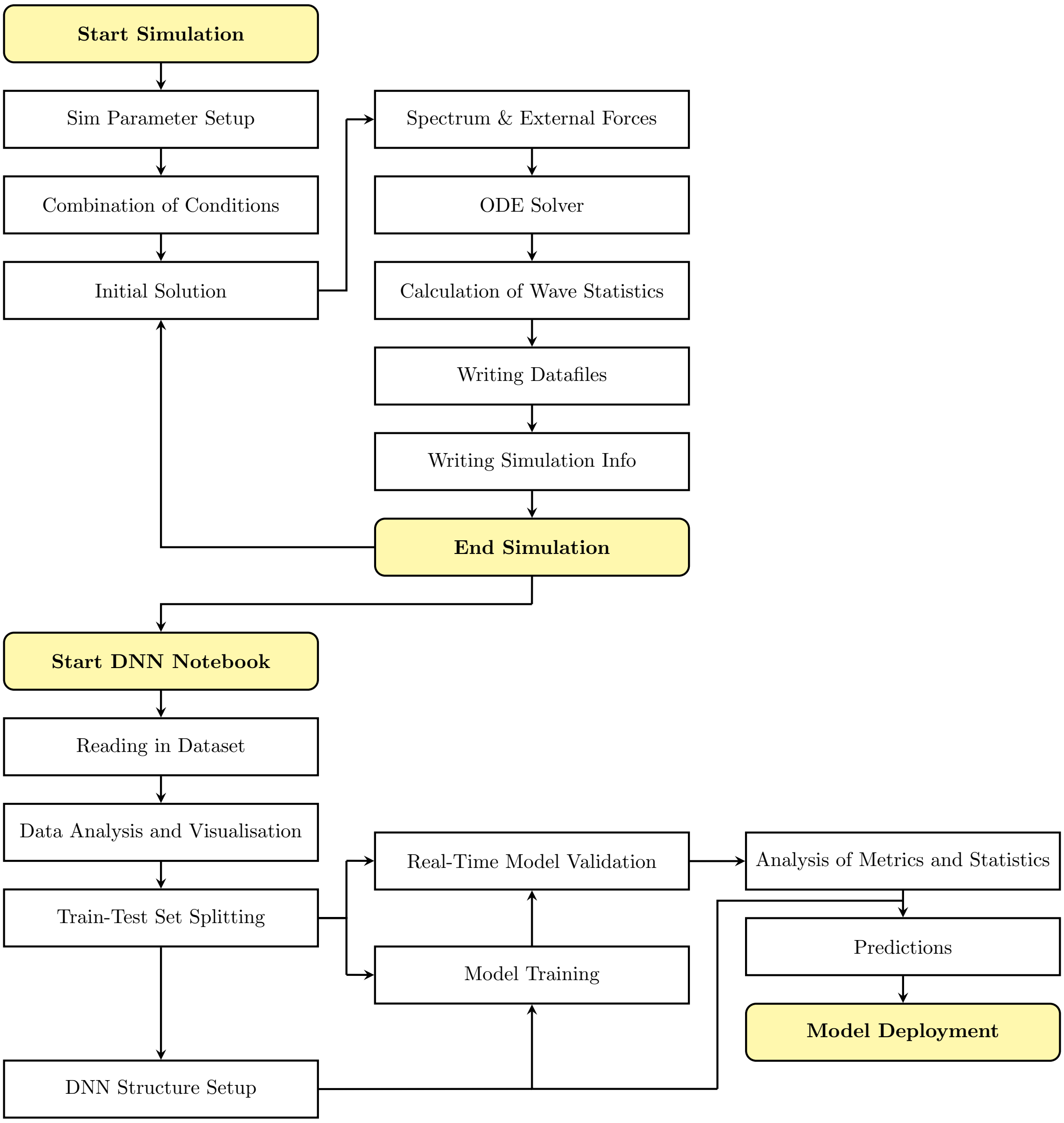

Figure 2: Flowchart of the complete simulation, dataset generation, visualisation and analysis and deep neural network training and validation processes.

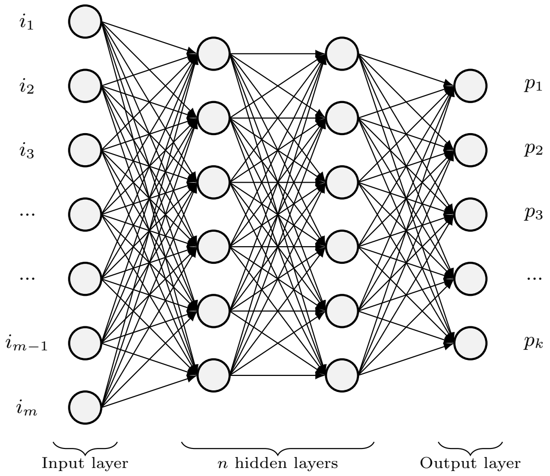

- Neurons per layer: 11 (input), 64, 8, 5 (output)
- Activation functions: RLU, Softmax (output)
- All fully-connected layers
- Trained for $\sim 15,000$ epochs
- Cost function: Categorical Cross-entropy
- Optimiser: Adam, learning rate $= 0.005$
- Early Stopping: Validation loss monitoring, patience $= 1,000$ epochs

Figure 3: Schematic representation and characteristics of the implemented deep neural network, where i_m and p_k represent the algorithm's inputs and output probabilities, respectively.

3 Analysis of Results

Validation loss and accuracy are presented in Figure 4 for the earliest simulations, where a proportional relation between sea state duration and network accuracy can be appreciated. However, and even after noticing a proper network behaviour during the training stage, it can be seen that, in the best-case scenario, overall percentages are only in the low seventies when it comes to accurately describe the mooring line's health status. An analysis of these results is therefore carried out yielding the results shown in Figure 5. It can be observed that the severe biofouling status, that is, significant increases in the mass and damping coefficients in the model, is well distinguished with respect to other conditions, much like variations of the linear stiffness of the system. The lack of overall accuracy, however, seems to arise among undamaged samples and those affected by minor biofouling and wear issues. The confusion matrix displayed on Figure 5(d) suggests that, even after a very strict description of mooring line failure modes, the algorithm understands there are differences among these states. These differences seem nonetheless too small for the network to make clear distinctions amongst these intermediate categories.

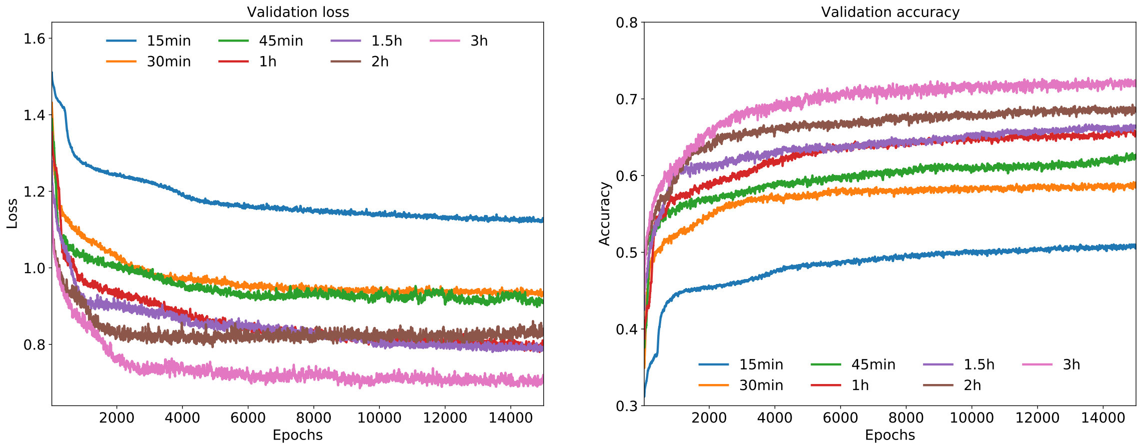

(a) (b)

Figure 4: Results from the five-output DNN's validation process: (a) categorical cross-entropy loss and (b) validation accuracy

	5-Output DNN			3-Output DNN		
Condition	**Precision**	**Recall**	**F1-Score**	**Precision**	**Recall**	**F1-Score**
Undamaged	0.709	0.730	0.719	0.983	0.962	0.972
Biofouling-sev1	0.610	0.569	0.589	–	–	–
Biofouling-sev2	0.941	0.941	0.941	0.964	0.976	0.970
Mooring	0.526	0.531	0.528	–	–	–
Anchoring	0.878	0.900	0.889	0.958	0.966	0.962
Accuracy	**0.738**	**0.738**	**0.738**	**0.968**	**0.968**	**0.968**

Table 3: Metrics and statistics for both the original and simplified DNNs.

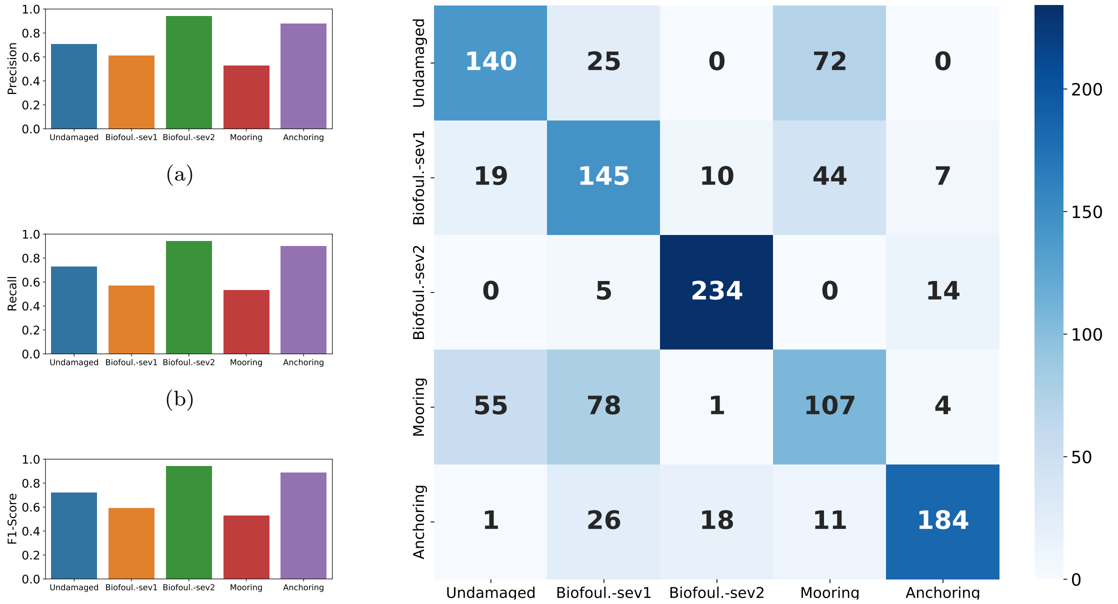

(a) (b) (c) (d)

Figure 5: Metrics and statistics for the original five-output DNN: (a) precision by category, (b) recall by category, (c) F1-Score by category and (d) heatmap relating predictions on the validation set to true conditions.

To verify the correct behaviour of the model, a simplified three-output network was also implemented considering only the most severe damage modes, producing the much more promising results seen in Figure 6, where it can be seen that the network is able to accurately describe the health status of the turbine for over 90% of the cases with sea states as short as half an hour. Not only that, but in this case, the network reaches over 80% accuracy using just 15-minute-long responses, leading to the conclusion that the more severe the damage, or the more lax the damage criterion, the shorter the sea state duration needed to obtain accurate predictions of the system's structural health status. Several common metrics and statistics for these type of networks are presented in Table 3, where it can be observed that, while the precision of the failure conditions increases ever so slightly, the lack of intermediate situations causes the accuracy of the undamaged samples to drastically improve, ultimately yielding a global accuracy of 96.8%. Sensitivity studies were performed to relate network accuracy with respect to the degree of failure severity, from which the obtained curves are displayed on Figure 7(a) and 7(b) for biofouling and anchoring damages, respectively. These individual studies allow for the prediction of multiple failure modes occurring at once, and the estimation of remaining component life if coupled with a compatible reliability model. In these analyses, a similar network was implemented with only two outputs and filtering the undamaged and damaged samples for an iterative training process, after which post-processing tasks were performed to determine the accuracy of the network with respect to each degree of severity. From

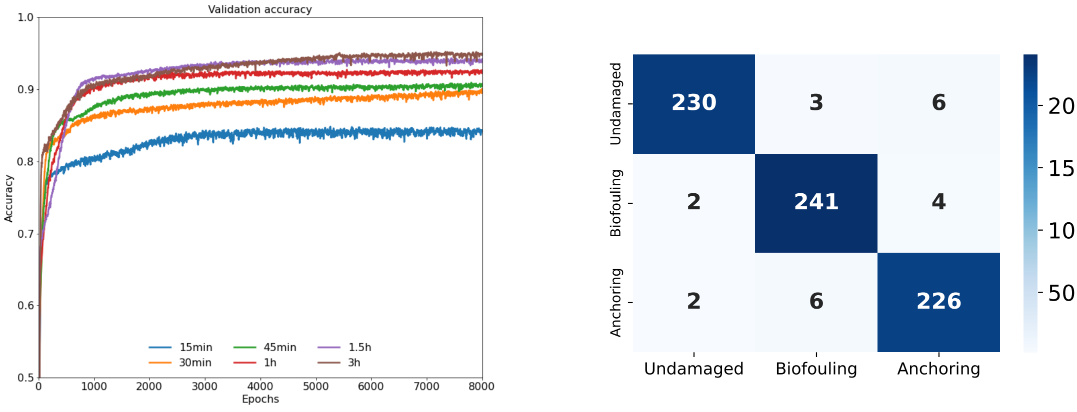

(a) (b)

Figure 6: Results from the three-output DNN, focusing on severe failures: (a) validation accuracy and (b) confusion matrix built from predictions of new cases.

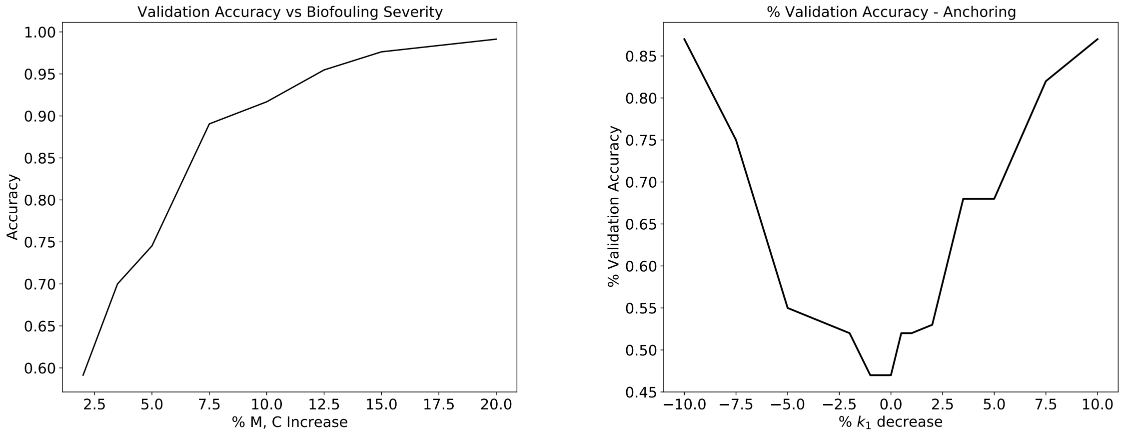

(a) (b)

Figure 7: Results from the performed individual sensitivity analyses: validation accuracy with respect to (a) biofouling severity and (b) anchoring severity.

Figure 7(a), it can be appreciated that the DNN can reach over 90% accuracy considering mass and damping increases of only 7.5%, which do not constitute terminal failure at all. Figure 7(b) shows how the network predicts both positive and negative variations of the mooring line's linear stiffness, thus identifying potential elongation of the chain caused by displacements of its anchor. A rapid increase of network accuracy is observed proportional to damage severity, with approximately 88% accuracy for a ±10% variation of the system's linear stiffness.

4 Conclusions

An innovative deep learning approach has been introduced to predict failing mooring lines for floating offshore wind turbines. The method consists on modelling a non-linear second-order differential equation to estimate the surge, that is, the horizontal displacement of the turbine's platform, from which several key statistics are obtained both in time and frequency domains. These parameters are then fed into an optimised deep neural network, which can ultimately determine whether a turbine is functioning properly or not, and what kind of damage, if any, might be affecting the system's performance. A large set of synthetic data has been generated considering a wide range of metoceanic and structural conditions, considering turbines affected by biofouling issues, as well as wear, fatigue and undesired foundation displacements. The model has proved effective when predicting damages of reasonable severity, with 97% accuracy when severe biofouling and anchoring failures are considered. A distinct correlation between damage severity and network accuracy has been observed, the latter also massively increasing proportionally to sea state duration. Further sensitivity analyses have enabled the algorithm to predict multiple failures occurring simultaneously, potentially allowing for the estimation of a mooring line's remaining life given a suitable reliability model. Further work is expected to add comprehensiveness to the model, which would be expanded to all degrees of freedom, including displacements and rotations in all directions, and to other subsystems within floating offshore wind turbines, such as blades, gearbox, main shaft, etcetera. Dataset optimisation is expected to keep computational costs without compromising accuracy when the complexity of the model is increased. An additional validation process is to be performed once real data is available.

Acknowledgements

This project was made possible thanks to the Energy and Environment Research Grants awarded by Iberdrola Foundation, towards whom the authors would like to express their gratitude. The authors would also like to thank Dr David Pardo for his collaboration as consultant and expert, as well as Mrs Ainara González for her administrative support.

References

[1] Wilson A B 2020 Offshore wind energy in europe European Parliamentary Research Service Briefing

[2] OffshoreWindbiz 2021 Iberdrola to invest over eur 1 billion in floating wind farm offshore spain [Online; accessed 18-February-2021] URL `https://www.offshorewind.biz/2021/02/16/iberdrola-to-invest-over-eur-1-billion-in-floating-wind-farm-offshore-spain/`

[3] Nava V, Ruiz-Minguela P, Perez-Moran G, Rodriguez Arias R, Lopez Mendia J and Villate-Martinez J L 2019 *Installation, operation and maintenance of offshore renewables* (Institution of Engineering and Technology) pp 397–424

[4] Carroll J, McDonald A and McMillan D 2016 *Wind Energy* **19** 1107–1119

[5] Arabian-Hoseynabadi H, Oraee H and Tavner P J 2016 *International journal of electrical power and energy systems* **32** 817–824

[6] Lifshitz J and Rotem A 1969 *Journal of Composite Materials* **3** 412–423

[7] Chang P, Flatau A and Liu S 2003 *Structural Health Monitoring - an International Journal* **2** 257–267

[8] Doebling S, Farrar C and Prime M 1998 *The Shock and Vibration Digest* **30** 91–105

[9] Li Y, Le C, Ding H, Zhang P and Zhang J 2019 *Journal of Marine Science and Engineering* **7** 115

[10] Antoniadou I, Manson G, Staszewski W, Barszcz T and Worden K 2015 *Mechanical Systems and Signal Processing* **64-65** 188–216

[11] Rafiee J, Arvani F, Harifi A and Sadeghi M 2007 *Mechanical Systems and Signal Processing* **21** 1746–1754

[12] Martinez-Luengo M, Kolios A and Wang L 2016 *Renewable & Sustainable Energy Reviews* **64** 91–105

[13] Joshuva A D, Aslesh A and Sugumaran V 2019 *International Journal of Mechanical Sciences* **9** 95–112

[14] Pierson Jr W J and Moskowitz L 1964 *Journal of Geophysical Research (1896-1977)* **69** 5181–5190

[15] Wan L, Gao Z, Moan T and Lugni C 2016 *Ocean Engineering* **111** 82–94

17th EAWE PhD Seminar on Wind Energy
3-5 November 2021
Porto, Portugal

Wind Turbine Condition Monitoring System

Rebeca Marini[a], **Cédric Peeters**[a], **Kayacan Kestel**[a], and **Jan Helsen**[a]

[a]Vrije Universiteit Brussel, Pleinlaan 2, 1050 Brussels, Belgium

`E-mail: rebeca.marini@vub.be`

Keywords: condition monitoring, vibration analysis, fault detection, cyclostationarity

1 Introduction

The European Union (EU) has set guidelines and targets to fulfil the United Nations' Agenda for 2030, to assure a better future for the next generations. One of these is to further decarbonize the current energy system, by investing in renewable energy. Wind energy in the last two decades has been rapidly growing, representing more than 35% of the produced renewable energy in the EU during 2020 [1]. The European Wind Energy Association (EWEA) estimates this growth to reach almost 400 GW production by 2030, with 25% being produced in offshore wind farms [2].

The construction costs of an offshore wind farm are higher than an onshore one, due to cabling, mooring and maintenance. However, the increased wind potential and nature preservation leads to a growing number of offshore wind farms every year [3]. Moreover, wind turbines have also been growing in size, reaching more than 100m of blade length. With a higher Levelized Cost Of Energy (LCOE), in comparison with onshore wind farms, it is important to investigate ways of decreasing, or at least maintain, the current LCOE associated with offshore wind farms.

When the components of a machine have faults, for example along the drivetrain, the annual energy production will decrease, which consequently increases the LCOE. Thus it is important to know how to decrease costs, for example, through predictive maintenance. This has lead to increased interest and acceptance of Condition Monitoring Systems (CMS) as a maintenance strategy. CMS is based on the capability of regular monitoring and prediction, carrying out the maintenance at an optimum time [4].

There are several non-destructive techniques for condition monitoring wind turbines, as reviewed in [5]. The most commonly used techniques are vibration and lubricant analysis, with the former being the most prevalent method. When processing vibration signals from rotating components, it is crucial to take into account the different statistical properties of the different vibration sources in order to enable proper analysis of the individual components. For example, gears typically produce deterministic vibrations due to being locked in place through the gear teeth, while bearing vibrations are generally considered (quasi-)cyclostationary due to the slippage of the rolling elements.

In this paper, an overview is given of the different topics that will be tackled in the near future. The focus of the research is on the development of signal processing methodologies for detecting faults in rotating components through vibration analysis. Additionally, given that an end-user typically does not have the time or resources to manually investigate each health indicator trend of all owned turbines, the developed fault detection pipelines will be automated to enable continuous tracking and assisting in the maintenance decision process.

2 Methodology

A cyclostationary signal is defined as a non-stationary continuous signal in which its statistical properties cyclically vary in time. In [6, 7, 8], Gardner established the first theoretical foundations and also predicted some possible applications. In [9, 10], the author provides a more practical approach to cyclostationarity from a mechanical rotating machine perspective. In literature there is still a research gap in data processing schemes capable of detecting damage or faults of the slowly rotating components during the wind turbine operation [11].

A concept that is central to many fault detection approaches is the fact that faults will often manifest as impulses or modulations in the vibration measurements. The tracking of these signatures is then commonly done through the concept of cyclostationarity. Using this concept enables more advanced fault detection techniques since it opens up the possibility of enhancing the detection rate of such fault modulations. The initial step, is to investigate and understand previously proposed techniques for tracking the modulations. An example of such a fault-enhancing technique can be found in [12], where the authors suggest a blind filtering approach based on the maximization of the sparsity of the squared envelope spectrum, which is an often-used tool for cyclostationary analysis. Direct maximization of a specific cyclic frequency is also possible and is proposed in [13]. Another cyclostationary approach that tries to find an optimal modulation frequency band is proposed in Schmidt et al. [14]. In this work the cyclic spectral correlation is used since it provides a two-dimensional cyclic-carrier frequency map which enables the search for the optimal demodulation band. Although this technique used to be associated with high computational costs, Antoni et al. proposed in [15] a faster implementation of this estimator, making it more feasible to use the spectral correlation on a larger scale with regards to data analysis.

The majority of proposed methods assume the vibration signals to have a Gaussian distribution with a periodic autocovariance function, i.e. second-order cyclostationarity. There is still a need for investigating higher-order cyclostationary moments, as in, approaches that are based on higher-order statistics to analyse cyclostationary signals. This need comes from the fact that impulses are inherently present in industrial machines but these impulses are often not linked to faults but rather to other sources. This is especially the case for vibrations on wind turbine drivetrains, where there are many measured impulses that can be considered random and thus as interfering content to the signals of interest. Given that this interfering content is strongly non-Gaussian, many of the methods in the current literature suffer greatly from heavy impulsive noise from other sources. A recent development has been the investigation of α-stable distributions, as in [16], to make current state-of-the-art methods more robust to such interfering impulsive noise.

While on one hand, it is necessary to improve the signal processing methods used to analyse cyclostationarity, on the other hand it is also relevant to develop an automated manner to deal with the resulting data. Machine learning (ML), either by supervised or unsupervised learning, is the process chosen to achieve that automation. By teaching the model, with a limited amount of data, it is possible to obtain a predictive model to then assist the decision-making process. In [17], the authors make a review of the recent literature regarding ML models for condition monitoring of wind turbines. An example of a hybrid physics-based and machine learning approach is proposed in [18] where the calculated signal processing health indicators are modeled using a Bayesian expected behavior model, which is then used to detect anomalies.

3 Conclusions

The goal of this research is to investigate and further advance the performance of state-of-the-art signal processing techniques exploiting cyclostationarity for damage detection in wind turbine drivetrains. From the initial literature study, it became clear that the different existing methodologies have the potential to further improve with regard to accuracy and automation. Additionally, the application scope in literature is often still limited to academic test benches or small-scale experimental data sets. This research will validate the developed methods on large-scale data sets to verify both the method performance and the industrial application capacity. The latter will be further enhanced by combining the signal processing methods with machine learning. This will allow the end-user to have a continuous monitoring framework that will assist the decision making with respect to wind turbine maintenance.

References

[1] Ritchie H and Roser M 2020 *Our World in Data*

[2] EWEA 2015 *The European Wind Energy Association*

[3] Bórawski P, Bełdycka-Bórawska A, Jankowski K J, Dubis B and Dunn J W 2020 *Renewable Energy* **161** 691–700 ISSN 0960-1481

[4] Randall R B 2021 *Vibration-based Condition Monitoring: Industrial, Automotive and Aerospace Applications* (John Wiley) chap 1-3

[5] Yang W, Tavner P J, Crabtree C J, Feng Y and Qiu Y 2014 *Wind Energy* **17** 673–693

[6] Gardner W 1986 *IEEE Transactions on Acoustics, Speech, and Signal Processing* **34** 1111–1123

[7] Gardner W 1991 *IEEE Transactions on Information Theory* **37** 216–218

[8] Gardner W 1991 *IEEE Signal Processing Magazine* **8** 14–36

[9] Antoni J 2007 *Mechanical Systems and Signal Processing* **21** 597–630 ISSN 0888-3270

[10] Antoni J 2009 *Mechanical Systems and Signal Processing* **23** 987–1036 ISSN 0888-3270

[11] Regan T, Beale C and Inalpolat M 2017 *Journal of Vibration and Acoustics* **139**

[12] Peeters C, Antoni J and Helsen J 2020 *Mechanical Systems and Signal Processing* **138** 106556 ISSN 0888-3270

[13] Buzzoni M, Antoni J and D'Elia G 2018 *Journal of Sound and Vibration* **432** 569–601 ISSN 0022-460X

[14] Schmidt S, Heyns P S and Gryllias K C 2021 *Mechanical Systems and Signal Processing* **158** 107771 ISSN 0888-3270

[15] Antoni J, Xin G and Hamzaoui N 2017 *Mechanical Systems and Signal Processing* **92** 248–277 ISSN 0888-3270

[16] Kruczek P, Zimroz R, Antoni J and Wyłomańska A 2021 *Mechanical Systems and Signal Processing* **159** 107737

[17] Stetco A, Dinmohammadi F, Zhao X, Robu V, Flynn D, Barnes M, Keane J and Nenadic G 2019 *Renewable Energy* **133** 620–635 ISSN 0960-1481

[18] Peeters C, Verstraeten T, Nowe A and Helsen J 2019 *Proceedings of the ASME 2019 38th International Conference on Ocean, Offshore and Arctic Engineering* **10**

O & M

Feature extraction investigation and fault detection in a wind turbine hydraulic pitch system

Panagiotis Korkos[a], **Matti Linjama**[b], **Jaakko Kleemola**[c], **Arto Lehtovaara**[a]

[a] Tribology and Machine Elements Group, Tampere University, Finland
[b] Automation Technology and Mechanical Engineering Unit, Tampere University, Finland
[c] Suomen Hyötytuuli Oy, Finland

E-mail: panagiotis.korkos@tuni.fi (P. Korkos)

Keywords: pitch system, PCA, fault detection, ANFIS, SCADA

1 Introduction

Processing the supervisory control and data acquisition (SCADA) data of wind turbines is vital, eliminating the downtime due to failures or unnecessary maintenance tasks. Pitch subsystem has the highest failure rate among the subsystems according to reliability surveys [1,2] and can be either hydraulic or electric. The hydraulic pitch system, which is the type examined in the present study, includes several components, such as hydraulic cylinders, accumulator tanks, valves, pumps, pitch bearing, pitch pawl, and slip ring. This work presents an investigation of feature extraction techniques including original ones based on previous studies and features extracted by Principal Component Analysis (PCA). Their effect is evaluated based on fault detection performance using Adaptive Neuro Fuzzy Inference System (ANFIS).

2 Methods

In this study, 10-min SCADA data were obtained from a windfarm consisted of five fixed-speed 2.3 MW wind turbines with a hydraulic pitch system. The data were pre-processed and scaled using min-max normalization. The dataset is based on the maintenance log, taking into account periods before and after a maintenance task. In this work, the training dataset consisted of nine pitch fault events referring to different component of pitch system such as valve failures, leakages and hydraulic cylinder failure. After collecting the training dataset, the data were labelled accordingly to perform binary classification.

The present work examined several cases of original features and new extracted features using Principal Component Analysis (PCA). According to Chen et al [3] there are the so called Critical Characteristic Features (CCFs) including power output vs. wind speed; blade angle a vs. wind speed; blade angle b vs. wind speed; blade angle c vs wind speed; and rotor speed vs. wind speed. In the first case, the average and standard deviation values were utilized against the average wind speed in 10 constructed models. 2nd case contains three CCFs, namely power output vs. wind speed, rotor speed vs. wind speed, as well as the average of the three blade angles (i.e., A, B, and C) vs. wind speed. 3rd case refers to the new extracted features using the first two principal components, derived after PCA implementation. PCA is a method to reduce the dimensions of feature set based on linear transformation of input space. In this study, PCA was implemented using all the average, standard deviation, maximum and minimum values of each feature. Regarding the fault detection task, ANFIS [4] was used assuming two inputs and one output. The ANFIS model is trained using 80% of the dataset and the remaining 20% is used for testing. The performance of the binary classification is based on F1-score.

3 Results and Discussion

Table 1 summarizes the performance of each feature set towards fault detection using ANFIS technique using a threshold of 0.5. It seems that when using PCA (case 3) and especially the first and second component to ANFIS the F1-score is close to 74%. Figure 1 presents the 1st and 2nd principal component as red points and the coefficients of each feature for each of these two principal components is demonstrated by the blue vectors. However, PCA indicated that more than the first two principal components should be used in order to include more than 95% of variance of the system response. In that case, using another technique which takes more than two inputs for training, may result to better performance than that of ANFIS. This can be investigated, also, if ANFIS architecture receives more than two inputs. Furthermore, usage of kernel PCA incorporating non-linear transformation can be investigated. Nonlinear transformation can be implemented as a next step, as well, using a Deep Autoencoder from the field of Deep Learning.

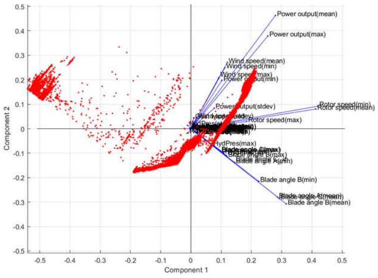

Figure 1 Figure representing the 1st and 2nd principal component and coefficients as blue vectors

No.	F1-score
Case 1	0.8223
Case 2	0.8677
Case 3	0.7427

Table 1 Performance Metrics in Each Case

4 Conclusion

In this study, usage of original features and new extracted features were addressed, and their evaluation was conducted based on the performance in fault detection task using ANFIS. 10 years of 10-min SCADA data were available to authors and nine pitch fault events consisted the dataset of this study covering different type of pitch system failures. New extracted features using PCA attained almost 74% F1-score having quite good results, but it is recommended to use more than the first two principal components in order to cover more than 95% of variance. Finally, the case containing the average values of all the CCFs, in which the three blade angles were aggregated into one, was demonstrated to have the best performance among the other cases.

Acknowledgements

This research was funded by the Doctoral School of Industry Innovations (DSII) at Tampere University and Suomen Hyötytuuli Oy.

Bibliography

[1] Wilkinson M, Hendriks B, Spinato F, Harman K, Gomez E, Bulacio H, Roca J, Tavner P, Feng Y, Long H 2010 *Eur. Wind Energy Conf. Exhib. EWEC* **3** 1984–2004.
[2] Carroll J, McDonald A, McMillan D 2016 *Wind Energy* **19** 1107–1119.
[3] Chen B, Matthews P C, Tavner P J 2015 *IET Renew. Power Gener.* **9** 503–513.
[4] Jang J R 1993 *IEEE Trans. Syst. Man. Cybern.* **23**

Onshore farm-wide fatigue evaluation based on fleet leader concept: construction of the damage matrix

J Pacheco[a], F Pimenta[a], F Magalhães[a], A Cunha[a]

[a] Construct-ViBest, Faculty of Engineering, University of Porto, Porto, Portugal

E-mail: joaop@fe.up.pt

Keywords: Fatigue Assessment, Strains Dynamic Monitoring, Onshore Wind Turbine

1 Introduction

Wind turbines are structures predominantly subjected to dynamic loads throughout their period of life. In that sense, the fatigue design has a key role. Since in the design stage it is difficult to predict the real operation condition in each installation site, conservative approaches with respect to fatigue evaluation may lead to real fatigue life considerably higher than 20 years (lifetime for which they are usually designed). Therefore, the implementation of a fatigue monitoring system can be an important advantage for the management of wind farms: (a) Estimation of the evolution of real fatigue condition; (b) Since the real fatigue damage is known, the results of the fatigue monitoring system can support decisions about extending the lifespan of the structure and the possibility of repowering or overpowering; (c) The results of the instrumented wind turbines can be extrapolated to other wind turbines of the same wind farm.

2 Tower Strains Monitoring System and Fatigue assessment

The monitoring system installed on the tower for forces characterization is composed by six 2D rosette strain gages, four temperature sensors and three clinometers connected to a central acquisition system, then linked with a modem for remote access to the data. Having in mind the evaluation of the static bending moment diagrams along the tower, the six strain gages are distributed in two tower sections: one with four sensors at 6.6m from the tower base and another section with 2 sensors at 7.8m from the tower base.

Strain gauges are very sensitive sensors and many factors can easily preclude accurate measurements. So, the experimental determination of bending moments in the tower requires the acquired raw data to be pre-processed to obtain the real deformation.

The fatigue assessment of the tower was performed by the traditional approach, combining S-N curves and the rainflow counting algorithm. The damage is estimated according to the hypothesis of linear damage accumulation, adopting the so-called Palmgren-miner rule [1]. The complete description of all the previous steps is presented in [2].

3 Fatigue Damage Extrapolation

Direct measurement of strains at wind turbine key tower sections allows to estimate the accumulated fatigue damage with good accuracy over the monitoring period at the instrumented wind turbine, so-called fleet leader [3]. The realistically evaluated damage during a representative time period represents an important source of information that can be used to extend the estimation of the damage prior to and after the monitoring period and to other wind turbines of the same wind farm. The approach described in Figure 1 combines a long-term measurement of strains with SCADA data. This methodology allows to achieve three major goals: (a) endured damage since wind turbine installation; (b) lifetime prediction of the wind turbine tower; (c) extrapolation of the fatigue analysis to neighbouring wind turbines.

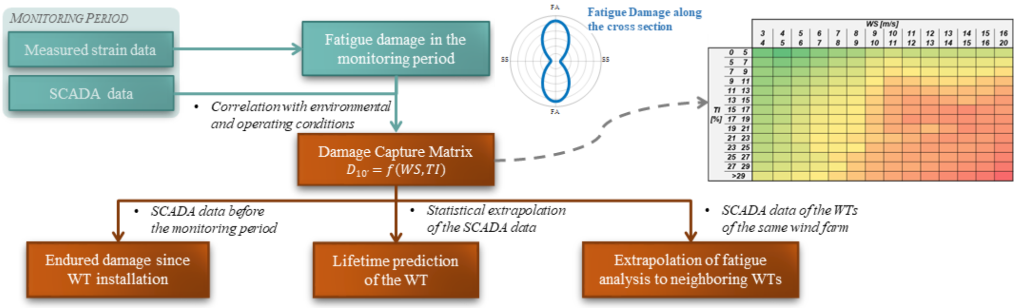

Figure 1 Extrapolation of the fatigue damage based on a monitored period of one wind turbine and damage matrix scheme for power production (red represents higher damage).

The extrapolation method based on the fleet leader concept consists of two main parts: construction of the damage capture matrix of the fleet leader and the damage extrapolation towards another turbine. In this work only the first part is introduced.

The construction of the damage capture matrix of the fleet leader is divided into three steps: (1) environmental and operational binning; (2) bin reduction; (3) Fill empty bins.

The short-term damages (e.g. 10-min) are first clustered into several load cases (e.g. power production, parked/idling and emergency shut-down). Based on the similar approach describe in IEC 61400-13 [4], the damage values are stored in a database according to the corresponding wind speed and turbulence intensity, so-called damage capture matrix (Figure 1).

The final damage matrix that will be used in the extrapolation methods is composed of a single representative damage value in each bin. This value represents the damage accumulated by the wind turbine in service in these environmental conditions during a specific time interval. The metric usually recommended to reduce the damage matrix is to consider the mean value of damage measurements in each bin. If conservative approximations are needed, any statistical metric can be used, as the 75th and 90th percentile.

The damage matrix is composed by the combination of environmental parameters and it is possible, and very likely, some of these combinations do not occur during the measurement period. The empty bins should be filled with a well-considered value. In that sense, depending on the available information, several methods can be followed: based on load case tables provide by design documents; considering the maximum value found in the neighbouring bins and based the two-dimensional extrapolation method, taking into to account the already filled bins.

Throughout the various steps of the matrix construction, several parameters must be defined and might influence the results significantly. For this paper, choices are made based on experience and existing bibliography. Some shortcomings and alternatives are also presented and discussed.

Acknowledgements

The support of EDP Renewables and VESTAS in greatly acknowledged. This work was financially supported by: PhD Grant SFRH/BD/129688/2017. This work was financially supported by: Base Funding - UIDB/04708/2020 and Programmatic Funding - UIDP/04708/2020 of the CONSTRUCT - Instituto de I&D em Estruturas e Construções - funded by national funds through the FCT/MCTES (PIDDAC).

Bibliography

[1] K.-T. Ma, Y. Luo, T. Kwan, and Y. Wu, “Chapter 6 - Fatigue analysis”, Eds. Gulf Professional Publishing, 2019, pp. 115–137.
[2] J. Pacheco, F. Pimenta and F. Magalhães, “Use of strain monitoring data for fatigue assessment of wind turbine tower”, Paper presented at 10th International Conference on Structural Health Monitoring of Intelligent Infrastructure (SHMII-10), Porto, 2021.
[3] Wout Weijtens et al 2016 J. Phys.: Conf. Ser. 753 092018
[4] International Electrotechnical Commission, “IEC 61400-13 Wind Turbine Generator Systems - Part 13: Measurement of Mechanical Loads,” 2015.

Automatic event detection of offshore wind turbines based on strain measurements

Y Bel-Hadj[a], F d N Santos[a], N Noppe[a], and C Devriendt[a]

[a]Vrije Universiteit Brussel (VUB)/Offshore Wind Infrastructure-Lab (OWI-LAB)

June 2021

`E-mail: yacine.bel-hadj@vub.be`

Keywords: Structural health monitoring, signal classification, event detection, signal processing

Abstract

The primary objective of this contribution is to build a data-driven algorithm capable of detecting events and identifying operational states of the turbine on the basis of strain measurements. The first goal is to create a signal classifier and the second is to make signal segmentation. Subsequently, a data-centric approach and a model-centric approach have been adapted to increase the model's classification performance. In the first approach, different studies were carried out. For instance, the advantage of data augmentation was shown using two different strategies. The motivation to adopt the model-centric approach was that the main model, a one-dimensional convolutional neural network, did not perform well in identifying a particular class due to its low presence in the training set. Therefore, an additional KNN-DTW model was added in parallel to the main model, allowing it to reach an acceptable accuracy of 98.3% on average and an F1-score of 0.89 for the underrepresented signal. Finally, the event detection is addressed using a sliding-window convolutional neural network. With proper post-processing the algorithm reaches an error rate of 20%, which is acceptable regarding the data quality.

1 Introduction

The interest in offshore wind turbines is growing and it is more and more present in the energy mix. Monitoring the structures' health helps reduce the Levelized Cost Of Energy (LCOE) by allowing for lifetime extensions, which require assessing accumulated damage. Events such as rotor stops/starts and severe pitch changes induce significant damage due to a sudden shift in the quasi-static load. Therefore, their identification provides valuable information in the evaluation of the remaining lifespan. Similarly, the operational condition is crucial and allows for a better fatigue assessment since a parked large wind turbine supported by a monopile suffers more damage due to wave loading.

2 Objectives and Problem Statements

The main objective of this contribution is to build an algorithm capable of detecting events and identifying operational states of the turbine from the bending moment signal which is derived from the strain measurement. The rationale for using bending moments (calculated from measured strains) instead of 1s SCADA is that strain measurements are already collected and used for other purposes in previous and ongoing research projects. For those specific projects, the strain data is generally more reliable than 1s SCADA, if the latter is available. The author wishes to emphasize that strain gauges on turbines will not be installed for the sole purpose of capturing events and operating status.

The objective of this paper seems quite broad at first glance, and it can be broken down into two smaller problems: In the first problem, the goal is to build an algorithm that classifies the 10-minute signal into four classes:

- standstill state: the turbine is not rotating
- generating state: the turbine is rotating
- event: start, stop or any other pitching action
- yaw action: turbine is yawing to unwind the cable

Figure 1 shows an example of each class:

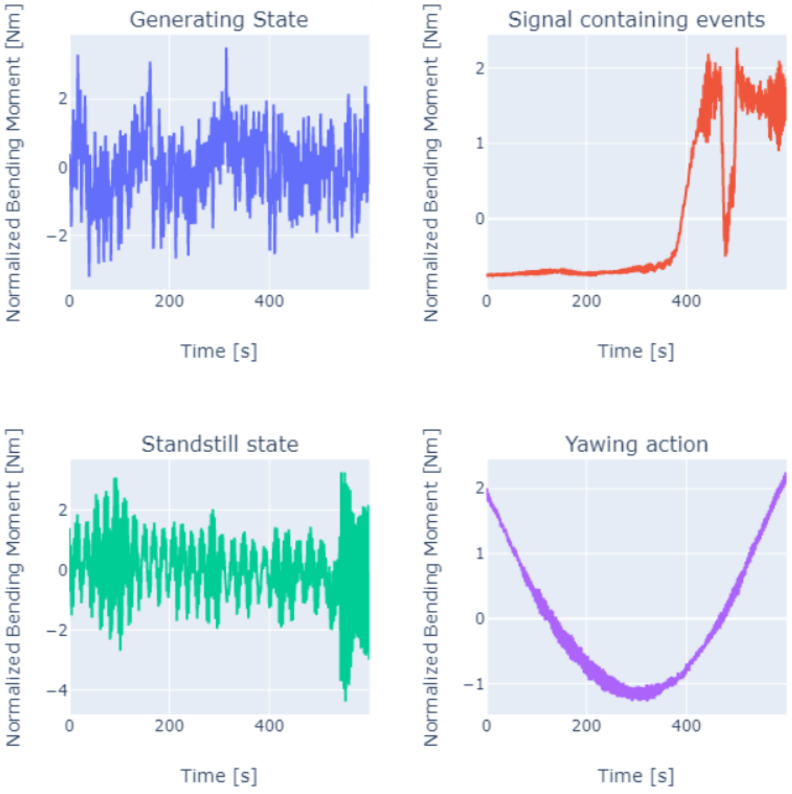

Figure 1: Illustration of the different signal types, the model will have to classify the signal into one of these classes. The normalization method used to make these figure is z-score normalization. In blue the generation state, in turquoise standstill, in red an example of a signal containing events, and in purple yawing action signal

The second objective is to characterize further the 10-minute signal containing events by performing segmentation, or in other words, determining when the event occurred and what type of event occurred.

3 Methodology & Results

3.1 Signal Classification

For the first objective (signal classification), a convolutional neural network (CNN) was used. This model is based on a filter that convolves with the input signal to extract features, passed to a classifier composed of fully connected layers. The classification model is shown in Figure 2

To improve the model performance a data-centric approach has been performed, followed by a model-centric approach. In the data-centric approach, the training data set has been augmented by creating

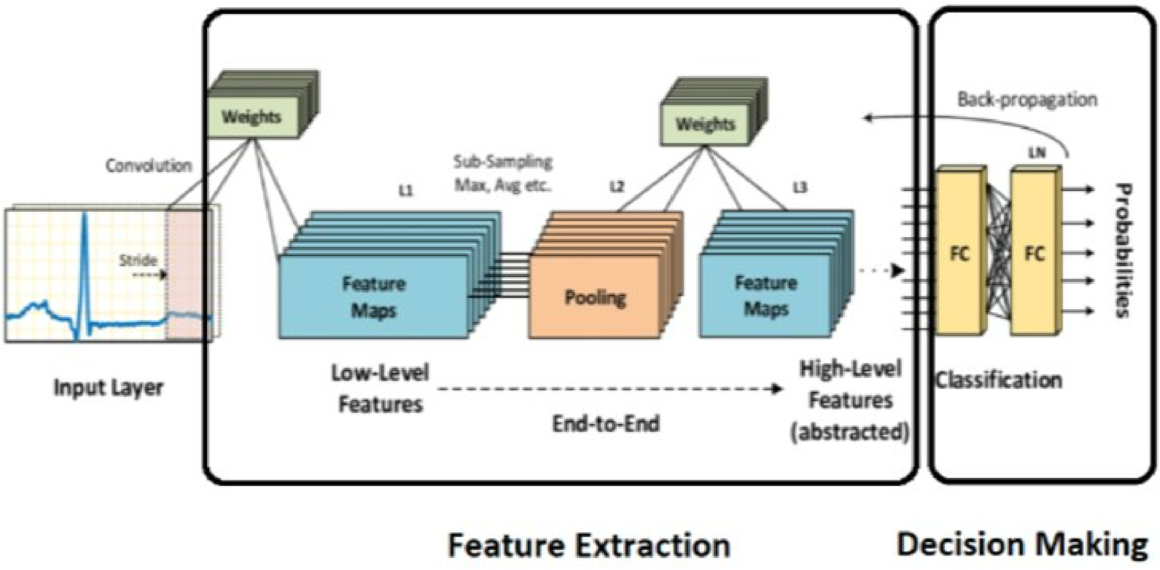

Figure 2: 1D convolutional neural network structure that involves convolution, pooling and fully connected layer [1].

new instances using time-domain manipulation and intrinsic mode functions (IMF) mixing. Augmenting the data with time-domain manipulation is the most obvious approach. Possible manipulations in the time domain are reversing, applying a drift and window wrapping (where a random time range is selected and compressed or extended). Augmenting the data using IMF mixing consists of decomposing the signals into a finite number of IMFs; the new signal is created by randomly selecting and summing IMF of different orders from different signals.

Before going further, let us present the metrics used to evaluate the model's performance: The accuracy allows to know the proportion of good predictions compared to all predictions. However, this latter can lead to a biased judgment when the data set is unbalanced. Therefore, the F1 score is used for the model assessment when the dataset is unbalanced and it is defined for each class in contrast to the accuracy which is defined for all the classes.

In Figure 3, the accuracy, F1 score of the event-containing signal, and F1 score of the yaw action signal are plotted as a function of the rate of increase in three separate graphs. When the rate of increase is equal to zero, the model is trained with the original data set consisting of 140 (10% of the whole dataset) signals. As can be seen, the optimal augmentation ratio is around 3 and 4. The F1 score for the yaw action increases relatively well but it is still not satisfactory. Note that the IMF mixing is only applied to the yaw action signal since it is the most underrepresented class.

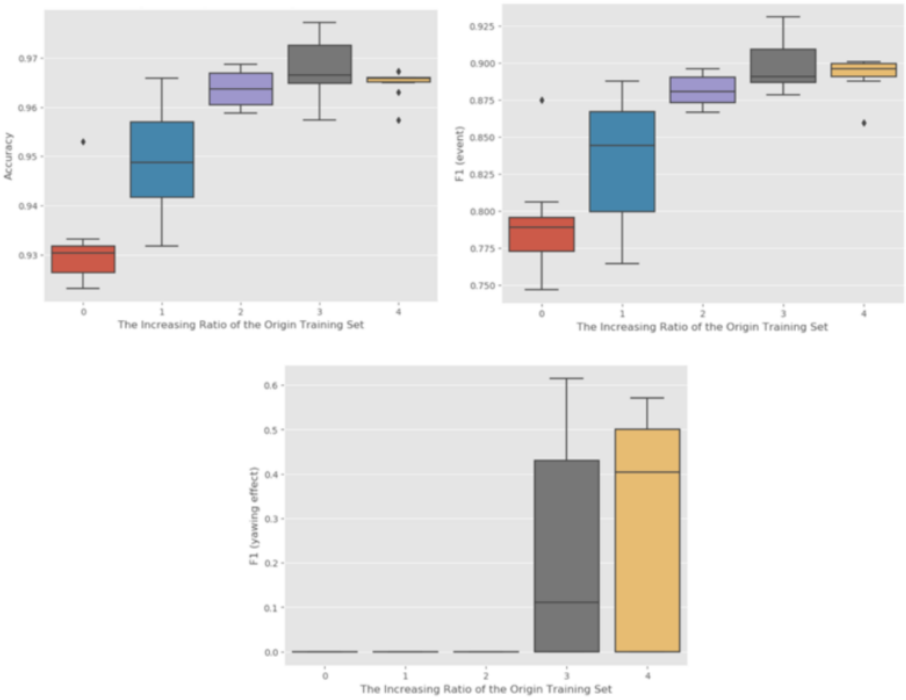

Figure 3: Model performance as function of the data augmentation ratio. The three plots show the F1-score (event), F1-score (yaw action) and accuracy of the model as function of augmentation ratio. The original dataset contains 10% of the whole dataset, and the testing dataset contains 50% of the total data.

The data-centric approach led to a significant improvement. However, the capability of the model in detecting the signals that contain yaw actions was still not satisfactory. This is mainly due to the small presence of instances of this class in the training set (only 16 examples). All the yawing action signals instances present in the used datasets are similar in shape. Thus, a similarity-based model is implemented in parallel to identify the yawing action signal.
Figure 4 shows how the signal is processed. As can be seen, there are two models in parallel. During the inference phase, the added model, measures the similarity between a reference yaw action signal (provided during the training) and the input signal. The similarity measurement used is the Dynamic Time Wrapping (DTW).

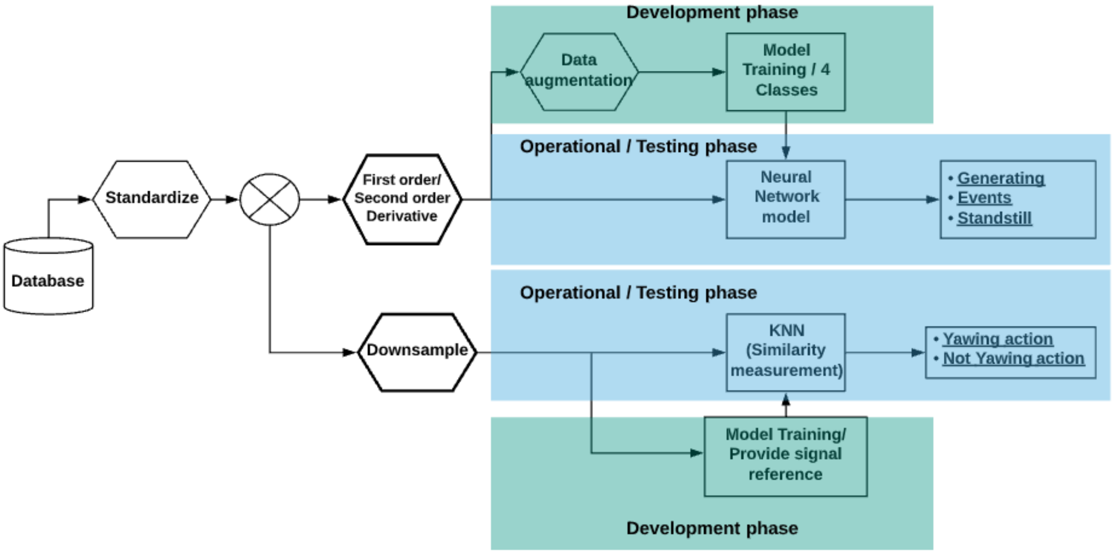

Figure 4: Data flow in development and operation phase. The stacked models are illustrated.

Before going further, let us introduce the concept of confusion matrix. The confusion matrix is a summary of the results of the predictions on a classification problem. The correct and incorrect predictions are highlighted and divided by class. The results are then compared to the real values. For example, in Figure 5, it can be seen in the confusion matrix on the right that 84% of the yaw action signals were correctly labeled, while 16% were classified as standstill signals.

This matrix allows us to understand how the classification model is confused during predictions. This tells us not only what errors are made, but more importantly what type of errors are made.
Figure 5 shows the improvement brought by data augmentation and the addition of KNN-DTW in parallel to the primary model. As can be seen, the model capability in detecting the signal containing an event has improved. Although, there are only 16 samples from the yawing action signal. KNN-DTW was able to correctly classify 84% of the yawing action signal in the test dataset which contains 5 yawing action samples (30% of the entire dataset is retained as a test dataset).

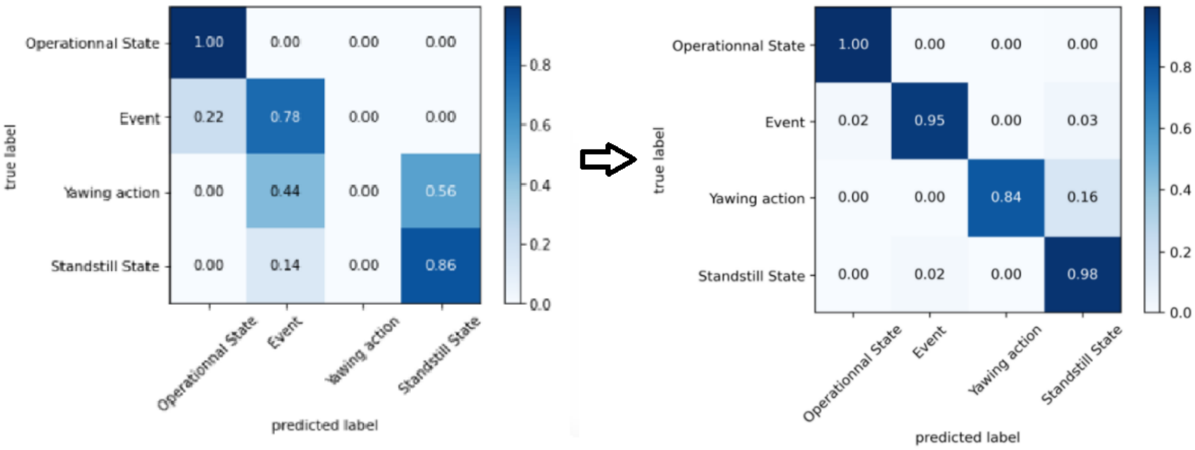

Figure 5: Two confusion matrices of the model before and after the improvement (Data-centric and model-centric approach)

3.2 Event Detection and Localization

The second objective aims to build a segmentation algorithm to further characterize signals containing events; a distinction between four types of mechanisms can be made:

The first two types of events are rotor stops and rotor starts. The rotor can be stopped manually, e.g. for maintenance, or automatically, e.g. when the wind speed is above the cut-out speed. The turbine will restart when the wind speed falls below the cut-out speed or when the manual stop is lifted. As can be seen in Figure 6, a start (or stop) involves an almost immediate increase (or decrease) in nominal bending moment.

The remaining two events are due to a high pitch change, where the operational state does not change. Therefore, a distinction between severe pitch change from a generating condition and a severe pitch change from a standstill condition is made. The severe pitch change often occurs when the Offshore Wind Turbine (OWT) tries to start or stop. Nevertheless, it's sometimes hard for a human to recognize the type of event occurring. Figure 6 illustrates these events.

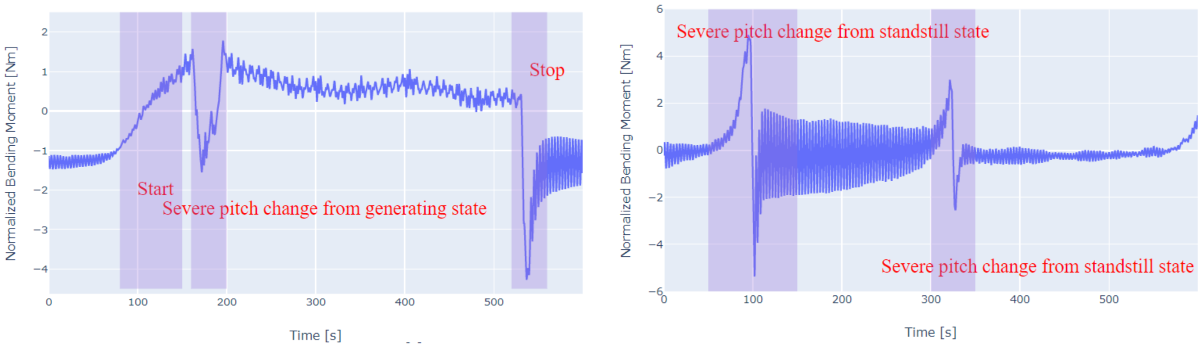

Figure 6: Two plots illustrating the four types of event

A Sliding Window CNN (SW CNN) has been used to perform the signal segmentation in a supervised machine learning fashion (similarly to the first part/objective). The required labels on the training and validation set were added manually by the author. For this technique a rolling window is implemented that cuts the input signal into segments. These segments are sent to a CNN, classifying them into five classes (four events and one non-event class).
During the testing of the SW-CNN, it appeared that the model output was too noisy (varying a lot). This can be explained by the fact that the model sees only small segments.Therefore, noise gains much importance and can disturb the model's training. To mitigate this, the input signal is filtered using a first order low-pass filter with a cut-off frequency of 0.4Hz. Moreover, the SW-CNN struggles to identify the events that are happening in the beginning and at the end. To overcome this issue, an array of constant values is concatenated at both edges of the signal. This "padding" forces the window to interfere during a larger period with the events occurring in the edges.

In Figure 7, the preprocessed signal (after filtering and padding, in red) and the model prediction (in turquoise) are displayed.
As can be seen, the model outcome is not perfect. For example, the severe pitch change from the standstill condition (happening around 80s) is preceded by a start in the model outcome. This is a result of the sliding window seeing a start before seeing a severe pitch change. It can be noted that there is also some variation in the model output (around 270s). Therefore, it is essential to postprocess the model outcome.

The established postprocessing strategy is composed of two steps, which are reducing the variation and interpretation. The first step aims at reducing the variation: the algorithm examines the events recognized by the model with a duration of less than 0.4s. If the two neighboring events are identical,

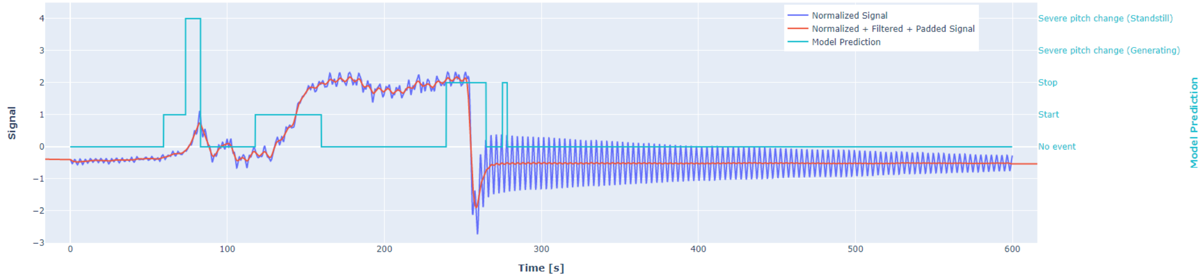

Figure 7: Signal and model prediction on the same graph. The first curve shows the normalized signal (blue) and the second one after filtering and padding (red). The third curve is the SW CNN event prediction (turquoise)

the short variation of the output is disregarded; if they are different, the algorithm assigns ”no event” to the event of short duration. In Figure 8 an illustration of this principal is shown.

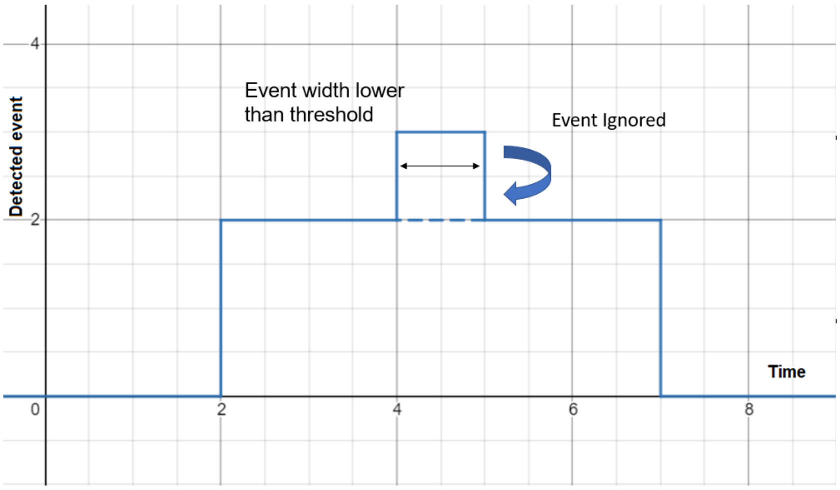

Figure 8: Illustration of the denoising postprocess. Events with short duration having the same neighboring events are assigned the same label as the neighboring event

This process is repeated with different thresholds to ignore short events of different durations: 0.8s, 1.6s, 2.4s, 4s, 6.4s, and 8s. The idea is first to aggregate the correct events detected by the model, separated by incorrect detections of short durations so that the correct events will have a longer and longer duration until the correct event is completely aggregated. The final threshold is 8s since this is the minimum duration of an event in general. This iterative filtering shows better performances compared to the one step filtering.
The second step concerns the output interpretation. If there is any succession of a start, a severe pitch change (standstill) and a stop, they are all counted as a severe pitch change (standstill). And if there is a succession of a stop, a severe pitch change (generation) and a stop, they are all considered a severe pitch change (generation).

In order to evaluate the performance of the model in detecting and locating events, only the error rate will be used throughout this contribution. The definition of the error rate is shown in the following equation:

$$ER = \frac{\sum_{i=1}^{K} S(i) + \sum_{i=1}^{K} D(i) + \sum_{i=1}^{K} I(i)}{\sum_{i=1}^{K} N(i)} \tag{1}$$

Where i represents a signal, K is the total number of signals in the dataset and S,D and I are then number of substitutions, deletions and insertions.
Substitutions are when the system produces an event different from the ground truth.
Insertions are the number of events predicted by the model when there are none (after taking substitutions into account).
Deletions are the number of ground truth events that were not identified, the model doesn't detect any event (after taking substitutions into account).

With proper postprocessing, the reached error rate is about 21%. The main reason for this high error rate is a high S (the number of substitutions). This could be explained by the fact that sometimes even for a human, it is hard to label the events

4 Conclusions

The proposed solutions have shown promising results in the case of classification and segmentation of bending signals, which can allow engineers to have a better knowledge of OWTs and a better lifetime evaluation. One of the main contributions of this paper is to improve the performances of artificial neural networks for classification problems using a relatively low amount of training data. Therefore, minimizing the human effort for manual labeling. This was achieved through the use of a data-centric approach (data augmentation) and a model-centric approach (adding a similarity-based model alongside the neural network).
A possible improvement of the sliding window CNN is to make a convolutional implementation of the sliding windows, which reduces the computational time. The framework of this work could be extended in several ways. First, readings from the accelerometer can be used instead of strain gauges, considering these sensors are more present in OWTs and cheaper than strain gauges. The next step could be to apply this algorithm to a much larger number of turbines, which would further validate the approach. Secondly, the signal segmentation algorithm can be further improved by adjusting the state-of-the-art object detection models (YOLO, U-Net, etc.) for signals.
These research directions can contribute to improving the models to detect and segment events using cheaper sensors, thus driving down the O&M cost of the OWT.

References

[1] Murat F, Yildirim O, Talo M, Baloglu U B, Demir Y and Acharya U R 2020 *Computers in biology and medicine* 103726

17th EAWE PhD Seminar on Wind Energy
3-5 November 2021
Porto, Portugal

Early results for data-driven DEL estimation on monopiles

F d N Santos[a,b], N Noppe[a,b], W Weijtjens[a,b], and C Devriendt[a,b]

[a]Offshore Wind Infrastructure-lab, OWI-Lab
[b]Vrije Universiteit Brussel, Pleinlaan 2, 1050 Elsene, Belgium

E-mail: `francisco.de.nolasco.santos@vub.be`

Keywords: artificial neural network, fatigue loads, XL monopiles

Abstract

Recent years have seen an increased interest in wind turbine fatigue, remaining lifetime and lifetime extensions as older wind farms begin to reach their desing lifetime. In order to quantify the progression of fatigue life for offshore wind turbines Structural Health Monitoring (SHM) has revealed itself as a valuable contribution. Building on results presented on previous research, a data-driven methodology, based on the use of artificial neural networks with SCADA and acceleration data, is developed to estimate the tower damage equivalent loads (DEL) on monopile-foundation XL offshore wind turbine, with the goal of avoiding the farm-wide use of strain gauges (of expensive installation).

Keywords: XL monopiles, artificial neural network, fatigue loads

1 Introduction

As previous research has shown [1, 2], it is currently feasible to replace an strain gauge-attained load history measurement approach [3] with a data-driven approach based on supervisory control and data acquisition (SCADA) and acceleration sensors. This alternative is enticing as the vast majority of current offshore wind turbines already collect some sort of SCADA data and the installation of accelerometers is less costly than the installation of strain gauges.

The group's previous research [1] in particular, has shown that this concept can be implemented for a jacket-foundation offshore wind farm. The results allowed to draw conclusions as to the efficacy of different structural health monitoring setups along with farm-wide application in determining the tower fore-aft (FA) bending moment DEM. This research lead to several questions, in particular, whether this methodology could equally be applied to XL monopiles.

As wind turbines are becoming increasingly bigger, the monopiles that fix these to the seabed must do the same. This means that the resonance frequency is lowered, coupled with an enlarged surface area for hydrodynamic loads and deeper locations. All of these factors lead to a greater impact of the wave loading on fatigue, with the latter becoming wave-driven [4]. Among other considerations, this means that side-to-side (SS) damage calculations are necessary to be included to understand the fatigue at-large.

Three months worth of data from the fatigue monitoring campaign is used to train an artificial neural network that predicts the damage equivalent moments (DEM) affecting monopile foundation offshore wind turbines. The data consists of 10-minute SCADA data and acceleration signals' metrics (mean, minimum, maximum, standard deviation and root mean square). Following the methodology prescribed in [1], this data is used to train an artificial neural network, after previously having undergone a feature selection routine. This methodology is applied both for the calculation of the tower fore-aft (FA) and side-to-side (SS) bending moment DEMs.

In Figure 1, two neural network models (trained on OWT1) - the one in blue calculating the fore-aft tower bending moment DEM and the one in orange the side-to-side DEM - make DEM predictions for two other turbines within the same farm, utilising solely SCADA data on the left and with selected features by recursive feature elimination (including accelerations) on the right. It can be observed that, for both models (FA, blue and SS, orange), including accelerations vastly reduces the spread, but also introduces some site-dependant bias (as seen on the right with positive absolute error for OWT2 and OWT3). Furthermore, the comparison between SS and FA models show us that the former benefits more with the inclusion of accelerations than the latter.

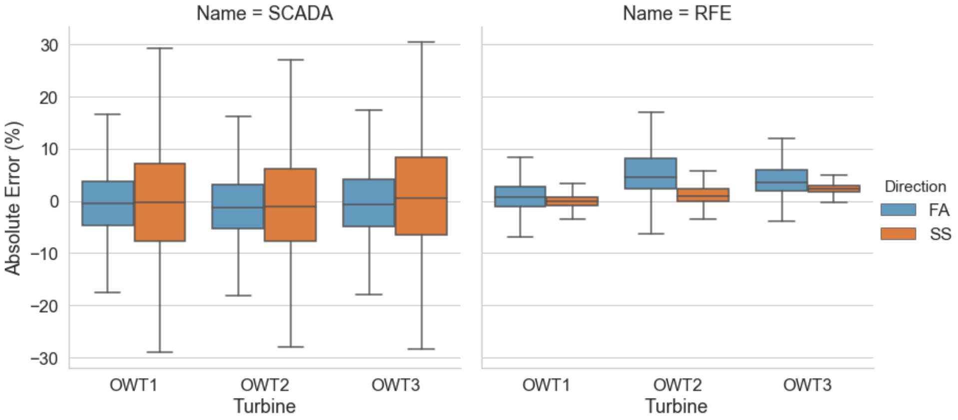

Figure 1: Error of neural network models expressed as a percentage of the maximal absolute training DEM (training turbine OWT1). In the left the performance for SCADA-only models (both fore-aft, FA and side-to-side, SS) for each turbine is presented. In the right the same is done for models that include accelerations and have undergone a feature selection process (Recursive Feature Elimination, RFE).

Finally, this contribution attempts to correlate environmental and operating conditions (EOCs) with the performance of models in order to understand the underlying physical causes and present novel results on XL monopile foundation offshore wind turbines.

References

[1] d N Santos F, Noppe N, Weijtjens W and Devriendt C 2021 *Wind Energy Science Discussions* 1–36

[2] Movsessian A, Schedat M and Faber T 2021 *Wind Energy Science* **6** 539–554

[3] Iliopoulos A, Weijtjens W, Van Hemelrijck D and Devriendt C 2017 *Wind Energy* **20** 1463–1479

[4] Gengenbach J, Mikkelsen K, Rudinger F, Brommundt M and Gretlund J 2015 *Proceedings of the EWEA (European Wind Energy Association) Offshore*

SOCIAL ACCEPTANCE
&
TECHNO-ECONOMICS

17th EAWE PhD Seminar on Wind Energy
3-5 November 2021
Porto, Portugal

Experimental quantification of low-frequency sound from wind turbines

E Blumendeller[a] and P.W. Cheng[a]

[a]Stuttgart Wind Energy @ Intitute of Aircraft Design - University Stuttgart,
Allmandring 5b, 70569 Stuttgart

E-mail: `blumendeller@ifb.uni-stuttgart.de`

Keywords: Acoustics, Wind turbines, Low-frequency sound, Long-term measurements

1 Introduction

The expansion of renewable energy usage is a major social challenge in Europe and requires acceptance and support from the population. Especially due to the expansion on land, a growing number of people lives closer to wind turbines (WTs), which leads to reported annoyance due to expected visual or acoustic disturbances caused by the planned WTs [1]. In many cases, it is argued that low frequency (20–200 Hz) and infrasonic (1–20 Hz) sound leads to the perceptibility of WT even at large distances.

This contribution will quantify the low-frequency sound emmissions of wind turbines and immission of the sound at resident buildings based on measurements. It briefly describes the procedure of the measurement campaigns. Additionally, first results will be presented. The measurement data of three different measurement positions are considered within the evaluation process (wind farm, outside building, inside building). The measured data are related to the WT operating conditions and differences in the averaged sound pressure levels or frequency spectra for the measurement locations are compared.

2 Measurements

Within this work measurement data is considered from measurements conducted at a wind farm site on the Swabian Alb located in the south of Germany. The wind farm is located at the top of the slope edge of the Swabian Alb and consists of three 2.5 MW WTs. Three microphones measured the sound pressure at the wind farm and at outside and inside locations of several residential buildings in appoximately 1 km distance to the wind farm. One microphone was placed in 140 m distance to one of the WT on an agricultural field. The two microphones at the residential buildings were moved every two weeks within the measurement period of two month (October to December 2020). Thus immission measurements were conducted at four residential locations in the vicinity of the wind park.

3 Data evaluation and results

In order to obtain an overview of the acoustic measurement data for all three locations, spectrograms were calculated for the period of one day. The power spectral density (PSD) of the acoustic data is calculated for a frequency range of 0.1-200 Hz (Figure 1) and 0.1-30 Hz (Figure 2).

During the measurement campaign, the turbines were shutdown in regular intervals during the night, to clearly measure the effect of the sound emission. In the diagram of Figure 1 a) the shutdown times are clearly visible on the basis of the reduced power spectral density over the entire frequency range of about 1 - 200 Hz, indicated by the colour coding. Signal components that are only present during WT operation are particular of interest. Several tones with increased density can be observed below 10 Hz, with a varying frequency above 20 Hz (Figure 2 a)) and with a strongly varying frequency between 100 Hz and 120 Hz, which disappeared instantly when the rotational speed of the WTs dropped to zero. The frequencies below 10 Hz (see Figure 2 for details) appeared to be directly correlated with the rotational speed of the wind turbine as multiples of the blade passing frequency (BPF).

In Figure 1 and 2 b) and c) acoustic signals measured at the place of immission are presented. Despite a reduction of the power spectral density from outside to inside location considering the overall noise, shutdown times of the wind farm can still be identified. The multiples of the BPF and the tone fluctuating around 20 Hz are still visible at the residential locations (Figure 2 b) and c)), in contrast to the multiples between 20 Hz and 100 Hz. The fluctuating signal component between 100 Hz and 120 Hz is faintly visible at the outside location. Other signal components can be assigned to the measurement location and are caused by other sound sources, the building structure or electrical noise at 50 Hz and 100 Hz. The vertical lines with high intensity both outside and inside can be caused by short-term sound sources such as passing trains in 20 m distance. Regularly occurring sounds at 60 Hz by household appliances and the continuous line at 20 Hz inside the building may be a structural resonance [2].

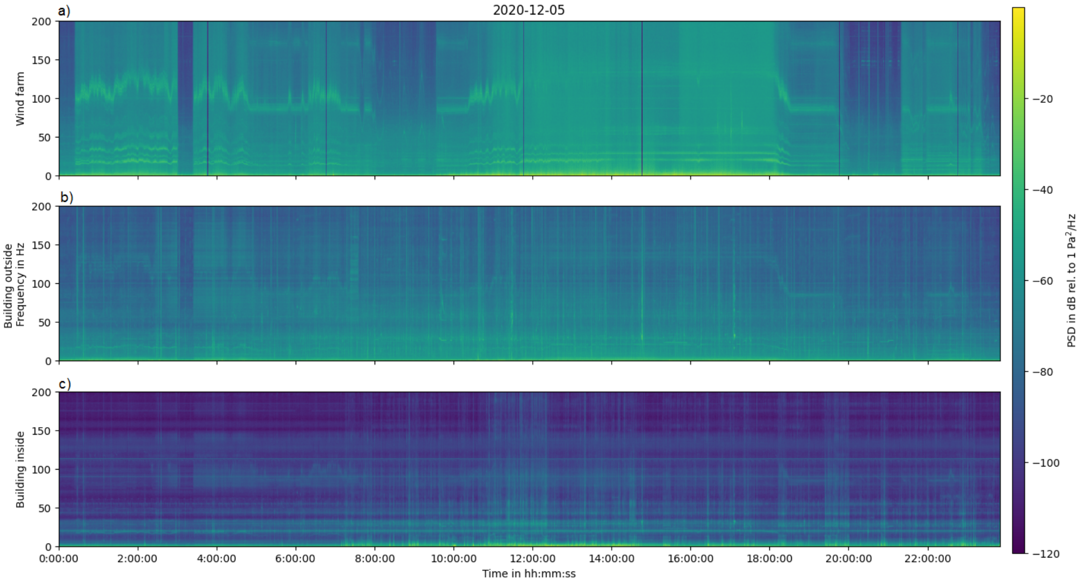

Figure 1: PSD for a frequency range of 0.1-200 Hz of all three measurement locations at the wind farm a), outside b) and inside c) of one residential location.

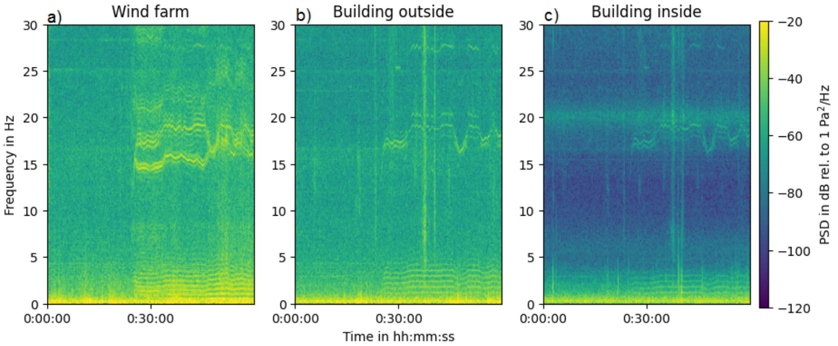

Figure 2: PSD for a frequency range of 0.1-30 Hz of all three measurement locations at the wind farm a), outside b) and inside c) of one residential location.

To analyze the WT sound at all three measurement locations the unweighted equivalent continuous sound pressure level (L_{eq}) was calculated for each 10 min period and a frequency range of 1-200 Hz. For a comparison between ambient and WT noise levels, data was selected for WTs operating in the full load range with rotational speeds between 11-12.6 rpm and compared to shutdown periods with rotational speeds between 0-0.5 rpm. For an increased contrast between ambient noise and WT sound data from night time was included into the evaluation.

Figure 3a shows filtered L_{eq} for the measurement locations at the wind farm, outside and inside one residential building. At all three locations, the sound pressure level is higher, when the turbine is operating. The sound pressure level (SPL) differences between WT and background noise is 10-15 dB. The L_{eq} decreases steadily from the wind farm to the indoor measurement location. However, the presentation of averaged L_{eq} does not allow any conclusions to be drawn about WT-specific noise characteristics. Therefore, the narrowband spectrum is calculated. Figure 3b and 3c shows the narrowband spectra for the frequency range 0.6 Hz to 200 Hz for similar conditions as the L_{eq} values (full-load range of WTs, night time data). The main difference between on/off spectra are tones below 10 Hz, around 20 Hz and 120 Hz. The BPF for a rotational rate of 11-12.6 rpm and a WT with three rotor blades is between 0.55 and 0.635 Hz. In both frequency spectra multiples of the BPF between 1.2 Hz and 7 Hz can be identified. The 20 Hz peak also stands out from the background noise at the wind farm and in the building. A broader peak occuring around 13 Hz (Figure 3c), both with and without WT operation can be attributed to a structural resonance of the building according to [3, 4].

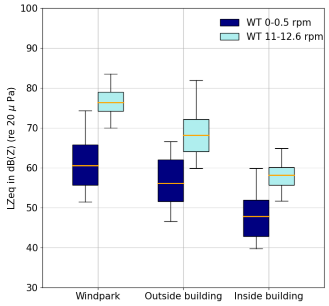

(a) $L_{Z,eq,10min}$ for the frequency range 1-200 Hz.

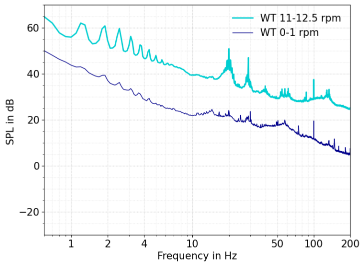

(b) Mean narrowband spectra for the microphone position at the wind farm location.

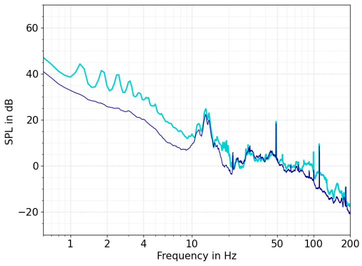

(c) Mean narrowband spectra for the microphone position at the residential indoor location.

4 Conclusion

In this work the procedure of acoutic measurements in the vicinity of a wind farm in southern Germany was described. Furthermore acoustic data of three simultaneous measurements at the wind farm, outside and inside residential buildings in 1 km distance were evaluated. To obtain an overview of the frequency components of the sound emissions and immissions and their intensity over time, a spectrogramm was presented for one exemplary day. The shutdown periods of the WTs are clearly recognisable in all measurements by a reduced intensity in the considered frequency range (1-200 Hz). The comparison enables the identification of frequency components that can be assigned to the WT operation. Moreover, averaged sound pressure level of a two weeks time period at one residential measurement location and for a frequency range of 1-200 Hz were caculated. For this purpose, only values at full load operation and stillstanding of the WT were considered. A level difference of about 10 dB was determined at all measurement locations between WT and background noise. Narrow band spectra were calculated to identify WT-specific noise characteristics. Especially frequency components due to WT operation below 10 Hz (mainly multiples of blade passing frequency), around 20 Hz, and above 100 Hz showed dominant peaks in narrowband spectra both at the wind park and inside the building, that can be assigned to WT operation. The low-frequency noise components of the wind turbines can be measured at all measurement positions considered and stand out from the background noise. This is the basis for further investigation to get a better understanding of the impact of environmental and WT-operational conditions on low-frequency WT sound, on its propagation and acoustic character.

References

[1] Doolan C 2013 *Wind Engineering* **37** 97–104 ISSN 0309524X

[2] Hansen K, Zajamšek B and Hansen C 2014 *INTERNOISE 2014 - 43rd International Congress on Noise Control Engineering: Improving the World Through Noise Control* 1–11

[3] Hansen K L, Hansen C H and Zajamšek B 2015 *Building and Environment* **94** 764–772 ISSN 03601323

[4] Hubbard H H 1982 *Noise Control Engineering Journal* **19** 49–55 ISSN 07362501

17th EAWE PhD Seminar on Wind Energy
3-5 November 2021
Porto, Portugal

Low-frequency noise computation from wind turbines using a FW-H acoustic analogy solver coupled with CFD

Anik H. Shah[a], Carlo R. Sucameli[a], and Carlo L. Bottasso[a]

[a]Chair of Wind Energy, Technical University of Munich, Garching, DE

September 14, 2021

`E-mail: anik.shah@tum.de`

Keywords: Wind turbine noise, Acoustic analogy, LES, Low-frequency, Blade passing frequency (BPF), Rotor-tower interactions

1 Introduction

Wind turbine (WT) noise is one of the major obstacles in scaling up the onshore wind generation. WTs emit noise ranging from low to high frequencies causing audible and inaudible issues to both humans and animals [1, 2, 3]. Several regulations have been imposed to reduce the discomfort associated with WTs [4, 5, 6]. Noise prediction enables an efficient design of WTs thereby improving their social acceptance. Majority of the research is focused on airfoil self-noise and inflow turbulence which are the main causes of high-frequency audible noise (20 Hz - 20 kHz) from WTs [7]. Infrasound and low-frequency noise is less explored due to their insensitivity for the human auditory system. However, blade passing frequency (BPF) modulates the audible, higher frequency sounds and thus produces a periodic sound known as *blade swish* [8]. The distinct beating character at BPF is a bigger problem at night due to higher atmospheric stability. Additionally, noise signals in this frequency range can travel long distances before dissipating completely. With modern WTs expected to be larger, the effect of these stronger fluctuations needs to be studied in detail.

2 Methodology

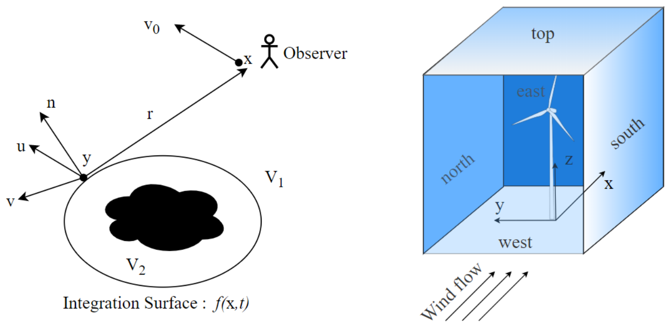

(a) FW-H acoustic analogy [9] (b) Permeable slices around WT.

Figure 1: Permeable FW-H implementation for WT

The current work initially focuses on the development of an aero-acoustic propagation solver coupled with CFD to predict low-frequency WT noise. It applies the Ffowcs Williams-Hawkings (FW-H) acoustic analogy [9]. Acoustic analogies derive propagation and source term formulations for the wave equation by rearranging the Navier Stokes equations. The initial acoustic analogy proposed by Lighthill describes noise generated by a turbulent region of a fluid in an unbounded quiescent medium [10]. FW-H acoustic analogy generalizes this work by including moving surfaces. A permeable integration surface around a stationary wind turbine is considered with a stationary observer in a fluid medium (air) moving with a uniform mean flow. Galilean transformation is used to account for the mean flow of fluid medium [11]. Fig. 1 shows the schematic for FW-H acoustic analogy for WT.

Incompressible LES-based flow field data is computed for DTU 10MW model[12] by using SOWFA [13], which couples OpenFOAM [14] and FAST [15]. The actuator line turbine model is used to project WT Rotor's aerodynamic response from FAST back to OpenFOAM via body forces [16]. Immersed Boundary method is used to model the WT tower [17]. The flow field data on the permeable surface is used to compute the far-field acoustic pressure through FW-H acoustic analogy. Casalino's advanced time approach is implemented to reconstruct the signal at observer location [18]. A detailed analysis of the low-frequency noise is carried out highlighting the influence of rotor-tower interactions. Dominant noise sources in the infrasound region are identified, thereby inspiring both control and design measures to reduce WT noise. The initial results are presented in the subsequent section.

3 Initial Results

Noise analysis was carried out for the same downstream observer location at ground for two simulation cases, Rotor-only and Rotor-tower. The difference in aeroacoustic noise spectrum at a given observer position can be obtained by evaluating the acoustic pressure signal in time and frequency domain, the power spectral density and the sound pressure levels in the frequency domain as shown in fig. 2.

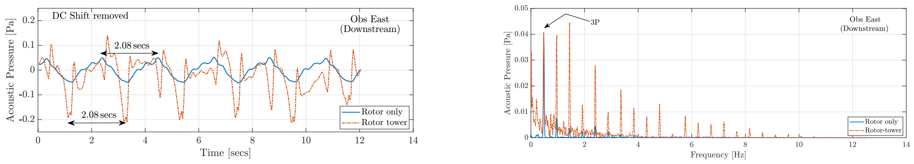

(a) Acoustic pressure signal - time domain (b) Acoustic pressure signal - frequency domain

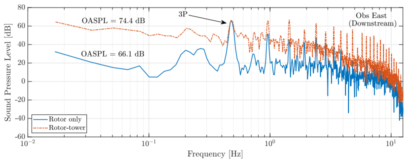

(c) Sound Pressure Level

Figure 2: Permeable FW-H implementation for WT

The Rotor-tower case shows a much more irregular signal with sharper peaks compared to the relatively smoother, almost sinusoidal signal for the Rotor-only case. The 2.08 sec interval highlighted for both cases shows the timeperiod for BPF. For the Rotor-tower case, the sharpness of the peaks indicates a presence of higher harmonics of 3P (BPF) as confirmed in the frequency domain. This type of impulsive signal is characteristic of the noise created when blade passes the tower. An overall sound pressure level (OASPL) is also computed from the SPL noise spectrum. It can be seen that the presence of tower significantly increases the noise due to the complex rotor-tower interactions and the subsequent wake of the WT.

The initial results highlight the dominant noise sources in the infrasound region, thereby inspiring control and design measures to reduce the noise. Design parameters such as Overhang, Tilt, and Yaw are currently being studied to alleviate the rotor-tower coupling. Open-loop control measures such as pitch control are also being explored. Ultimately, a better understanding of low-frequency noise sources can help optimize WT control and design from a social acceptance point of view.

References

[1] van Kamp I and van den Berg F 2018 *Acoustics Australia* **46** 31–57 ISSN 1839-2571 URL `https://link.springer.com/article/10.1007/s40857-017-0115-6`

[2] Kageyama T, Yano T, Kuwano S, Sueoka S and Tachibana H 2016 *Noise & Health* **18** 53–61 ISSN 1463-1741

[3] Schmidt J H and Klokker M 2014 *PLoS ONE* **9** e114183

[4] 2018 Environmental Noise Guidelines for the European Region (2018) URL `http://www.euro.who.int/en/publications/abstracts/environmental-noise-guidelines-for-the-europea`

[5] European Wind Energy Association 2012 Noise regulation and wind energy deployment in EU member states

[6] E Nieuwenhuizen 2015 Differences in noise regulations for wind turbines in four European countries

[7] Sucameli C R, Bortolotti P, Croce A and Bottasso C 2018 *Journal of Physics: Conference Series* vol 1037 (IOP Publishing) p 022038

[8] van den Berg G 2005 *Journal of Low Frequency Noise, Vibration and Active Control* **24** 1–23

[9] Williams J F and Hawkings D L 1969 *Philosophical Transactions for the Royal Society of London. Series A, Mathematical and Physical Sciences* 321–342

[10] Lighthill M J 1952 *Proceedings of the Royal Society of London. Series A. Mathematical and Physical Sciences* **211** 564–587

[11] Ikeda T, Enomoto S, Yamamoto K and Amemiya K 2017 *AIAA Journal* **55** 2307–2320

[12] Bak C, Zahle F and Bitsche R 2013 The DTU 10-MW Reference Wind Turbine

[13] Matthew Churchfield, Sang Lee and Patrick Moriarty 2012 Overview of the Simulator fOr Wind Farm Application

[14] About openfoam URL `https://www.openfoam.com/documentation/guides/latest/doc/index.html`

[15] Jonkman J M and Buhl Jr M L 2005 FAST User's Guide Tech. rep. NREL

[16] Sørensen J N and Shen W Z 1999 *1999 European Wind Energy Conference and Exhibition* pp 156–159

[17] Jasak H, and Tukovic Z 2015 Immersed Boundary Method for FOAM

[18] Casalino D 2003 *Journal of Sound and Vibration* **261** 583–612 ISSN 0022460X

17^{th} EAWE PhD Seminar on Wind Energy
3-5 November 2021
Porto, Portugal

Environmental impact of wind energy and paths to improvement from design phase

A Guilloré[a], H Canet[a], and C.L. Bottasso[a]

[a]Wind Energy Institute, Technische Universität München, Garching bei München, Germany.

September 15, 2021

`E-mail: adrien.guillore@tum.de`

Keywords: Beyond LCoE; Environmental Impact; Life-Cycle Assessment

1 Introduction

The multi-disciplinary design of wind turbine is commonly based on the minimization of the Levelized Cost of Energy (LCoE). Some recent research is looking for alternative merit figures, aiming at considering some effects that are not captured by the LCoE, such as market value or grid integrability, designing towards *"Beyond LCoE"* [1]. This work proposes to integrate the consideration of the environmental Impact of Energy (IoE) into the design of wind turbine. The Greenhouse Gases (GHG) emissions of wind energy have been studied in various publications already [2, 3, 4, 5, 6], but most usually in a post-design approach to inform policy makers and civil society. It is here proposed to integrate this consideration from the design phase perspective. The research objectives of this work are to determine the potential reduction of environmental burden related to wind turbine by different technological choices, and study the trade-offs that can be found with relation to monetary costs.

2 Methodology

The Life-Cycle Assessment (LCA) methodology [7] is used to estimate the Climate Change impact from cradle to grave, which is expressed as equivalent CO2 emissions by unit of produced energy (in $gCO_{2,eq}/kWh$). As can be seen on Figure 1, the raw material extraction and processing, and the components manufacturing were identified to be the main sources of greenhouse gases emissions in the wind turbine life cycle, mostly due to the intensive use of materials for the tower and the foundations. But the recycling of most of these materials at the turbine end-of-life has an important environmental benefit. The fiberglass thermoset composites for the blades were estimated to be the third most emitting component, mostly due to their lack of end-of-life recyclability potential at the current state of large-scale technology.

3 Results

The influence of the wind resource, the rated power, the rotor diameter and the hub height on the environmental IoE is quantified. Similarly to the Levelized Cost of Energy (LCoE), the design space based on environmental consideration is generally characterized by parabola-shaped curves. These represent the design trade-offs that need to be found between increasing the energy capture and limiting the use of materials. Furthermore, several different technological improvement opportunities were considered for parametric studies to estimate their potential influence on the IoE: the tower type, the drivetrain technology, the introduction of carbon-fiber composites in the blades, and the use of thermoplastics

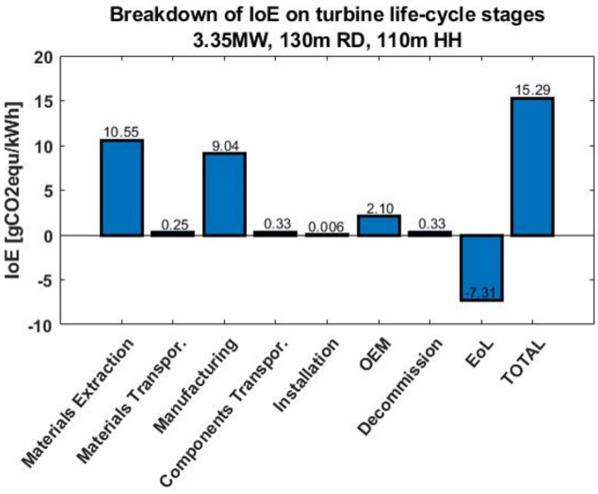

Figure 1: Breakdown of the IoE by life-cycle stages

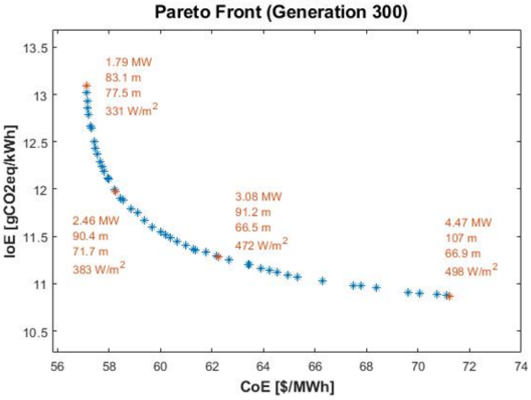

Figure 2: Results of the Pareto front from multi-objective optimization of the rated power, rotor diameter, hub height and corresponding specific power (in order of vertical appearance on the figure) with double objective of costs and environmental impact of energy

composites instead of thermosets. The hybrid tower (with some concrete) and the thermoplastics were estimated to be the most promising options to reduce the overall life-cycle environmental impact.

This automated LCA model is then used for the computational optimization of the general turbine parameters (rated power, rotor diameter, hub height). The IoE is introduced as a new merit function, to identify some preliminary design trends. It is shown that the LCoE and the IoE are not equivalent merit functions in the design of wind turbines. Multi-objective optimizations are conducted to obtain a Pareto front (Figure 2), which represents the best possible design trade-offs between the costs (consumer perspective) and the environmental impact (societal perspective).

References

[1] Dykes, K., Kitzing, L., Andersson, M., Pons-Seres de Brauwer, C. & Canét, H. (2020). *Beyond LCOE: New Assessment Criteria for Evaluating Wind Energy R&I.* SETWind.

[2] Schleisner, L. (2020). *Life-cycle assessment of a wind farm and related externalities*, Renewable Energy, vol. 20, no. 3, pp. 279-288.

[3] Ozoemena, M., Cheung, W., Hasan, R. (2018). *Comparative LCA of technology improvement opportunities for a 1.5 MW wind turbine in the context of an onshore wind farm.* Clean Technologies and Environmental Policy, vol. 20, p. 173-190.

[4] Al-Behadili, S.H., El-Osta, W. (2015). *Life Cycle Assessment of Dernah (Libya) wind farm.* Renewable Energy, vol. 83, pp. 1227-1233.

[5] Garrett, P., Ronde, K. (2020). VESTAS LCA reports with critical review by third party, online access at https://www.vestas.com/en/about/sustainability#!lcareports.

[6] Tremeac, B. and Meunier F. (2009). *Life cycle analysis of 4.5MW and 250W wind turbines.* Renewable and Sustainable Energy Reviews, vol. 13, pp. 2104-2110.

[7] JRC European Commission ILCD Handbook (2010). *General Guide for Life Cycle Assessment - Detailed guidance.* EUR 24706 EN.

STRUCTURAL ANALYSIS

Evaluation, classification and conditioning of experimental measurement data for structural health monitoring, using a machine learning approach

Matthias Fankhänel[a], Tanja Grießmann[a], and Raimund Rolfes[b]

[a]a) Leibniz University Hannover, Institute of Structural Analysis, ForWind, Appelstr. 9a, D-30167 Hannover, Germany

June 29, 2021

`E-mail: m.fankhaenel@isd.uni-hannover.de`

Keywords: Data pre-selection, Data classification, Field measurement, Environmental conditions, Machine learning

Abstract

The maintenance of offshore wind turbines is usually associated with high effort due to their difficult accessibility. Therefore, the field of structural health monitoring (SHM) aims at monitoring those structures using indirect damage indicators such as variations in natural frequencies, mode shapes or structural damping. This gives the ability of a condition-based statement on the structure without the need for regular maintenance. Methods of operational modal analysis (OMA) are well established for the purpose of feature extraction, but difficulties arise when applying them to a complex system such as an offshore wind turbine. In that case, the assumptions of a linear time invariant system behavior and an excitation with white noise are violated. In addition, the distinction between environmental and operational variations (EOVs) and damage has shown to be complicated. Therefore, a trade-off between many 'false alarms' and features that are not sensitive enough has to be made.

The very first step before monitoring a structure using the methods of OMA is the evaluation of suitable measurement data. For this purpose, data sets are selected, using a series of quality characteristics such as a feasible signal to noise ratio (SNR). The investigated measurement data is taken from a steel lattice mast test structure The data comprises acceleration measurements as well as environmental conditions (wind speed, air temperature, radiation, etc.). The quality criteria are set concerning their influence on the uncertainty in the determination of modal parameters and spectral densities. For the detection of significant errors in the data, arising for example from poorly attached sensors, a machine learning approach is considered. The selected data is then prepared for further processing by eliminating detected measurement errors, as well as normalization and conditioning (e.g. digital filtering or averaging in frequency or time domain). Further, a classification of the measured data is made by the environmental conditions to decide whether the data should be further processed separately by class.

Keywords: Data pre-selection, Data classification, Field measurement, Environmental conditions, Machine learning

Comparison of methodologies to combine strain cycle histograms to an accumulated damage figure at a point of interest along the circumference of an offshore wind support structure

N Sadeghi*[a], K Robbelein[a], P D'Antuono[a], N Noppe[a], and C Devriendt[a]

[a] Offshore Wind Infrastructure lab (OWI-lab)/Vrije Universiteit Brussel (VUB), Belgium

E-mail: Negin.Sadeghi@vub.be

Abstract. This work is part of the research activities by OWI-lab within MAXWind project on the subject of data-driven lifetime assessment of offshore wind support structures (OWSS). To this stage, the recorded strain signals are converted into fore-aft (FA) and side-side (SS) bending moments to calculate the corresponding damage metrics, such as Palmgren-Miner damage, damage equivalent load (DEL) or damage equivalent moment (DEM). A refined lifetime analysis requires the damage/DEL/DEM calculation at a specific heading rather than in the FA and SS directions, which would be achieved either by directly rotating the strain signals at the required heading or through a yaw transformation of the averaged fore-aft and side-side bending moments. Given the amount of data that OWI-lab has collected over the years, performing such operation has multiple disadvantages, as it easily becomes computationally prohibitive and highly storage demanding. The lack of flexibility of such approaches is just as important, in fact changing the heading would mean starting the processing from scratch. The research aims at finding a low-computational cost yet accurate methodology to derive the accumulated damage at any point along the circumference of the support structure without reprocessing the data. That way, the lifetime of the critical sections/welds could be accurately and quickly evaluated based on real-life strain measurements on an OWSS. This study compares different methodologies based on FA and SS bending moments to quantify the accumulated damages at any desired point. A reference method based on individual strain gauge signals is used to validate the current methodologies.

Keywords: Offshore wind turbine, Fatigue, Damage, Wind direction, Monitoring

1 Introduction

Wind turbines are among the industrial structures bearing the most intensively varying loads, being exposed to natural forces like wind and waves throughout their whole lifetime. As a consequence, they experience an impressively high number of fatigue cycles (crf. Figure 1). [1] The older (and smaller) generation of wind turbines is less affected by the wave loads since their natural frequency is not close to the waves frequency, but just like the turbines installed on XL monopiles, they must withstand winds of variable speeds and directions. These structures are mostly fatigue driven, and to monitor the induced fatigue damage, installed sensors on the peripheral of the tower or transition piece (TP) record signals with millions of cycles. Processing this enormous amount of data needs particular methodologies. Otherwise, the fatigue analysis is unmanageable in terms of computing time and space.

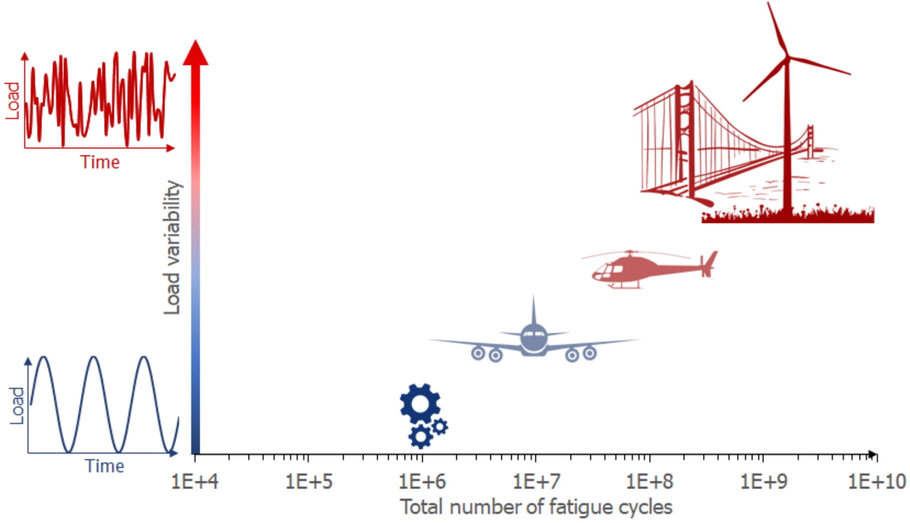

Figure 1 Fatigue cycles variability on some engineering components and structures

2 Objectives

As the wind direction varies in time, the loads on different wind turbine components also vary. As stated by Nozari et al., [2] “the wind direction affects the estimated fatigue damage significantly, and it may change the predicted critical points in the monopile supporting structures”. Based on the large dataset that OWI-lab has collected on different wind turbines during years of measurement, this study used the M_{tn} and M_{tl} (also known as fore-aft and side-side bending moments) that are available for a wind turbine in a wind farm in Belgium to calculate the damage. The current approach considers the maximum damage calculated from FA or SS bending moment. The primary purpose of this research is to save computational and storage costs not to be limited to one critical point but to specify damage for any desired heading. The goal is to first find the accuracy of the current methods and then propose and validate a method that can increase damage estimation accuracy for each point on the circumference of the tower/TP. Therefore, first, a sensor heading is considered as the critical point because the actual damage of this point is available from analyzing the sensor's strain signals. The proposed method will rotate the FA and SS bending moments to the two directions of normal and lateral to the critical point. Therefore, we expect that the residual between the measured reference damage and the predicted damage decreases. Once the method is validated, the damage can be calculated for every heading.

3 Current Processing method to calculate fatigue damage from strain measurements

The primary step to calculate the fatigue damage is to import the strain signals and convert them into stresses using Hooke's law and then convert the stress time series into bending moments. According to wind industry standards, the bending moments acting on the tower are given in two directions, the fore-aft and the side-side. The fore-aft direction is the same as the wind direction, while the side-side is perpendicular. These bending moments are shown in Figure 2.

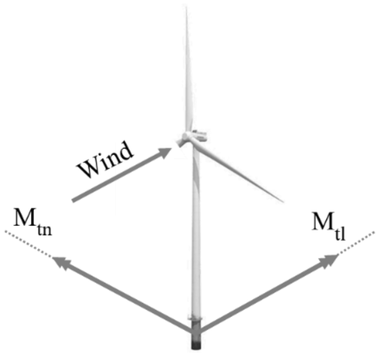

Figure 2 Tower loads on a wind turbine (fore-aft and side-side)

In the customary approach, based on Eq1-2, the gathered strain measurements from at least three strain gauges (installed on the circumference of the tower/TP) are necessary to extract the normal load F_N and bending moments in both directions M_{NS} and M_{EW} (North-South and East-West).

$$\sigma_z = \frac{F_N}{A_{CS}} + \frac{R_i}{I_C}(M_{NS} sin\theta_h - M_{EW} cos\theta_h) \tag{1}$$

$$\begin{bmatrix} \sigma_{z1} \\ \sigma_{z2} \\ \sigma_{z3} \end{bmatrix} = \begin{bmatrix} \frac{1}{A_{CS}} & \frac{R_i}{I_C} sin\theta_{h,1} & -\frac{R_i}{I_C} cos\theta_{h,1} \\ \frac{1}{A_{CS}} & \frac{R_i}{I_C} sin\theta_{h,2} & -\frac{R_i}{I_C} cos\theta_{h,2} \\ \frac{1}{A_{CS}} & \frac{R_i}{I_C} sin\theta_{h,3} & -\frac{R_i}{I_C} cos\theta_{h,3} \end{bmatrix} \begin{bmatrix} F_N \\ M_{NS} \\ M_{EW} \end{bmatrix} \tag{2}$$

Where normal stress σ_z is induced by a normal force F_N, A_{CS} represents the surface area of the cross-section, R_i is the inner radius, θ_h is the heading (clockwise starting North) and I_C is the area moment of inertia. Through the rotation matrix in Eq 3, these two bending moments are turned into fore-aft (M_{tn}) and side-side (M_{tl})bending moments. This operation enables us to have the most severe damage (maximum of FA and SS) independent of the exact headings. Therefore to be conservative, we assume the worst wind condition for each point on the peripheral as if the wind always hits them in their heading direction. However, to achieve a more accurate prediction, damage calculation should be performed for each heading instead of assuming the most destructive direction (FA or SS).

$$R = \begin{bmatrix} cos(-\psi + 180^{\circ}) & sin(-\psi + 180^{\circ}) \\ -sin(-\psi + 180^{\circ}) & cos(-\psi + 180^{\circ}) \end{bmatrix} \tag{3}$$

Where ψ is the turbine yaw angle coming from the supervisory control and data acquisition (SCADA) system.

Therefore, M_{tn} and M_{tl} are stored as the cycle count histograms after processing each 10-minute subset of strain time history. To do so, after rotating the M_{NS} and M_{EW} signals into M_{tn} and M_{tl} , first, the signals are converted into turning points, and after a four-point cycle count on each 10-minute window, the full cycles, the turning points that constitute the residuals, and the corresponding stress ranges are stored in histograms. Recording M_{tn} and M_{tl} as histograms has opportunities and obstacles. On the one hand, it decreases the storage space and the processing time significantly, whereas the indication of time is missing due to grouping cycles. The main drawback of this procedure is that the rotation of M_{tn} and M_{tl} to a specific heading through a histogram is much more challenging than using a time signal.

Once the cycle count histograms of M_{tn} and M_{tl} are stored for each 10-min subset, these histograms can be easily imported and merged together to calculate the damage further. Finally, by applying the Palmgren-Miner rule on the merged histogram, the highest damage caused by FA or SS can be calculated. From the Palmgren-Miner rule, [3], [4] the accumulated fatigue damage D is obtained as the sum of the ratios of occurred cycles n_i over cycles to failure N_i for all occurred stress ranges $\Delta\sigma_i$, which is given by Eq 4.

$$D = \sum_{i=1}^{k} \frac{n_i}{N_i} \tag{4}$$

The number of cycles to failure for a given stress range is defined by an S-N curve [5] (Figure 4). An S-N curve represents how many cycles (N) of a constant stress range ($\Delta\sigma$) a specimen can hold before failure. Therefore, the fatigue damage can be calculated using these bending moments, as presented in Figure 3**Erreur ! Source du renvoi introuvable.**.

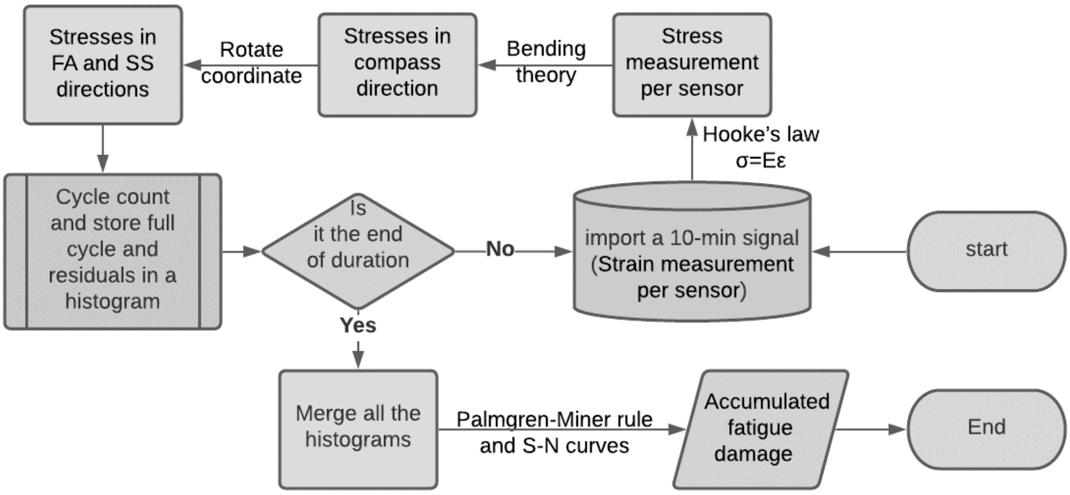

Figure 3 Customary processing flowchart from strain measurement to fatigue damage

4 Methodology

Different approaches are suggested to calculate the fatigue damage on the critical point for small wind turbines, usually where the thrust loading caused by the wind is prevalent. In this research, we tried to reconstruct the fatigue histogram at every location along the circumference of the tower/TP by using the wind rose and the fatigue histograms of FA and SS bending moments. So after the first step, which is to import the FA and SS bending moment histograms for the desired period, the methodology can follow five different approaches:

- The 'FA' approach, which assumes that each point only receives damage from FA bending moments.
- The 'SS' approach considers each point's damage only based on the SS bending moments.
- The 'FA+SS' approach, which is the most conservative and unrealistic one, assumes that the critical point always faces the FA and SS in the normal direction, so it receives 100% of the fore-aft and side-side bending moments.
- The 'scaled N' approach, which is more realistic, uses the wind rose and divides the section of the tower/TP into four quarters and first finds two factors (f_fa and f_ss) based on the

frequency of wind direction in pairs of (first and third) and (second and fourth) quarters (Figure 6). The calculated factors are directly applied to the cycle number of M_{tn} and M_{tl} so that both bending moments contribute partially to the damage of the critical point.

- The 'scaled Δσ' approach, which instead of applying the factors derived from the wind rose, rotates the FA and SS bending moment histograms to the critical heading. This method is briefly explained in the future work section.

The first four methods have been tested by comparing their results with damage of the reference stress histogram from the strain time series of the desired point, but the last method is still under study. In the following part of this section, the 'scaled N' approach is explained in more detail, and the 'scaled Δσ' procedure is briefly described in the future work section.

A sensor heading can be assumed as the critical point to compare and validate the first four methods since the reference damage can be easily achieved using the sensor's punctual signals. Then based on the first four methods and considering four different S-N curves, shown in Figure 4, the damage of these sensors is calculated for a one-month duration.

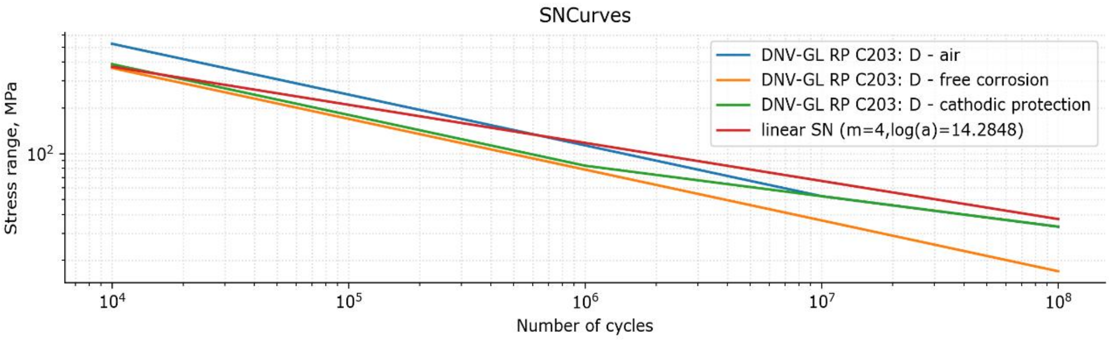

Figure 4 S-N curves used in the damage validation

As an example shown in Figure 5, when the wind direction is from South West, the damage of a sensor on the third quarter is mainly affected by the FA bending moment, while a sensor on quarter two has its damage primarily because of the SS bending moment. On the other hand, when the wind direction is from South East, the damage of a sensor on the third quarter is mainly affected by the SS bending moment, while a sensor on quarter two has its damage primarily because of the FA bending moments. Considering this concept, based on the windrose in Figure 6, the majority of wind direction (66.3%) is from South West, which means that damage of sensor on heading 222° is 66.3% of the time from FA and 33.7% of the time from SS bending moments, while for sensors 135° and 315°, which are in quartile two and four, the opposite is true. Therefore, f_fa and f_ss factors are 66.3 and 33.7%, respectively, for the first (Q1) and third (Q3) quartile, while f_fa and f_ss are 33.7 and 66.3%, quartile two (Q2) and four (Q4).

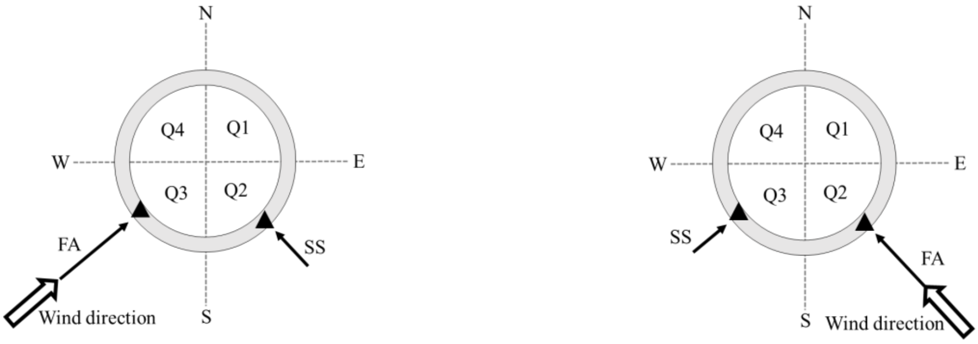

Figure 5 How different quarters see the effect of FA and SS

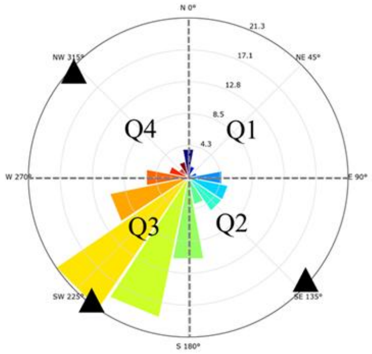

Figure 6 Windrose or distribution of wind direction and frequency of occurrence in the four quarters, with 66.3% in Q1 and Q3 and 33.7% in Q2 and Q4. The three sensors are shown with triangle symbols.

5 Results and Validation

Three sensors on headings 135°, 222°, and 315° were selected as the points of interest (critical points) to calculate the reference damages. Figure 6 to Figure 8 give the damages calculated by considering only FA, only SS, FA+SS, and a factorized sum of FA and SS by scaling the number of cycles using wind rose factors ('scaled N' approach). These four damages were compared with the damage produced from the strain time series of the selected sensor (critical point). We see similar results for all three critical points: the FA+SS and FA damage has the most significant predicted damage, while the SS damage has the lowest values. This result is expected since we are validating smaller wind turbines, where the thrust loading is dominant. For these turbines, the FA damage is typically much greater than the SS damage. This fact is also visible in the following plots since FA and FA+SS overestimate the damage, but SS underestimates the damage. Looking at the 'scaled N' method, we see it matches the reference damage better for sensors 222 and 315 than sensor 135. The reason can be either a failing sensor or inaccuracy of this approach. To control the accuracy of the proposed methods in using different S-N curves,

Finally, to control the accuracy of the proposed methods, we checked if the predicted damage and the reference damage match in all different S-N curves. Although the 'Scaled N' approach shows pretty accurate results in all four types of S-N curves, it aligns less with the reference damage when using the S-N curves with a knee (bilinear curves in Air and Cathodic protection conditions). A fifth method is proposed to reduce this effect which scales the stresses independent of the number of cycles, and therefore, it might be less affected by the type of the used S-N curve.

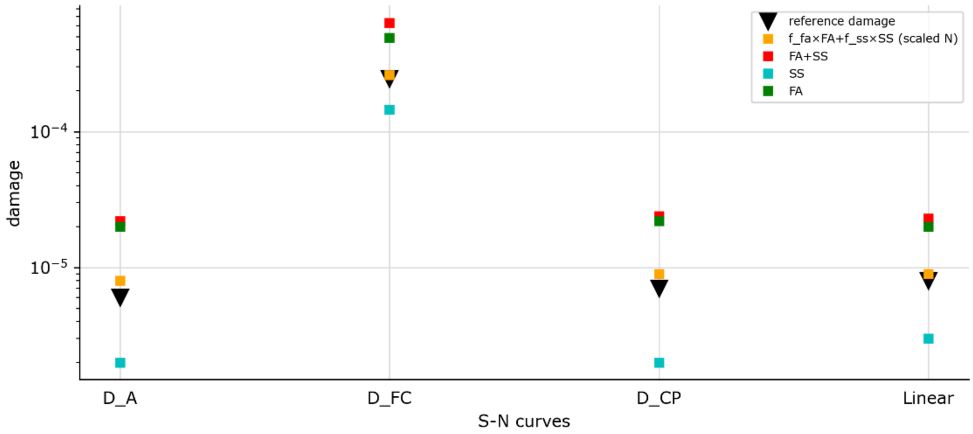

Figure 1 Comparison of damage based on different calculation methods for the sensor on heading 135°

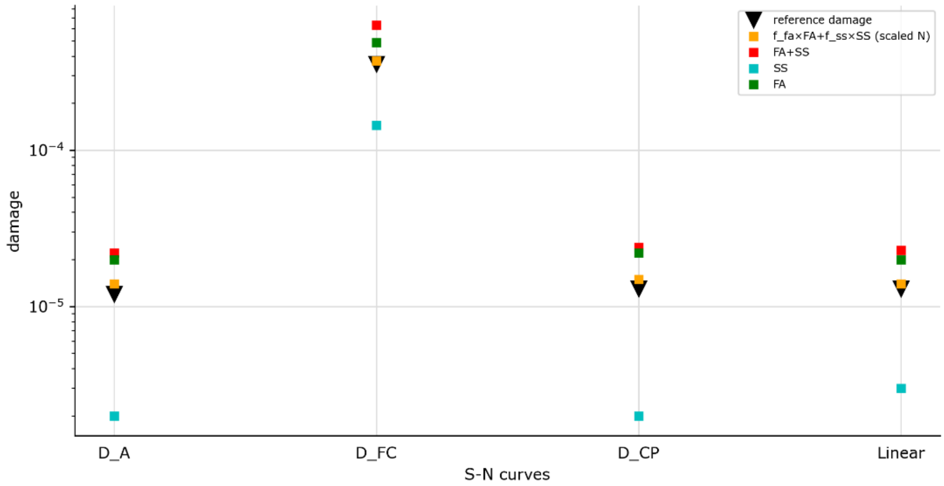

Figure 2 Comparison of damage based on different calculation methods for the sensor on heading 222°

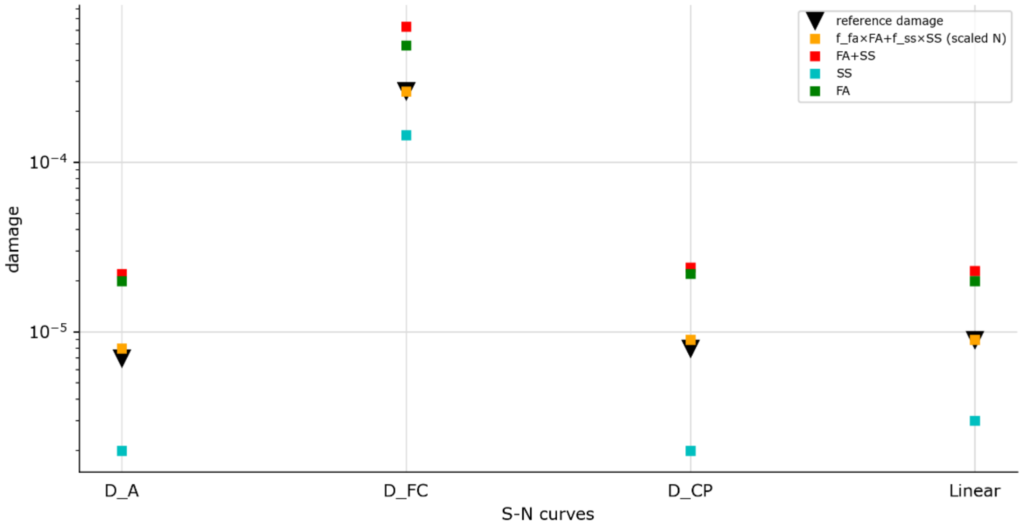

Figure 3 Comparison of damage based on different calculation methods for the sensor on heading 315°

6 Conclusions

In this study, four different methods were investigated to predict the damage in a critical point around the circumference of a wind turbine tower. By comparing their results with the defined reference damages, it can be concluded that the best match to the reference damage is achieved by applying the 'scaled N' method, while the most conservative approach is to view the full effect of FA and SS simultaneously. Also, the least predicted damage is from considering only the impact of SS bending moments. In addition, the accuracy of the life-scaling approach was high for all different types of S-N curves, although using bilinear S-N curves causes more inaccuracy in the calculated damage of the 'scaled N' method. Since the accuracy of this method might be affected by the type of S-N curve, the authors will further study a new approach to calculate the damage in a point of interest by scaling the stress ranges instead of factorizing the number of cycles.

7 Future work

Because the 'scaled N' method is not sufficiently accurate in the damage prediction of different headings, the future work plan of authors is to refine and validate a new technique to decrease this gap between the predicted damage in the point of interest and the actual damage in that point. This method will introduce some necessary hypotheses to apply a rotation to the stress range histograms from FA and SS bending moments to the normal and lateral directions of the location of interest (scaled $\Delta\sigma$). It will be then validated using the same method mentioned in this article. Therefore, the predicted damage will be dependent on the heading instead of conservatively assuming the most destructive damage in the wind direction for all the headings. As for the 'scaled N', the 'scaled $\Delta\sigma$' will calculate the damage in the desired heading needless of reprocessing the whole strain signals.

Acknowledgments

This research is being conducted within the project MAXWind, funded by the Energy Transition Fund (ETF).

Bibliography

[1] H. J. Sutherland, ‘On the Fatigue Analysis of Wind Turbines’, Sandia National Labs., Albuquerque, NM (US); Sandia National Labs., Livermore, CA (US), SAND99-0089, Jun. 1999. doi: https://doi.org/10.2172/9460.
[2] A. Nozari, D. Kuchma, and E. M. Hines, ‘Effect of wind directionality on fatigue life of monopile support structures for offshore wind turbines’, *J. Phys. Conf. Ser.*, vol. 1618, p. 052080, Sep. 2020, doi: 10.1088/1742-6596/1618/5/052080.
[3] A. G. Palmgren, ‘Die Lebensdauer von Kugellagern (Life Length of Roller Bearings. In German)’, *Z. Vereines Dtsch. Ingenieure VDI Z. ISSN*, pp. 0341–7258, 1924.
[4] M. A. Miner, ‘Cumulative Damage in Fatigue’, *J. Appl. Mech.*, vol. 3, pp. 159–164, 1945.
[5] ‘DNV-RP-C203: Fatigue Design of Offshore Steel Structures’, p. 176, 2011.

Geometrically nonlinear cross-sectional deformations of a very large wind turbine blade

J Gebauer[a], C Balzani[a], E Werthen[b], and C Hühne[b]

[a]Leibniz University Hannover, Institute for Wind Energy Systems, Appelstr. 9A, 30167 Hannover, Germany
[b]German Aerospace Center, Institute of Composite Structures and Adaptive Systems, Lilienthalplatz 7, 38108 Braunschweig, Germany

E-mail: `julia.gebauer@iwes.uni-hannover.de`

Abstract

Offshore wind turbines with rated capacities of more than 20 MW will feature rotor blade lengths of more than 150 m. Increasing the rotor area means higher loads due to weight and aerodynamic forces. The rotor blade structure must bear these loads.

For an optimal structural rotor blade design the loads need to be known. Cross-sectional deformations, however, are not taken into account in load calculations. So far, it is assumed that there is a connection between the cross-sectional deformation and the aeroelastic behaviour of rotor blades. Particularly for very large and ultra slender rotor blades, we expect considerable cross-sectional deformations parallel and perpendicular to the cross-section planes, especially in the inboard third of the blade span. We thus conduct research to determine a possible impact of such deformations on the loads.

The overall goal is to develop an extension of a geometrically exact beam formulation. Therein, the relationships between the internal load states in the blades and the cross-sectional deformations on the one hand, and the relations between the cross-sectional deformations and the aerodynamic behaviour on the other hand, are to be taken into account in an aero-servo-elastic turbine simulation. For this purpose, initial investigations of the IEA 15 MW rotor blade [1] are carried out by generating a finite element model using the tool MoCA (Model Creation and Analysis) [2]. By applying extreme loads, possible cross-sectional warping is examined. The results of this investigation will be discussed in this presentation.

Keywords: Cross-sectional warping, Finite Element simulation

References

[1] Gaertner, E., Rinker, J., Sethuraman, L., *et al.* (2020). IEA wind TCP task 37: Definition of the IEA 15-megawatt offshore reference wind turbine. Technical Report No. NREL/TP-5000-75698, National Renewable Energy Lab. (NREL), Golden, CO (United States).

[2] Noever-Castelos, P., Haller, B., and Balzani, C. (2021). Validation of a modelling methodology for wind turbine rotor blades on a full scale blade test. *Wind Energ. Sci. Discuss.* [preprint], `https://doi.org/10.5194/wes-2021-24`, in review.

17th EAWE PhD Seminar on Wind Energy
3 – 5 November 2021
Porto, Portugal

Preliminary Investigation on the Limitations of Existing S-N Design Curves

J DeFrancisci[a], D Kuchma[a], M Sanayei[a], A Nozari[a]

[a] 200 College Avenue, Department of Civil and Environmental Engineering,
Medford, MA 02155

E-mail: john.defrancisci@tufts.edu

Keywords: Corrosion, Faitgue, Corrosion-Fatigue, and Foundations

1 Introduction

From 2019 to 2020, a team of researchers from Tufts University led a research project on "Design Life Issues Related to Corrosion and Fatigue" of support structures for offshore wind turbines. This project was funded by the Bureau of Ocean and Energy Management (BOEM; U.S. regulator for offshore wind) and the Massachusetts Clean Energy Center (MassCEC). A broad group of consultants and advisory panel members from across the U.S. and European marine construction communities contributed substantially to this work (see Acknowledgements section.) This project reviewed the state-of-the-art in corrosion-fatigue modelling, design requirements, and field performance, Six workshops with more than 200 total participants were held that identified areas of consensus, uncertainty, and best practices [5]. One key area of identified uncertainty was limitations of the S-N-based fatigue analysis method for making fatigue life assessments. These limitations include lag time between foundation installation and cathodic protection installation, quality and quantity of existing fatigue test data, influence of nonproportional multiaxial stresses on fatigue life, and the impact of variable amplitude loading on the initiation of fatigue cracks. The poster presents a brief summary of the various uncertainties identified in this project as well as a preliminary comparison of different S-N curves. This preliminary comparison identifies areas where future work is needed.

2 Methods

Some of the key challenges identified through the literature review, workshops, and advisory panel discussions were [5]:

1. Lack of fatigue test data for variable amplitude loading in the very high cycle range and influence of nonproportional multiaxial stresses

2. Relatively low numbers of fatigue tests done under in-situ corrosion conditions compared with in-air testing

3. Modern equipment makes it easier to collect important data about the corrosion pit development, however this kind of information has not been collected for corrosion-fatigue tests.

4. Uncertainty about the accuracy of the impact of specimen thickness on fatigue life for very thick specimens.

The analysis in the table comes from a preliminary set of fatigue analyses that used different pre-existing S-N curves to compare the impact of curve selection on fatigue life. These preliminary analyses did not include a comparison of how the thickness coefficient impacts the fatigue life across the different design documents. The stresses used in this analysis are from work done by Amin Nozari modelling a 15MW wind turbine located near a Nantucket weather buoy in OPENFast.

3 Curve Comparison

This analysis compared Det Norske Veritas and Germanischer Lloyd (DNV GL), American Bureau of Shipping (ABS), and International Institute of Welding (IIW) design curves [1][3][4]. These fatigue design documents were identified in the literature review for the report. DNV GL curves are most commonly used in the design of wind turbine support structures, the ABS curves were identified but not often discussed, and the IIW document was identified in the Bundesamt für Seeschifffahrt und Hydrographie (BSH) requirements, but they do not include corrosion curves [2][4]. The table shows that even subtle differences in curve parameters cause large changes in fatigue life.

Table 1 Summary of Fatigue Life for Each Curve

Org	Cat_Name	Total PM Sum	Fatigue Life (years)	Fatigue Life w/ Max DFF
DNVGL	D Air	0.145	137	46
ABS	D Air	0.138	144	29
IIW	90 (D) Air	0.145	138	46
DNVGL	C Air	0.015	1361	454
ABS	C Air	0.007	2829	566
IIW	112 (C) Air	0.025	786	262
DNVGL	D Cathodic Protection	0.076	263	88
ABS	D Cathodic Protection	0.071	282	56
DNVGL	C Cathodic Protection	0.015	1361	454
ABS	C Cathodic Protection	0.007	2829	566
DNVGL	D Free Corrosion	0.557	36	12
ABS	D Free Corrosion	0.809	25	5
DNVGL	C Free Corrosion	0.315	64	21
ABS	C Free Corrosion	0.137	146	29

Acknowledgements

The team would like to thank BOEM and the MassCEC for financial support for this project. We would also like to thank the many researchers and industry experts who gave their time to the advisory panel on this project. Their contributions were critical to the completion of the final report. We'd like to give special thanks to: Feargal Brennan (U Strathclyde & Chair of Advisory Panel); George Wang (Formerly of ABS); Lars Lichtenstein & David Quintana (DNV GL); Jens Rettke & Daniel Kaufer (Ramboll); James Strout & Per Sparrevik (NGI); James Battensby, Hyunjoo Lee, Alistair Lee, Jonathan Hughes, & Tony Fong (ORE-Catapult); Richard Pijpers (TNO); Peter Schaumann (U. Hannover); Lothar Breuss (Bachmann Electronic); Athanasios Kolios (U. Strathclyde); Brian Wyatt (Corrosion Control Ltd.); Geoffrey Swain (Florida Institute of Technology); and Amy Robertson (National Renewable Energy Lab; In addition to time on the advisory panel, many of these people volunteered time to help with the planning and running of the workshops. The research team is indebted to everyone for their exceptional contributions.

Bibliography

[1] ABS. 2018. Guide for Fatigue Assessment of Offshore Structures.
[2] BSH. 2015. “Standard Design Minimum Requirements Concerning the Constructive Design of Offshore Structures within the Exclusive Economic Zone (EEZ)”.
[3] DNV GL. 2016. Dnvgl-Rp-C203 Fatigue Design of Offshore Steel Structures.
[4] IIW. 2008. “IIW Document IIW-1823-07 Recommendations for Fatigue Design of Welded Joints and Components.”
[5] Tufts University. 2020. Design Life Issues Related to Corrosion and Fatigue of Offshore Wind Support Structures.

17th EAWE PhD Seminar on Wind Energy
3-5 November 2021
Porto, Portugal

On the influence of a pile stick-up towards the dynamic behaviour of a jacket support structure.

S Drexler[a] and M Muskulus[a]

[a]Department of Civil and Environmental Engineering, Norwegian University of Science and Technology (NTNU), Trondheim, Norway

2021-06-30

E-mail: `sebastian.drexler@ntnu.no`

Keywords: offshore wind turbines, support structures, jackets

Abstract

The design of offshore wind turbine (OWT) support structures for a given wind farm can be challenging. Depended on the characteristics of the offshore area, the individual site conditions, such as soil properties or water depth, can differ significantly among each turbine location. This range of different support requirements is typically handled through implementation of several distinct substructure designs, which are then used for multiple locations with similar site conditions. To make such an approach feasible, a height adjustment is required to adapt such a design for different water depths.

For jacket structures one possibility to elevate the complete support is the application of pile stick-ups. These can be understood as simple extensions of the foundation piles. The usage of stick-ups do not require a change of the jacket design, but they will have an impact on its dynamic behavior. And since it is intended to deploy such a design variant at a number of locations, each with slightly different water depths, it is important to understand how these stick-ups influence the jacket's dynamic behaviour and how their impact can be considered during its structural design.

Therefore, this study investigates the influence of the pile stick-up height on the dynamic behavior of a jacket structure for an OWT. This is done exemplarily for the UpWind reference jacket [1, 2] together with the NREL 5-MW Offshore Baseline Turbine [3] located at the UpWind design site. To quantify a possible dynamic impact, simplified fatigue analyses based on a frequency domain approach referring to Seidel [4] are implemented for different stick-up heights. The obtained results are then compared and discussed.

References

[1] Vorpahl F, Strobel M, Jonkman J, Larsen T and Passon P 2014 *Wind Energy* **17** 519–547

[2] Fischer T, de Vries and Schmidt B 2010 Upwind Design Basis - WP4: Offshore Foundations and Support Structures Tech. rep.

[3] Jonkman J, Butterfield S, Musial W and Scott G 2009 *National Renewable Energy Laboratory (NREL)*

[4] Seidel M 2014 *Stahlbau* **83** 535–541

WIND RESOURCE, TURBULENCE AND WAKE

17^{th} EAWE PhD Seminar on Wind Energy
3-5 November 2021
Porto, Portugal

Optimal autoregressive models for synthetic generation of turbulence. Implications of reproducing the spectrum or the autocovariance function

Mohanad Elagamy[a], Cristobal Gallego-Castillo[a], Alvaro Cuerva-Tejero[a], Oscar Lopez-Garcia[a], and Sergio Avila-Sanchez[a]

[a]Aircraft and Space Vehicles Department, Universidad Politécnica de Madrid, Plaza Cardenal Cisneros 3, 28040 , Madrid, Spain.

E-mail: `mohanad.elagamy@upm.es`

Keywords: turbulence , synthetic generation , autoregressive models , power spectral density , pole-placement

Abstract

In this paper, a methodology to obtain the coefficients of an autoregressive (AR) scheme with the aim of reproducing the PSD of the von Kármán turbulence model is developed. The proposed methodology consists in the optimal placement of the poles of the model. The optimisation is constrained to guarantee stationarity, and it is performed through the interior-point method. Results are compared with a recent proposal based on reproducing the autocovariance function by Gallego-Castillo. In this work, the longitudinal component of stationary, homogeneous and isotropic (SHI) turbulence at one single spatial point (univariate framework) is considered. The Taylors' Frozen Turbulence Hypothesis (TFTH) is assumed to relate a time series with a spatial series along the main wind direction. The discussion covers some implications derived from approaching the model determination in the frequency domain (through fitting a target PSD) or the time domain (through fitting a target autocovariance function). The findings are relevant for future steps, where more complex turbulence models (i.e. Mann uniform shear model), originally described in the frequency domain, will be considered in a multivariate framework for synthetic generation of turbulent Atmospheric Boundary Layer (ABL).

1 Introduction

Numerical simulations of turbulent wind velocity fields are required to evaluate dynamic loads on a wind turbine during different wind events. The simulated wind fields are relevant inputs for several problems in the wind energy sector, such as aeroelastic simulations of wind turbines under conditions determined by IEC standards [1]. Solving the Navier-Stokes equations of an atmospheric flow using Direct Numerical Simulation (DNS) is the most rigorous and precise way to simulate the wind field. However, this approach is unfeasible due to physical limitations, such as unknown initial and boundary conditions of the corresponding partial differential equations. Moreover, the computational cost is enormous. Similarly, Large Eddy Simulation (LES) is still computationally costly for the complete aeroelastic designing process of wind turbines. An alternative approach, which can be used for generating turbulent wind fields, is Numeric generation, in which pre-defined statistical features, such as autocovariances or power spectral densities, are required as inputs. There are various types of numerical generation approaches [2]. However, the most used methods in the numeric generation of wind fields are the spectral representation method (SRM) and the sequential method. The SRM was formally proposed by Shinozuka [3] and it typically relies on inverse Fast Fourier Transform (FFT) [4][5]. In SRM approach, a wide sense stationary univariate one dimensional random process can be represented by an infinite sum of cosine terms with deterministic coefficients, which are obtained in terms of a target power spectral density function of the random process, deterministic frequencies and random phases. The sequential method is achieved through generating synthetic fields, usually based on time series linear models, such as autoregressive (AR) model, moving average (MA) model and autoregressive moving average (ARMA) model and their multi-variate versions (VAR, VMA and VARMA). Under this framework, any value of the time series can be expressed as a combination of a deterministic component of past values, plus a random term. The paper utilizes the sequential method, specifically AR model, as it has some interesting advantages. Among others, the AR model has theoretical expressions for autocovariance and power spectral density (PSD) functions, which can be computed from the parameters of the model. This allows to directly compare between target autocovariance function or target PSD with the theoretical autocovariance function or theoretical PSD function of the models. This is useful to check the reliability of the AR model in reproducing the required statistical characteristics instead of relying on sampled functions estimated from generated time series. Furthermore, the sequential method is computationally efficient and the simulation can be restarted from a small amount of stored data as only the parameters of the model need to be stored. A methodology based on pole-placement is here introduced to optimally calibrate the parameters of an AR model for reproducing a predefined target spectrum. Moreover, the proposed method is compared to another approach which is based on reproducing a pre-defined autocovariance function [6]. In this article, the sections are arranged as follows. Section 2 describes the relationship between the AR poles and its PSD. In Section 3, details of a case study are explained. In Section 4, the results obtained using pole-placement approach are compared to the results obtained using autocovariance approach. In Section 5, concluding remarks concerning to the entire study are provided.

2 Methodology

The AR model [7] [8] is considered in order to generate a synthetic time series. In the AR model, a random variable at time t, u_t, is expressed as a weighted linear combination of past values, u_{t-l}, for $l > 0$ and p being the AR order, plus a random term, ε_t. The general formulation of an AR model of order p, AR(p), is:

$$u_t = \varphi_1 u_{t-1} + \varphi_2 u_{t-2} + \cdots + \varphi_p u_{t-p} + \sigma\varepsilon_t, \tag{1}$$

where φ_j are the regression coefficients, for $j = 1, \ldots, p$ and σ is the noise coefficient. By selecting the noise coefficient σ and the regression coefficients φ_j, a large number of time series realizations, ideally infinite, could reproduce, in the ensemble sense, statistical features defined beforehand.

The time series $\{u_t\}$ can be seen as the output to a linear filter with white noise ε_t as the input [9], as shown in Figure 1. The transfer function $H(z)$ is the ratio between the z-transform of the output sequence $Y(z)$ and the z-transform of the input sequence $X(z)$. The transfer function $H(z)$ is obtained by applying the z-transform to Equation (1) to get the following:

$$A(z)Y(z) = B(z)X(z),$$

where $A(z) = 1 - \varphi_1 z^{-1} - \cdots - \varphi_p z^{-p}$ and $B(z) = 1$. Thus, for an AR process, the transfer function $H(z)$ is defined as follows:

$$H(z) = \frac{Y(z)}{X(z)} = \frac{B(z)}{A(z)} = \frac{1}{1 - \varphi_1 z^{-1} - \cdots - \varphi_p z^{-p}}. \tag{2}$$

The transfer function $H(z)$ can be presented on a complex plane, as shown in Figure 2, where the vertical axis is the imaginary axis and the horizontal axis is the real axis. This representation is useful, because the location of poles and zeros to a unit circle, $z = e^{i\theta}$, in z-domain, define some features in the PSD, such as the local maxima. The poles are the roots of the denominator of the transfer function, $A(z)$ and the zeros are the roots of the nominator of the transfer function, $B(z)$. However, the AR model is an all-poles model and it has no zeros. The characteristic equation, $A(z) = 0$, is defined as:

$$1 - \varphi_1 z^{-1} - \cdots - \varphi_p z^{-p} = 0, \tag{3}$$

which can be factorized as follows:

$$(1 - G_1 z^{-1})(1 - G_2 z^{-1}) \ldots (1 - G_p z^{-1}) = 0, \tag{4}$$

where $G_1, \dots, G_p$ are the poles of the AR model and the roots of the characteristic equation are $G_1^{-1}, \dots, G_p^{-1}$. Equations 3 and 4 represent the relationship between the regression coefficients of the AR model, φ_j, and the poles of the AR model, G_j. Thus, the regression coefficients can be obtained by placing the poles. For stationary AR model, the modulus of the poles of the AR model has to be less than 1 ($|G_j| < 1, j = 1, \dots, p$) or the roots of the characteristic equation have to be greater than one ($|G_j^{-1}| > 1, j = 1, \dots, p$). The poles of an AR process can be real poles P_r or/and complex conjugate poles P_c. The real poles are located on the real axis in the interval [-1,1] and the complex poles P_c are defined by a radial location r within the interval $[0, 1]$ and a phase angle θ within the interval $[0, \pm\pi]$, where $P_c = re^{i\theta}$. Moreover, the locations of the poles of the AR model to the unit circle affect the shape of the peaks of the AR spectrum [10].

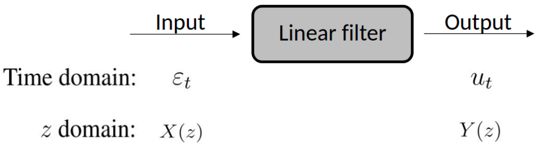

Figure 1: Representation of the time series u_t as the output to a linear filter and the input is the white noise ε_t

The one-sided AR spectrum $S^{AR}(k)$ in terms of wavenumber k [11] is written as:

$$S^{AR}(k) = \frac{1}{k_{max}} \frac{\sigma^2}{\left|1 - \sum_{j=1}^{p} \varphi_j \exp(-ij\pi\dfrac{k}{k_{max}})\right|^2}, \qquad 0 \le k \le k_{max} \tag{5}$$

where $i = \sqrt{-1}$, the superscript indicates AR model and k_{max} is the maximum wavenumber, $k_{max} = \pi/(U\Delta t) = \pi/\Delta x$, U is the mean velocity, Δt is the sampling time and Δx is the spatial step. Note that Taylors' Frozen Turbulence Hypothesis (TFTH) is assumed to relate the wavenumber to the frequency as $k = 2\pi f/U$. The definition of non-dimensional one-sided AR spectrum $\mathring{S}^{AR}(\mathring{k}) = S^{AR}(k)/(L\sigma_u^2)$, where L is an integral length scale, in terms of non-dimensional wavenumber $\mathring{k} = kL$ is:

$$\mathring{S}^{AR}(\mathring{k}) = \frac{1}{\mathring{k}_{max}} \frac{\sigma^2/\sigma_u^2}{\left|1 - \sum_{j=1}^{p} \varphi_j \exp(-ij\pi\dfrac{\mathring{k}}{\mathring{k}_{max}})\right|^2}, \qquad 0 \le \mathring{k} \le \mathring{k}_{max} \tag{6}$$

where $\mathring{k}_{max}$ is the non-dimensional maximum wavenumber (the employed value for $\mathring{k}_{max}$ is justified in Section 3) and σ_u^2 is a characteristic variance, which is selected to be equal to the autocovariance of the AR model for time lag $l = 0$, γ_0^{AR}, which is the variance of the process. Subsequently, $\int_0^\infty \mathring{S}^{AR}(\mathring{k})d\mathring{k} = 1$ and since γ_0^{AR} is proportional to σ^2[11], therefore, in Equation (6), the parameters which are required to be determined are only the regression coefficients φ_j.

The effect of changing the phase angle θ of the complex poles on the theoretical spectrum of an AR(2) model is shown in Figure 2. Three cases, with different complex conjugated poles P_{c_1}, P_{c_2} and P_{c_3} for each case, were considered. The complex conjugate poles P_{c_1}, P_{c_2} and P_{c_3} have values $0.8e^{\pm i\pi/9}, 0.8e^{\pm i2\pi/9}$ and $0.8e^{\pm i\pi/3}$ respectively. The regression coefficients φ_j obtained for each case, are evaluated using equations (3) and (4). Finally, the regression coefficients φ_j obtained from each case are utilized to evaluate the AR spectra $\mathring{S}_1^{P-AR}, \mathring{S}_2^{P-AR}$ and $\mathring{S}_3^{P-AR}$ using Equation (6), where the superscript $P-AR$ indicates that the regression coefficients φ_j are obtained by applying poles-placement approach. As shown in Figure 2, by increasing the phase angle, the peak of the AR spectrum $\mathring{S}^{P-AR}$ is shifted from a low frequency to a higher frequency. Moreover, the effect of the changing radial location on the theoretical spectrum of AR(2) model was considered. AR spectra, $\mathring{S}_4^{P-AR}, \mathring{S}_5^{P-AR}$ and $\mathring{S}_6^{P-AR}$ obtained from three different complex poles P_{c_4}, P_{c_5} and P_{c_6} with values $0.7e^{\pm i\pi/4}, 0.8e^{\pm i\pi/4}$and $0.9e^{\pm i\pi/4}$ respectively. As shown in Figure 3, changing the radial location of the poles, changes the amplitude of the peak obtained in the AR spectrum. As the pole gets closer to the unit circle, it will lead to a rise and sharpening of the peak in the AR spectrum. Ultimately, increasing the number of poles N leads to increasing the number of peaks of the AR spectrum $\mathring{S}_7^{P-AR}$. For a AR(3) model, with one real pole $P_{r_7} = -0.8$ and two complex conjugate poles $P_{c_7} = 0.8e^{\pm i\pi/3}$, two peaks were obtained, as depicted in Figure 4. The first peak is at $\mathring{k} \approx 8$ due to the complex conjugate poles. The second peak is at $\mathring{k}_{max}$ due to the negative real pole, as a positive real pole leads to a peak in the AR spectrum at $\mathring{k} = 0$ and a negative real pole leads to a peak in the AR spectrum at $\mathring{k}_{max}$.

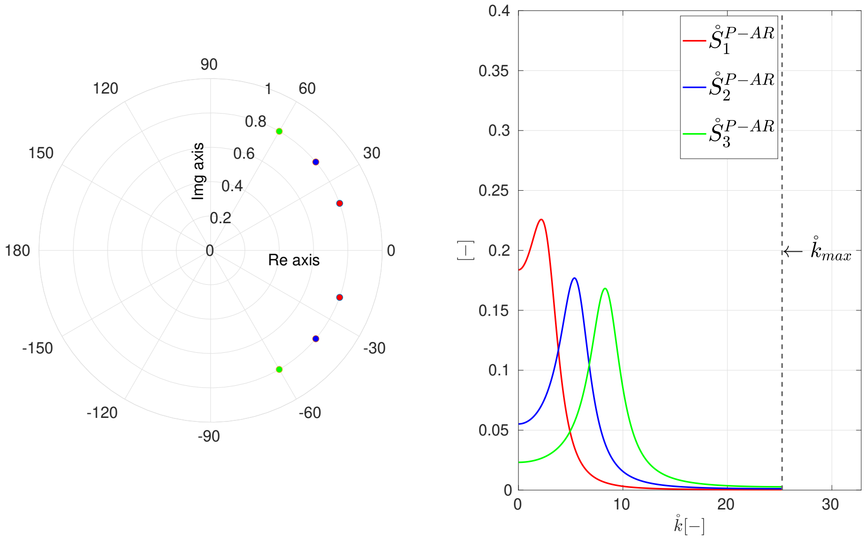

Figure 2: Non-dimensional one-sided AR spectrum of the AR(2) models, $\mathring{S}_1^{P-AR}(\mathring{k}), \mathring{S}_2^{P-AR}(\mathring{k})$ and $\mathring{S}_3^{P-AR}(\mathring{k})$, obtained from three different poles, P_{c_1}, P_{c_2} and P_{c_3} with a fixed radial location r.

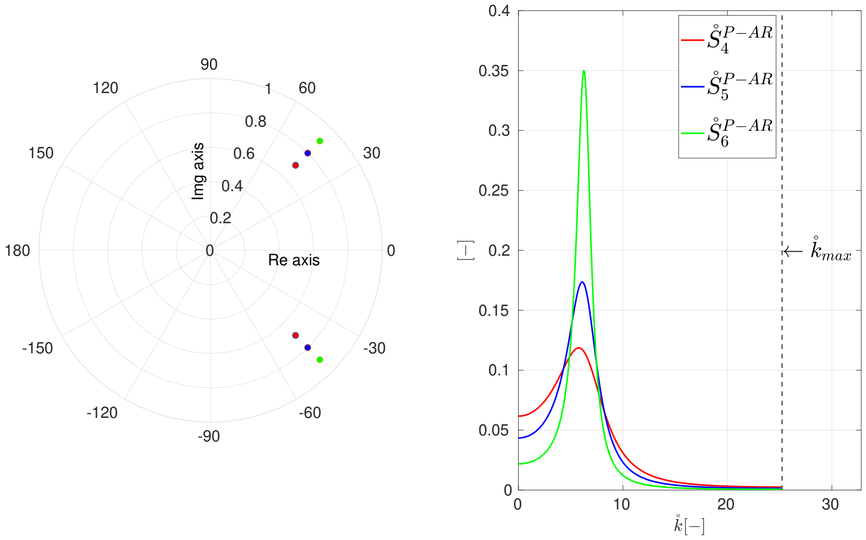

Figure 3: Non-dimensional one-sided AR spectrum of the AR(2) models, $\mathring{S}_4^{P-AR}(\mathring{k}), \mathring{S}_5^{P-AR}(\mathring{k})$ and $\mathring{S}_6^{P-AR}(\mathring{k})$, obtained from three different poles, P_{c_4}, P_{c_5} and P_{c_6} with a fixed phase angle θ.

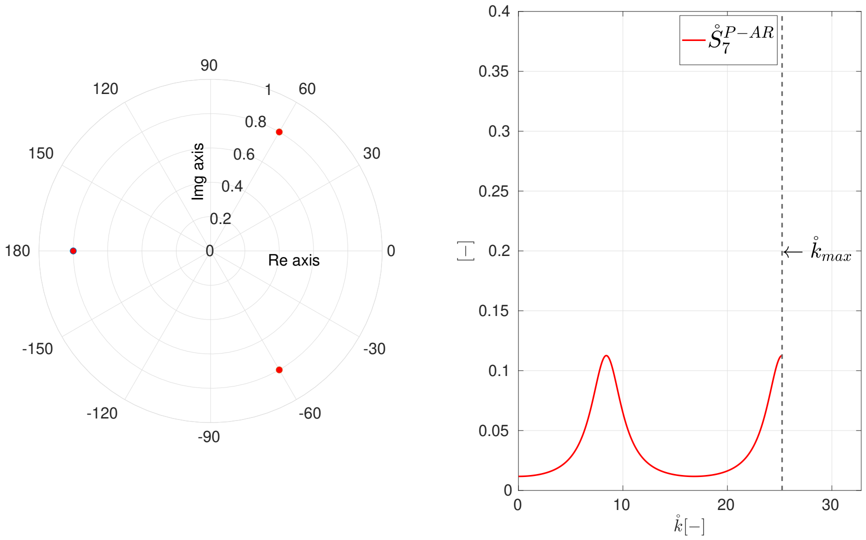

Figure 4: Non-dimensional one-sided AR spectrum of the AR(3) model $\mathring{S}_7^{P-AR}(\mathring{k})$ with a real pole and complex conjugate poles.

The proposed approach is to use pole-placement approach to obtain the AR spectrum from a predefined target spectrum. The poles of the AR model are obtained through optimization process to get the optimal poles for AR(p) model, where optimal poles means that the obtained AR spectrum from the poles provides minimum error. The error criterion employed is based on Minimum Square Error (MSE), as in [6], and it is defined as follows:

$$MSE = \frac{1}{M}\sum_{n=0}^{M} e_n^2, \tag{7}$$

where $e_n = \mathring{k}_n \mathring{S}^T(\mathring{k}_n) - \mathring{k}_n \mathring{S}^{AR}(\mathring{k}_n)$. The MSE between target and AR spectrum was evaluated at M points in the interval $\mathring{k} = [0, \mathring{k}_{max}]$. The inequality constraints $-1 \leq P_r \leq 1$, $0 \leq \theta \leq \pi$ and $0 \leq r \leq 1$, were defined in the optimisation problem, where these constraints are required to ensure the stationarity of the AR model. The optimisation is performed by using the interior-point method.

3 Case Study

The proposed method is applied to a stationary homogeneous isotropic turbulence model. The von Kármán (vK) spectrum model [12] is employed as a target spectrum. The non-dimensional one-sided vK spectrum $\mathring{S}^{vK}(\mathring{k})$ in terms of non-dimensional wavenumber $\mathring{k}$ [13] is given by:

$$\mathring{S}^{vK}(\mathring{k}) = C_1 \frac{1}{[(\mathring{k})^2 + 1]^{m-2}}, \tag{8}$$

where $C_1 = 3C_{vK}/2(m-2)(m-1)$ and $C_{vK} = \Gamma(m)/\Gamma(5/2)\Gamma(m-5/2)$. $\Gamma(\cdot)$ is the Gamma function and m is a parameter, which takes the value 17/6. For the sake of comparison to Gallego-Castillo et al. [6], $\mathring{k}_{max}$ is selected to be $\pi/0.1245$. The MSE is evaluated at $M = 1000$ points over the non-dimensional wavenumber interval $[0, \mathring{k}_{max}]$. Based on the discussion presented in [14], the area of the AR spectrum is imposed to be smaller than one, in particular, equal to the area of the target spectrum corresponding to the interval $[0, k_{max}]$ to prevent the appearance of spurious peaks at high wavenumbers. In this case, this means imposing the AR variance of 0.9171. Moreover, different combinations of real and complex conjugate poles are tested to obtain the combination of poles, which give the least MSE, for each N case.

4 Results

The theoretical AR spectrum $\mathring{S}^{AR}(\mathring{k})$ is obtained for cases $N = 1, 2, \ldots, 10$ using the pole-placement approach. In Figure 5, the MSE is plotted for different values of N, where the theoretical AR spectrum $\mathring{S}^{AR}(\mathring{k})$ fits the target spectrum $\mathring{S}^{T}(\mathring{k})$ better with increasing N value. The combination of the real and complex conjugates poles, which gave the least MSE for each N case, is shown in Figure 6. The proposed approach is simpler and faster than the multi-point approach [14]. It was observed that for even N case, the number of real poles N_{real} is 2 and the the real poles take positive and negative values, whereas for odd N case, the number of real poles N_{real} is 1 and the real pole takes a positive value, and the number of complex poles $N_{complex} = N - N_{real}$. The AR spectrum obtained by using poles-placement approach $\mathring{S}^{P-AR}(\mathring{k})$, for case $N = 6$, is shown in Figures 7 and 9 together with AR spectrum obtained by utilizing autocovariance approach $\mathring{S}^{GA-AR}(\mathring{k})$, from [6], and the target spectrum $\mathring{S}^{T}(\mathring{k})$. The AR spectrum $\mathring{S}^{P-AR}(\mathring{k})$ shows a good fit to the target spectrum $\mathring{S}^{T}(\mathring{k})$ within the wavenumber interval $\mathring{k} = [\mathring{0}, \mathring{k}_{max}]$, while the AR spectrum $\mathring{S}^{GA-AR}(\mathring{k})$ shows the aliasing effect due to discretization of the target autocovariance function (see [6] for details). The non-dimensional autocovariance function $\mathring{R}_u^{P-AR}$, where $\mathring{R}_u = R_u \sigma_u^{-2}$, does not match the target autocovariance function, $\mathring{R}_u^{T}$, at the first time lag due the aforementioned constraint on the AR spectrum area [14], as shown in Figure 8. Conversely, the non-dimensional autocovariance $\mathring{R}_u^{GA-AR}$ shows a perfect match to the non-dimensional target autocovariance $\mathring{R}_u^{T}$. In conclusion, this comparison shows that the choice of fitting either the autocovariance or the spectrum has diverse implications that need to be considered when selecting the approach to be used. These implications are summarized in Table 1.

Approach	Advantages	Disadvantages
fitting Autocovariance function	• The fitting of the target autocovariance function can be asymptotically improved (with increasing the number of model parameters). • In particular, the variance of the process is properly reproduced.	• Discretization of target autocovariance leads to aliasing effect in target spectrum, which is reproduced in the AR spectrum. • Pre-processing to obtain the target autocovariance function will be required when turbulence models described in spectral domain (e.g. Mann uniform shear model).
fitting PSD	• The fitting of the target PSD function can be asymptotically improved (with increasing the number of model parameters). • In particular, no aliasing effect decreases the quality of the fitting.	• Only a fraction of the target variance (corresponding to the range $[0, \mathring{k}_{max}]$) is properly reproduced.

Table 1: A comparison between the implications of fitting autocovariance function [6] and fitting PSD.

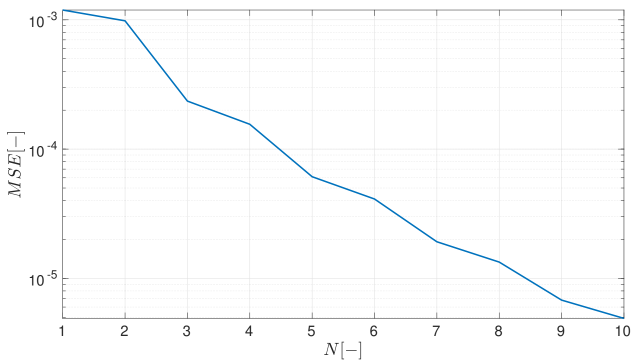

Figure 5: MSE obtained for different N values.

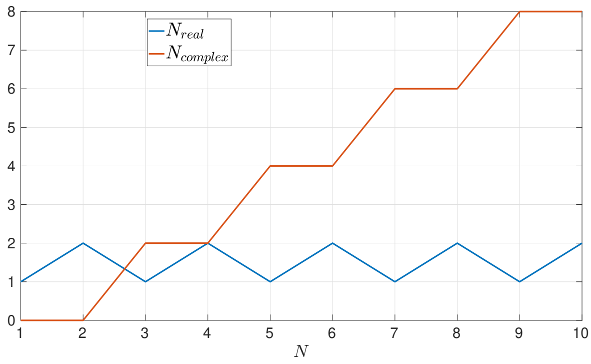

Figure 6: Optimal poles combination for different N cases.

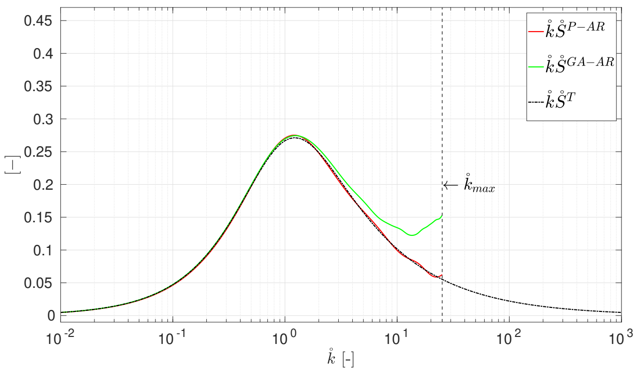

Figure 7: Normalized one-sided target spectrum, $\mathring{k}\mathring{S}^{T}(\mathring{k})$, together with the corresponding theoretical spectrum of the AR models obtained by using the poles-placement approach, for reduced variance (0.9171) $\mathring{k}\mathring{S}^{P-AR}(\mathring{k})$ and by using the autocovariance approach $\mathring{k}\mathring{S}^{GA-AR}(\mathring{k})$ [6]. Case $N = 6$.

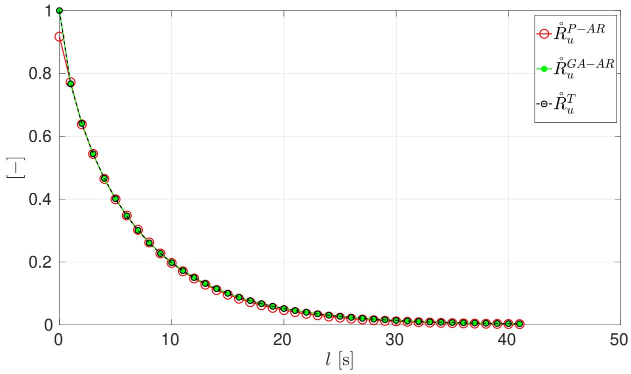

Figure 8: Non-dimensional target autocovariance, $\mathring{R}_u^{T}$, together with the corresponding theoretical autocovariance of the AR models obtained by using the poles-placement approach, for reduced variance (0.9171) $\mathring{R}_u^{P-AR}$ and by using the autocovariance approach $\mathring{R}_u^{GA-AR}$ [6]. Case $N = 6$.

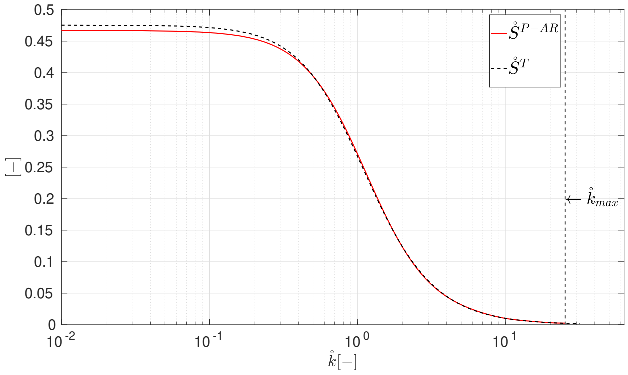

Figure 9: Non-dimensional one-sided target spectrum, $\mathring{S}^{T}(\mathring{k})$, together with the corresponding theoretical spectrum of the AR model obtained by using the pole-placement approach, for reduced variance (0.9171), $\mathring{S}^{P-AR}(\mathring{k})$. Case $N = 6$.

5 Conclusions

This study presents a comparison between two approaches related to the determination of the coefficients of AR models for synthetic generation of turbulence. One approach consists on fitting a target PSD, for which a pole-placement based method was presented. The other approach consists on fitting a target autocovariance function, for which a methodology presented in a previous research was employed. As case study, the von Kármán turbulence model was used to obtain both the target autocovariance function and the target PSD for each of the two approaches. While the autocovariance function and the PSD function represent the same underlying information in either time or frequency domains (they are Fourier pairs), it was found that the choice of the target function (PSD or autocovariance) to be reproduced by an AR model has implications in the reproduced statistical features. In particular, on the one hand, fitting a target autocovariance function with an AR model requires previous discretization of such target function, which could introduce aliasing in the spectrum reproduced by the obtained AR model if the discretization is not fine enough, as shown in a previous research [6]. On the other hand, fitting a target PSD function with an AR model can only be done in a range of frequencies, in this work defined by the wavenumber interval $\mathring{k} \in [0, \mathring{k}_{max}]$. This means that the target variance corresponding to frequencies $\mathring{k} > \mathring{k}_{max}$

cannot be accounted for by the AR model while optimally fitting the PSD in the range $\mathring{k} \in [0, \mathring{k}_{max}]$. Consequently, the AR model only reproduces a fraction of the target variance. The described limitations of both approaches decrease as the sampling time decreases (i.e. the maximum frequency increases), making both approaches virtually similar in terms of reproduced statistical features. However, in practice this parameter is usually constrained due to measurement equipment resolution or computational simulation cost. Thus, the implications described in this work provide a basis for discussing which approach would be more convenient to employ, depending on the application of the generated wind field.

Acknowledgements

This research has been undertaken as a part of the zEPHYR project. This project has received funding from the European Union's Horizon 2020 research and innovation programme under Grant Agreement No EC grant 860101.

References

[1] International Electrotechnical Commision IEC 61400-1 *Wind energy generation systems*

[2] Kleinhans D, Friedrich R, Schaffarczyk A and Peinke J 2009 *Progress in Turbulence III* (Springer) pp 111–114

[3] Shinozuka M 1971 *The Journal of the Acoustical Society of America* **49** 357–368

[4] Shinozuka M and Deodatis G 1991 *Applied Mechanics Reviews* **44** 191–204

[5] Shinozuka M and Deodatis G 1996 *Applied Mechanics Reviews* **49** 29–53

[6] Gallego-Castillo C, Cuerva A, Elagamy M, Lopez-Garcia O and Avila S *(under review)* `https://arxiv.org/abs/2105.11409`

[7] Spanos P D and Mignolet M P 1992 *Journal of Applied Mechanics* **59** S270–S277

[8] Mignolet M P and Spanos P D 1992 *Journal of Applied Mechanics* **59** S260–S269

[9] Takalo R, Hytti H and Ihalainen H 2005 *Journal of clinical monitoring and computing* **19** 401–410

[10] Chao B F 1984 *On the maximum-entropy/autoregressive modeling of time series* (National Aeronautics and Space Administration, Goddard Space Flight Center)

[11] Box G E, Jenkins G M, Reinsel G C and Ljung G M 2015 *Time series analysis: forecasting and control* (John Wiley & Sons)

[12] Von Karman T 1948 *Proceedings of the National Academy of Sciences of the United States of America* **34** 530

[13] Wyngaard J C 2010 *Turbulence in the Atmosphere* (Cambridge University Press)

[14] Elagamy M, Gallego-Castillo C, Cuerva-Tejero A, Lopez-Garcia O and Avila-Sanchez S 2021 *17th International Conference of Computational Methods in Sciences and Engineering*

17th EAWE PhD Seminar on Wind Energy
3-5 November 2021
Porto, Portugal

Influence of local terrain and vertical height in thermal stability calculations over complex terrain

Kartik Venkatraman[a], Sophia Buckingham[a], and Boris Conan[b]

[a]von Karman Insitute for Fluid Dynamics
[b]Ecole Centrale de Nantes

E-mail: `kartik.venkatraman@vki.ac.be`

Keywords: Atmospheric stability, Monin-Obhukhov length, Richardson number

Abstract

Accurately quantifying thermal stability is important for several applications such as wind resource assessment and wind turbine noise propagation modelling. Sonic anemometer data over a one month period from 1sh May 2017 to 31st May 2017 at the double ridge complex terrain site at Perdigao, Portugal [1]. is analyzed to deduce the influence of local terrain on thermal stability metrics. Thermal stability can be classified using several metrics such as the gradient Richardson number, bulk Richardson number and Monin-Obhukov length (MOL). These metrics are computed at different met masts at the summit of the North-East ridge, inside the valley, and on top of the South-West ridge as shown in Fig. 3 over 10 min averaged periods for the two predominant wind directions. Most of the existing classification criteria for thermal stability ranging from very unstable to very stable conditions have been derived from field measurements over flat terrain. However, the classification criteria for these metrics do seem to hold when applied for a flow over complex terrain. It is found to be dependent on the location of the mast and shows variability over height. The analysis indicates that an adpative classification of thermal stability needs to be defined based on the met-mast location and wind direction sector.

1 Introduction

The increasing scarcity of land resources for wind turbine siting in flat terrain pushes wind-farm developers to look for alternative sites along complex terrains. Improving existing wind resource assessment tools requires an accurate classification of thermal stability. This paper aims to study the variation of different thermal stability metrics over a complex terrain and provide insights into development of classification metrics.

The paper is organized as follows: First, a brief overview of the existing thermal stability classification metrics applied for flat terrain conditions is described. Second, a short overview of the Perdigao field measurement campaign is described. Third, the methodology used to prepare the dataset is outlined. Fourth, an analysis of the different thermal stability metrics is provided. Finally, the conclusions are discussed.

2 Literature Review

2.1 Theory on Atmospheric stability

Turbulence in the atmosphere can be a result of either wind shear over height (mechanical turbulence) or thermal turbulence due to a surface heating or cooling as shown in Fig 1.

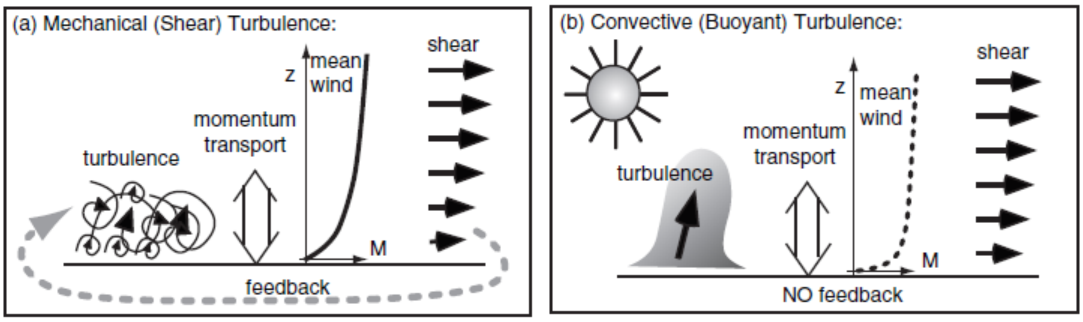

Figure 1: a) Mechanical Turbulence b) Buoyant Turbulence [2].

When thermal fluxes are zero, the thermal stratification is said to be neutral and follows a logarithmic profile. The daily heating and cooling results in a daily cycle of thermal stability. Daytime heating is associated with rising hot air and an unstable atmospheric conditions. The ground is warmer than the adjacent air due to surface heating, resulting in a upward heat flux (assigned as a positive value). The profile is well mixed with lower wind shear. On the other hand, during night, radiative cooling results in the ground being cooler than the adjacent air, resulting in a sinking of air towards the ground (assigned a negative value), resulting in a profile with stronger wind shear. The bottom 5% of the atmospheric boundary layer is defined as the surface layer, where the wind profile varies logarithmically for a neutral atmospheric boundary layer. Typical wind profiles in the surface layer are shown in Fig 2.

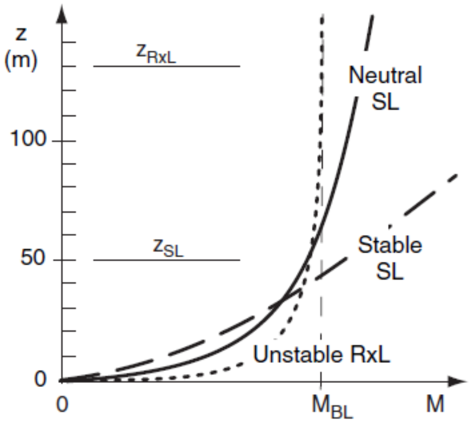

Figure 2: Typical wind speed profiles seen in the surface layer for different static stabilities [2].

2.2 Thermal stability metrics

A review of the definition of different thermal stability parameters is briefly provided. Turbulence intensity is formulated as the ratio of standard deviation of fluctuating wind velocity to the mean wind speed,

$$TI = \frac{\sigma}{\bar{U}}$$

Wind shear exponent is a parameter that relates wind speeds at two different heights and is formulated as follows.

$$\alpha = \frac{\ln\left(\frac{v_u}{v_l}\right)}{\ln\left(\frac{h_u}{h_l}\right)}$$

Temperature gradient is taken as the temperature difference over two given heights divided by their height difference.

$$\frac{dT}{dZ} = \frac{\Delta T}{\Delta Z} \times 100$$

The Monin-Obhukov length (MOL) is defined as the height at which the turbulence generated by buoyancy effects exceeds the turbulence generated by wind shear. MOL was proposed as a parameter for thermal stability classfication. The dimensionless stability parameter is defined as $\zeta = z/L$ which is the height divided by MOL.

$$L_{MO} = \frac{-u_*^3}{\kappa\beta\overline{w'\theta'}}$$

where u_* is the friction velocity, $\overline{w'\theta'}$ is the vertical heat flux, β is the buoyancy parameter. The friction velocity is computed from the fluxes as,

$$u_*^2 = \sqrt{\overline{u'w'}^2 + \overline{v'w'^2}}$$

The thermal stability classification into several thermal stability classes for a flat terrain based on the z/L based on observation data is shown in the table below [3].

Stability	Range
Very unstable (vu)	$-2 < \zeta \leq -0.6$
Unstable (vu)	$-0.6 < \zeta \leq -0.2$
Slightly unstable (su)	$-0.2 < \zeta \leq -0.02$
neutral (n)	$-0.02 < \zeta \leq 0.02$
Slightly stable (ss)	$0.02 < \zeta \leq 0.2$
Stable (s)	$0.2 < \zeta \leq 0.6$
Very stable (vs)	$0.6 < \zeta \leq 2$

The Richardson number is defined as a dimensionless parameter that is the ratio of the buoyancy term to the wind shear term. It is derived in several forms as gradient Richardson number (R_g), flux Richardson number (R_f), bulk Richardson number (R_b). The gradient Richardson number is formulated as the ratio of the gradient of the potential temperature levels to the velocity magnitude gradient. Bulk Richardson number is an approximation of the gradient Richardson number, where a velocity at a single height (either the highest point or at the mid-height between the surface and highest point) is utilized.

$$R_f = \frac{(g/\bar{\theta})\overline{w'\theta'}}{u'w'(\partial\bar{u}/\partial z)} \qquad R_g = \frac{(g/\bar{\theta})(\partial\bar{\theta}/\partial z)}{(\partial\bar{u}/\partial z)^2} \qquad R_b = \frac{(g/\bar{\theta})\left(\bar{\theta}_z - \bar{\theta}_0\right)/2}{(\bar{u}_z/z)^2}$$

where $\bar{\theta}_0$ is the potential temperature at the surface. Potential temperature is defined as the temperature if the air parcel is transported to the ground dry adiabatically. It accounts for the pressure change with height.

2.3 Complex Terrain

The flow in complex terrain is governed by local terrain features such as hills, ridges, and the surface roughness based on the land class. The influence and heterogeneity of the canopy, the re-circulation zone inside the valley play a key role in the variability of thermal stability metrics locally. During the night, stable atmospheric conditions resulting in the formation of a low-level jet as seen from the lidar scans shown by Fernando *et al.* [4] results in much higher spatial variability of stability parameters.

3 Perdigao Field measurement campaign

The Perdigao field campaign was a field test campaign at the double ridge site located at Perdigão (Portugal). The test site was an ideal candidate to study flow separation effects on mean wind speeds and turbulence at the upstream and downstream vegetated hills. An intensive measurement period was undertaken during the months of May & June 2017 with significant availability of data. The instrumentation comprised of several met Mast towers of 60m, 100m height and remote sensing instruments such as LiDARs. The parallel ridges and the different met masts are shown in Fig 3.

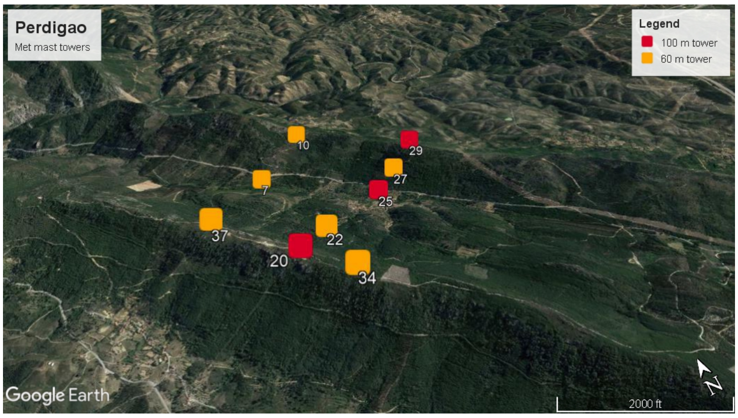

Figure 3: Three 100m towers - Tower 20 on the SW ridge, Tower 25 inside the valley, 29 on the NE ridge shown in red, and the 60m towers shown in yellow.

4 Methodology

The raw tilt corrected 20 Hz sonic anemometer data, temperature & relative humidity datasets are processed from the Perdigao website to obtain 10min averaged datasets with all the wind statistics such as the mean, standard deviation and co-variances. The required parameters for thermal stability defined earlier such as friction velocity, Monin-Obukhov length are also computed. The histogram of wind direction for the three 100m towers i.e Tower 20 (tse04), Tower 25 (tse09), Tower 29 (tse13) is utilized to identify the predominant wind directions. A 30 degree sector is defined around the centre of the main wind directions for further analysis. The sector binned data is further binned for thermal stability and different metrics are plotted as a function of the z/L on a logarithmic scale. To compute the shear exponent, a difference in height of 100m and 10m is used, while for the temperature gradient calculations a difference in height of 100m and 2m close to the ground is used. The shear exponent and temperature gradient is further utilized to compute the bulk Richardson number. All analysis and data processing is executed using Python on Jupyter notebooks.

5 Data Analysis

The first analysis is made on the wind directions at the different towers. The two main wind directions at the Towers 20 and 29 as seen in the wind roses shown in Fig 4 are South-West and North-East sectors. The predominant wind directions are perpendicular to the ridges. On the other hand, inside the valley at Tower 25, the predominant wind direction is from the South sector, indicating the flow is channeled along the valley. Also a greater spread over different sectors is seen, as the valley is a re-circulation zone with significant flow mixing.

The second analysis is performed by a study of the correlation plots to study the effect of flow turning over the height of the met-mast. A correlation is performed between the 100m and 10m wind directions for the three different met masts is shown in Fig 5. It is seen there is greater flow turning on at Tower 29 on the North-East ridge compared to Tower 25 on the South-West ridge. Inside the valley the flow is re-oriented significantly over the measured met-mast heights. The flow turning highlights the importance of local surface heterogeneity over the complex terrain at different locations. This leads to an impact in calculation of the different thermal stability metrics that require computing a gradient over two different heights.

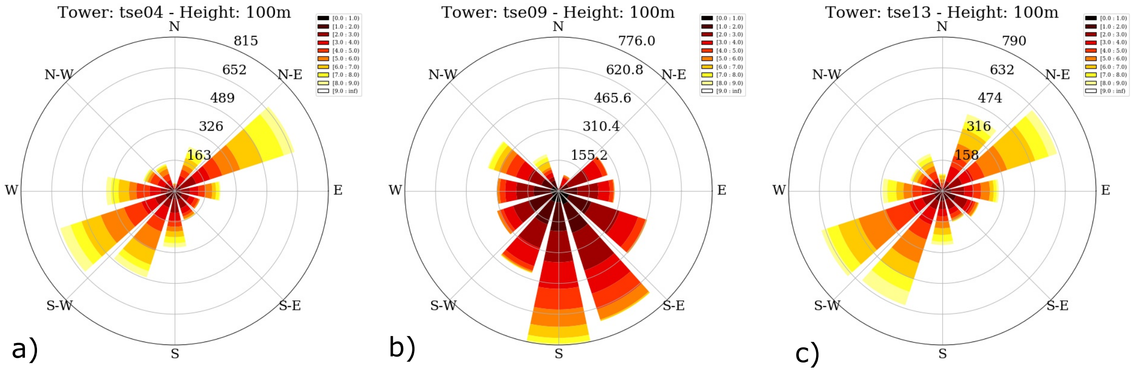

Figure 4: a) Tower 20 (tse04) b) Tower 25 (tse09) c) Tower 29 (tse13)

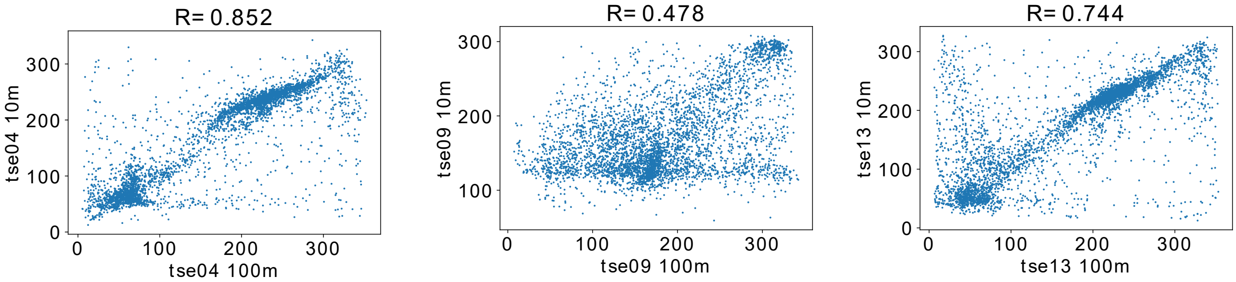

Figure 5: Correlation plots between 10m and 100m at different towers

5.0.1 Stability metric plots

The data from Towers 20 and 25 is sorted around a 30 degree sector centered around the North-East and South-West sectors, while for Tower 25, the analysis is performed around the South sector. All the plots shown is on a logarithmic scale, with the parameter z/L on the x-axis. For the preliminary analysis, the following binning criteria is chosen for classification of thermal stability with sufficiently distributed samples across all bins. This criterion needs to be studied.

Stability	Range
Very unstable (vu)	$-100 < \zeta \leq -1$
Unstable (vu)	$-1 < \zeta \leq -0.01$
neutral (n)	$-0.01 < \zeta \leq 0.01$
Stable (s)	$1 < \zeta \leq 0.1$
Very stable (vs)	$1 < \zeta \leq 100$

5.1 Towers 20 and 29

The following plots are shown for different stability metrics for each of the towers along North-East (NE) & South-West(SW) sectors.

5.1.1 Wind Shear exponent

Figs 6(a), 6(b) show the wind shear exponent for the NE sector, the same parameter is shown in Figs 7(a), 7(b) for the SW sector. The general trend for increasing wind shear with increase z/L parameter is more clearly visible for the South-West sector. For the SW sector, the very stable cases on average, have a wind shear of 0.2 or higher, while for the North-East sector the wind shear is higher for all values of z/L. Majority of the stable conditions are observed from this sector.

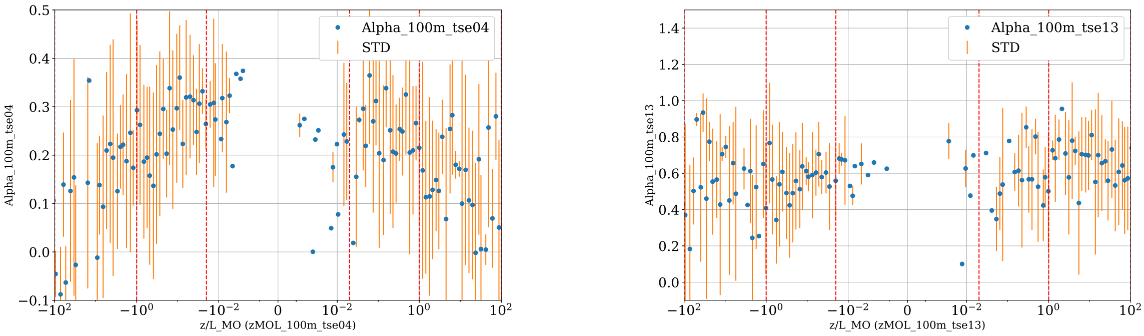

(a) Tower 20

(b) Tower 29

Figure 6: Sector NE: Shear Exponent (α)

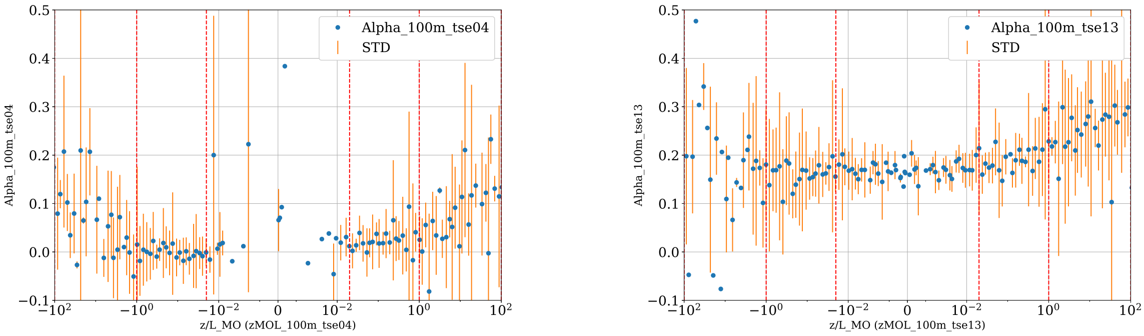

(a) Tower 20

(b) Tower 29

Figure 7: Sector SW: Shear Exponent (α)

5.1.2 Temperature Gradient

The temperate gradient plots for the NE sector is shown in Figs 8(a), 8(b) while for the SW sector is seen in Fig 9(a), 9(b). As seen for the shear exponent, the expected trends are more succinct for the SW sector, with positive temperature gradients skewed towards positive values of z/L, negative temperature gradients skewed towards negative values of z/L and very small values for neutral conditions. On the contrary, for the NE sector, a greater spread in the dataset is seen although the general trend is observed.

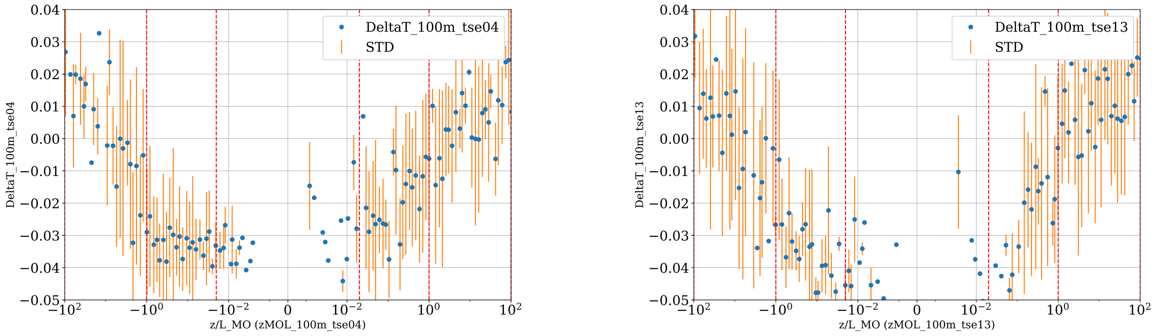

(a) Tower 20

(b) Tower 29

Figure 8: Sector NE: Temperature Gradient (ΔT)

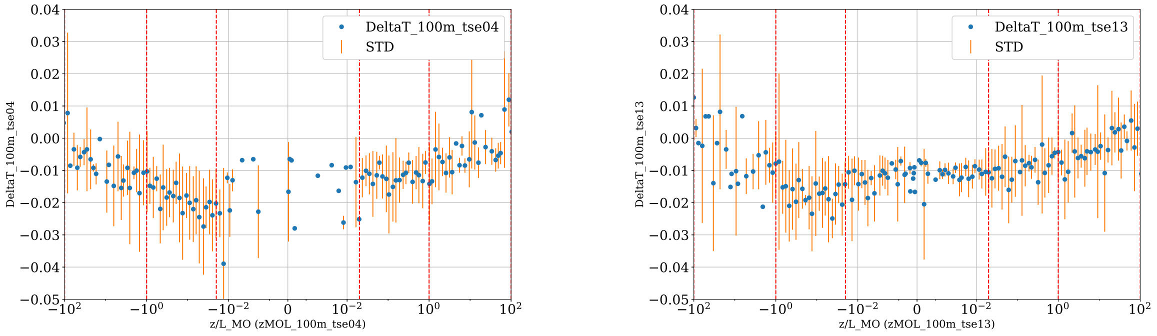

(a) Tower 20

(b) Tower 29

Figure 9: Sector SW: Temperature Gradient (ΔT)

5.1.3 Turbulence Intensity

The turbulence intensity plots are seen for the NE sector in Figs 10(a), 10(b) and for the SW sectors in Figs 11(a), 11(b) respectively. As expected higher values of turbulence intensity are seen for the unstable class corresponding to negative z/L. The turbulence intensities go up to as high as 30%. Interestingly, the wind from the NE sector is more turbulent on average.

5.1.4 Bulk Richardson number

The computed values of the bulk Richardson number is shown for SW sector in Figs 12(a)12(b), and for NE sectors in Figs 13(a)13(b) . For the SW sector, as expected for neutral conditions the data points are clustered around zero, and are positive for stable conditions and negative for unstable conditions. The same trend is seen for the NE sector albeit with lesser number of data points clustered for the neutral conditions and with a higher standard deviation of data points overall.

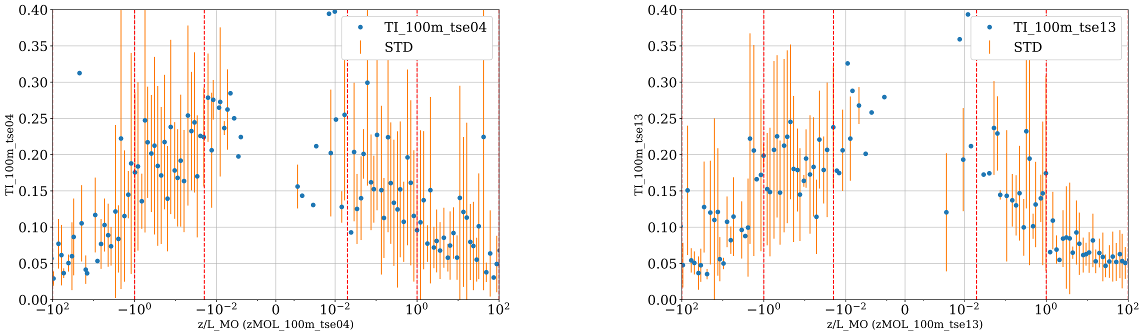

(a) Tower 20 (b) Tower 29

Figure 10: Sector NE: Turbulence Intensity (TI)

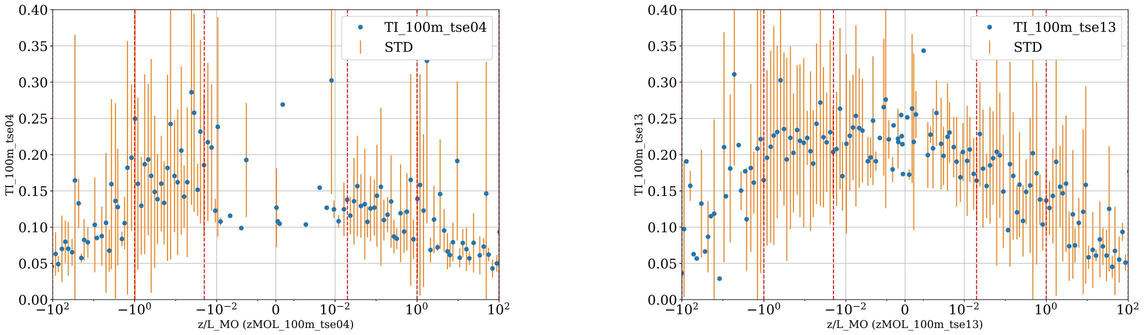

(a) Tower 20 (b) Tower 29

Figure 11: Sector SW: Turbulence Intensity (TI)

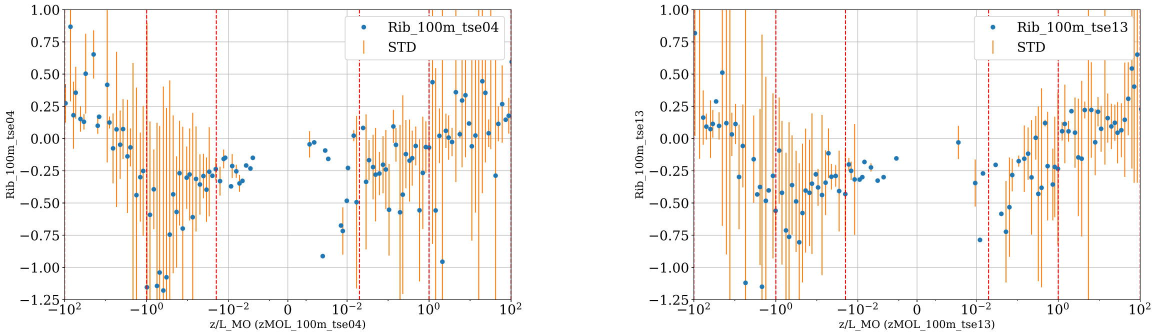

(a) Tower 20 (b) Tower 29

Figure 12: Sector NE: Bulk Richardson number (Ri_b)

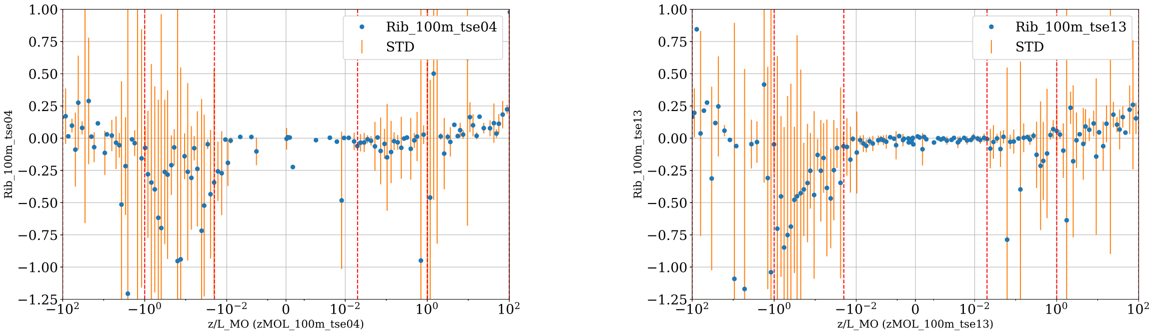

(a) Tower 20

(b) Tower 29

Figure 13: Sector SW: Bulk Richardson number (Ri_b)

5.2 Tower 25

Figs 14(a),14(b),14(c),14(d) show the thermal stability metrics for Tower 25. The turbulence intensity is on average about 40% and the wind shear exponent about 0.3 for all thermal stability classes, shown that mechanical turbulence due to mixing is dominant. A large standard deviation of the binned data is seen for all the stability metrics.

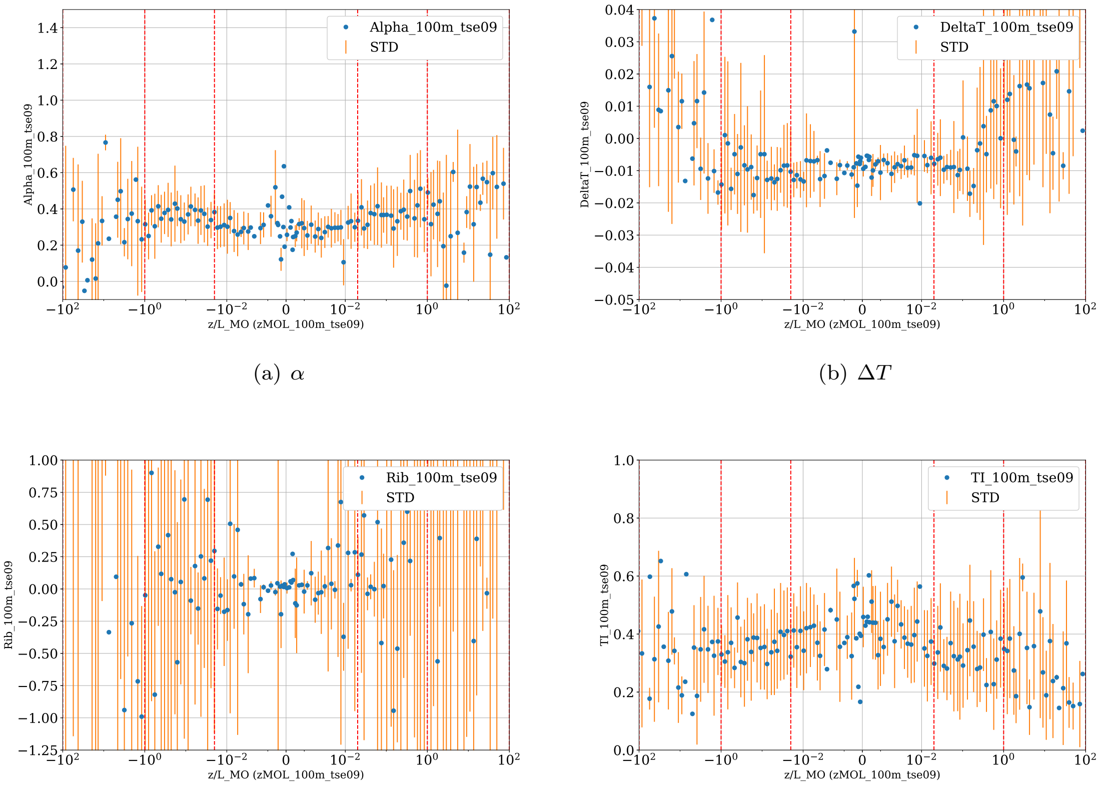

(a) α

(b) ΔT

(c) Ri_b

(d) TI

Figure 14: Sector South: Tower 25

6 Conclusion

The wind speed and temperature datasets from the Perdigao field measurement campaign are analyzed over a period of one month in May 2017. Different thermal stability parameters such as Monin-Obhukov length, bulk Richardson number, shear exponent and temperature gradient are computed. The data is analyzed for the predominant wind directions, which are perpendicular to the ridges on the Towers 20 and 29 and along the valley for Tower 25. The expected theoretical trends for different metrics are more clearly visible on Tower 29 from for the SW sector.

Inside the valley, which is a re-circulation zone, the mechanical turbulence due to mixing is dominant as observed in the turbulent intensity data. Here, the influence of thermal stability is negligible.

The choice of stability metrics in a complex terrain remains dependent on the specific location and wind direction sector. This is attributed to the local terrain heterogeneity. An adaptive classification based on the measured parameters appears to be a viable approach for defining the site-dependent stability bound. As a future work, the adaptive classes for each wind sector and stability parameters needs to be defined. Such binned average data would be useful for validation of numerical simulations that include thermal effects.

References

[1] Perdigão Perdigão field experiment `https://perdigao.fe.up.pt/`

[2] Stull R 2016 *Practical Meteorology: An Algebra-Based Survey of Atmospheric Science.* (University of British Columbia, British Columbia, 797-801.)

[3] Sorbjan Z and Grachev A 2010 *Boundary-Layer Meteorology* **135** 385–405

[4] Fernando H, Mann J, Laginha Palma J, Lundquist J, Barthelmie R, Belo-Pereira M, Brown W, Chow F, Gerz T, Hocut C, Klein P, Leo L, Matos J, Oncley S, Pryor S, Bariteau L, Bell T, Bodini N, Carney M and Wang Y 2018 *Bulletin of the American Meteorological Society* **100**

Variation of u^*

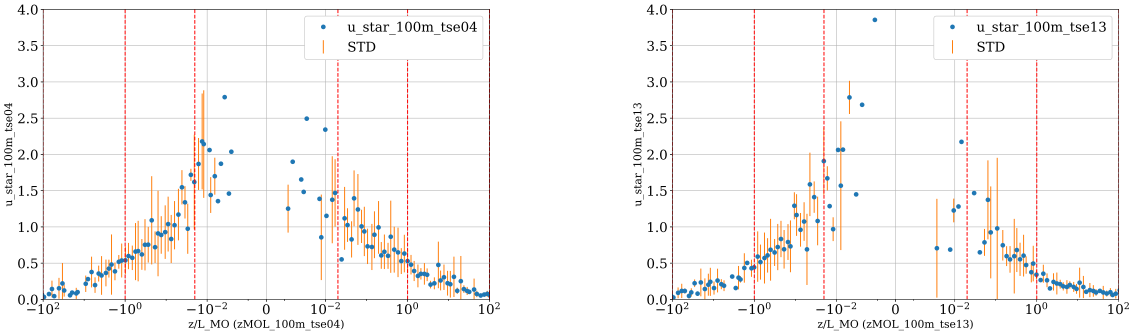

(a) Tower 20

(b) Tower 29

Figure 15: Sector NE: Friction velocity u^*

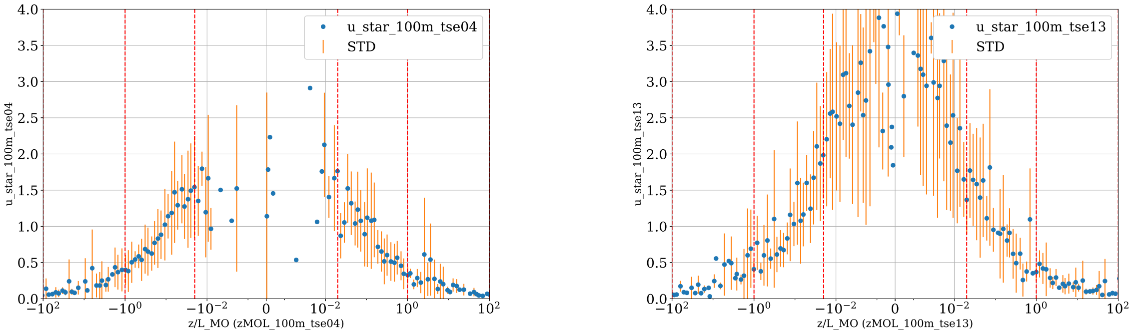

(a) Tower 20

(b) Tower 29

Figure 16: Sector SW: Friction velocity u^*

Optimisation of long-range lidar trajectories for wind speed forecast using large eddy simulations

Marcos Ortensi[a], **Martin Kühn**[a]

[a] ForWind, University of Oldenburg, Germany

E-mail: marcos.ortensi@uol.de

Keywords: forecasting, very-short-term, wind energy, lidar, lidar trajectory, simulation, large eddy simulation

1 Introduction

The transient and stochastic behaviour of wind has made the energy transition quite challenging in terms of power grid stability. In addition, the growing development of offshore wind farms has created regions with high energy capacity density, which can significantly influence the grid balance. Because of that, minute-scale forecasting (lead time below 1 hour) has gained more attention in the last years [1].

The definition of the lidar trajectory parameters can significantly impact the lidar forecasting results, therefore they should be carefully chosen. In a real measurement campaign, however, it is very costly to test several lidar trajectories in order to find the one that would generate the most accurate forecasting results. Unlike with simulations, on real campaigns it is not possible to assert the quality of the wind flow reconstruction, since the real wind flow is unknow. Furthermore, the atmospheric conditions change constantly, making it very hard to correlate the changes made on the scanning trajectories to the forecasting results.

In order to study the effects of the trajectory configurations on the accuracy of lidar forecasting, this work uses a lidar simulator, similar to the one presented by Trabucchi et al. [2], and large eddy simulations (LES) to test several scanning trajectories. The conclusion of this study will help to optimize the lidar trajectories in an ongoing lidar measurement campaign in the offshore wind farm Nordergründe which contains 18 wind turbines and is located close to the German coast in the North Sea.

2 Objectives

This work aims to study the effects of lidar trajectory configurations on the wind field reconstruction and, consequently, on the lidar forecasting results. LES and a lidar simulator are used to generate lidar measurements, which are used to reconstruct the wind fields and to perform wind speed forecasting. The results of the wind field reconstruction for each scan trajectory are compared to the original LES wind field in terms root-mean-square error.

3 Methodology

To obtain the simulated line-of-sight wind speed (V_{LOS}) with the lidar simulator, three main inputs are required: a LES wind field, the lidar's characteristics and a trajectory. The lidar's characteristics include its position and the features of the light pulse. The scan trajectory is defined by azimuth and elevation angles, temporal and angular resolution and range gates.

The LES wind field simulates unstable atmospheric conditions within a 15 km x 12 km domain, with a 50 m x 50 m x 10 m resolution. Its duration is 1 hour, with a temporal resolution of 1s, and it presents a mean wind speed around 10 m/s, as shown in Figure 1 (a).

The lidar simulator was configurated to simulate a long-range lidar with a probe length of 150 m. The lidar position was set to be on the nacelle of the wind turbine 17 following the layout of the wind farm Nordergründe. Finally, to analyse the effects of the trajectory parameters, many trajectories with different opening angles, temporal and angular resolutions, range gate spacing values, and scan orientations were tested. Only Plan Position Indicator (PPI) scans with 0° elevation at 90 m height were tested. Figure 1 (b) shows the V_{LOS} of a lidar scan example, plotted over the layout of Nordergründe (black dots).

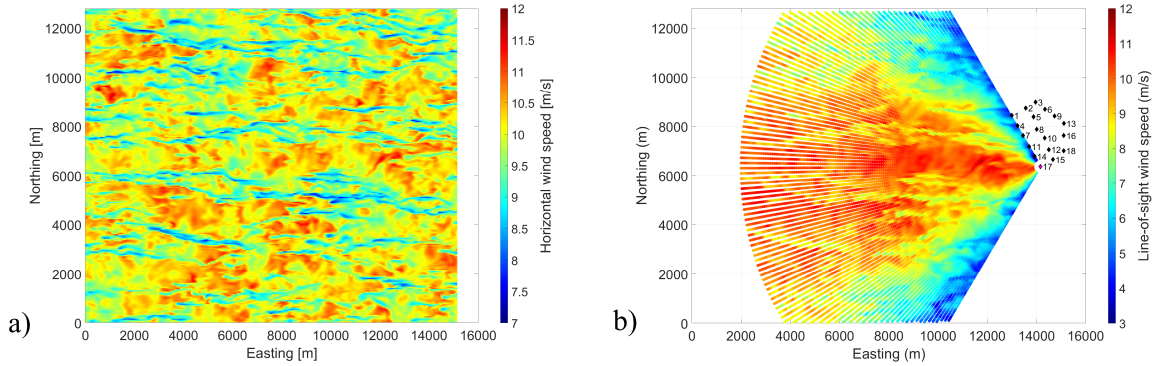

Figure 1: (a) Snapshot of the LES wind field; (b) V_{LOS} of a scan trajectory generated in the lidar simulator with 120° opening angle, temporal resolution of 1 s, angular resolution of 1°, and range gates spaced by 75 m.

The simulated V_{LOS} are then used to reconstruct the wind field with a VAD (velocity azimuth display) fitting approach. Next, the lidar reconstructed wind fields are synchronised in time using the approach introduced by Beck and Kühn [3].

The lidar forecasting approach is based on the work from Theuer et al. [4]. The wind vectors of the synchronized wind fields are propagated to a lead time of 5 minutes ahead. The ones reaching the wind turbines at a time interval around the lead time are considered for the calculation of the forecasted wind speed.

The validation of the lidar forecasting in terms of correlation factor, root-mean-square error (RMSE) and bias was made with the hub height wind speed of each turbine, which was calculated based on the LES wind field. No wake effect is considered in these calculations. The lidar forecasting was also compared to the benchmark persistence [1].

4 References

[1] I. Würth, L. Valldecabres, E. Simon, C. Möhrlen, B. Uzunoğlu, C. Gilbert, G. Giebel, D. Schlipf and A. Kaifel. *Minute-Scale Forecasting of Wind Power - Results from the Collaborative Workshop of IEA Wind Task 32 and 36. Energies,* 12(4), p. 712, 2019.

[2] D. Trabucchi, J. J. Trujillo, G. Steinfeld, J. Schneemann, M. Machta, J. P. Cariou and M. Kühn. *Numerical Assessment of Performance of Lidar WindScanners for Wake Measurements*. In EWEA, Brussels, 2011.

[3] H. Beck and M. Kühn. *Temporal Up-Sampling of Planar Long-Range Doppler LiDAR Wind Speed Measurements Using Space-Time Conversion. Remote Sensing,* 11(7), p. 867, 2019.

[4] F. Theuer, M. F. van Dooren, L. v. Bremen and M. Kühn. *Minute-scale power forecast of offshore wind turbines using long-range single-Doppler lidar measurements. Wind Energ. Sci.,* 5(4), p. 1449–1468, 2020.

eawe
european academy of wind energy

U.PORTO
FEUP FACULDADE DE ENGENHARIA
UNIVERSIDADE DO PORTO

17th EAWE PhD Seminar on Wind Energy
3-5 November 2021
Porto, Portugal

Review of standalone small-scale Darrieus wind turbines – a Nottingham case study

Shubham[a], A Ianakiev[a], and N Wright[a]

[a]Department of Civil Engineering, Nottingham Trent University, UK

E-mail: `shubham.shubham@ntu.ac.uk`

Abstract

A detailed review is conducted on H-rotor Darrieus vertical axis wind turbine. The purpose is to study different designs for urban rooftop applications in the City of Nottingham. Parameters such as aspect ratio, rotor solidity, airfoil profile, preset pitch, innovative blade designs, external structures, etc. are investigated as studied by previous authors. Focus is put on aerodynamic, power performance and also on aeroacoustic studies due to noise limits set in the urban environment and public acceptance. At the end, various areas are mentioned where more studies are needed to make Darrieus VAWT more acceptable and feasible in the urban rooftop settings in Nottingham.

Keywords: Darrieus, Small-scale, Vertical Axis Wind Turbine, Wind resource, Urban environment, Aerodynamics, Power, Aeroacoustics, Noise

1 Introduction

The focus on sustainable development has risen significantly in the past few years. The Paris Agreement 2015 [1] has further intensified investments in renewable energy sector throughout the world such as wind and solar energy. Within the UK, a major source of energy consumption happens within cities either through domestic, services or transport sector [2]. Non-renewable sources contribute a significant part of this energy, thereby keeping the carbon footprint of cities high. The United Nations estimate that from 2018 to 2050, world's urban population will rise by 2.5 billion, or 68% of world's population will live in urban areas from the current 55% [3]. Extensive utilization of renewable sources of energy is therefore needed to foster sustainable urban growth.

Rooftop solar installation is not sufficient for decarbonization goals due to the power vacuum during nighttime and during winter and monsoon seasons when sun days are less. Integrating wind turbines with solar panels on urban rooftops thus becomes a viable alternative. Such standalone off-grid systems also increase efficiency of power generation due to less transmission losses and can play a significant role in the energy transition process [4] [5].

Urban rooftop wind turbines are small-scale in design and operate in wind conditions where the flow is more chaotic and turbulent in nature than in rural or offshore areas [6]. Vertical Axis Wind Turbines (VAWT) are better suited for such wind conditions, as compared to Horizontal Axis Wind Turbines (HAWT) [7]. Their advantages include: lower cut-in wind speed and noise, omni-directional in nature and therefore no need of yaw mechanism, higher performance in turbulent and gusty wind conditions. Furthermore, VAWTs have less wear and tear of mechanical components, lower manufacturing costs, simple assembly and installation process and easier maintenance [8] [9], the factors which are very important for its success in the urban environment. VAWTs are further divided into two types: Lift-based Darrieus [10] [11] and Drag-based Savonius [12] [13]. Savonius turbine uses differential drag force for power generation and is less efficient (in terms of energy extracted per unit swept area and Annual Energy Output (AEO)) than Darrieus turbine which utilizes lift generated by airfoil-shaped blades for the same purpose. The design of Darrieus is more complex than Savonius but has more potential to enhance the power generation capability without compromising city noise limits.

In this study, a detailed review is conducted on Darrieus VAWTs and the studies performed so far. Focus will be on aerodynamic and aeroacoustic characteristics of such turbines, understanding the effect of each design parameter on Darrieus performance, and innovative designs that can be taken up in the future.

2 Darrieus VAWT

The basic configuration of a Darrieus VAWT consists of a number of airfoil-shaped blades rotating vertically about an axis perpendicular to the wind direction, as shown in Figure 1 (a) and (b). The Darrieus design is highly dependent on aerodynamic characteristics of such blades. In addition, aeroacoustic behaviour puts additional constraint on such design choices especially for urban rooftop applications. Therefore, it is important to understand the basic aerodynamics to further approach the study of such turbines.

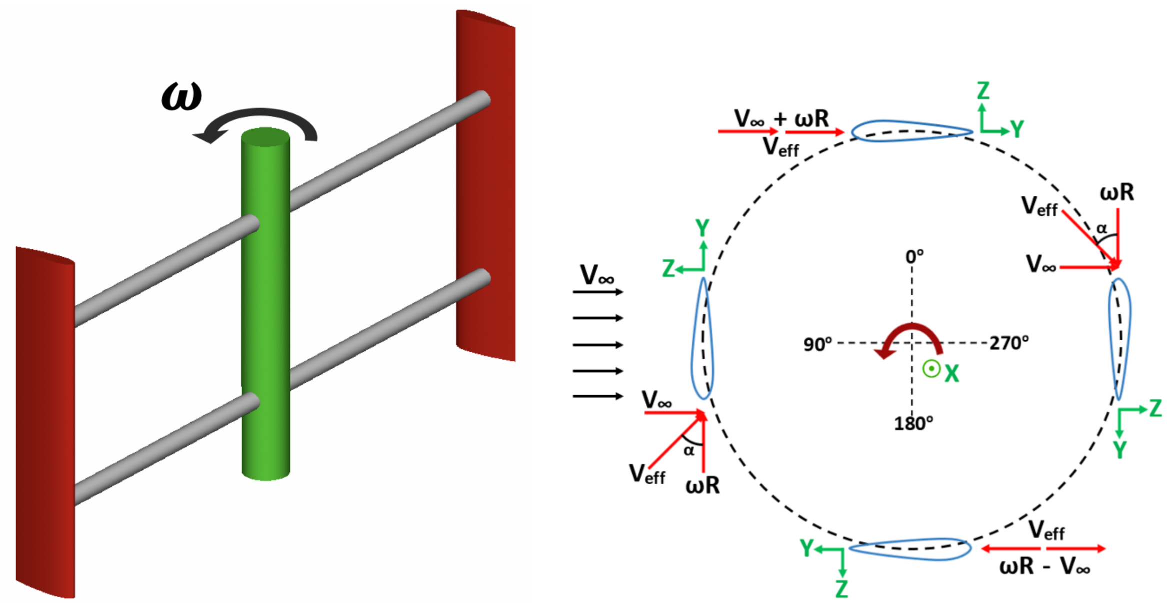

(a) 2-bladed Darrieus turbine

(b) Position of Darrieus blades over a single rotation

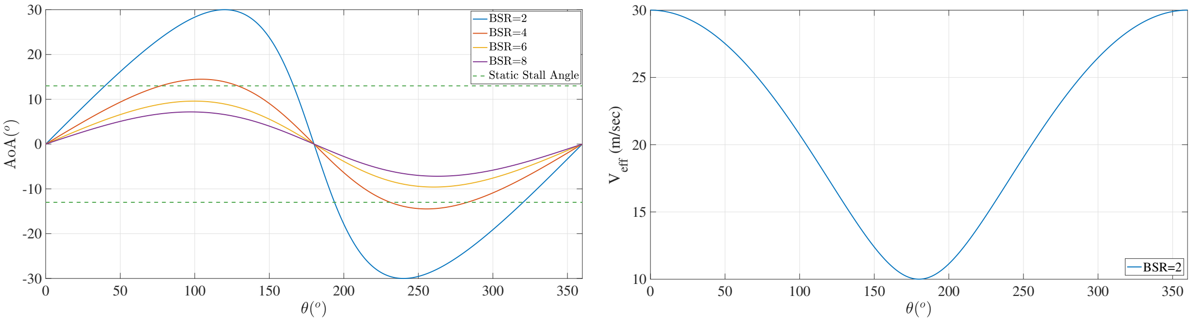

(c) Angle of Attack variation as perceived by the blade (without induction)

(d) Effective velocity perceived by a VAWT blade (without induction) for $TSR = 2$ and $V_\infty = 10 m/sec$

Figure 1: Darrieus VAWT

2.1 Aerodynamic Performance

Over a single rotation from 0^o to 360^o, blades experience varying Angle of Attack (AoA). The AoA values depend on Blade Speed Ratio (BSR) which in-turn depends on freestream velocity of the wind (V_∞) and rotational velocity of the VAWT (ω). An approximate estimation of AoA and effective velocity (V_{eff}) experienced by the blades can be calculated using simple geometry and is shown in Figure 1 (c) and (d). As BSR increases, maximum and minimum values of AoA in a single rotation decreases.

Highest values are obtained close to the most upstream and downstream position of the blades, which also contributes to higher lift produced. Maximum velocity is experienced at azimuth=0° and minimum velocity at azimuth=180°, when the blade is just entering the upstream and downstream half of the rotation, respectively. VAWT aerodynamics is therefore fundamentally unsteady and the lift produced by the blades is the major contributor to the torque (or power) production, therefore making Darrieus a lift-type VAWT.

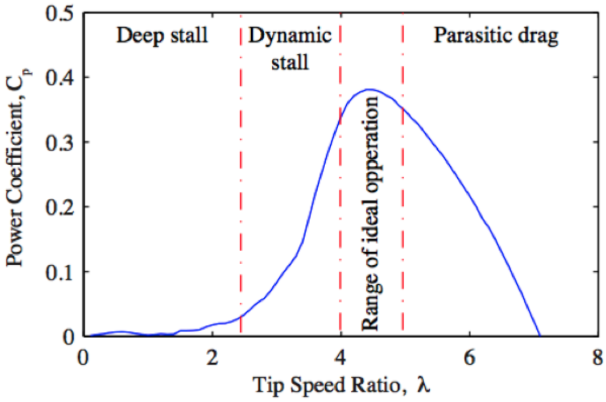

Figure 2: Power coefficient vs Tip Speed Ratio curve for a Darrieus VAWT (taken from McIntosh [14])

Figure 2 shows a typical curve for the variation in Darrieus power performance (C_P) with Tip Speed Ratio (also referred to as Blade Speed Ratio (BSR)). In case of lower BSR, AoA values cross the static stall value while approaching the most upstream and downstream point of rotation. Due to constantly changing nature of AoA, blades experience dynamic stall at lower BSR. As BSR increases, the severity of dynamic stall decreases which increases the rotor torque generated. At higher BSR values, parasitic drag on blades become important which in-turn decreases the rotor torque generated. Darrieus VAWT is therefore designed in such a way that it compromises the stall and drag characteristics to maximize performance.

Another important aerodynamic phenomenon is the blade-wake interaction. Blades in the upstream half of rotation generate wake which interacts with the blades in the downstream half, which degrades the performance of blades in the latter half [15]. Generation of tip vortices further intensifies this phenomenon as due to the direction of rotation, wake from top and bottom part of rotor gets deflected towards the mid-span of the downstream blades, as shown by simulations of both Scheurich [16] and Ferreira [17]. This also results in increased unsteady loading fluctuations on rotor blades which can potentially increase the VAWT noise signature.

2.2 Historical development of Darrieus configurations

A detailed chronological sequence of various Darrieus configurations is shown by Tjiu [11]. Darrieus VAWT was initially proposed by Darrieus in 1925, the design of which is shown in Figure 3 from his 1931 patent [18]. Both the curved and straight-bladed Darrieus evolved through the 2^{nd} half of 20th century when a number of designs were experimented. In case of curved blades, Guy-wired phi (ϕ) rotor was experimented from 1968-early 1990s. The rotors were large-scale ranging from 30-500 kW, even going towards 2.5-4 MW (largest VAWT in the world by NRC Canada) from 1988-93. Following the lessons learnt from these designs and some failures happening in 1978-81, the design evolved towards Fixed on tower/Cantilevered phi (ϕ) rotor from 2000s-present, especially in USA and Canada.

In case of straight blades, initially large-scale rotors were experimented. Variable-geometry (Musgrove) and Variable-pitch (Giromill) rotors evolved during 1970s-80s. A number of problems arose with these configurations such as high manufacturing cost, high COE (Cost of Operation) and less competitive nature in the market. After a review on the wind turbine technology by Musgrove [19] [20] and his efforts into designing a simpler VAWT, straight-bladed Darrieus became more common after 1988. The design further evolved into Fixed-pitch H-rotor which had a similar design to the 1931 patent by Darrieus. Large-scale H-rotor proved to be quite costly as compared to its HAWT counterpart, therefore a number of small-scale H-rotor and its variations started coming up in 2000s, such as Articulating and Helical

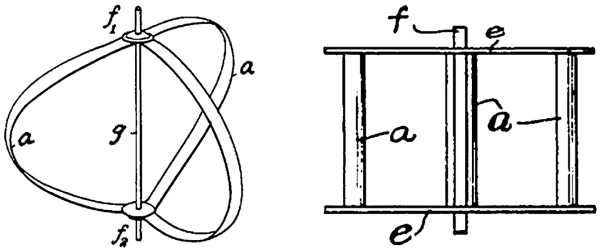

Figure 3: Design of Darrieus VAWT proposed in 1931 patent [18]; left: curved-bladed, right: straight-bladed; a: blades, e: supporting plates, f and g: rotor shaft, f1 and f2: hubs

H-rotor. Small-scale design allowed the researchers to easily experiment with different design parameters at a relatively lower cost. This paper focuses purely on small-scale Darrieus H-rotor and the research performed till now on its design and analysis.

3 H-rotor: State of the Art

Most of the research is focussed on to increase the power production of Darrieus turbine by increasing the lift on blades and decreasing the drag forces [10] [21] [22]. Small-scale design allows the flexibility to chose from multiple geometrical parameters for efficient operation of the VAWT in turbulent and comparatively scarce urban wind resource. Since the VAWT will be placed in built-up areas, a major focus is also towards reducing the noise produced by a Darrieus turbine [23] [24] [25]. This will go a long way in public acceptance of such sustainable energy systems [26] [27].

3.1 Aerodynamics and Performance analysis

Since a multitude of design parameters are available for a Darrieus rotor, it is important to understand the effect of each on overall torque/power production of the rotor to design an optimum wind turbine. Such parameters include Aspect Ratio, Solidity, Airfoil Profile, Preset Pitch, Blade Design, etc. examined over a range of Blade Speed Ratio (BSR), both experimentally and numerically.

3.1.1 Experimental benchmark studies

Kaushik [9] provides a review of experiments conducted on various designs of Darrieus rotor. Blackwell [28] presents a detailed wind tunnel performance data for the Darrieus wind turbine with NACA 0012 blades for different wind velocities, rotational speed, solidities and Reynolds number. Battisti [29] examines both H-shaped and troposkien Darrieus rotor using experimental methods, compares their aerodynamic performance and provides a benchmark for validation of computational tools. Previously, Battisti [30] performed wind tunnel measurements on a H-rotor and examines the effect of blockage and full 3D flow features including tip vortices effect. Howell [8] tested a small-scale H-rotor for different wind velocities, BSR, solidities (2-bladed and 3-bladed rotor) and rotor blade surface finish, while making comparisons with 2D and 3D CFD results. Li [31] investigated the effects of ice and snow attached to the rotor blades, on Darrieus rotor power performance. This assumes special significance in the northern UK and north-western Europe, where there is significant snowfall in cold climates. Fiedler [32] investigated a high-solidity 3-bladed Darrieus H-rotor to study the effects of blade pitch, both positive and negative values, and blade mount-point offset on VAWT performance. LeBlanc [33] [34] presented an experimental benchmark to validate studies on using active variable pitch on individual rotor blades.

3.1.2 Aspect Ratio

Aspect Ratio (AR) for a Darrieus VAWT is defined as the ratio of rotor span with rotor diameter. This is also related to the AR of airfoil blades used. Ghonim [35] showed that an optimum value of AR is required to get the maximum C_P value; for $V_\infty = 10$ m/sec the value of AR is 1.3 for a 3-bladed Darrieus H-rotor. The reason is: a higher AR rotor will help in reducing the adverse effect of tip vortices on rotor blade loads, thus potentially producing higher rotor torque and requiring lower BSR values [15]. Although, higher AR requires higher structural strength of the rotor, thus requiring a number of supporting struts as can be seen for WindSpire turbine [36]. This increases the parasitic drag and also turbulence content in the rotor wake. Due to increased interaction between downstream blades and higher turbulent wake, there is a potential decrease in torque. An optimum value of AR is also required for a good self-starting capability. This is shown by opposite conclusions of Ghonim [35] who proposed to decrease AR, and Du [37] who proposed to increase AR, for increasing the self-starting capability of the rotor at lower wind velocities. Brusca [38] highlighted similar results to the former by showing that lower AR rotor produces higher power coefficients due to higher blade Reynolds number. This can help in self-starting of the rotor and also provide higher structural stability.

3.1.3 Solidity

VAWT solidity is defined as the ratio of blade area to rotor swept area, which signifies the level of blockage rotor blades provide for the oncoming flow. Mathematically, it is defined as $\sigma = Nc/R$, where σ is VAWT solidity, N is number of blades, c is blade chord and R is rotor radius. Mohamed [39] simulated S-1046 airfoil for solidities ranging from 0.1-0.25. Higher solidities performed better (higher C_P) at lower BSR values and lower solidities performed better at higher BSR values, which is also shown by Howell [8]. When solidity increases, stronger wake is produced which leads to more blade-wake interaction. This is more stronger at higher BSR values, which leads to lower rotor performance. Therefore, adding blades (increasing solidity) reduces optimum rotor performance. The results also show that self-starting can be improved with high-solidity rotors (due to higher C_P at low BSR), although this will compromise the higher BSR performance where the Darrieus rotor may operate for majority of its service life. A good work on self-starting capability is done by Baker [40], Dominy [41] and Hill [42]. On the other hand, lower solidities provide higher operating range for any Darrieus rotor which makes it more suitable for urban environments where wind velocities vary significantly. Also, the power curve is smoother around the optimum TSR point (highest C_P), so easier for the control system to operate around that point [43]. The design of Darrieus is therefore a compromise between self-starting characteristics (low BSR) and higher operating range (mid to high BSR). For a city like Nottingham which has a mix of both congested and open spaces within the inner city limits, this design compromise assumes special relevance for different localities.

3.1.4 Airfoil Profile

The choice of airfoil profile can significantly affect the power and noise output of a Darrieus turbine. Since the AoA perceived by the blade varies from both positive and negative values, symmetrical airfoil are commonly used such as NACA 00XX series. Mohamed [39] simulated 20 different airfoil shapes using URANS simulation. In case of symmetrical NACA series, maximum C_P of 0.2964 was obtained by NACA 0018. Lower thickness airfoil perform better at higher BSR values while higher thickness airfoil perform better at lower BSR values. Same conclusion was obtained by Roh [44] and Healy [45]. Additionally, non-symmetrical airfoils were also simulated by Mohamed [39] and it was shown that symmetrical airfoils both performed better and has higher operating range than the former. The main reason being, symmetrical airfoils delay stall, thus reducing the adverse effects on blade loads. Highest C_P value amongst all 20 airfoils was obtained for S-1046 airfoil.

3.1.5 Preset Pitch

Preset pitch is defined as the angle between Darrieus blade chord line and tangent line to the circumferential path of the rotor blade. Similar to the reasons in case of airfoil profile, the preset pitch is normally kept at 0°, although positive or negative angles in some cases can lead to higher C_P values. Armstrong [46] experimented with 3-bladed H-rotor with NACA 0015 profile. C_P value increased by 15% if preset pitch was changed from 0° to -6° i.e toe-out position and this happens due to a change in AoA perceived by the blades. Toe-out reduces the AoA on upwind part and increases on downwind part, and a balance between the optimum AoAs decides the overall change in performance. Generally, performance increases upto a value of toe-out angle and then decreases. A number of authors such as LeBlanc [33] [34] and Tavernier [47] have also suggested using active variable pitch for individual blades, to improve power extraction by creating optimal loading and minimizing losses at every azimuthal locations. The same method can also be used to control the direction of rotor wake for wind farm control and structural fatigue reasons [48].

3.1.6 Blade Design

As seen in previous discussions, straight-bladed rotor designs (H-rotor) are most common as they are easier and less costly to manufacture and maintain. Additionally, innovative blade designs can be used to increase the C_P values while having negligible impact on aerodynamic noise and mechanical bearing loads of the Darrieus turbine. Helical-bladed Darrieus rotor, as in the case of Quiet Revolution [49], provides multiple benefits such as slightly higher effective chord, smoother blade loads or driving torque in a single rotation which can help to reduce mechanical vibrations and aerodynamic noise produced. It also improves aesthetics which is important for public acceptance. A similar design was experimented by Bussel [50] in 2004, named as TURBY, which is designed specifically for the built environment. Although, helical blades are expensive to manufacture than simple straight blades [7]. A number of authors use zig-zag trip, both on the suction and pressure side of the blade, to force boundary-layer transition at a specific chord location [15]. This helps to reduce flow separation which in-turn increases power performance and reduces laminar boundary layer noise [51]. Another commonly experimented blade design is the 3D troposkien shape [29] which gives better performance than straight-bladed rotor at higher BSR values. Different available blade designs make it imperative to compare individual performances for a given wind velocity at the desired urban location.

3.1.7 Special structures for Darrieus VAWT

A few authors experimented with additional structures placed around the Darrieus rotor to increase its power performance. The concept is similar to ducted HAWT in which the rotor is shrouded by a diffuser to direct the oncoming flow direction. Kim [52] placed a flat plate deflector in front of a pair of counter-rotating Darrieus rotors, which increased the flow velocity on each rotor by 10-30% more than the freestream velocity. Longer and narrower deflector produced higher C_P values (2-3 times) than shorter and wider deflector. Also, closer the rotors were to the deflector (in the streamwise direction), higher the values of C_P were. One major drawback of using such structures is that it makes the turbine more directional, which can be disadvantageous in an urban setting.

3.2 Aeroacoustic studies

Since the focus is on urban wind turbines in Nottingham, UK, reduction of Darrieus noise signature assumes relevance. This is also coupled to strict regulations imposed by Nottingham City Council for the noise limits in a crowded built-up urban locality. The major source of noise in a Darrieus turbine is the unsteady loading on rotor blades due to the interaction of solid blades and air flow around it. A number of studies have been undertaken to understand the Darrieus noise generation mechanisms and methods to reduce its acoustic signature.

Dumitrescu [53] compared noise for a HAWT and a VAWT at similar power performance (C_P=0.4) and found that the latter produced less overall noise (47 dB) than the former (56 dB). Pearson [15] experimented with 3-bladed Darrieus H-rotor, for different BSRs, freestream velocities, rotational speeds and solidities. Higher harmonic content was found in case of lower BSR values, due to dynamic stall being dominant at lower rotational speeds and at blade loading harmonics (dynamic stall is periodic in nature). At higher BSR, BVI is a bigger noise source which is more stochastic in nature. Increasing solidity (number of blades) decreases harmonic content. This happens due to decrease in Angle of Attack (AoA) on blades in the upstream half of rotation and therefore, dynamic stall, as solidity increases. Increase in turbulence inflow leads to a reduction in harmonic content in the noise spectra due to periodic loading being disrupted by stochastic loading of turbulent eddies on Darrieus blades. Using Boundary Layer (BL) trips on both the outer and inner blade surfaces can avoid the laminar BL noise. A general trend was found that noise decreases with increase in BSR due to increase in induction factor. This rate of increase or decrease is higher for high solidity rotors due to its higher induction factors. This means that off-design penalty for noise will be more for high solidity rotors, which is similar to the penalties in aerodynamics. This makes turbine control significant for such rotors especially in regions of rapidly varying wind speeds.

Goccmen [54] optimized 6 different airfoils, such as FX 63-137, S822, S834, etc. both for noise and power performance. Generally speaking, reducing airfoil thickness and increasing camber helps to reduce noise and increase the ratio of lift/drag over a range of AoA. Weber [55] tested a 3-bladed H-rotor and showed that in a flowfield, some major noise sources are present around vortices generated in the wake, flow separation over blades and karman vortices behind the turbine shaft. BPF noise is mainly caused due to Blade-Vortex Interaction (BVI) and unsteady loading on the blade. Changing lift and drag forces on a blade in a single rotation is also a source of loading noise and contributes to higher harmonics. Mohamed [56] simulated a 3-bladed H-rotor with different airfoils, with S-1046 producing the lowest noise. Increasing BSR and solidity both contributed to increased overall noise, due to higher BVI and unsteady loading on blades. The findings for increasing BSR values is opposite to what is mentioned by Pearson [15]. This shows that there will be an optimum value of BSR where the noise will be maximum or minimum.

Higher AR can also lead to increase in noise generated due to increased blade-wake interaction [15]. Availability of vertical space and wind resource in urban locality can also play a significant role in the same [57]. Venkatraman [58] simulated noise generated due to flow non-uniformity experienced by a Darrieus turbine on an urban rooftop. The directivity of overall sound increases in the direction of the velocity gradient with a little increase in higher BPF and broadband noise. Understanding such behaviour is important to figure out the noise impact of rooftop wind turbines. There is a potential to design Darrieus turbines with directivity opposite to humans settlements.

4 Conclusions and future scope

In this study, a detailed review was conducted for H-rotor Darrieus VAWT. After the first design in 1925, a significant amount of research has been conducted on the aerodynamic design and analysis of such turbines. Initially, the focus was on large scale design for multi-megawatt applications. In the 21st century, the focus has shifted towards small-scale applications in urban settings. Small-scale turbine allows to easily experiment with different design parameters to achieve the highest performance for a given wind resource. Overall, there is sufficient work done on performance analysis of such turbines. In the coming years, there is a need to understand the detailed flow physics of a Darrieus turbine. Studies on AoA variation, flow separation, dynamic stall, blade-wake interaction, Reynolds number effect are needed. Power performance analysis is required in case of oblique wind conditions, turbulent inflow, wind gusts, etc.

Since the aim is to install wind turbines on rooftops, special focus is needed to reduce the noise signature of such machines due to close proximity with humans. For that, studies are needed to understand the noise generation mechanisms and methods to mitigate them. Apart from high-fidelity computational studies, low-fidelity analyses are also needed to understand each of those mechanism separately and focus on the most relevant ones. New innovative Darrieus designs can be taken up, such as blade tips to mitigate tip vortices, trailing-edge serrations, external structures around VAWT, helical blades, etc. Darrieus clusters can be investigated which can enhance the power generation capacity on a single rooftop. The objective will be to lower community noise generation without impacting the power generation capacity of a wind turbine. This will go a long way in increasing public adoption of small-scale urban vertical axis wind turbines.

Acknowledgements

This project has received funding from the European Union's Horizon 2020 Marie Curie zEPHYR research and innovation programme under grant agreement No EC grant 860101. (https://www.h2020-zephyr.eu/)

References

[1] UNFCCC 2015 *Available online at: https://unfccc.int/process-and-meetings/the-paris-agreement/the-paris-agreement*

[2] UK-BEIS *Available online at: https://www.gov.uk/government/statistics/energy-consumption-in-the-uk*

[3] Desa U N 2018 *New York: NY. Available online at: https://population.un.org/wup/Publications/(Accessed December 20, 2018)*

[4] Van Kuik G, Peinke J, Nijssen R, Lekou D, Mann J, Sørensen J N, Ferreira C, van Wingerden J W, Schlipf D, Gebraad P *et al.* 2016 *Wind energy science* **1** 1–39

[5] Quintero Pulido D F, Ten Kortenaar M V, Hurink J L and Smit G J 2019 *Energies* **12** 2033

[6] Micallef D and Van Bussel G 2018 *Energies* **11** 2204

[7] Kumar R, Raahemifar K and Fung A S 2018 *Renewable and Sustainable Energy Reviews* **89** 281–291

[8] Howell R, Qin N, Edwards J and Durrani N 2010 *Renewable energy* **35** 412–422

[9] Kaushik V and Shankar R N 2021 *Innovative Design, Analysis and Development Practices in Aerospace and Automotive Engineering* (Springer) pp 473–480

[10] Jin X, Zhao G, Gao K and Ju W 2015 *Renewable and Sustainable Energy Reviews* **42** 212–225

[11] Tjiu W, Marnoto T, Mat S, Ruslan M H and Sopian K 2015 *Renewable energy* **75** 50–67

[12] Savonius S J 1931 *Mechanical engineering* **53** 333–338

[13] Menet J L 2004 *Renewable energy* **29** 1843–1862

[14] McIntosh S C 2009 *Wind energy for the built environment* Ph.D. thesis University of Cambridge

[15] Pearson C 2014 *Vertical axis wind turbine acoustics* Ph.D. thesis University of Cambridge

[16] Scheurich F 2011 *Modelling the aerodynamics of vertical-axis wind turbines* Ph.D. thesis University of Glasgow

[17] Simao Ferreira C 2009 *The near wake of the vawt - 2d and 3d views of the vawt aerodynamics* Ph.D. thesis Delft University of Technology

[18] Marie D G J 1931 Turbine having its rotating shaft transverse to the flow of the current uS Patent 1,835,018

[19] Musgrove P 1985 *Passive and Low Energy Ecotechniques* 290–309

[20] Musgrove P 1987 *Solar & wind technology* **4** 37–49

[21] Wekesa D W, Wang C, Wei Y and Zhu W 2016 *Journal of Wind Engineering and Industrial Aerodynamics* **157** 1–14

[22] Sun X, Chen Y, Cao Y, Wu G, Zheng Z and Huang D 2016 *Advances in Mechanical Engineering* **8** 1687814016629349

[23] Alamir M A, Hansen K L and Catcheside P 2021 *Journal of Cleaner Production* 126393

[24] Fredianelli L, Carpita S and Licitra G 2019 *Science of the total environment* **648** 728–736

[25] Deshmukh S, Bhattacharya S, Jain A and Paul A R 2019 *Energy Procedia* **160** 633–640

[26] Bakker R H, Pedersen E, van den Berg G P, Stewart R E, Lok W and Bouma J 2012 *Science of the total environment* **425** 42–51

[27] Klæboe R and Sundfør H B 2016 *International journal of environmental research and public health* **13** 746

[28] Blackwell B F, Sheldahl R E and Feltz L V 1976 Wind tunnel performance data for the darrieus wind turbine with naca 0012 blades Tech. rep. Sandia Labs., Albuquerque, N. Mex.(USA)

[29] Battisti L, Persico G, Dossena V, Paradiso B, Castelli M R, Brighenti A and Benini E 2018 *Renewable energy* **125** 425–444

[30] Battisti L, Zanne L, Dell'Anna S, Dossena V, Persico G and Paradiso B 2011 *Journal of energy resources technology* **133**

[31] Li Y, Tagawa K and Liu W 2010 *Current Applied Physics* **10** S335–S338

[32] Fiedler A J and Tullis S 2009 *Wind engineering* **33** 237–246

[33] LeBlanc B and Simao Ferreira C 2018 *2018 Wind Energy Symposium* p 1243

[34] LeBlanc B and Ferreira C 2021 *Wind Energy*

[35] Ghonim T A, Nebiewa A and El-Askary W

[36] Royall-Products *Available online at: https://www.windspireenergy.com/*

[37] Du L, Ingram G and Dominy R G 2019 *Energy Science & Engineering* **7** 2421–2436

[38] Brusca S, Lanzafame R and Messina M 2014 *International Journal of Energy and Environmental Engineering* **5** 333–340

[39] Mohamed M 2012 *Energy* **47** 522–530

[40] Baker J 1983 *Journal of Wind Engineering and Industrial Aerodynamics* **15** 369–380

[41] Dominy R, Lunt P, Bickerdyke A and Dominy J 2007 *Proceedings of the Institution of Mechanical Engineers, Part A: Journal of Power and Energy* **221** 111–120

[42] Hill N, Dominy R, Ingram G and Dominy J 2009 *Proceedings of the Institution of Mechanical Engineers, Part A: Journal of Power and Energy* **223** 21–29

[43] Kjellin J, Bülow F, Eriksson S, Deglaire P, Leijon M and Bernhoff H 2011 *Renewable energy* **36** 3050–3053

[44] Roh S C and Kang S H 2013 *Journal of Mechanical Science and Technology* **27** 3299–3307

[45] Healy J 1978 *Wind Engineering* 1–9

[46] Armstrong S, Fiedler A and Tullis S 2012 *Renewable energy* **41** 13–22

[47] De Tavernier D, Ferreira C and van Bussel G 2019 *Wind Energy* **22** 547–562

[48] Leblanc B and Ferreira C 2020 *Journal of Physics: Conference Series* vol 1618 (IOP Publishing) p 052030

[49] Quiet-Revolution *Available online at: https://www.quietrevolution.com/products/*

[50] Van Bussel G, Mertens S, Polinder H and Sidler H 2004 *Proceedings of the EAWE/EWEA Special Topic conference" The Science of making Torque from Wind", Delft, The Netherlands*

[51] Paterson R and Amiet R 1982 *Journal of Sound and Vibration* **85** 551–577

[52] Kim D and Gharib M 2013 *Journal of Wind Engineering and Industrial Aerodynamics* **115** 48–52

[53] Dumitrescu H, Cardos V, Dumitrache A and Frunzulica F 2010 *Proceedings of the Romanian Academy* **11** 47–54

[54] Göçmen T and Özerdem B 2012 *Energy* **46** 62–71

[55] Weber J, Becker S, Scheit C, Grabinger J and Kaltenbacher M 2015 *International Journal of Aeroacoustics* **14** 883–902

[56] Mohamed M 2014 *Energy* **65** 596–604

[57] Ferrigno K J 2010 *Challenges and strategies for increasing adoption of small wind turbines in urban areas* Ph.D. thesis Massachusetts Institute of Technology

[58] Venkatraman K, Christophe J, Schram C F and Moreau S 2021 *AIAA AVIATION 2021 FORUM* p 2216

17th EAWE PhD Seminar on Wind Energy
3-5 November 2021
Porto, Portugal

Canopy models evaluation over forests in flat terrain

J R Monteiro[a], **J M L M Palma**[a], and **V T P Batista**[a]

[a]Faculdade de Engenharia da Universidade do Porto, Departamento de Engenharia Mecânica, Rua Dr. Roberto Frias, s/n, 4200-465 Porto, Portugal

`E-mail: jesus.monteiro@fe.up.pt`

Keywords: Forest canopy, Canopy model, $k-\varepsilon$ turbulence model

1 Introduction

Installing wind farms near or inside forested areas requires accurate canopy flow modelling, and the existence of many canopy models based on Reynolds-averaged Navier-Stokes (RANS) equations [1] poses the question of which of the canopy models is the most suitable. This study evaluated seven canopy models [1–7] over forests in homogeneous (stand) and edge-flow configuration. The models' appraisal was based on the root mean square error (rmse) and bias between the computational results and measurements.

2 Methodology

The flow governing (mass and momentum) equations were solved for a statistically steady turbulent flow. The canopy aerodynamic drag (F_i (1)) that consists of the sum of pressure and viscous forces on all vegetation, is added to the momentum equation and turbulence production/destruction inside the canopy are accounted for via additional terms (S_k and S_ε (2) (3)) in the turbulence model (k-ε) transport equations.

$$\begin{aligned} F_i &= -C_d \alpha(z) |\mathbf{U}| \overline{U_i} && (1) \\ S_k &= C_d(\beta_p |\mathbf{U}|^3 - \beta_d |\mathbf{U}| k) && (2) \\ S_\varepsilon &= C_d(C_{\varepsilon 4} \beta_p |\mathbf{U}|^3 \frac{\varepsilon}{k} - C_{\varepsilon 5} \beta_d |\mathbf{U}| \varepsilon) && (3) \end{aligned}$$

Here, C_d is the mean drag coefficient, $a(z)$ is the leaf area density, a function of the distance to the ground, and $|U|$ is the mean scalar velocity. $\beta_p, \beta_d, C_{\varepsilon 4}$ and $C_{\varepsilon 5}$ are constants, whose value depend on the canopy model [1–7].

For evaluation of the models, we used the experimental data of Ref. [8], measurements within a maritime pine forest (Le Bray site, $44°43'$ N, $0°46'$ W), with an average tree height (h_c), leaf area index and canopy drag coefficient equal to 22 m, 1.8 and 0.2, respectively. The atmosphere was considered to be neutrally-stratified, and the site configuration allowed studies in stand and edge conditions with measurements performed at $4h_c$ and $9h_c$ from the forest edge.

3 Results and discussions

Results were normalised with the reference streamwise wind (U_{ref}) and the friction velocity (u_*) at $x = 9h_c$ and $y = 41.50$ m (highest measurement height). For the streamwise wind velocity (U_h) (Fig. 1a), all models behave similarly, with maximum and minimum rmse equal to 0.1036 and 0.0448 at sonic 2008, 0.1032 and 0.0541 at sonic 2006, and 0.1280 and 0.0690 at cup. The turbulence kinetic energy (tke) (Fig. 1b) was well represented by the models (minimum rmse = 0.0041 at sonic 2006 and maximum rmse = 0.0229 at sonic 2008). Apart from Svensson [2], which overestimated (bias = 0.1064, rmse = 0.1121 at sonic 2008; bias = 0.0766, rmse = 0.0807 at sonic 2006), and Liu [4], which underestimated (bias =

-0.0144 at 2008 sonic; bias = -0.0121 at sonic 2008) tke slightly inside and further above the canopy. In terms of Reynolds shear stress, Liu [4] had the lowest rmse = 0.0529 at sonic 2006 (result not shown), which is attributed to the low kinematic viscosity. The results found in the stand case were similar to those of the edge case, although in the edge case (results not shown), the canopy models had more difficulty mimicking the measurement results.

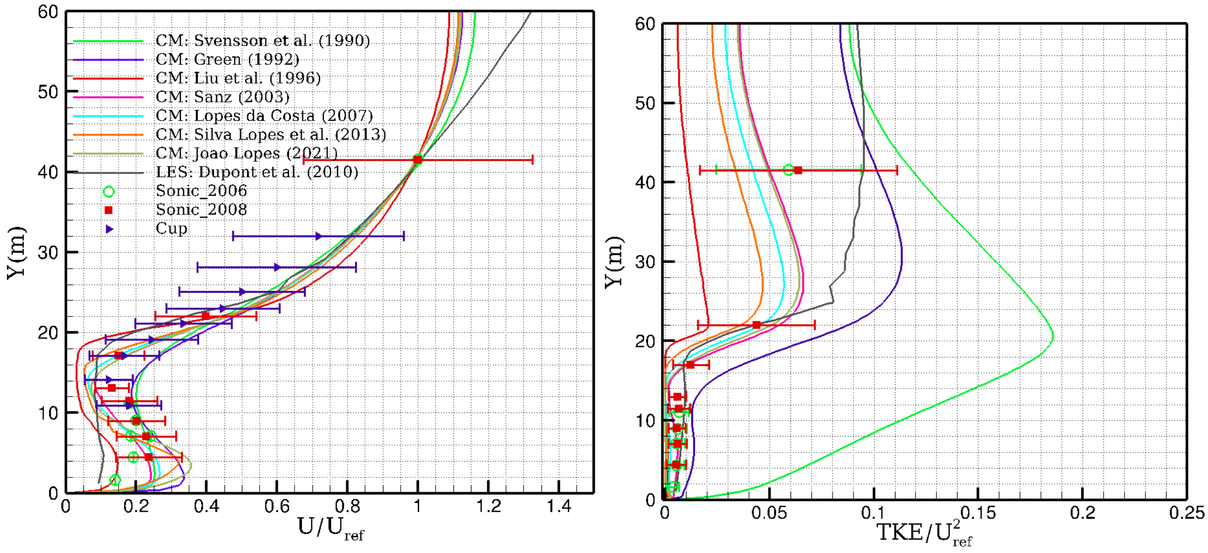

(a) Wind speed

(b) Turbulent kinetic energy

Figure 1: Results for the homogeneous case

4 Conclusions

Seven canopy models were evaluated in neutrally-stratified flow over flat terrain in stand and edge flow. The stand case, models Svensson [2] and Sanz [5] had the lowest rmse (0.0541 at sonic 2006 and 0.0448 at sonic 2008) the U_h. Turbulent kinetic energy was well represented by Sanz [5] and Viana [1] (rmse = 0.0066 and 0.0074 at sonic 2008). In terms of mimic of Reynolds shear stress, Liu [4] yielded the best results (rmse = 0.1907 at sonic 2008). For the edge case, the U_h profile was better represented by Lopes [7] (rmse = 0.2575), which yielded also the lowest rmse = 0.0075 for the tke, whereas Liu [4] was the best in terms of the Reynolds shear stress (rmse = 0.8346). In general, Lopes [7] was the one that consistently showed lower rmse in these two cases.

Acknowledgements:
The first author acknowledges the support of Ministry of Higher Education, Science, Technology and Innovation (MESCTI) of Angola.

References

[1] Viana Parente Lopes J M, Palma J M L M and Lopes A S 2021 *J. Fluid Mech.* **910** 7

[2] Svensson U and Häggkvist K 1990 *J. Wind. Eng. Ind. Aerodyn.* **35** 201–211

[3] Green S 1992 *PHOENICS J. Comput. Fluid Dyn. its Appl.* **5** 294–312

[4] Liu J, Chen J M, Black T A and Novak M D 1996 *Bound.-Layer Meteorol* **77** 2–44

[5] Sanz C 2003 *Bound.-Layer Meteorol* **108** 191–197

[6] Lopes da Costa J C, Castro F A, Palma J and Stuart P 2006 *J. Wind. Eng. Ind. Aerodyn.* **94** 603–620

[7] Lopes A S, Palma J M and Lopes J V 2013 *Bound.-Layer Meteorol* **149** 231–257

[8] Dupont S and *et al* 2011 *Agric. For. Meteorol.* **151** 328–344